
Electronic Thesis and Dissertation Repository

9-18-2014 12:00 AM

Radiation Induced Corrosion of Stellite-6

Mehran Behazin

The University of Western Ontario

Supervisor

Dr. J.C. Wren

The University of Western Ontario

Graduate Program in Chemistry

A thesis submitted in partial fulfillment of the requirements for the degree in Doctor of Philosophy

© Mehran Behazin 2014

Follow this and additional works at: <https://ir.lib.uwo.ca/etd>

 Part of the [Physical Chemistry Commons](#)

Recommended Citation

Behazin, Mehran, "Radiation Induced Corrosion of Stellite-6" (2014). *Electronic Thesis and Dissertation Repository*. 2434.

<https://ir.lib.uwo.ca/etd/2434>

This Dissertation/Thesis is brought to you for free and open access by Scholarship@Western. It has been accepted for inclusion in Electronic Thesis and Dissertation Repository by an authorized administrator of Scholarship@Western. For more information, please contact wlsadmin@uwo.ca.

RADIATION-INDUCED CORROSION OF STELLITE-6

(Thesis format: Integrated Article)

by

Mehran Behazin

Graduate Program in Chemistry

A thesis submitted in partial fulfillment
of the requirements for the degree of
Doctor of Philosophy

The School of Graduate and Postdoctoral Studies
The University of Western Ontario
London, Ontario, Canada

© Mehran Behazin 2014

Abstract

This thesis presents a study on the aqueous corrosion of a cobalt-based alloy, Stellite-6. Since aqueous corrosion kinetics are strongly influenced by water chemistry conditions (pH, temperature, and redox agents), a systematic study of Stellite-6 corrosion was carried out. The aim was to develop an ability to predict corrosion behaviour and particularly metal dissolution rates for cobalt alloys under a range of conditions. The work focused on a study of the influence of ionizing radiation on corrosion. This is of particular interest in the nuclear industry where radiation fields are present. Ionizing radiation creates oxidizing radiolysis products and alters the redox potential of a corroding solution.

A series of electrochemical measurements and corrosion tests along with post-test surface analyses were performed. In doing these tests we gathered information on the state of the oxide formed during corrosion and the sensitivity of the oxide growth to the corrosion conditions. This is a more sophisticated approach than that used in many corrosion experiments that only examine a few facets of oxide formation. The combination of electrochemical measurements and surface analyses provided a highly detailed picture of oxidation. We found that corrosion proceeds through the formation of different oxides at different corrosion potentials. At higher potentials the result is the formation of a $\text{Co}(\text{OH})_2$ oxide layer on top of a CoCr_2O_4 layer.

The rate and extent of oxidation and the rate of metal dissolution were sensitive to all parameters studied and particularly the pH of the corroding solution. Oxide growth is promoted and metal dissolution is suppressed at $\text{pH} \sim 10$ where the solubility of Co^{II} is the lowest. The production of water radiolysis products via gamma irradiation was seen to have

a net oxidizing effect and stimulated oxide growth at high pH. At all temperatures studied (25 to 150 °C) irradiation did not result in significant oxide compositional changes. However the extent of metal dissolution was seen to be dependent on a combination of both pH and solution electrolyte concentration, as well as the presence of ionizing radiation.

Keywords:

Stellite-6, cobalt-chromium alloy, cobalt oxides, film conversion, oxide dissolution, interfacial reactions, electrochemical reactions, water radiolysis

Dedication

To my wonderful parents

Co-Authorship Statement

This Thesis includes published data (chapters 4 and 5). For the published parts, I was the experimental investigator and writer.

Acknowledgments

The contributions of many special people, in their unique ways, have made this long journey possible. I would like to extend my sincere gratitude to the following people.

I would like to thank my supervisor, Dr. Clara Wren. She gave me the opportunity to challenge myself and encouraged me to think beyond the “surface”. Not only did she aid in the research aspect of my project, she also provided emotional support and encouragement that helped guide me through the rocky voyage finishing my thesis. This work would not have been possible without her mentorship. I cannot thank her enough; one day I hope to make her proud.

I would like to thank Dr. Jamie Noël for all of our scientific discussions and, in particular, his patience during the process of preparing my manuscripts. Dr. Jiju Joseph has been caring and a great source of support over the past five years. Dr. Dave Wren played an important role in the writing process and has provided valuable professional advice.

I would like to thank my wonderful friends and also all of my student peers, both past and present, in the Wren lab and Shoemsmith lab. A special acknowledgement goes to two of my friends, Justin Chiodo and Nastaran Yousefi, who have been extremely supportive in every way.

Most importantly, I would like to thank my parents and my brother from the bottom of my heart for their unconditional support, both financially and emotionally, throughout my academic career. Words cannot express the full extent of my appreciation.

Table of Contents

Abstract.....	ii
Dedication.....	iv
Co-Authorship Statement.....	v
Acknowledgments.....	vi
Table of Contents.....	vii
Symbols and Acronyms.....	xv
List of Tables.....	xvii
List of Figures.....	xix
List of Appendices.....	xxxi
Chapter 1. Introduction.....	1
1.1 Thesis Motivation.....	1
1.2 Research Objectives and Approaches.....	4
1.3 Thesis Outline.....	5
1.4 References.....	6
Chapter 2. Technical Background and Literature Reviews.....	8
2.1 Cobalt and Cobalt-based Alloys.....	8
2.2 Corrosion Principle.....	10
2.2.1 Corrosion Potential and Corrosion Rate.....	15

2.2.2	Effect of Aqueous Redox Conditions on E_{corr} and i_{corr}	19
2.2.3	Corrosion of Stellite-6.....	21
2.2.3.1	Cobalt and Chromium Oxides.....	21
2.2.3.1.1	CoO/Co(OH) ₂	21
2.2.3.1.2	Co ₃ O ₄ and CoOOH.....	23
2.2.3.1.3	Cr ₂ O ₃ and CoCr ₂ O ₄	24
2.2.4	Review of Cobalt Oxide Formation	26
2.2.4.1	The Behaviour of the Co-H ₂ O System at 25-150 °C	26
2.2.4.2	The Behaviour of the Cr-H ₂ O System at 25-150 °C	33
2.2.4.3	Cobalt Oxide Formation.....	35
2.2.4.4	The Role of Other Stellite-6 Constitutes in Oxidation.....	36
2.2.4.4.1	Effect of Chromium-Carbon	37
2.2.4.4.2	Effect of Mo and W.....	37
2.3	Oxide Growth Mechanism.....	39
2.4	Radiation and Water Radiolysis	42
2.4.1	Radiation Chemistry.....	42
2.4.2	The Effect of Radiation on Transition Metal Alloy Corrosion	53
2.5	References	55

Chapter 3. Experimental Techniques and Procedures.....	61
3.1 Electrochemical Techniques.....	61
3.1.1 Electrochemical Cell	61
3.1.2 Cyclic Voltammetry	62
3.1.3 Potentiostatic Polarization.....	64
3.1.4 Electrochemical Impedance Spectroscopy.....	64
3.2 Surface Analysis	71
3.2.1 Scanning Electron Microscopy	71
3.2.2 X-Ray Photoelectron Spectroscopy	73
3.2.3 Auger Electron Spectroscopy.....	75
3.2.4 Inductively-Coupled Plasma Mass Spectrometry	76
3.3 Experimental Procedures.....	77
3.3.1 Electrochemical Setup.....	77
3.3.2 Surface Analysis Instrumentation	79
3.3.3 Solution Analysis	80
3.4 References	81
Chapter 4. Comparative Study of Film Formation on Pure Co and Stellite-6: Probing The Roles of a Chromium Oxide Layer and Gamma-Radiation.....	82
4.1 Introduction	82
4.2 Experimental.....	83

4.2.1	Solutions.....	84
4.2.2	Radiation Source	85
4.2.3	Procedure.....	85
4.3	Result and Discussion.....	86
4.3.1	Corrosion Potentials under γ -irradiation	86
4.3.2	Oxide Formation and Conversion under Potentiodynamic Conditions	88
4.3.3	Oxide Formation and Conversion under Potentiostatic Conditions.....	101
4.3.3.1	Film Growth on Cobalt	108
4.3.3.1.1	Film Growth at $-0.7 V_{SCE}$	108
4.3.3.1.2	Film Growth at $-0.2 V_{SCE}$	110
4.3.3.1.3	Film Growth at $+0.2 V_{SCE}$	112
4.3.3.2	Film Growth on Stellite-6	114
4.3.3.2.1	Film Growth at $-0.7 V_{SCE}$	114
4.3.3.2.2	Film Growth at $-0.2 V_{SCE}$	115
4.3.3.2.3	Film Growth in Potential Range of 0.1 to 0.4 V_{SCE}	117
4.4	Conclusions	119
4.5	References	120

Chapter 5. Combined Effects pH and γ-Irradiation on Corrosion of Stellite-6	123
5.1 Introduction	123
5.2 Experimental.....	124
5.2.1 Solution Preparation.....	124
5.2.2 Aqueous Corrosion Experiments	125
5.3 Aqueous Corrosion Tests.....	126
5.3.1 SEM Results.....	126
5.3.2 XPS Results.....	128
5.3.3 AES Results.....	131
5.3.4 ICP-MS Results.....	137
5.3.5 Summary of the Corrosion Study.....	138
5.4 Electrochemical Experiments	138
5.4.1 Corrosion Potential Measurements	139
5.4.2 Potentiostatic Polarization Experiments.....	140
5.4.2.1 Long-term Steady-state Current Behaviour	140
5.4.2.2 Short-term current behaviour	148
5.5 Corrosion Kinetic Mechanism.....	151
5.5.1 General Corrosion Kinetic Mechanism.....	151

5.5.2	Effects of pH and γ -Radiation on Corrosion Kinetics.....	155
5.5.2.1	Effect of pH in the Absence of Radiation	155
5.5.2.2	Combined Effects of Radiation and pH	157
5.6	Conclusions	159
5.7	References	160

Chapter 6. Corrosion Kinetics on Co-Cr Alloy Stellite-6 Under Potentiostatic Polarization at 25 °C Versus 80 °C 163

6.1	Introduction	163
6.2	Experimental Procedures	164
6.3	Results and Discussion	164
6.3.1	Potentiostatic Polarization Results	164
6.3.2	Electrochemical Equilibrium Potentials.....	174
6.3.3	Surface Analyses of Oxides Formed by Potentiostatic Polarization	177
6.3.4	Effect of Temperature on Corrosion Kinetics	186
6.4	Conclusion.....	187
6.5	References	188

Chapter 7. Combined Effects of pH and γ -Radiation on Corrosion of Co-Cr Alloy Stellite-6 at 80 °C and 150 °C 190

7.1	Introduction	190
7.2	Experimental.....	191

7.3	Results	193
7.3.1	Effects of pH and γ -radiolysis at 80 °C.....	194
7.3.1.1	SEM and XPS Analysis Results.....	194
7.3.1.2	AES and ICP-MS Analysis Results	199
7.3.2	Effects of pH and γ -radiolysis at 150 °C.....	207
7.3.2.1	SEM and XPS Analysis Results.....	207
7.3.2.2	AES and ICP-MS Analysis Results	211
7.4	Discussion.....	217
7.4.1	Corrosion Mechanism	218
7.4.2	Corrosion Rate Parameters.....	222
7.4.3	Effects of pH, Temperature and γ -radiolysis on Rate Parameters .	226
7.5	Conclusions	232
7.6	References	233
Chapter 8. Effects of Borate on Corrosion of Stellite-6.....		236
8.1	Introduction	236
8.2	Experimental.....	237
8.3	Results and Discussion	238
8.3.1	Results at 80 °C.....	238
8.3.2	Results at 150 °C.....	247
8.4	Conclusion.....	255

8.5	References	255
Chapter 9.	Summary and Future Work	257
9.1	Summary.....	257
9.2	Future Work.....	261
Appendix A.	264
Curriculum Vitae	277

Symbols and Acronyms

Symbols

a_A	Anodic transfer coefficient
a_c	Cathodic transfer coefficient
atm	Atmosphere pressure
α	Transfer coefficient of anodic reaction
β	Transfer coefficient of cathodic reaction
C	Capacitance
$^{\circ}\text{C}$	Degrees Celsius
D_R	Dose rate
E	Electrochemical potential
E	Applied potential
E_{amp}	Amplitude of EIS sinusoidal potential
E_{eq}	Equilibrium potential
E_o	Standard potential
E_{APP}	Applied potential
E_{corr}	Corrosion potential
ΔE_f	Oxide potential drop
ΔE_{rdx}	Different between equilibrium potentials of two half reactions
E_{initial}	Initial potential
E_{final}	Final potential
F	Faraday constant
Gy	Gray
$\Delta_r G$	Free energy change of a reaction
$\Delta_r G_o$	Standard free energy of a reaction
h	Plank constant
i	Current (density)
i_a	Anodic current
i_0	Exchange current
i_{amp}	EIS current amplitude
i_{ox}	Oxidation current density
i_c	Cathodic current density
i_{corr}	Corrosion current
i_{red}	Reduction current density
i_{SS}	Steady state current density
k_{ox}	Rate constant of oxidation
k_{red}	Rate constant of reduction
K_{eq}	Equilibrium constant
K_w	Equilibrium constant of water
n	Number of electrons
Q	Charge

R	Universal gas constant
R_x	General resistance
R_P	Solution resistance
R_s	Solution resistance
R_{film}	Film resistance
t	Time
T	Absolute temperature (K)
V_{SCE}	Potential vs. SCE
Y_0	CPE parameter
Z	Impedance
Z'	Real impedance
Z''	Imaginary impedance
Z_{CPE}	Impedance from CPE
α	CPE exponent
η	Overpotential
η^{eff}	Effective overpotential
ρ	Density
θ	Phase shift
ν	Light frequency
Φ	Work function
ω	Angular frequency

Acronyms

AES	Auger Electron Spectroscopy
BE	Binding Energy
BSE	Backscattered Electron
CANDU	CANada Deuterium Uranium
CPE	Constant Phase Element
CV	Cyclic Voltammetry/Voltammogram
EIS	Electrochemical Impedance Spectroscopy
Fcc	Face Cubic Centre
HIP	Hot Isostatically Pressed
hcp	Hexagonal Close Packed
KE	Kinetic Energy
LET	Linear Energy Transfer
PDM	Point defect model
PTFE	Polytetrafluoroethylene
St-6	Stellite-6
SCE	Saturated Calomel Electrode
SEM	Scanning Electron Microscopy
SHE	Standard Hydrogen Electrode
EDX	Energy dispersive X-Ray Spectroscopy
XPS	X-Ray Photoelectron Spectroscopy

List of Tables

Table 2.1: Elemental composition of some of the most frequently used Stellite alloys (wt.%).	9
Table 2.2: Crystallographic structures of cobalt oxides [38].	26
Table 2.3: The primary yields ($\mu\text{mol}\cdot\text{J}^{-1}$) from γ -radiolysis of liquid water at different temperatures [72].	48
Table 5.1: Cobalt speciation in the top 9 nm layer as determined by XPS analysis at 25 °C.	130
Table 5.2: Dissolved cobalt content after 3-d corrosion.	138
Table 5.3: Summary of the potentiostatic polarization experiments.	145
Table 7.1: Cobalt speciation in the surface layer on the Stellite-6 coupons corroded at 80 °C determined by the analysis of the high resolution XPS of the Co 2p bands.	198
Table 7.2: The concentrations of Co and Cr dissolved in the test solutions after 3-d corrosion at 80 °C determined by ICP-MS.	203
Table 7.3: Cobalt speciation in the surface layer on the Stellite-6 coupons corroded at 150 °C determined by the analysis of high resolution XPS of the Co 2p bands.	210
Table 7.4: Dissolved concentrations of Co and Cr after 3-d corrosion at 150 °C determined by ICP-MS.	213

Table 8.1: Dissolved Co and Cr concentrations after 3-d corrosion at 80 °C determined by ICP-MS. 246

Table 8.2: Dissolved Co and Cr concentrations after 3-d corrosion at 150 °C determined by ICP-MS. 252

List of Figures

- Figure 1.1:** The arrow shows the location of Stellite-6 balls for the fuelling machine ram screw drive at the rear of the fuelling machine..... 2
- Figure 1.2:** Schematic of the release of ^{59}Co to a reactor coolant circuit, transformation to ^{60}Co , and deposition elsewhere..... 3
- Figure 2.1:** SEM image of freshly polished Stellite-6. 9
- Figure 2.2:** Illustration of corrosion reactions a) in the presence of only the natural oxide layer (Cr_2O_3), b) incorporation of Co^{II} into Cr_2O_3 to form CoCr_2O_4 , and c) the formation of $\text{CoO}/\text{Co}(\text{OH})_2$ 12
- Figure 2.3:** Current-potential relationships for the anodic and cathodic half reactions and the net corrosion reaction, illustrating the effect of coupled aqueous half reactions on E_{corr} and i_{corr} 17
- Figure 2.4:** Simplified plot of current- potential relationship for a corroding system consisting of a metal oxidation half reaction and a hydrogen peroxide reduction half reaction. The concentration of H_2O_2 is higher in b) than in a). 20
- Figure 2.5:** Crystal structures of (a) CoO and (b) $\text{Co}(\text{OH})_2$, and (c) a primitive cell of α - $\text{Co}(\text{OH})_2$ and β - $\text{Co}(\text{OH})_2$ (the box shown in (b)) [29]. 22

Figure 2.6: Unit cell (on the left) and primitive cell (on the right) of Co_3O_4 . Light cyan and navy blue balls indicate Co^{2+} and Co^{3+} ions, respectively, and red balls indicate O^{2-} ions [31].	23
Figure 2.7: Layered crystal structure of CoOOH (ball and stick model).	24
Figure 2.8: Crystal structure of Cr_2O_3 [33].	25
Figure 2.9: Solubility of hydrolyzed Co^{2+} species as a function of pH at 25 °C.	29
Figure 2.10: Pourbaix diagram of the Co- H_2O system at 25 °C with all ions at an activity of 10^{-6} M. The potential scale is with respect to the standard hydrogen electrode (SHE) [40]. .	31
Figure 2.11: Pourbaix diagram of the Co- H_2O system at 75 °C with all ions at an activity of 10^{-6} M. The potential scale is with respect to the standard hydrogen electrode (SHE) [40]. .	32
Figure 2.12: Pourbaix diagram of the Co- H_2O system at 100 °C with all ions at an activity of 10^{-6} M. The potential scale is with respect to the standard hydrogen electrode (SHE) [40]. .	32
Figure 2.13: Pourbaix diagram of the Co- H_2O system at 150 °C with all ions at an activity of 10^{-6} M. The potential scale is with respect to the standard hydrogen electrode (SHE) [40]. .	33
Figure 2.14: Influence of pH on the solubility of Cr_2O_3 and $\text{Cr}(\text{OH})_3$, at 25 °C [9].	34
Figure 2.15: Pourbaix diagram of the Cr- H_2O system at 25 °C with all ions at an activity of 10^{-5} M. The potential scale is with respect to the standard hydrogen electrode (SHE) [9]. The lines labelled 0, -2, -4 and -6 correspond to order of concentrations of Cr^{3+}	35

Figure 2.16: The radiation track of a fast electron showing spurs (spur size not to scale)....	47
Figure 2.17: The effect of ionizing radiation on water.	48
Figure 2.18: Model simulation results that illustrate the effect of pH on radiolysis chemistry in deaerated water at a dose rate of $5.5 \text{ kG}\cdot\text{h}^{-1}$ at $25 \text{ }^\circ\text{C}$ [15].	50
Figure 2.19: Model simulation results that illustrate the effect of pH on radiolysis chemistry in deaerated water at a dose rate of $5.5 \text{ kG}\cdot\text{h}^{-1}$ at $150 \text{ }^\circ\text{C}$ [15].	51
Figure 3.1: Standard three-electrode electrochemical cell.	62
Figure 3.2: The potential-time profile applied in a cyclic voltammetry experiment.	63
Figure 3.3: Schematic of the applied sinusoidal potential and the current response for electrochemical impedance spectroscopy. The parameters are defined in the text.	65
Figure 3.4: Schematic of the linear current-potential response measured when a small $\pm E_0$ is applied in electrochemical impedance spectroscopy for a corrosion reaction occurring at steady state.	66
Figure 3.5: Relationship of the real and imaginary components of impedance in a series one-RC circuit.	68
Figure 3.6: EIS data presentation: (a) Nyquist plot and (b) Bode plot.	69
Figure 3.7: Equivalent circuits containing: a) one time constant and b) two time constants.	70

Figure 3.8: Schematic demonstrating the principles of XPS and the ejection of a photoelectron.....	74
Figure 3.9: Schematic demonstrating the principles of AES and the ejection of an Auger electron.....	76
Figure 4.1: SEM images of the surfaces of freshly prepared Co on the left hand panels and freshly prepared Stellite-6 on the right hand panels. Two magnification scales are used to show the degree of surface uniformity.....	84
Figure 4.2: E_{corr} as a function of time recorded on Co and Stellite-6 electrodes in an Ar-purged borate solution at pH 10.6 and room temperature, in the presence and absence of γ -irradiation.....	88
Figure 4.3: Calculated equilibrium potentials for various redox reactions (at pH _{25°C} 10.6) are indicated by vertical lines. The coloured bar at the top indicates the potential regions for Co oxidations.....	89
Figure 4.4: Cyclic voltammograms obtained on Co. The CVs were recorded at a scan rate of $5 \text{ mV}\cdot\text{s}^{-1}$	90
Figure 4.5: Cyclic voltammograms recorded on Stellite-6 for two potential scan ranges: (a) $-1.1 \text{ V}_{\text{SCE}}$ to $0.1 \text{ V}_{\text{SCE}}$ and (b) $-1.1 \text{ V}_{\text{SCE}}$ to $0.6 \text{ V}_{\text{SCE}}$. The first cycle of a CV recorded on Co is also shown in Figure 4.5a for comparison.	96

Figure 4.6: Cyclic voltammograms recorded on pure chromium for two potential scan ranges and compared with Stellite-6: (a) $-1.1 V_{SCE}$ to $0.3 V_{SCE}$, and (b) $-1.1 V_{SCE}$ to $0.6 V_{SCE}$ 97

Figure 4.7: Electrochemical impedance spectra recorded at various times during film growth at $0.2 V_{SCE}$ on Stellite-6: Bode plots of the impedance magnitude and phase angle. 103

Figure 4.8: Electrochemical impedance spectra recorded at various times during film growth at $0.2 V_{SCE}$ on Stellite-6: Bode plots of an example of a model fit to an experimental spectrum. The equivalent circuit used for the EIS analysis is shown inset. 103

Figure 4.9: Polarization resistance (\square) and capacitance (\circ) as a function of time during potentiostatic film growth at $-0.2 V_{SCE}$ (upper figures) and $0.2 V_{SCE}$ (lower figures) on Co and Stellite-6. The resistance and capacitance values were obtained from fits to EIS spectra using the equivalent circuit model shown in the inset of (b). The error bars include only the model-fitting errors which in most cases are smaller than the sizes of the symbols representing the data. 105

Figure 4.10: High resolution XPS spectrum of the Co 2p band (and its deconvoluted components) for a film grown at $0.15 V_{SCE}$ on Stellite-6. The inset shows that the CoOOH spectrum consists of multiple peaks. 106

Figure 4.11: Speciation on the surface of Co as a function of applied potential determined by XPS analysis: (a) Co oxides and (b) O^{2-}/OH^- 107

Figure 4.12: Speciation on the surface of Stellite-6 as a function of applied potential determined by XPS analysis: (a) Co oxides and (b) ratios of metallic Cr/total Cr and O^{2-}/OH^{-} .	108
Figure 4.13: Current as a function of time observed during potentiostatic film growth at -0.7 , -0.2 , and $0.2 V_{SCE}$, on Co. The + and – signs indicate anodic and cathodic currents, respectively.	109
Figure 4.14: Current as a function of time observed during potentiostatic film growth at -0.7 , -0.2 , and $0.2 V_{SCE}$, on Stellite-6. The + and – signs indicate anodic and cathodic currents, respectively.	115
Figure 4.15: Current as a function of time observed during potentiostatic film growth at 0.1 , 0.15 , 0.25 , 0.3 and $0.4 V_{SCE}$ on Stellite-6.	118
Figure 5.1: SEM images of Stellite-6 coupons corroded under different conditions: freshly polished, at pH 10.6 without and with irradiation (Rad), and at pH 6.0 and pH 8.4 with irradiation.	127
Figure 5.2: High resolution XPS spectrum of the Co 2p band region and its deconvoluted components for a coupon irradiated at pH 10.6.	129
Figure 5.3: Depth profiles of the elements determined by AES of Stellite-6 coupons corroded for 3 d (a) at pH 6.0 without irradiation and (b) irradiated at pH 10.6.	131

Figure 5.4: Depth profiles of $O/(Co+1.5 Cr)$ and $Co/(Co+Cr)$ on coupons corroded at different pHs: 10.6 (—■—), 8.4 (—●—), and 6.0 (—▲—). The left panels (a) present the results obtained in the absence of radiation and the right panels (b) present the results obtained in the presence of radiation. 134

Figure 5.5: E_{CORR} as a function of time recorded on the Stellite-6 electrodes with (—) and without (----) γ -irradiation at different pHs. 140

Figure 5.6: Net charge, Q , accumulated as a function of time during potentiostatic polarization at pH a) 10.6, b) 8.4, c) 6.0. The numbers in the figure represent the applied potential, E_{APP} . The Roman numerals represent different oxide growth regions as summarized in Table 5.3. Different colors and styles differentiate four regions. 144

Figure 5.7: Calculated equilibrium potentials for cobalt oxidation reactions at different pH values at 25 °C. In calculating the equilibrium potential for the oxidation to $Co^{2+}(aq)$, two concentrations of $Co^{2+}(aq)$ (10^{-6} and 10^{-9} M) were used. Vertical dashed line indicates pH 8.4..... 146

Figure 5.8: Current density observed as a function of time during potentiostatic polarization at $E_{APP} > 0.0 V_{SCE}$ at a) pH 6.0, b) pH 8.4, and c) pH 10.6. 150

Figure 5.9: Schematic illustration of corrosion reactions in the presence of an oxide layer. Five distinct processes are numbered on the diagram: (1) metal oxidation, (2a) water reduction, (3) mass transport across the existing oxide, (4) oxide growth, and (5a and b) metal cation hydration and dissolution. 152

Figure 5.10: Schematic diagram showing the relationship between the energetics and kinetics of the corrosion half-reactions taking place on an oxide-covered metal surface. ... 154

Figure 6.1: Current as a function of time observed during potentiostatic polarization on Stellite-6 at a) 25 °C and b) 80 °C. The Roman numerals correspond to the potential region. The numbers indicate the applied potentials in V_{SCE} 166

Figure 6.2: Accumulated charge as a function of time observed during potentiostatic polarization on Stellite-6 at a) 25 °C and b) 80 °C. The results are separated based on the oxidation potential regions discussed in the text. The numbers indicate the applied potentials in V_{SCE} 167

Figure 6.3: Electrochemical equilibrium potentials for the redox reactions of Co and Cr species at $pH_{25^{\circ}C}$ 10.6. The vertical bars show the equilibrium potentials and the corresponding redox pairs are listed on both sides of these bars. The potential ranges where the different oxides are thermodynamically stable are shown in the bar at the top of the graph. Above the graph are two additional bars that show the locations of the potential regions determined from the polarization experiments at 25 °C and 80 °C. 176

Figure 6.4: Speciation of the cobalt oxide on the surface of Stellite-6 as a function of applied potential determined by XPS analysis at 25 °C. 177

Figure 6.5: SEM images of Stellite-6 surfaces corroded following 3 h polarization at $-0.7 V_{SCE}$, $-0.4 V_{SCE}$, $-0.2 V_{SCE}$, and $0.1 V_{SCE}$ at $pH_{25^{\circ}C}$ 10.6 at 80 °C..... 179

Figure 6.6: Speciation of the cobalt oxide on the surface of Stellite-6 as a function of applied potential determined by XPS analysis at 80 °C.	181
Figure 6.7: Depth profiles of all of the elements determined by AES of Stellite-6 surfaces corroded following 3 h polarization at $-0.7 V_{SCE}$, $-0.4 V_{SCE}$, $-0.2 V_{SCE}$ and $0.1 V_{SCE}$, at $pH_{25^{\circ}C}$ 10.6, at 80 °C.	182
Figure 6.8: Depth profiles on the Stellite-6 surfaces following 3-h polarization at potentials in different regions at 80 °C showing the ratio of a) $O/(Co+1.5Cr)$ and b) $Co/(Co+Cr)$	183
Figure 7.1: Schematic diagram of the experimental set-up, showing the test vial arrangement in the pressure vessel.	193
Figure 7.2: SEM images of the surfaces of Stellite-6 coupons corroded for 3 d at $pH_{25^{\circ}C}$ 6.0, 8.4 and 10.6 in the absence (no Rad) and in the presence of radiation (Rad) at 80 °C. The darker coloured region corresponds to the Cr-rich phase.	196
Figure 7.3: Ratio of the Co oxide component to the sum of the Co oxide and Co metal components in the high resolution XPS of the Co 2p bands (f_{oxide}) taken for a) the un-irradiated and b) the irradiated coupons at three $pH_{25^{\circ}C}$ values at 80 °C.	198
Figure 7.4: Depth profiles of the elements on Stellite-6 coupons corroded for 3 d in the absence of radiation (no Rad) and in the presence of radiation (Rad) at three pHs at 80 °C.	200

Figure 7.5: Depth profiles of O/(Co + 1.5 Cr) and Co/(Co + Cr) determined by AES on Stellite-6 coupons corroded at pH_{25°C}: 10.6 (—■—), 8.4 (—●—), and 6.0 (—▲—). The left panel a) presents the results obtained in the absence of radiation and the right panel b) presents the results obtained in the presence of radiation at 80 °C..... 201

Figure 7.6: SEM images of the surfaces of the Stellite-6 coupons corroded for 3 d at three different pH_{25°C} values, in the absence and presence of radiation, at 150 °C..... 209

Figure 7.7: Ratio of oxide to sum of oxide and Co metal (f_{oxide}) as determined by XPS analysis of a) un-irradiated, and b) irradiated coupons at three pH values at 150 °C..... 210

Figure 7.8: Depth profiles of the elements determined by AES of Stellite-6 coupons corroded for 3 d in the absence of radiation (left hand side) and in the presence of radiation (right hand side) at pH_{25°C} 10.6, 8.4, 6.0, at 150 °C..... 212

Figure 7.9: Depth profiles of O/(Co + 1.5 Cr) and Co/(Co + Cr) determined by AES on Stellite-6 coupons corroded at pH_{25°C}: 10.6 (—■—), 8.4 (—●—), and 6.0 (—▲—). The left panel a) presents the results obtained in the absence of radiation and the right panel b) presents the results obtained in the presence of radiation, at 150 °C..... 213

Figure 7.10: Schematic illustration of corrosion reactions in the presence of an oxide layer.
..... 220

Figure 7.11: Solubility of hydrolyzed Co²⁺ species as a function of pH at 25 °C. 227

Figure 7.12: The solubility of Co(II) oxides as a function of temperature at different pHs [30].....	228
Figure 7.13: E_{corr} as a function of time recorded on the Stellite-6 electrodes at and 25 °C in the absence (—), and the presence of radiation (—) at (a) $\text{pH}_{25^\circ\text{C}}$ 10.6 and (b) $\text{pH}_{25^\circ\text{C}}$ 8.4....	230
Figure 7.14: E_{corr} as a function of time recorded on the Stellite-6 electrodes at 25 °C (—), 80 °C (—), and 150 °C (—) in absence of radiation at $\text{pH}_{25^\circ\text{C}}$, (a) 10.6, (b) 8.4.....	231
Figure 8.1: SEM images of samples corroded in NaOH-only and borate solutions at pH 10.6 in the presence and absence of radiation at 80 °C.	239
Figure 8.2: Backscattered electron images of surfaces corroded in an NaOH-only solution in the presence of radiation at 80 °C.....	240
Figure 8.3: EDX analysis of a selected crystallite on the surface corroded in an NaOH-only solution in the presence of radiation at 80 °C.....	241
Figure 8.4: Depth profiles of the elements determined by AES of Stellite-6 coupons corroded for 3 d in the absence of radiation (left hand side) and in the presence of radiation (right hand side) in (a,c) borate, and (b,d) NaOH-only solutions at 80 °C.....	242
Figure 8.5: Depth profiles of O/(Co+1.5 Cr) and Co/(Co+Cr) determined by AES on coupons corroded in NaOH-only and borate solutions at pH 10.6, a) in the absence, and b) in the presence of radiation at 80 °C.....	243

Figure 8.6: SEM images of coupons corroded in NaOH-only at pH 10.6 in the presence and absence of radiation at 150 °C. 248

Figure 8.7: Depth profiles of the elements determined by AES of Stellite-6 coupons corroded for 3 d in the absence of radiation (left hand side) and in the presence of radiation (right hand side), in (a,c) borate and (b,d) NaOH-only solutions at 150 °C. 249

Figure 8.8: Depth profiles of O/(Co+1.5 Cr) and Co/(Co+Cr) determined by AES on coupons corroded in NaOH-only and borate solutions at pH_{25°C} 10.6, a) in the absence and b) in the presence of radiation at 150 °C. 250

List of Appendices

Appendix A: Copyrights

CHAPTER 1

Introduction

1.1 THESIS MOTIVATION

Stellite-6, a Co-based alloy, is the material of choice in the nuclear industry for special applications that require strength and corrosion/wear resistance. It has been employed in hardfacing surfaces on valves and ball-screw bearings in the fuelling machines in CANDU[®] nuclear reactors [1,2]. The approximate location of the ball-screw bearings in a fuelling machine is shown in Figure 1.1. It should be noted that in this location, the Stellite is in a water environment whose temperature can range from 50 °C to 200 °C, and this location will be exposed to a high flux of γ - radiation over long periods when the fuelling machine is loaded with highly radioactive spent fuel bundles.

While Stellite-6 has excellent corrosion and wear resistance, but when subjected to a combination of heat, an oxidizing environment, and wear, the thin, protective oxide film on the alloy could fail, resulting in degradation and dissolution of alloy constituents, particularly Co. The release of Co and the consequent deposition of Co particles in the primary coolant circuit of the nuclear reactor have been important challenges in the nuclear industry [3]. Aside from the material degradation and deposition of corrosion products, there is also a radiological hazard associated with the release of Co into the coolant system. Any ⁵⁹Co (the only natural isotope of cobalt) that is released by corrosion into the reactor coolant may be

transported to the reactor core where it can be transformed into ^{60}Co by neutron absorption. This radioactive ^{60}Co (with a half-life of 5.27 years) can be transported out of the core and deposited in other locations in the reactor coolant system, schematically shown in Figure 1.2. The radioisotope ^{60}Co is the predominant source of out-of-core radiation levels in nuclear reactors during reactor shutdown for maintenance [3]. Although Stellite-6 constitutes only 0.03 % of in-reactor materials it contributes to as much as 70% of the out-of-core activity [4]. The ^{60}Co constitutes a safety hazard for plant workers during shutdown maintenance.

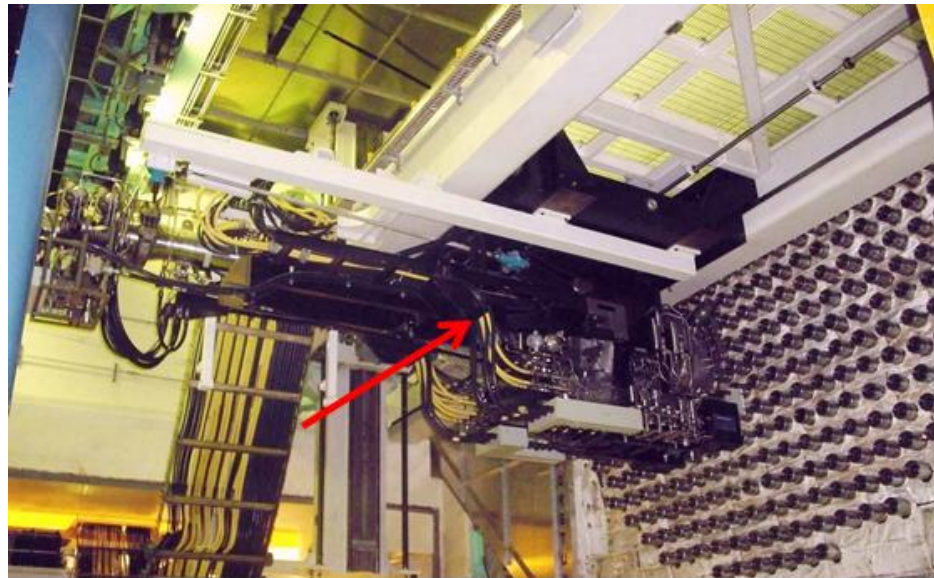


Figure 1.1: The arrow shows the location of Stellite-6 balls for the fuelling machine ram screw drive at the rear of the fuelling machine.

Aside from the safety concerns, additional costs and time are required to decontaminate reactor systems and remove ^{60}Co from radioactive hot spots using decontamination solutions, water cleanup systems and robotic tooling.

Understanding the aqueous corrosion of Co-based alloys is an essential basis for developing strategies and options to limit their corrosion and its consequences. The majority of corrosion research on Stellite alloys has been carried out from a metallurgical perspective [5–12] and there is a lack of clear understanding about the corrosion behaviour of this alloy under different aqueous redox conditions, temperatures and γ -radiation fields.

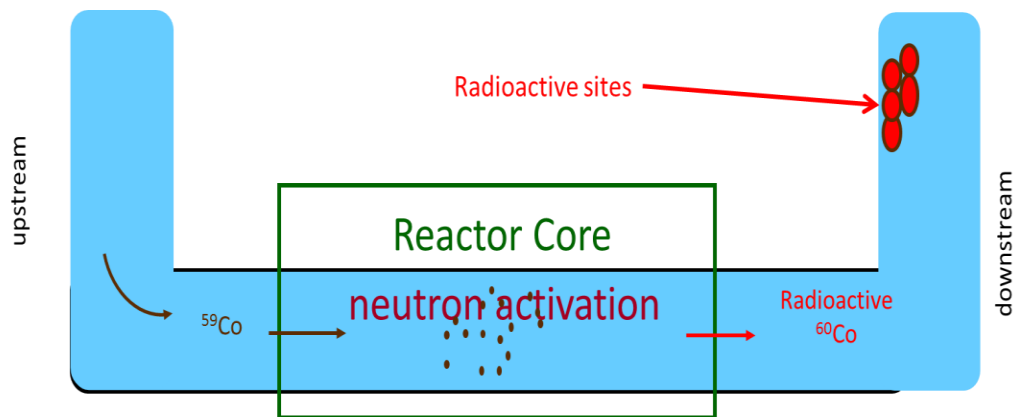


Figure 1.2: Schematic of the release of ^{59}Co to a reactor coolant circuit, transformation to ^{60}Co , and deposition elsewhere.

1.2 RESEARCH OBJECTIVES AND APPROACHES

The overall goal of the Stellite-6 corrosion research is to develop a mechanistic corrosion model that can predict the Stellite-6 corrosion rate under the aqueous conditions to which it is exposed. Towards this goal, the objectives of this research project were: (1) to determine the mechanism of Stellite-6 corrosion and the dependences of the corrosion rate on solution parameters, including pH, temperature, ionic strength and redox potential, (2) to determine the mechanism by which γ -radiation influences the corrosion kinetics of Stellite-6, and (3) to determine, if it exists, the synergistic effect of γ -radiation and any of the solution parameters on the corrosion rate.

Interaction of ionizing radiation with water leads to the formation of primary water radiolysis products that include both highly oxidizing and reducing species (this is further discussed in Chapter 2, section 2.4). Assessing the corrosion rate of in-reactor materials is complicated by the presence of these water radiolysis products, as they significantly alter the water chemistry and, hence, affect the corrosion of materials. Several studies on the effects of ionizing radiation on aqueous corrosion of other reactor materials are available (reviewed in chapter 2). However, no study on cobalt and cobalt alloys has been reported. To achieve the thesis objectives, a number of electrochemical and surface analytical techniques were employed to investigate the effect of γ -radiation on corrosion when the solution environment changes. Since solution parameters also affect radiolysis chemistry, it is important to develop a clear understanding of the separate effects of these parameters.

1.3 THESIS OUTLINE

Chapter 1 includes the thesis motivation, objectives, and approaches, along with the thesis outline.

Chapter 2 presents the materials background, literature reviews, and all the principles required to illustrate and interpret the experimental results in chapters 4-8.

Chapter 3 includes the descriptions of the techniques used to obtain the data reported in Chapters 4-8.

Chapter 4 consists of a comparative study of oxide formation on high-purity Co and Stellite-6 to probe the roles of a chromium oxide layer and gamma-radiation. The oxides that formed were studied both electrochemically and by using surface analytical methods.

Chapter 5 presents the results of experiments on the combined effects of pH and gamma-irradiation on corrosion of Stellite-6. This work was limited to ambient pressure and room temperature.

Chapter 6 includes the results of experiments on the effect of temperature on oxide growth kinetics on Stellite-6. The oxides were formed at ambient pressure, at 80 °C. Both electrochemical and surface analyses were performed.

Chapter 7 present the results of experiments on the combined effects of pH and gamma-irradiation on corrosion of Stellite-6 as a function of temperature

(25 °C < T ≤ 150 °C). Analysis focused on the effects of pH and temperature on oxide formation and Co dissolution.

Chapter 8 includes the results of a study on the effect of borate in solution on corrosion of Stellite-6 at pH 10.6, at 80 °C and 150 °C.

Chapter 9 summarizes the work of this thesis. Scope for future work in this area of research is also discussed briefly.

1.4 REFERENCES

- [1] W.H. Hocking, F.W. Stanchell, E. McAlpine, D.H. Lister, Mechanisms of corrosion of Stellite-6 in lithiated high temperature water, *Corros. Sci.*, 25 (1985) 531–557.
- [2] W.H. Hocking, D.H. Lister, Corrosion of Stellite-6 in lithiated and borated high-temperature water, *Surf. Interface Anal.*, 11 (1988) 45–59.
- [3] C.C. Lin, A review of corrosion product transport and radiation field buildup in boiling water reactors, *Prog. Nucl. Energy.*, 51 (2009) 207–224.
- [4] C. Maffiotte, M. Navas, M.L. Casta, XPS characterization of oxide films formed on cobalt-based alloys during corrosion tests at high temperature, *Surf. Interface Anal.*, 166 (2000) 161–166.
- [5] M.I.T. Honda, A. Minato, Inhibition of radioactive contamination of stainless steel in boiling water reactor, *J. Nucl. Sci. Technol.*, 873 (1983) 871–873.
- [6] S.E. Ziemniak, M.A. Goyette, K.E.S. Combs, Cobalt (II) oxide solubility and phase stability in alkaline media at elevated temperatures, *J. Solution Chem.*, 28 (1999) 809–836.
- [7] C.D. Opris, R. Liu, M.X. Yao, X.J. Wu, Development of Stellite alloy composites with sintering/HIPing technique for wear-resistant applications, *Mater. Des.*, 28 (2007) 581–591.
- [8] U. Malayoglu, A. Neville, G. Beamson, Characterisation of the passive film on HIPed Stellite 6 alloy using X-ray photoelectron spectroscopy, *Mater. Sci. Eng. A.*, 393 (2005) 91–101.
- [9] F.R. Morral, Corrosion of cobalt and cobalt alloys, *Corros. NACE*, 25 (1969) 307.
- [10] U. Malayoglu, A. Neville, H. Lovelock, Assessing the kinetics and mechanisms of corrosion of cast and HIPed Stellite 6 in aqueous saline environments, *Corros. Sci.*, 47 (2005) 1911–1931.
- [11] N.S. McIntyre, D. Zetaruk, E.V. Murphy, X-ray photoelectron spectroscopic study of the aqueous oxidation of Stellite-6 alloy, *Surf. Interface Anal.*, 1 (1979) 105–110.

- [12] A.J. Bard, L.R. Faulkner, *Electrochemical Methods: Fundamentals and Applications*, 2nd Ed., John Wiley & Sons, New York, 2000.
- [13] R. Kelly, J. Scully, D.W. Shoesmith, R. Buchheit, *Electrochemical Techniques in Corrosion Science and Engineering*, CRC Press, New York, 2003.
- [14] M. Pourbaix, *Atlas of Electrochemical Equilibria in Aqueous Solution*, NACE, Houston, Texas, 1996.
- [15] F.M. Tack, O.W. Callewaert, M.G. Verloo, Metal solubility as a function of pH in a contaminated, dredged sediment affected by oxidation, *Environ. Pollut.*, 91 (1996) 199–208.
- [16] N. Perez, *Electrochemistry and Corrosion Science*, Kluwer Academic Publishers, Boston, 2004.
- [17] M.A. Brett, A.M.O. Brett, *Electrochemistry: Principles, Methods, and Applications*, Oxford, New York, 1994.
- [18] J.A.V. Butler, Studies in heterogeneous equilibria. Part II. The kinetic interpretation of the Nernst theory of electromotive force, *Trans. Faraday Soc.*, 19 (1924) 729–733.

CHAPTER 2

Technical Background and Literature Reviews

2.1 COBALT AND COBALT-BASED ALLOYS

Cobalt is a brittle, hard, silver-grey transition metal with magnetic properties similar to those of iron (it is ferromagnetic). The use of cobalt as a constituent in metal alloys is due to the high melting point and strength at elevated temperatures.

The use of Co-based alloys for wear resistance was initiated in the early 1900s with the development of the cobalt-chromium-tungsten family of alloys. The applications of Co-based alloys cover a wide range of sectors from oil and gas to biomedical [1,2]. The cobalt alloys were called "Stellites" because of their bright, shiny, non-tarnished appearance, and quickly became important industrial materials [3,4]. The Stellite alloy family adopted different numbers depending on their Cr, W, and Mo contents. Table 1.1 shows the most frequently used Stellite alloys with their compositions. The work of this thesis used the alloy Stellite-6 because it is the alloy of choice for application in CANDU[®] nuclear reactors.

Stellite alloys contain two phases, a matrix that is enriched in Co with a face-centered cubic (fcc) crystal structure, and dark-coloured islands enriched in Cr in the form of chromium carbide with an orthorhombic structure. The SEM image of a freshly polished Stellite-6 surface is shown in Figure 2.1. The microstructures of Stellite alloys vary considerably with composition, manufacturing process and post-treatment [5].

Table 2.1: Elemental composition of some of the most frequently used Stellite alloys (wt.%).

	W	Mn	Mo	Si	C	Ni	Fe	Cr	Co
Stellite-6	0.27	0.27	0.41	1.1	1.2	3	3	28	bal.
Stellite-3	4.5	1	-	1.1	1.2	3	3	31	bal.
Stellite-20	17.5	1	-	1	2.45	2.5	2.5	33	bal.
Stellite-31	7.5	1	-	1	0.5	10.5	2	25.5	bal.
Stellite-190	14	0.5	-	1	3.3	1	2.5	26	bal.

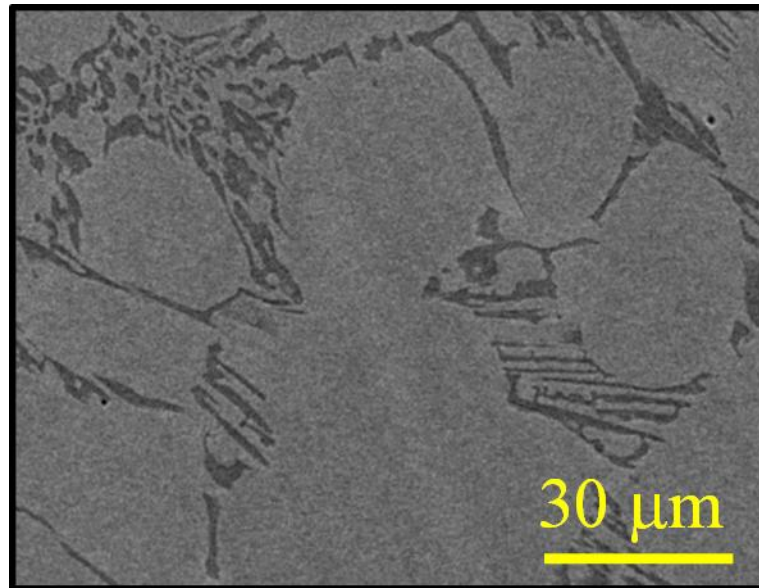
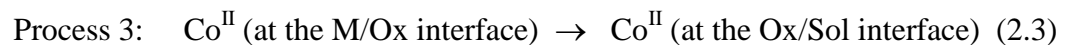
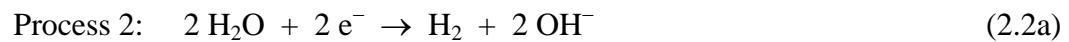
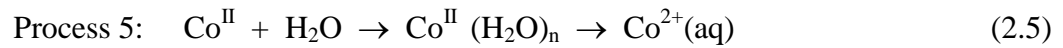


Figure 2.1: SEM image of freshly polished Stellite-6.

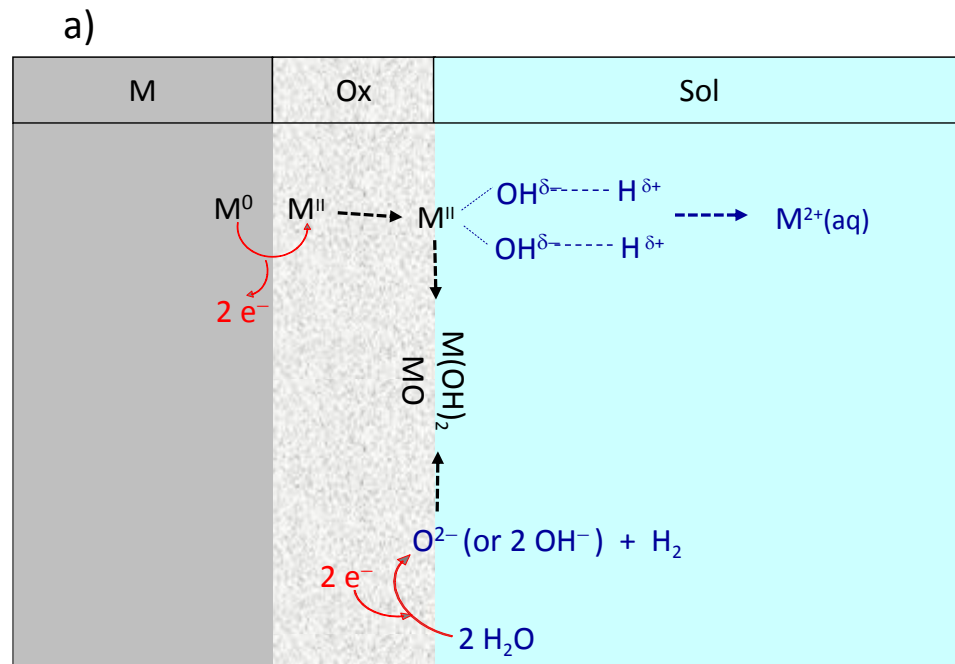
2.2 CORROSION PRINCIPLE

To study the corrosion of Stellite-6 a good understanding of corrosion principles is required. Aqueous corrosion is an electrochemical process involving two redox half-reactions, metal oxidation coupled with reduction of an aqueous species [6–8]. In the presence of a uniform oxide layer, the metal oxidation occurs at the metal/oxide (M/Ox) interface (referred to as Process 1) whereas the reduction of an aqueous species occurs at the oxide/solution (Ox/Sol) interface (Process 2). In order to complete the electrochemical reaction, a net flux of metal cations must proceed from the M/Ox interface to the Ox/Sol interface (or a flux of anions in the other direction) (Process 3). The metal cations can combine with oxygen anions (O^{2-} or OH^-) to form metal oxides or hydroxides (Process 4), or they can dissolve into the solution from the Ox/Sol interface (Process 5) [7,8]. We can thus propose that corrosion of Stellite-6 with an insoluble but defective chromium oxide layer consists of similar steps:





Process 4 (sum of reactions 2.4a and 2.4b) and Process 5 occur in parallel, albeit at different rates, whereas Processes 1, 2, 3 and the sum of 4 and 5 occur in series. Cobalt dissolution (Process 5) competes with oxide formation (Process 4) and the slowest of the processes in series dictates the oxidation rate. In the case of Stellite-6 there is always a natural air-formed Cr_2O_3 oxide layer initially present. Schematics of the processes involved in corrosion are shown in Figure 2.2. Figures 2.2b and 2.2c show the corrosion reactions and how the oxide progressively grows.



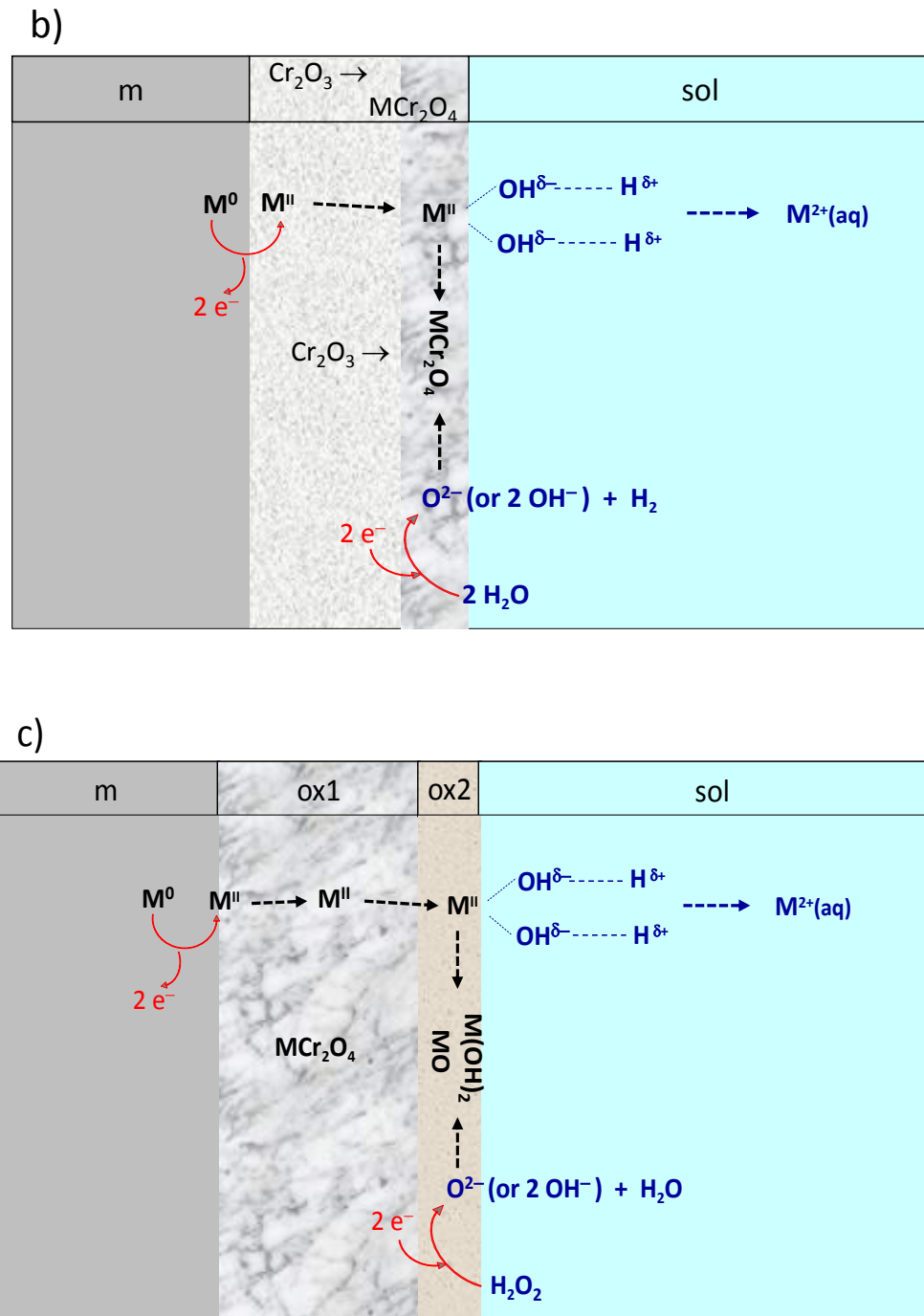
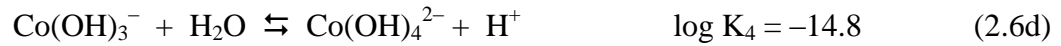
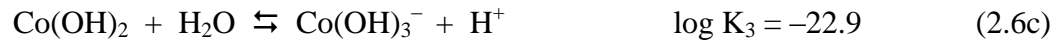
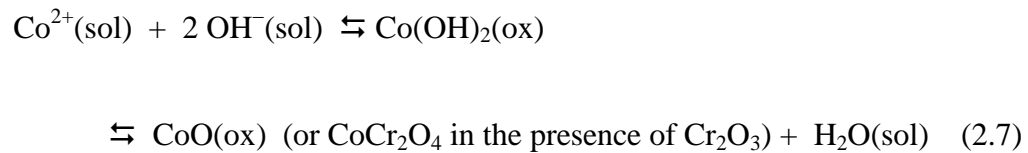


Figure 2.2: Illustration of corrosion reactions a) in the presence of only the natural oxide layer (Cr_2O_3), b) incorporation of Co^{II} into Cr_2O_3 to form CoCr_2O_4 , and c) the formation of $\text{CoO}/\text{Co(OH)}_2$

Once a metal cation is formed, Co^{2+} , it can dissolve into the aqueous phase or combine with an oxygen or hydroxide ion to form an oxide/hydroxide. The extent of dissolution is highly dependent on the aqueous environment. For example, the hydrolyzed cobalt species are in an acid-base equilibrium (reactions 2.6a - 2.6c) and their solubilities are highly pH dependent [9,10]. The behaviour of cobalt species in aqueous media is further discussed in section 2.2.4.1.



These hydrolysis reactions are acid-base equilibrium reactions and the equilibrium in the solution phase is reached relatively quickly compared to other reactions involved in the corrosion process. The hydrated Co^{II} species ($\text{Co}^{2+}(\text{sol})$) are also in phase equilibrium with solid Co^{II} hydroxide and Co^{II} oxides:



Since corrosion reactions involve both mass and charge transfer, their reaction dynamics depend not only on a thermal-chemical potential but also on the Coulombic potential along the reaction coordinate, with the sum of these terms forming the electrochemical potential

[11]. Furthermore, since corrosion involves movement of species in at least two phases (the solid metal and the aqueous phases in the simplest case), it also results in a concentration gradient near the phase interface. For charge transfer reactions, the Coulombic potential will affect the motion of ions and establish an ionic concentration gradient that will affect the transport rates of ions across the interfacial region.

The rates of anodic and cathodic reactions on a surface will depend on the composition of surface species, surface area, and the concentrations of aqueous redox species at the surface/solution interface. Changes in surface and aqueous conditions will affect the anodic and cathodic reaction rates, and therefore, change the E_{corr} . In an electrochemical cell, we can control the potential and measure the anodic (or cathodic) current of the half reaction occurring on metal surface (although not directly while in open circuit).

In an unforced system undergoing corrosion, mass and charge must be conserved (mass and charge conservation also applies under polarization or forced corrosion conditions). These conservation laws require the rate of metal oxidation to be the same as the rate of aqueous species reduction. Since mass or charge cannot build up, the conservation laws also result in the fact that the overall corrosion rate is determined by the rate of the slowest step (or the rate-determining step) of all the processes that are occurring. The rates of the individual steps can vary as functions of the electrochemical potential, pH, temperature and other solution parameters. As a result, the identity of the rate-determining step may change as the solution conditions change. Thus, an important aspect of corrosion studies

involves identifying the rate determining step and establishing the aqueous redox conditions in which the rate- determining process is controlling.

2.2.1 Corrosion Potential and Corrosion Rate

The parameter most commonly used in evaluating corrosion is the corrosion potential, E_{corr} (the term electrochemical open circuit potential, or E_{OCP} , is sometimes used in place of E_{corr}). The corrosion potential is the electrochemical potential which a corroding system establishes in the absence of other external electrochemical drivers [12]. This potential arises on a naturally corroding surface when the net oxidation rate (or anodic current) equals the net reduction rate (or cathodic current) due to mass and charge conservation [13]. The rate of each oxidation or reduction reaction on the surface is a strong function of the electrochemical potential at the interface and there is only one potential at which both the anodic and cathodic rates are equal. It can be easily seen from Figure 2.3 that E_{corr} lies between the E_{eq} values of the two coupled half reactions of the corrosion process. While the net current is zero at E_{corr} , the anodic and cathodic currents are not zero, but they are equal. The anodic current at E_{corr} corresponds to the corrosion rate and is, therefore, referred to as the corrosion current:

$$i_a = -i_c = i_{\text{corr}} \quad (2.8)$$

The rates of anodic and cathodic reactions on a surface will depend on the composition of surface species, surface area, and the concentrations of aqueous redox species at the surface/solution interface. Changes in surface and aqueous conditions will affect the anodic and cathodic reaction rates and therefore change E_{corr} . In an

electrochemical cell, we can control the potential and measure the anodic (or cathodic) current of the half reaction occurring on metal surface (although not directly while in open circuit).

The relationship between current and potential for each redox half-reaction, for example, reactions 2.1 and 2.2a, can be represented by the Butler-Volmer equation in equations 2.9 and 2.10 [14] and it is schematically shown in Figure 2.3,

$$i_{\text{ox}}(\eta_{\text{ox}}) = i_0 \cdot \left(\left\{ \exp \left(\alpha \cdot \eta \cdot \frac{nF}{RT} \right) \right\} - \left\{ \exp \left(-\beta \cdot \eta \cdot \frac{nF}{RT} \right) \right\} \right) \quad (2.9)$$

$$i_{\text{red}}(\eta_{\text{red}}) = i_0 \cdot \left(\left\{ \exp \left(\alpha \cdot \eta \cdot \frac{nF}{RT} \right) \right\} - \left\{ \exp \left(-\beta \cdot \eta \cdot \frac{nF}{RT} \right) \right\} \right) \quad (2.10)$$

where i_{ox} and i_{red} represent the current density for oxidation and reduction reactions, α and β are the transfer coefficients for the half-reactions proceeding in the forward (anodic) and reverse (cathodic) directions, respectively, ($\alpha+\beta=1$), i_0 is the exchange current (the exchange current is the current at zero overpotential), n is the number of electrons transferred in the half-reaction, F is the Faraday constant ($96485 \text{ C}\cdot\text{mol}^{-1}$), R is the gas constant ($8.3145 \text{ JK}^{-1}\cdot\text{mol}^{-1}$), and T is the temperature in Kelvin. The overpotential, η is defined as,

$$\eta_{\text{ox}} = E - E_{\text{ox}}^{\text{eq}} \quad (2.10)$$

$$\eta_{\text{red}} = E_{\text{red}}^{\text{eq}} - E \quad (2.11)$$

where the $E_{\text{ox}}^{\text{eq}}$ for the cobalt oxidation (reaction 2.1) and the $E_{\text{red}}^{\text{eq}}$ for the water reaction (reaction 2.2a) can be obtained from equations 2.12 and 2.13,

$$E_{\text{ox}}^{\text{eq}} = E_0 - \frac{RT}{2F} \ln[\text{Co}^{2+}] \quad (2.12)$$

$$E_{\text{red}}^{\text{eq}} = E_0 - \frac{RT}{2F} \ln[\text{OH}^-]^2 \quad (2.13)$$

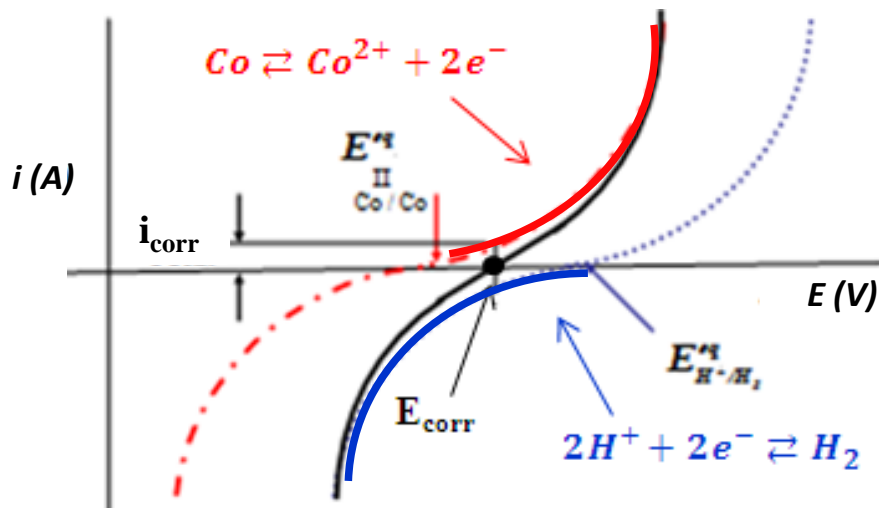


Figure 2.3: Current-potential relationships for the anodic and cathodic half reactions and the net corrosion reaction, illustrating the effect of coupled aqueous half reactions on E_{corr} and i_{corr} .

For the case of a corrosion reaction (2.4a or 2.4b), two half reactions are coupled and are reacting at the combined corrosion potential (solid red and blue line in Figure 2.3). Each half-reaction will have its own independent Butler-Volmer relationship. The net observable current-potential relationship is then obtained from the sum of the two Butler-Volmer equations. The summed Butler-Volmer equations of two half reactions of a corrosion process is called the Wagner-Traud equation [9-11].

$$i = i_{\text{corr}} \left[\exp\left(\frac{a_{\text{A}}nF}{RT}(E - E_{\text{corr}})\right) - \exp\left(\frac{a_{\text{C}}nF}{RT}(E - E_{\text{corr}})\right) \right] \quad (2.14)$$

where a_{A} is the anodic transfer coefficient and a_{C} is the cathodic transfer coefficient.

In the Wagner-Traud equation, one half of the Butler-Volmer equation of each half reaction is negligible (dash dot red line and dot blue line of Figure 2.3), resulting in an equation composed of an anodic exponential term for the oxidation reaction and a cathodic exponential term for the reduction reaction (the solid red and blue lines in Figure 2.3). For the Wagner-Traud equation, the transfer coefficients are similar to those in the Butler-Volmer equation, though in this case they correspond to the activation barriers for the two different half-reactions. The current, i_{corr} , as described above, is the corrosion current and is the short-circuited current occurring when the system is not polarized away from the corrosion potential. The term $E - E_{\text{corr}}$ represents the degree of polarization (overpotential) away from the corrosion potential. In the presence of an oxide layer, E_{corr} increases and the effective overpotential for oxidation, $\eta_{\text{OX}}^{\text{eff}}$ decreases since charged species must transport across the oxide layer [14].

An increase in E_{corr} does not necessarily translate into an increase in i_{corr} since the change in E_{corr} may arise as a result of a change in the oxide film and hence a decrease in η . As the oxide layer grows, its growth rate will slow until it eventually equals the oxide dissolution rate and the oxide layer reaches steady state. At this stage the corrosion rate will be dictated by the rate of the oxide dissolution. The more insulating the oxide layer is, the faster this steady state will be achieved. As we showed in Figure 2.2b the film can be

stationary or growing during corrosion. In the latter case the net corrosion rate will be affected and accordingly the formulation of corrosion rates will be changed. For example, as mentioned above, the overpotential should be an effective overpotential $\eta_{\text{ox}}^{\text{eff}}$, and therefore, there would be a modified version of the Butler-Volmer equation.

2.2.2 Effect of Aqueous Redox Conditions on E_{corr} and i_{corr}

The corrosion potential depends on the redox reactions of the metal and aqueous species. Exposed to ionizing radiation water decomposes into both oxidizing and reducing species and under long-term irradiation these radiolysis products achieve low steady-state levels [15,16]. The corrosion potential of various metals has been observed to increase when the metals are exposed to γ -irradiation [17–21]. One of the questions in evaluating radiation-induced corrosion is how the radiolysis products affect E_{corr} and hence the corrosion rate.

Since corroding environments are dynamic systems, significant changes in the surface oxide composition or the aqueous redox species concentrations may occur. It has been shown that H_2O_2 is the key radiolytically-generated oxidant [22]. Consider the reduction of hydrogen peroxide,



To obtain the E_{eq} of the reduction reaction, Nernst equation can be used,

$$E_{\text{eq}} = E_0 - \left(\frac{RT}{2F}\right) \cdot \ln \left(\frac{[\text{OH}^-]^2}{[\text{H}_2\text{O}_2]}\right) \quad (2.16)$$

$$E_{\text{eq}} = E^0 - 0.059 \text{ pH} + 0.059 \log[\text{H}_2\text{O}_2] \quad (2.17)$$

Equation 2.17 shows that the E_{eq} is dependent on $[H_2O_2]$. Figure 2.4 shows how a change in $[H_2O_2]$ affects the E_{corr} .

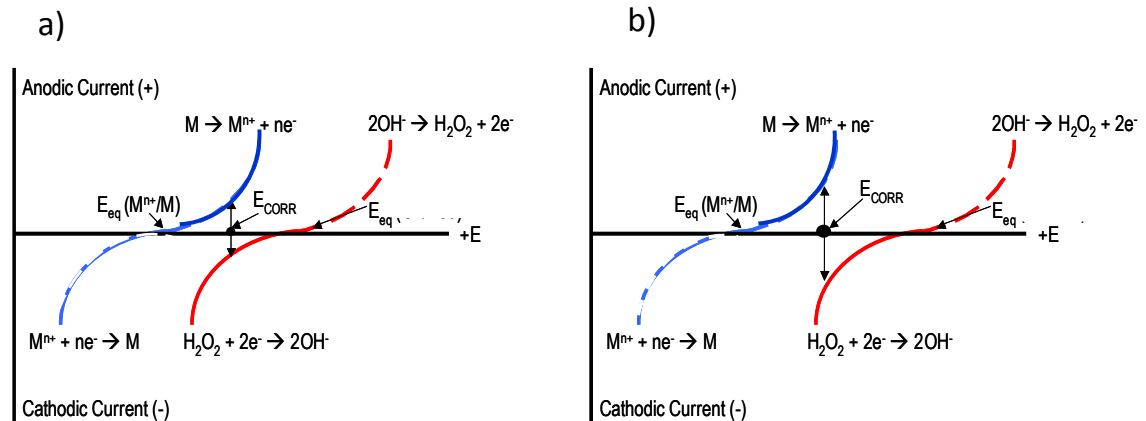


Figure 2.4: Simplified plot of current- potential relationship for a corroding system consisting of a metal oxidation half reaction and a hydrogen peroxide reduction half reaction. The concentration of H_2O_2 is higher in b) than in a).

A shift in potential in one of the half reactions will lead to a change in E_{corr} since the charge balance of $i_a = i_c$ must be maintained, and therefore a new i_{corr} will be achieved. For example if the $[H_2O_2]$ increases, the E_{eq} of H_2O_2 reduction will increase and, hence, the E_{corr} will increase. By experimentally measuring the corrosion potential reached in the irradiation environment, and through the establishment of the current-potential relationship through the application of the Butler-Volmer equation, the corrosion rate can be estimated at a given corrosion potential.

2.2.3 Corrosion of Stellite-6

Before examining the corrosion of Stellite-6, a review of the oxides that can be formed during corrosion of Stellite-6 is valuable. While there are a number of minor alloying elements in Stellite alloys, we will only examine the oxides of the major components of Stellite, Co and Cr. The oxides of these elements control the corrosion of Stellite-6. Also considered are the oxy-hydroxides of these elements since they may be present, particularly on the hydrolyzed outermost layer of the oxide that is in contact with water.

2.2.3.1 Cobalt and Chromium Oxides

A brief overview of the crystal structures and electronic properties of cobalt oxides and oxy-hydroxides is provided below and also listed in Table 1.2. The oxides and oxy-hydroxides reviewed are those that are most commonly formed on Co and which are stable under our experimental conditions.

2.2.3.1.1 CoO/Co(OH)₂

Cobalt has two oxidation states of interest in this work, Co^{II} and Co^{III}. The simplest Co^{II} oxide is CoO (cobalt monoxide). Cobalt oxide has a rock salt structure (NaCl structure) that consists of two interpenetrating fcc sub-lattices of Co²⁺ and O²⁻. CoO is an antiferromagnetic material, which finds applications in electroanalysis [23].

The hydrated analog of CoO is cobalt hydroxide, Co(OH)₂. This species exists in two polymorphic forms, designated as α - and β -Co(OH)₂. Both forms have a hexagonal layered structure. The α -Co(OH)₂ form is isostructural with hydrotalcite-like compounds while the

β -Co(OH)₂ form is isostructural with brucite-like compounds. Both hydroxides consist of hydroxy groups with Co²⁺ ions occupying octahedral sites [24]. The hydrotalcite-like structure is metastable and easily transforms to the more stable brucite-like form [25]. The α -Co(OH)₂ has a larger interlayer spacing ($> 7.0 \text{ \AA}$) when compared to β -Co(OH)₂ (with a layer spacing of 4.6 \AA). As shown in Figure 2.5, the interlayer spacing for CoO is 4.26 \AA . Both hydroxide forms are very promising materials for various important technological applications, for example, supercapacitors [26], and electrocatalysts [27]. Co(OH)₂ is a p-type semiconductor with a band gap of around 2.4 eV [28]. Crystal structures of CoO and Co(OH)₂ are shown in Figure 2.5.

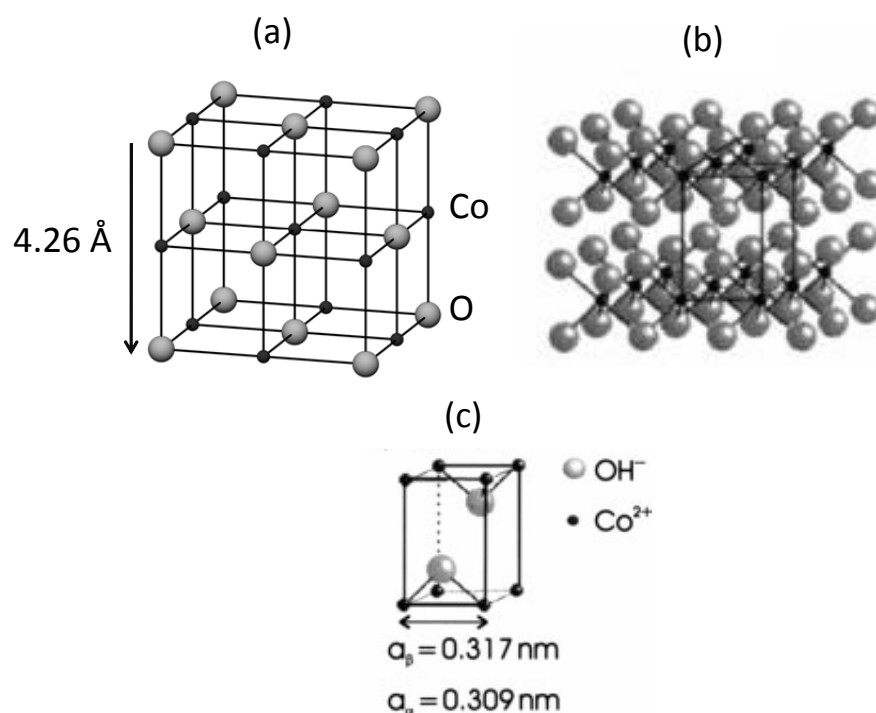


Figure 2.5: Crystal structures of (a) CoO and (b) Co(OH)₂, and (c) a primitive cell of α -Co(OH)₂ and β -Co(OH)₂ (the box shown in (b)) [29].

2.2.3.1.2 Co_3O_4 and CoOOH

The next cobalt oxide (on a scale of degree of overall oxidation) is tricobalt tetroxide, Co_3O_4 . This species is a mixed-valence compound with a cubic close-packed normal spinel structure where Co^{2+} ions occupy the tetrahedral sites and Co^{3+} ions occupy the octahedral sites. Tricobalt tetroxide is a p-type semiconductor with a band gap of 1.4-1.8 eV [30]. It is stable up to 800 °C and decomposes to cobalt oxide CoO above 900 °C [4]. Cobalt oxyhydroxide, CoOOH , is a Co^{III} oxide with a layered structure and a hexagonal primitive cell in which the divalent metal cation is located in an octahedral site coordinated with six hydroxyl groups. The crystal structures of Co_3O_4 and CoOOH are shown in Figures 2.6 and 2.7, respectively. It is kinetically more feasible to oxidize $\text{Co}(\text{OH})_2$ to CoOOH , and CoO to Co_3O_4 .

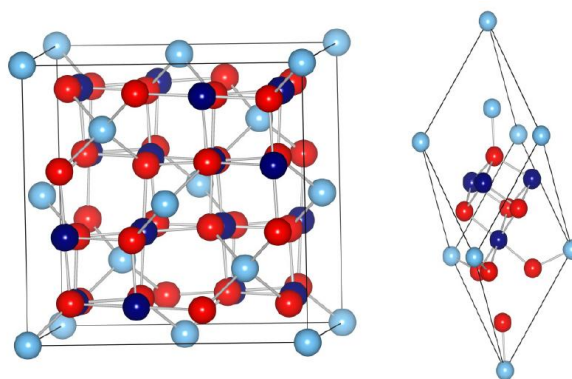


Figure 2.6: Unit cell (on the left) and primitive cell (on the right) of Co_3O_4 . Light cyan and navy blue balls indicate Co^{2+} and Co^{3+} ions, respectively, and red balls indicate O^{2-} ions [31].

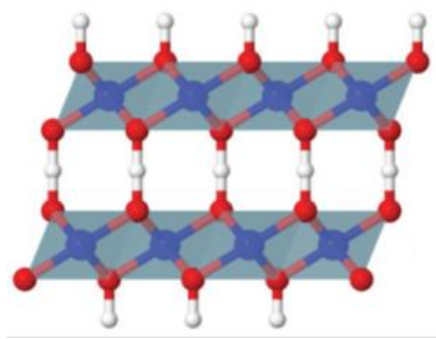


Figure 2.7: Layered crystal structure of CoOOH (ball and stick model).

2.2.3.1.3 Cr_2O_3 and CoCr_2O_4

Stellite-6 contains approximately 30% Cr. Even brief contact of chromium with moist air is sufficient to create a thin oxide layer, Cr_2O_3 , on the alloy surface, which protects the alloy from further rapid oxidation [32]. This oxide has a corundum structure which consists of a hexagonal close packed array of oxide anions with $2/3$ of the octahedral holes occupied by chromium atoms, Figure 2.8 [33]. Similar to corundum, Cr_2O_3 is a hard, brittle material. The band gap of Cr_2O_3 is 3.3 eV [34]. Chromium oxide is a stable oxide (section 1.4.5.2.2 for the further explanation). However, in highly oxidizing conditions Cr^{3+} oxidizes to Cr^{6+} . This leads to the dissolution of Cr as a chromate, CrO_4^{2-} [32].

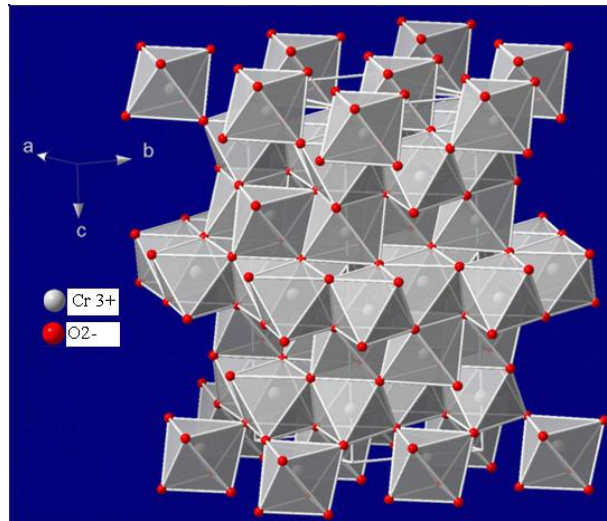


Figure 2.8: Crystal structure of Cr₂O₃ [33].

Chromium is known to form mixed oxides with many transition metal ions in a spinel structure. In Stellite the Cr can combine with Co to form CoCr₂O₄ [35]. This is the only Cr/Co compound that is of importance in the corrosion of Stellite under the conditions that we have studied. Similar to Co₃O₄, CoCr₂O₄ is another spinel oxide in which Co²⁺ occupies the tetrahedral sites and Cr³⁺ lies at the octahedral sites. It has been reported that the formation of CoC₂O₄ is promoted at high temperatures [36]. This mixed oxide is a p-type semiconductor with a band gap of about 3.4 eV [37].

Table 2.2: Crystallographic structures of cobalt oxides [38].

Compound	Structure type	Cell parameter [Å]	Atom	Supercell
CoO	Rocksalt	4.263	Co ²⁺	Cubic 4x4x4
α -Co(OH) ₂	Hydrotalcite	3.17	Co ²⁺	Cubic 4x4x4
β -Co(OH) ₂	Brucite	3.09	Co ²⁺	Cubic 4x4x4
Co ₃ O ₄	Spinel	8.08	Co ²⁺ , Co ³⁺	Cubic 2x2x2
CoOOH	Layered	a=2.851, c=13.150	Co ³⁺	Hex 3x3x1
CoCr ₂ O ₄	Spinel	8.33	Co ²⁺ , Cr ³⁺	Cubic

2.2.4 Review of Cobalt Oxide Formation

2.2.4.1 The Behaviour of the Co-H₂O System at 25-150 °C

It is important to have a good understanding of the behaviour of pure Co metal in aqueous media to predict the corrosion behaviour of cobalt alloys. In particular, a good understanding of the solubility and stability of applicable Co species in water at 25-150 °C is essential.

In aqueous solutions Co^{II} ions are stable and the Co²⁺ ion can exist in acidic and neutral media. The Co²⁺ ion precipitates as Co(OH)₂(s) around pH 7.5 (at a Co concentration of about 10⁻² M) [39]. The known cobaltous hydroxyl monomers in solution are: CoOH⁺, Co(OH)₂ (or CoO), Co(OH)₃⁻, and Co(OH)₄²⁻. The Co³⁺ ion only exists in acidic media, it precipitates around pH 0 (at a Co concentration of about 10⁻² M) [39]. The only known hydroxyl form of this oxidation state is CoOH²⁺.

The solubility of each species can be determined by a thermodynamic relationship (for example for reaction 2.6a),

$$\log K = \frac{-\Delta G_{\text{reaction}}^0}{2.303 RT} = \frac{[\text{Co(OH)}^+][\text{H}^+]}{[\text{Co}^{2+}]} = -\text{pH}_T + \log[\text{Co(OH)}^+] - \log[\text{Co}^{2+}] \quad (2.18)$$

where ΔG^0 is the free energy of a reaction ($\text{kJ}\cdot\text{mol}^{-1}$), R is ideal gas constant ($8.314 \text{ J}\cdot\text{mol}^{-1}\cdot\text{K}^{-1}$), and T is a temperature at which reaction takes place (K). The pH_T is the pH of the solution at the temperature T of the reaction. The total solubility for a given set of conditions is equal to the sum of the concentrations from the individual reactions which contribute to the dissolution of the solid.

To obtain the solubility of Co^{II} at $T > 25 \text{ }^\circ\text{C}$, the standard free energy of each reaction must be calculated to enable us to determine the K of each individual reaction. According to chemical thermodynamics the free energy of formation of a substance at temperature T_2 , can be determined from the free energy of formation of that substance at T_1 , by evaluating equation 2.19,

$$\Delta G^0(T_2) = \Delta G^0(T_1) + \int_{T_1}^{T_2} dG^0(T) \quad (2.19)$$

Where $\Delta G^0(T_1)$ and $\Delta G^0(T_2)$ are the standard free energy of formation of the substance at temperature T_1 and T_2 , and $\int_{T_1}^{T_2} dG^0(T)$ is the change in the standard free energy between T_1 and T_2 .

Equation 2.19 can be transformed to,

$$\Delta G^0(T_2) = \Delta G^0(T_1) + \int_{T_1}^{T_2} (-S^0 dT + V^0 dP) \quad (2.20)$$

where S_0 is the standard entropy of the substance and V_0 is the standard molar volume and P is vapour pressure.

The contribution of $V_0 dP$ to the free energy of solid and dissolved substances due to the change in vapour pressure of water between 25 °C and 300 °C is small, and may be neglected [34]. Thus equation 2.20 reduces to

$$\Delta G^0(T_2) = \Delta G^0(T_1) - \int_{T_1}^{T_2} (S^0 dT) \quad (2.21)$$

which be written as,

$$\Delta G^0(T_2) = \Delta G^0(T_1) - \int_{T_1}^{T_2} d(S^0 T) + \int_{T_1}^{T_2} T dS^0 \quad (2.22)$$

and subsequently,

$$\Delta G^0(T_2) = \Delta G^0(T_1) - [T_2 S^0(T_2) - T_1 S^0(T_1)] + \int_{T_1}^{T_2} T \left(\frac{\partial S^0}{\partial T} \right) dT \quad (2.23)$$

The change in entropy with temperature can be expressed as,

$$S^0(T_2) = S^0(T_1) + \int_{T_1}^{T_2} \left(\frac{C_p^0}{T} \right) dT \quad (2.24)$$

where C_p^0 is the heat capacity of the substance of interest. Since,

$$\left(\frac{\partial S^0}{\partial T} \right)_p = \frac{C_p^0}{T} \quad (2.25)$$

then substitution of equations (2.24) and (2.25) into equation (2.23) gives:

$$\Delta G^0(T_2) = \Delta G^0(T_1) - [S^0(T_1)(T_2 - T_1)] - T_2 \int_{T_1}^{T_2} \left(\frac{C_p^0}{T}\right) dT + \int_{T_1}^{T_2} C_p^0 dT \quad (2.26)$$

This is the basic equation for determining the free energies of substances at elevated temperatures from known free energies at 25 °C and heat capacities. Figure 2.9 shows the solubility of all Co^{2+} hydrolyzed species as a function of pH at 25 °C.

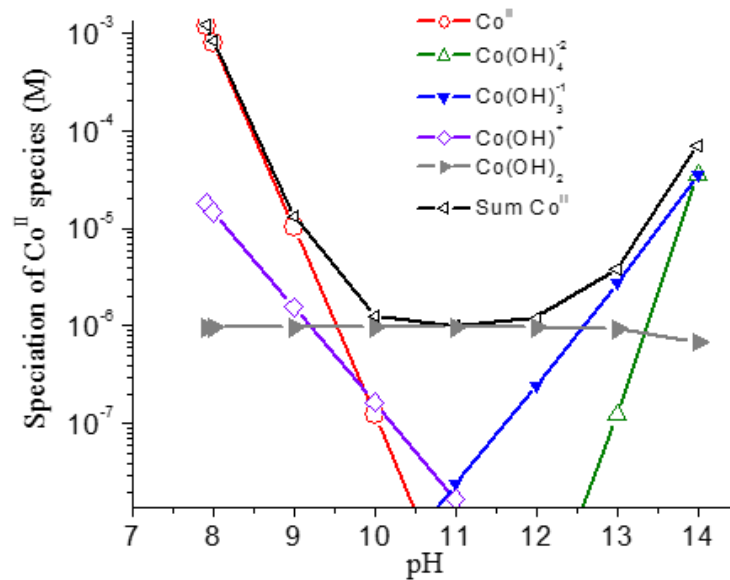


Figure 2.9: Solubility of hydrolyzed Co^{2+} species as a function of pH at 25 °C.

One of the most common ways to represent the thermodynamic stabilities of the different metal species in water is with a Pourbaix, or E-pH diagram [11]. An E-pH diagram shows the regions of potential and pH within which a particular species is the most thermodynamically stable (stability region). Because Pourbaix diagrams do not include

kinetic information, they only provide an indication of the driving direction for a system [40]. The diagram can be generated from the Nernst equations of the metal oxy-hydroxides [10]. The E-pH diagram for the Co-H₂O system at 25 °C is presented in Figure 2.10. The areas between two red lines (a and b) represent the stability domain of water. Below line a, water is reduced into H_{2(g)} and above line b, water is oxidized into O_{2(g)}. The dashed lines depict the predominance domains of the dissolved cobalt species and the solid lines outline the stability domains of solid phases in the Co-H₂O system.

The E-pH diagrams for the Co-H₂O system at 75 °C, 100 °C, and 150 °C are presented in Figures 2.11, 2.12, and 2.13, respectively. The E-pH diagrams at 25-150 °C indicate that the stability domains of Co₃O_{4(s)} increase with increasing temperature. When the temperature exceeds 100 °C, solid Co(OH)₂ is no longer the most stable species. Increasing the temperature results in narrower predominance domains for Co³⁺ and Co²⁺ and the rest of the hydrolyzed species. The E-pH diagrams indicate that increase in temperature up to 75 °C does not alter the E_{eq} of Co/Co(OH)₂ and Co(OH)₂/Co₃O₄ redox pairs at a given pH. However, as the temperature exceeds 100 °C, the E_{eq} potentials shifted to a lower value.

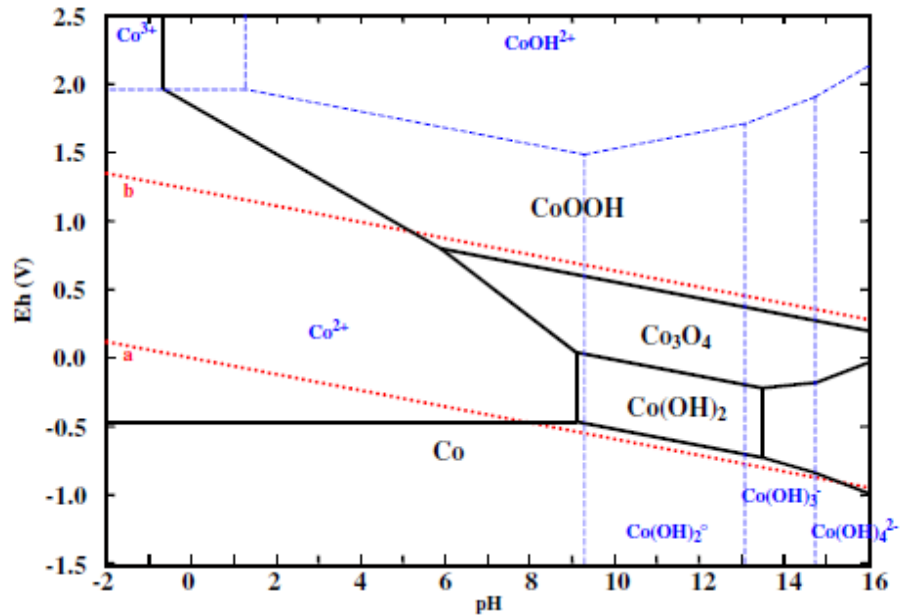


Figure 2.10: Pourbaix diagram of the Co-H₂O system at 25 °C with all ions at an activity of 10⁻⁶ M. The potential scale is with respect to the standard hydrogen electrode (SHE) [40].

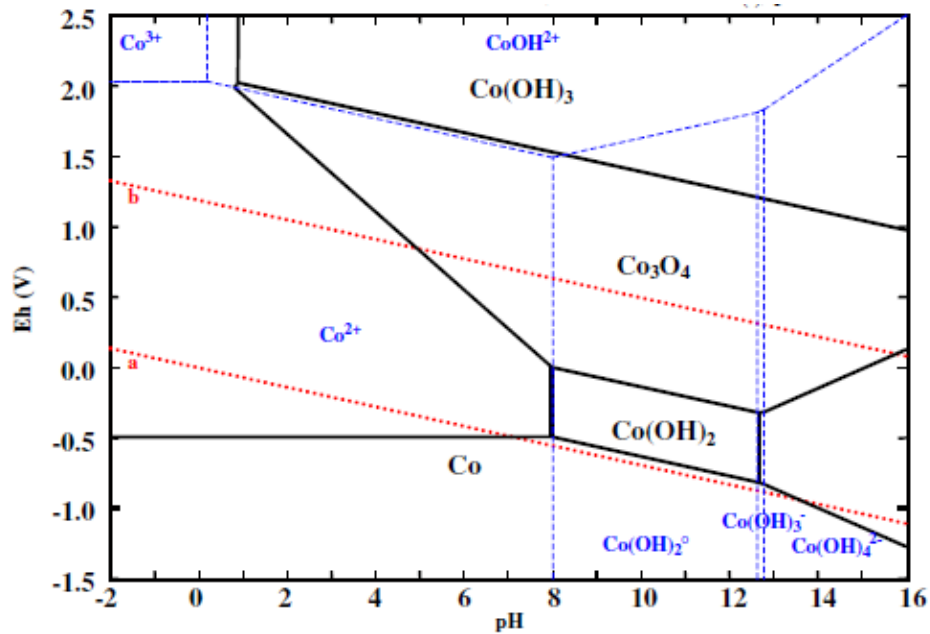


Figure 2.11: Pourbaix diagram of the Co-H₂O system at 75 °C with all ions at an activity of 10⁻⁶ M. The potential scale is with respect to the standard hydrogen electrode (SHE) [40].

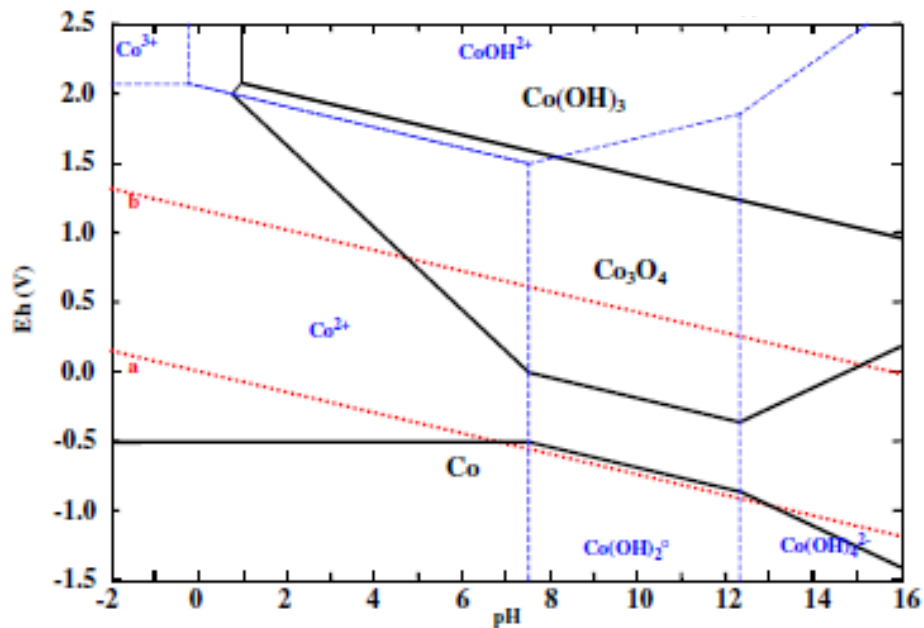


Figure 2.12: Pourbaix diagram of the Co-H₂O system at 100 °C with all ions at an activity of 10⁻⁶ M. The potential scale is with respect to the standard hydrogen electrode (SHE) [40].

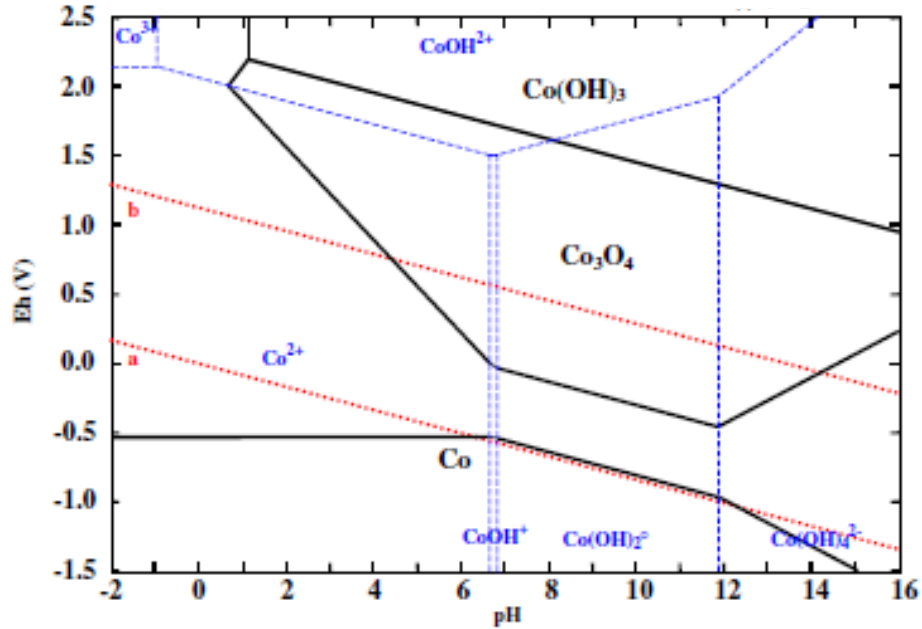


Figure 2.13: Pourbaix diagram of the Co-H₂O system at 150 °C with all ions at an activity of 10⁻⁶ M. The potential scale is with respect to the standard hydrogen electrode (SHE) [40].

2.2.4.2 The Behaviour of the Cr-H₂O System at 25-150 °C

Figure 2.14 shows the solubility of chromic oxide Cr₂O₃ as Cr³⁺, CrO₂⁻, CrO₃³⁻ ions as a function of pH. It can be seen that the minimum solubility of Cr₂O_{3(s)} is at pH 7.0.

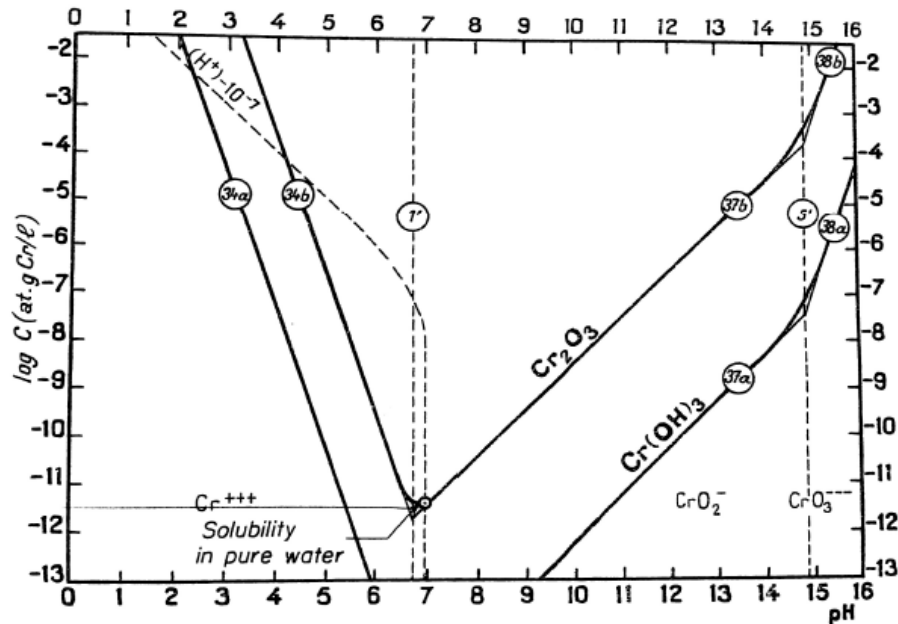


Figure 2.14: Influence of pH on the solubility of Cr_2O_3 and $\text{Cr}(\text{OH})_3$, at $25\text{ }^\circ\text{C}$ [9].

The E-pH diagram for the Cr-H₂O system at $25\text{ }^\circ\text{C}$ is shown in Figure 2.14. It can be seen that in alkaline solutions Cr_2O_3 is stable and can dissolve as CrO_4^{2-} only at high potentials ($E > 0.25\text{ V}_{\text{SHE}}$). For Co-Cr alloys such as Stellite-6, very brief contact with moist air is sufficient to form Cr_2O_3 on alloy surface. This naturally-formed air oxide acts as a protective layer and suppresses further oxidation. Being very insoluble in a neutral and mildly basic solutions ($10^{-11.6} < \log C < 10^{-9}$) being not easily oxidized accounts for the high stability of Cr_2O_3 . The Cr/Cr²⁺ equilibrium is unchanged in the temperature range of 25-150 °C, but the stability region for the Cr²⁺ and Cr³⁺ decreases, and the stability region for CrO_4^{2-} increases. The stability of $\text{Cr}(\text{OH})_3/\text{Cr}_2\text{O}_3$ increases at low pHs. However, at high pHs the region stability of $\text{Cr}(\text{OH})_3/\text{Cr}_2\text{O}_3$ decreases [41].

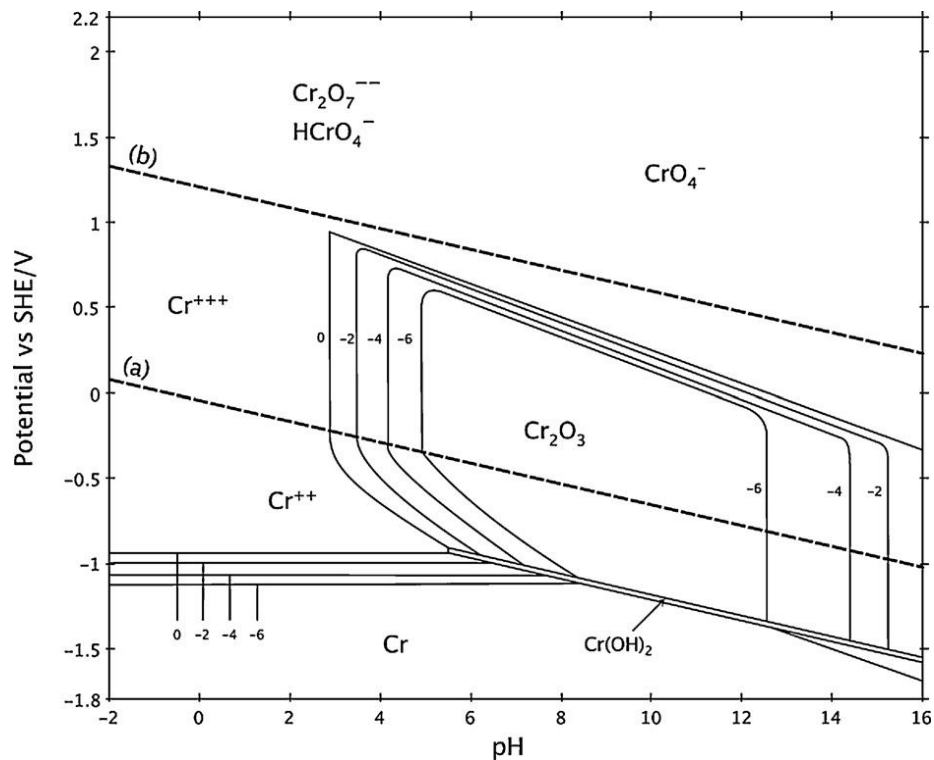


Figure 2.15: Pourbaix diagram of the Cr-H₂O system at 25 °C with all ions at an activity of 10⁻⁵ M. The potential scale is with respect to the standard hydrogen electrode (SHE) [9]. The lines labelled 0, -2, -4 and -6 correspond to order of concentrations of Cr³⁺.

2.2.4.3 Cobalt Oxide Formation

The formation of CoO/Co(OH)₂ on cobalt during corrosion in basic solutions was observed by Bewick et al. using in-situ IR spectroscopy [42]. They also observed the transformation of Co(OH)₂ during oxidation. Their work explains the change in the characteristics of the cobalt oxide film recorded by the electrochemical experiments and the XPS measurements in basic solutions [43]. In acidic solutions, CoO/Co(OH)₂ is unstable and

can dissolve which is consistent with the E-pH diagram [40]. The formation of either CoOOH or Co₃O₄ increases the stability of the passive film due to their lower solubility compared to CoO/Co(OH)₂ [39,40]. In sufficiently oxidizing environments, these species can be present as a second layer on the top of a CoO/Co(OH)₂ film. Behl and Toni [44] electrochemically studied the oxidation of cobalt in highly basic solutions (pH 13.3 to 14.9 KOH solutions) in the potential range from -1.1 to 0.64 V_{Hg/HgO} (-1.23 to 0.51 V_{SCE}). They found that the first layer of oxide that grows at lower potentials consists of CoO; its thickness is 2.3 nm. A second oxide layer forms on top of the CoO with a thickness of about 3.7 nm at higher potentials.

Foelske and Strehblow have also seen that Co forms two different passive layers at two ranges of potentials in a NaOH solution at pH 13. The inner layer is Co(OH)₂ that forms between -0.4 to 0.2 V_{SHE} (-0.64 to -0.04 V_{SCE}). Longer corrosion times led to dehydration of this layer and an increase in its thickness. A second layer is formed at higher potentials (0.3 to 0.8 V_{SHE}) (0.06 to 0.56 V_{SCE}) and this consists of Co₃O₄ and CoOOH [29]. It's known that the formation of either Co₃O₄ or CoOOH increases the stability of the oxide layer on cobalt metal due to the lower solubility of Co^{III} than Co^{II} in basic media [43].

2.2.4.4 The Role of Other Stellite-6 Constitutes in Oxidation

In this section the role of Cr, C, W, and Mo in the oxidation and corrosion behaviour of Stellite-6 is discussed.

2.2.4.4.1 Effect of Chromium-Carbon

In cobalt-based alloys, small amounts of carbon are included to impart some measure of solid-solution strengthening. The chromium in Stellite plays a role in this strengthening through the formation of a number of chromium carbides such as Cr_7C_3 and Cr_{23}C_6 [45–47]. The morphology of the microstructure and the incoherent phase distribution of these carbides are important factors in the thermal fatigue crack susceptibility of Stellite 6 [48]. The ternary Co–Cr–C alloy family has attractive high-temperature properties and ease of fabrication. Indeed, this ternary system is the base of more complex alloys which also include, for example, less than 10 wt.% Ni (Table 2.1, Stellite-31) [49]. Here the Ni stabilizes the fcc matrix at intermediate temperatures by preventing the appearance of the hcp (hexagonal close packed) low-temperature structure of cobalt [49]. Rosalbino et al. studied the corrosion behaviour of HIPed and cast Stellite-6 alloy in a chloride-containing solution (3.5% NaCl) using electrochemical impedance spectroscopy (EIS) and polarization methods [50]. There is evidence that a chromium-carbide rich area can act as a kinetic barrier to the dissolution of Co, thus enhancing the protective properties of a Cr_2O_3 oxide layer and the corrosion resistance of the alloy [40].

2.2.4.4.2 Effect of Mo and W

A high Cr content in a Co-based alloy improves corrosion resistance. However, a high chromium content may also lower the solidus temperature of the alloy and its creep resistance [47]. To minimize this drawback, alloying elements such as tungsten and molybdenum have been added to Co-based superalloys for solid solution strengthening. Shin

et al. investigated the effect of molybdenum on the microstructure and wear resistance properties of Stellite hardfacing alloys [51]. They showed that with an increase in molybdenum content, $M_{23}C_6$ and M_6C type carbides were formed instead of a chromium-rich M_7C_3 type carbide. They concluded that this microstructural change was responsible for the improvements in the hardness and wear resistance of molybdenum-containing Stellite-6 [45].

Yao et al. compared the beneficial effects of Mo with W in Stellite alloys [52]. Using Mo in place of W results in changes in the carbide morphology and an increased volume fraction of carbides in the microstructure (because of the higher metal content of the now preferred $M_{23}C_6$ carbides). The Mo-containing Stellite alloys exhibit excellent abrasive and adhesive wear resistance. The W-containing Stellite alloys have better corrosion resistance, for example in boiling, oxidizing 10% HNO_3 whereas the Mo-containing Stellite alloys exhibit exceptional corrosion resistance in reducing 5% HCl at 40 °C and in 10% H_2SO_4 at 66 °C [53].

In addition to W and Mo, addition of Ni and Fe are used in some Stellites. The latter elements promote the stability of an fcc structure in the Co rich matrix (stable at temperatures up to the melting point, 1495 °C). The elements Cr, Mo, and W tend to stabilize an hexagonal close-packed (hcp) crystal structure which is stable at temperatures below 417 °C [51].

2.3 OXIDE GROWTH MECHANISM

Metals exposed to oxidizing conditions gradually corrode. This is a process in which the outer surface of the metal is converted to an oxide (or oxy-hydroxide). Some alloys exhibit protective corrosion behaviour; they form an inert oxide layer which isolates them from the environment, effectively limiting further oxidation. This behavior is known as passivation. Since the nature of the oxide on a metal surface plays an important role in its corrosion resistance, understanding of this oxide behaviour is crucial. The study of oxide formation, growth and dissolution is the foundation of corrosion science. This field is too extensive to be fully reviewed here. However, we will highlight some important aspects of this field as they relate to the work of this thesis.

A key element in explaining the corrosion behaviour of a metal is a model for oxide growth on its surface. Several different film growth models have been proposed and published [54–59]. An oxide growth model should enable us to accurately describe the physio-electrochemical processes that occur at the interface and also to ensure a confluence between theory and experiment. To develop any model for oxide growth in water a series of factors need to be considered. These include the nature of the chemical species responsible for oxide growth, the changing electric field across the oxide layer, and the solution conditions (e.g., pH and temperature). Not all oxide growth models address all possible influences. Some of these models do not consider the potential drop across the oxide layer [55,57,58]. Mott and Cabrera assumed that only cation diffusion via interstitial sites causes film growth and they neglected the contribution of anion diffusion [58]. Macdonald's point

defect model I (PDM) [60] was essentially an attempt to transfer the idea of Wagner for the growth of oxide films on metal surfaces under dry oxidation conditions to the growth of oxide films on metals in aqueous solutions. This model accounted for a number of important observations, including the linear dependence of the film thickness on voltage after a certain time of polarization and the kinetics of film growth. A number of important assumptions were made in the development of this model including: (1) the oxide layer is a point defect phase containing cation vacancies and oxygen vacancies, (2) the concentration of point defects is much greater than in the isolated, bulk oxides, indicating the presence of continuous defect generation/annihilation processes, (3) defects are generated and annihilated at the M/Ox and Ox/Sol interfaces, (4) the electric field strength is independent of voltage and distance through the film, (5) the potential is distributed across the interphase region with drops at the M/Ox interface, the Ox/Sol interface and across the film, and (6) the potential drop across the Ox/Sol interface is linearly dependent upon the applied potential and pH. This model successfully predicts the inverse logarithmic law for oxide growth, and can be extended to deal with passivity breakdown [59,61]

$$x = A + B \ln t \text{ (Logarithmic law)} \quad (2.27)$$

where x is the oxide film thickness, A and B are modelling constants, and t is time. In all oxide growth models it is assumed that the field strength is constant through the film. The models were initially only applicable to pure metals rather than alloys and recent models such as conduction and atomistic models [62,63] have addressed this deficiency. As is the case with the Fehlnert/Mott and Mott/Cabrera models, the point defect model cannot account

for the existence of steady-states in both the passive current density and film thickness, and the formation of the bilayer films that are known to be present on many metals and alloys [54,58]. The second generation of the PDM, PDM-II, incorporated a bilayer structure on the metal surface to address this deficiency [56]. While many assumptions from PDM I remain in the revised model, specific additional features include: (1) the recognition of the role played by barrier layer dissolution, (2) the possibility that interstitial as well as cation and oxygen vacancies can be involved in the growth of the barrier layer, (3) changes in the steady state barrier layer thickness linearly with potential and pH, and (4) a steady state current that is independent of the applied potential for n-type films and exponentially dependent on the applied potential for p-type films. Development of these oxide growth models led to different rate laws for oxide growth,

$$\frac{1}{x} = C - D \ln t \text{ (Inverse logarithmic law)} \quad (2.28)$$

$$x^2 = E \cdot t \text{ (parabolic law)} \quad (2.29)$$

where C, D, and E are modelling constants.

Recently Leistner et al. developed a new, generalized growth model and they reported a numerical simulation of the transient behaviour of oxide film growth [64]. In contrast to previously developed models, their model described the time dependent behaviour of oxide and oxide/solution potential differences and it confirmed that the potential differences could be expressed as exponential functions of the oxide thickness. They validated their model with

experimental oxide thickness measurements on stainless alloys that were corroded at high-temperature.

2.4 RADIATION AND WATER RADIOLYSIS

2.4.1 Radiation Chemistry

This thesis examines the effect of ionizing radiation on the corrosion of a metal alloy in solution. Hence, a foundation of the work is the chemistry that ionizing radiation induces in water. This section provides a brief overview of that chemistry and the physics that drives it.

Ionizing radiation exists in three forms: a high energy (fast) ${}^4\text{He}^{2+}$ nucleus (referred to as α -particle), a high energy electron (β -particle), and a high energy γ photon. The most common source of ionizing radiation is nuclear fission, or radioactive isotope decay, but ionizing radiation can also be created by high energy particle accelerators. The energy of a radiation particle or photon emitted from a radionuclide is characteristic of the nuclide [65]. For example, the γ -rays emitted during the β -decay of ${}^{60}\text{Co}$ have energies of 1.332 MeV and 1.173 MeV. The energy of β particles and photons from radionuclide decay typically range from 0.1 MeV to 5 MeV [65]. Particles with this energy cannot induce nuclear reactions but the energy is much higher than that required to ionize atoms and molecules (typically 10s of eV). When radiation interacts with matter it leaves a track of ionized particles and hence is known as ionizing radiation. The main energy transfer mechanism from a radiation particle or photon to an interacting solvent medium is an inelastic collision whose probability

depends on the electron density of the solvent molecules. The rate of energy loss from the radiation particle (or the rate of energy absorbed by the coolant) is nearly independent of the initial energy of the radiation particle or photon. In determining the chemical effects of ionizing radiation on a medium it is the energy transfer rate per unit mass of the medium that counts. This is referred to as the linear energy transfer (LET) rate. The LET rate depends on the type of radiation and the interacting medium. For a given medium, it is higher for α -particles (due to their large size and charge), lower for β -particles, and lowest for γ -photons [22]. The different LET rates result in different average penetration depths. The depth depends on the mass density (and more importantly the electron density) of the medium. For water at room temperature the penetration depths are: 20 – 25 μm for α -particles, 0.5 – 1.0 cm for β -particles, and tens of cm for γ -photons. These depths are the distances into the medium at which the incident energy flux is reduced by 50%. For α -radiation, the incident energy is deposited in a small volume very near the radiation source, while for β and γ the energy is deposited throughout the medium. Because α -particles can be ‘stopped’ by thin layers of material and because they deposit their energy in very small volumes, they play little role in the radiolysis of water systems. Alpha radiation is largely confined to nuclear fuel and fuel cladding in a nuclear reactor. Hence in the following discussion we only focus on the interaction of low LET radiation with water. The total radiation energy depends on not only the energy of individual particles or photons but also on the number of the particles/photons. The estimated radiation flux (or radiation dose rate) of low LET radiation to the coolant in the core of a nuclear reactor ranges from 1000 to 4500 $\text{kGy}\cdot\text{h}^{-1}$ ($1 \text{ Gy} = 1 \text{ J}\cdot\text{kg}^{-1}$) [66]. The LET rate is important in determining the density of ions and electronically

excited molecules that are formed along the radiation track. Since this density can affect further collision/reactions of species in the track, it will have consequences on the yields of radiolysis products that reach the bulk phase (after diffusing out of the localized zone near the track) where they can undergo bulk chemical reactions.

Due to their high initial energy, each β -particle or γ -photon undergoes many collisions while it loses energy. Eventually the collisions will reduce the energy of the residual electrons to the average kinetic energy of the medium being irradiated and the electrons are “thermalized”. The high energy β or γ interactions do not depend on the chemical nature of the target matter; to a first order they only depend on the relative abundance of electrons in the interacting matter. This is an important consideration when irradiating dilute solutions. The total mass of the solutes in such solutions is very much less than the mass of the surrounding water. Hence, the probability of an incident β particle or γ photon interacting with a solute molecule is very small compared to the probability of interacting with a water molecule. For this reason, chemical processes induced by low LET radiation of solutions are often referred to as solvent-oriented processes (as opposed to solute-oriented processes).

Ionizing radiation transfers its energy to an interacting medium mainly by colliding non-discriminately with the electrons bound to atoms and molecules in the medium. The difference between β -and γ -radiation lies mainly in the different nature of the interactions. For β particles the energy is transferred directly via inelastic collisions between the incident fast electron and the quasi-stationary bound electrons. Such collisions can result in the

ejection of a secondary electron from the target molecule leaving behind an ionized and excited molecule (or atom). For γ -radiation the interaction is more complicated. It involves a photo-electron process called Compton scattering which results in a lower energy photon and an ejected electron [22,67–69]. The Compton-scattered electron (a high energy ‘primary’ electron) behaves very much like a β -particle in its subsequent collisions with medium molecules and this is why the chemical effects induced by both β and γ radiation in water (for the same absorbed energy) are essentially the same. The probability of a Compton scattering event is much lower than the probability of an electron scattering event (because the latter is a direct charge-charge interaction). This allows gamma rays to penetrate a medium much more deeply than a β -particle with the same incident energy. However, once a γ -photon produces a high energy secondary electron, the subsequent radiation deposition is the same for β and γ . Hence we do not distinguish between them in their chemical impacts on solutions and refer to both as a radiation particle hereafter.

The average energy transferred from a radiation particle to a water molecule, per collision, typically ranges from 60 to 100 eV [22,70,71]. This amount of energy is a very small fraction of the initial energy of the radiation particle so that individual collisions do not slow the particle much or change its path direction appreciably. The radiation particle moves in a straight line that is designated a radiation track. The initial consequence of each energy transfer collision is ionization and/or electronic excitation of a water molecule. The result is creation of ion pairs (H_2O^+ and e^-_{hot}) or electronically excited water molecules (H_2O^*) along the radiation track. The electron of this ion pair is labelled as ‘hot’ because it has a kinetic

energy that is sufficient to excite or ionize one or more neighbouring water molecules (the 60 - 100 eV transferred in a collision is well in excess of the ionization energy of a water molecule (12.6 eV) [69]. Secondary (or even tertiary) ionization caused by this 'hot' electron will occur very near the location of the first ionization that created the 'hot' electron (because the 'hot' electron kinetic energy is low, it won't move very far). This results in clusters of 2-3 ion pairs (or excited water molecules) along the radiation track. This cluster is referred to as a "spur" and is illustrated in Figure 2.16 [22,70]. Any electronically excited water molecules that arise as a result of a 'hot' electron impact have the option of being stabilized (by radiative decay and de-excitation collisions with other water molecules), dissociating into an ion pair (with a low kinetic energy), or separating into free radical fragments (such as $\bullet\text{OH}$ and $\bullet\text{H}$).

The density of spurs along a radiation track is an important parameter in determining the chemical yields of radiolysis products. The spur density depends mainly on the collision rate of the radiation particle with the bound electrons in the water molecules. If the spurs are close enough together the ions and radicals in a spur can interact with those of an adjacent spur before they diffuse into the bulk water phase. Also, if the spur density is sufficiently high, these interactions can lead to a lower net decomposition rate of water (per absorbed energy unit) and a higher ratio of molecular to radical primary radiolysis products.

The yields of these primary radiolysis products are expressed in G-values, which have units of number of molecules produced per 100 eV absorbed energy, or the standard units of $\mu\text{mol}\cdot\text{J}^{-1}$. G values of liquid water at different temperatures are listed in Table 2.3. [22]. The

primary radiolysis products listed in Table 2.3 are not actually the first species formed upon the absorption of radiation energy, but rather the first set of chemical species that will undergo bulk phase chemistry. Even the primary radiolysis products are very chemically active and will continually react with one another, with water molecules as other water species, and, if present, with solute species.

Figure 2.17 illustrates in detail the process breakdown of water into radiolysis products in the presence on ionizing radiation and subsequent reactions starting from the instantaneous interaction of a radiation particle with a molecule to the formation of the primary radiolysis products. In a constant radiation field where a continuous flux of incoming radiation produces primary radiolysis products, these species will reach steady-state concentrations on a time scale of seconds [15,16,22].

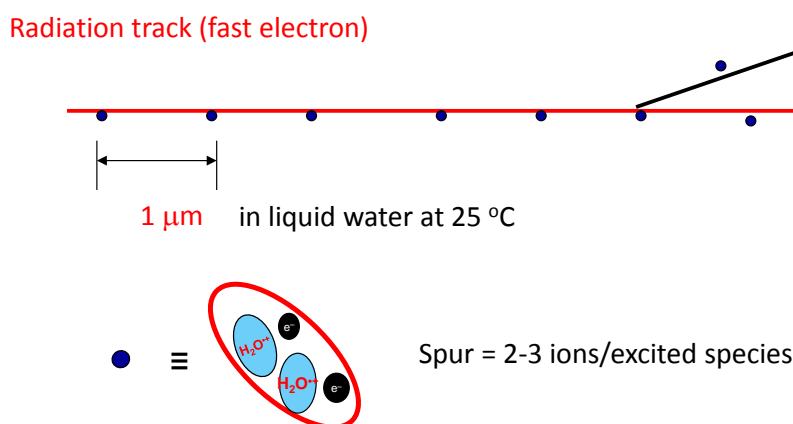


Figure 2.16: The radiation track of a fast electron showing spurs (spur size not to scale).

Table 2.3: The primary yields ($\mu\text{mol}\cdot\text{J}^{-1}$) from γ -radiolysis of liquid water at different temperatures [72].

Temperature (°C)	$G(e_{\text{aq}}^-)$	$G(\text{H}_2)$	$G(\cdot\text{H})$	$G(\text{OH}^-)$	$G(\text{H}_2\text{O}_2)$
25	2.75	0.44	0.6	2.81	0.71
50	2.85	0.45	0.64	3.07	0.67
100	3.10	0.47	0.71	3.57	0.59
150	3.31	0.49	0.8	4.07	0.51
200	3.46	0.51	0.94	4.57	0.43
250	3.51	0.56	1.18	5.12	0.35
300	3.43	0.64	1.56	5.74	0.43
350	3.19	0.76	2.11	6.45	0.19

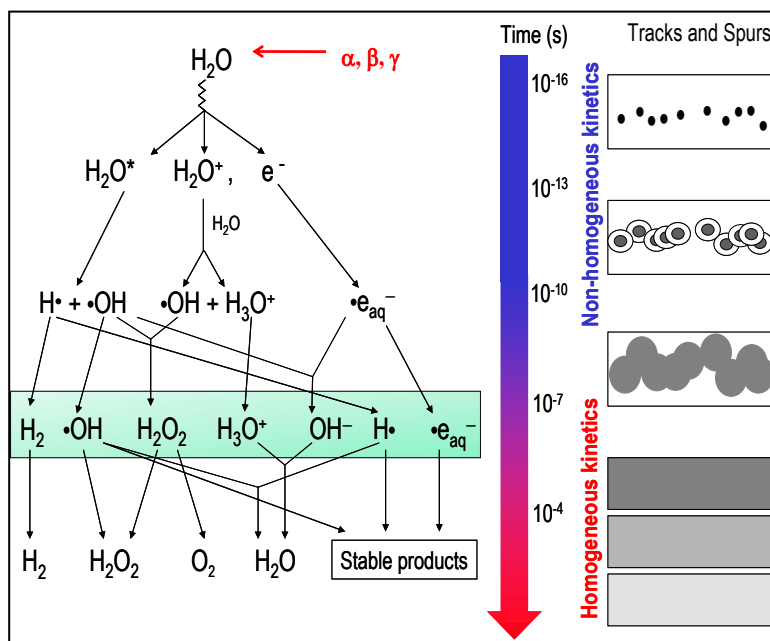
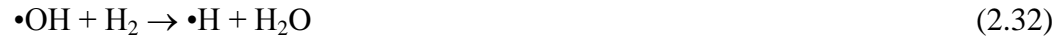


Figure 2.17: The effect of ionizing radiation on water.

Examples of the reactions of primary radiolysis products are,



Solid/liquid interfacial reactions, such as corrosion generally occur over much longer time scales (hours to years). Thus, the rates of the interfacial reactions are dictated by long-term steady-state concentrations of reactive species. In a system which is at a fixed state and where there is a steady-state flux of ionizing radiation (such as a nuclear reactor which operates continuously for periods up to years), the chemically reactive species that are generated by water radiolysis will remain at steady-state concentrations.

To determine the effect of pH and temperature on the net radiolytic production of H_2 , O_2 and H_2O_2 and to establish the relationship between the measurable quantities (concentrations of the molecular products) and non-measurable quantities (the concentrations of radical species) a computational model has been developed [15].

Model calculations illustrate the effect of pH on the net radiolysis under deaerated conditions at 25 °C and 150 °C with dose rate $5.5 \text{ kG}\cdot\text{h}^{-1}$ as shown in Figures 2.18 and 2.19. These figures show the time evolution of the chemistry in water when exposed to a

continuous flux of radiation that is turned on at time 0. The model results show that the radiolysis product behaviour at $\text{pH}_{25^\circ\text{C}} 6.0$ and 10.6 are the same at short times ($< 10 \mu\text{s}$) but diverge considerably at longer times ($> 1 \text{ s}$). This is because the short-term chemistry is mostly determined by the primary radiolysis rate while longer term chemistry involves more chemical reactions.

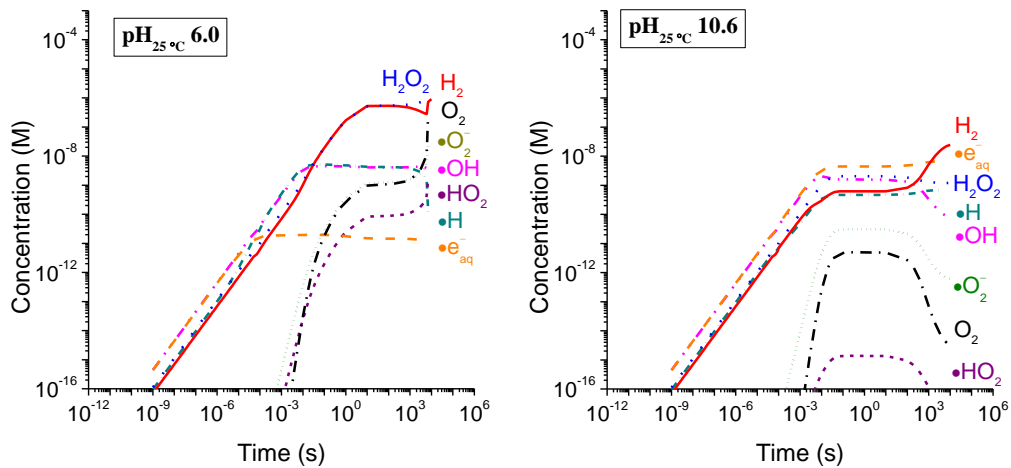


Figure 2.18: Model simulation results that illustrate the effect of pH on radiolysis chemistry in deaerated water at a dose rate of $5.5 \text{ kG}\cdot\text{h}^{-1}$ at 25°C [15].

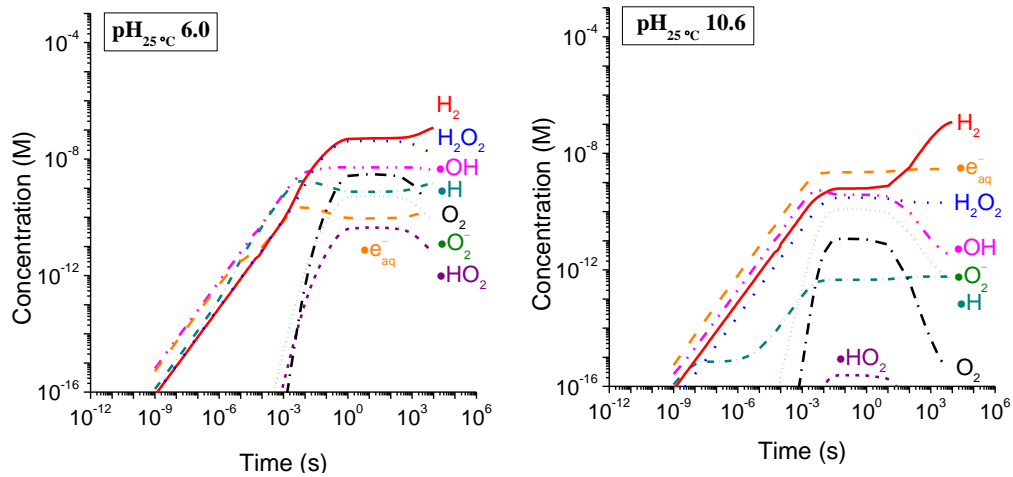


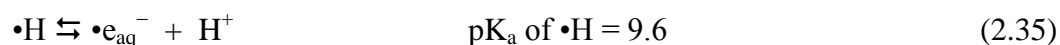
Figure 2.19: Model simulation results that illustrate the effect of pH on radiolysis chemistry in deaerated water at a dose rate of $5.5 \text{ kG}\cdot\text{h}^{-1}$ at $150 \text{ }^\circ\text{C}$ [15].

The primary radiolysis rate is obtained from,

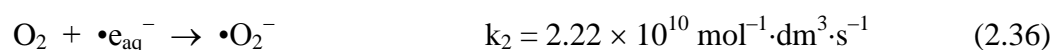
$$\dot{i} = \frac{d[i]}{dt} = D_R \cdot (10^{-6} \cdot G_i) \cdot \rho \quad (2.34)$$

where D_R is the absorbed dose rate in units of $\text{Gy}\cdot\text{s}^{-1}$ where $1 \text{ Gy (Gray)} = 1 \text{ J}\cdot\text{kg}^{-1}$, G_i is the G-value of species i in units of $\mu\text{mol}\cdot\text{J}^{-1}$, and ρ is the density of water in units of $\text{kg}\cdot\text{dm}^{-3}$. At a given temperature, the $G_i \cdot \rho \cdot D_R$ values are independent of pH. This explains the similarities in the concentrations of the primary radiolysis products at the two different pHs at early times.

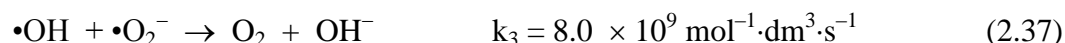
The concentrations of the primary radiolysis products deviate from a linear dependence on time after 1 ms. The model results show that the onset of the deviation occurs earlier at pH 6.0 than at pH 10.6. This effect of pH on the long-term behaviour arises mainly from a change in the rate of the reaction of $\bullet e_{\text{aq}}^-$ with H^+ :



At $\text{pH} < 9.6$, the pK_a of $\bullet\text{H}$, the reverse reaction is favorable, and it is the main loss path for $\bullet\text{e}_{\text{aq}}^-$ at long times. At $\text{pH} > 9.6$, the net rate of reaction 2.35 is extremely small. Thus, $\bullet\text{e}_{\text{aq}}^-$ accumulates until the concentration of the secondary product O_2 reaches a sufficient level to react with $\bullet\text{e}_{\text{aq}}^-$ at an appreciable rate:



This reaction, however, produces $\bullet\text{O}_2^-$ that can react with another primary radiolysis product, $\bullet\text{OH}$, reforming O_2 :

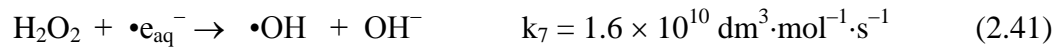
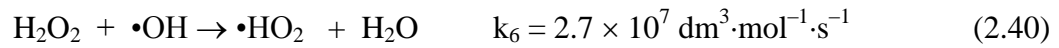


Once the reaction cycle between reactions (2.36) and (2.37) is established, $\bullet\text{OH}$ and $\bullet\text{e}_{\text{aq}}^-$ are continually removed and their concentrations decrease steadily. Since the molecular radiolysis products, H_2 and H_2O_2 , are removed primarily via reactions with the radical species, the decreases in $[\bullet\text{OH}]$ and $[\bullet\text{e}_{\text{aq}}^-]$ result in an increase in $[\text{H}_2]$ and $[\text{H}_2\text{O}_2]$.

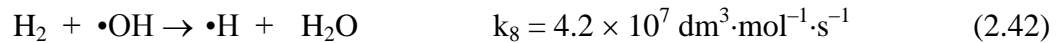
Temperature has a significant effect on the radiolysis product behaviour. This is due to the fact that the rate of thermal decomposition of H_2O_2 increases steeply with temperature. The thermal decomposition can occur via two reaction pathways:



Due to faster decomposition, the pseudo-steady-state concentration of H_2O_2 is reached at an earlier time and is lower at 150 °C than at 25 °C. This decrease in $[\text{H}_2\text{O}_2]$ slows the reactions of $\bullet\text{OH}$ and $\bullet\text{e}_{\text{aq}}^-$ with H_2O_2 :



Consequently, the steady-state concentrations of $\bullet\text{OH}$ and $\bullet\text{e}_{\text{aq}}^-$ increase. In turn, the steady-state concentration of H_2 decreases by reaction with $\bullet\text{OH}$.



At pH 10.6, similar trends are observed for radical and molecular species.

2.4.2 The Effect of Radiation on Transition Metal Alloy Corrosion

There are several studies on iron-based alloys and copper metal [20,21,73–77] in a radiation environment, but studies on corrosion and oxide formation on Stellite-6 at high temperature, and in particular under irradiation are limited [78–82]. The majority of corrosion research on Stellite alloys has been carried out from a metallurgic perspective [36,45,46,50,51,53,83,84].

The electrochemical studies on different stainless steel alloys have shown that exposing the alloy to radiation can lead to both a decrease [73,74,85–87] and an increase [18,75–77] in the measured corrosion potential (E_{corr}). In these studies, the increase in E_{corr} was attributed to the reaction of the steel with an oxidizing water radiolysis product. The

oxidizing species may be H_2O_2 [18,88,89], O_2 [75,77], or $\bullet\text{OH}$ [18,90]. The composition of the oxide formed on the metal often indicate which water radiolysis product is acting as the key oxidant. For example, an analysis of iron deposit products suspended in solution found that when O_2 was the key oxidizing species the oxidation product was Fe_3O_4 , whereas when H_2O_2 was the key oxidizing species the main oxidation product was Fe_2O_3 [91].

In some other cases, radiation has been shown to lower the corrosion rates of carbon steels [92]. Ahn et al. studied the corrosion of several steel alloys which differed in their carbon content (0.07 to 0.25 %) in high concentration of synthetic groundwater solutions at pH 10.3, at temperatures between 80 °C and 150 °C, and with a gamma radiation dose rate of 10 $\text{kGy}\cdot\text{h}^{-1}$ [92]. They found, for tests lasting two months, the corrosion rates of irradiated samples were 2 to 5 times lower than those of un-irradiated samples. For 4 month-long tests the corrosion rates of both irradiated and un-irradiated samples were similar.

Investigating the effect radiation on corrosion of copper has received more attention because copper is proposed for use in the construction of multi-barrier canisters for geological disposal of spent nuclear fuel [21,93]. Under the normal operating conditions of a repository, an intact canister and part of the surrounding bentonite clay will be penetrated by gamma radiation originating from the enclosed spent fuel. When water in the clay absorbs gamma radiation aqueous radiolysis generates water radiolysis products. Two oxidants from water radiolysis, hydrogen peroxide (H_2O_2) and the hydroxyl radical ($\bullet\text{OH}$), have significantly higher standard reduction potentials than copper and are thermodynamically capable of initiating corrosion of a copper canister. Therefore, several investigations have

been dedicated to study of the effect of gamma-radiation on corrosion of copper in anoxic water [21,93,94]. Björkbacka et al. [21] studied the effect of total gamma dose on radiation-induced corrosion of copper in anoxic pure water. Their experimental results showed that the rate of copper dissolution as well as the oxide layer thickness increased upon radiation. The same authors studied effect of radiation on copper corrosion in anoxic aqueous solutions with other ions present [94]. Samples exposed to dose rates of 0.37 or 0.77 kGy·h⁻¹ corroded significantly compared with un-irradiated samples. Corrosion products, mainly cuprite, and local circular cavities on the copper surface were observed. Neither the size nor the distribution of the corrosion features seemed to be dependent on the dose received.

2.5 REFERENCES

- [1] S.E. Ziemniak, M.A. Goyette, K.E.S. Combs, Cobalt (II) oxide solubility and phase stability in alkaline media at elevated temperatures, *J. Solution Chem.*, 28 (1999) 809–836.
- [2] C.D. Opris, R. Liu, M.X. Yao, X.J. Wu, Development of Stellite alloy composites with sintering/HIPing technique for wear-resistant applications, *Mater. Des.*, 28 (2007) 581–591.
- [3] U. Malayoglu, A. Neville, G. Beamson, Characterisation of the passive film on HIPed Stellite 6 alloy using X-ray photoelectron spectroscopy, *Mater. Sci. Eng. A.*, 393 (2005) 91–101.
- [4] F.R. Morral, Corrosion of cobalt and cobalt alloys, *Corros. NACE*, 25 (1969) 307.
- [5] U. Malayoglu, A. Neville, H. Lovelock, Assessing the kinetics and mechanisms of corrosion of cast and HIPed Stellite 6 in aqueous saline environments, *Corros. Sci.*, 47 (2005) 1911–1931.
- [6] A.J. Bard, L.R. Faulkner, *Electrochemical Methods: Fundamentals and Applications*, 2nd Ed., John Wiley & Sons, New York, 2000.
- [7] J.O'M. Bockris, A. Reddy, *Modern Electrochemistry 2A: Fundamentals of Electrode Processes*, 2nd Ed., Springer, New York, 1998.
- [8] P. Marcus, *Corrosion Mechanisms in Theory and Practice Corrosion Technology*, 3rd Ed., CRC Press., New York, 2011.
- [9] M. Pourbaix, *Atlas of Electrochemical Equilibria in Aqueous Solution*, NACE, Houston, Texas, 1996.

- [10] F.M. Tack, O.W. Callewaert, M.G. Verloo, Metal solubility as a function of pH in a contaminated, dredged sediment affected by oxidation., *Environ. Pollut.*, 91 (1996) 199–208.
- [11] R. Kelly, J. Scully, D.W. Shoesmith, R. Buchheit, *Electrochemical Techniques in Corrosion Science and Engineering*, CRC Press, New York, 2003.
- [12] N. Perez, *Electrochemistry and Corrosion Science*, Kluwer Academic Publishers, Boston, 2004.
- [13] C.M.A. Brett, A.N.A. Maria, O. Brett, *Electrochemistry: Principles, Methods, and Applications*, Oxford, New York, 1994.
- [14] J.A.V. Butler, Studies in heterogeneous equilibria. Part II. The kinetic interpretation of the Nernst theory of electromotive force, *Trans. Faraday Soc.*, 19 (1924) 729–733.
- [15] J.M. Joseph, B.S. Choi, P.A. Yakabuskie, J.C. Wren, A combined experimental and model analysis on the effect of pH and O₂(aq) on γ -radiolytically produced H₂ and H₂O₂, *Radiat. Phys. Chem.*, 77 (2008) 1009–1020.
- [16] P.A. Yakabuskie, J.M. Joseph, J.C. Wren, The effect of interfacial mass transfer on steady-state water radiolysis, *Radiat. Phys. Chem.*, 79 (2010) 777–785.
- [17] Q.W. Knapp, J.C. Wren, Film formation on type-316L stainless steel as a function of potential: Probing the role of gamma-radiation, *Electrochim. Acta.* 80 (2012) 90–99.
- [18] R.S. Glass, G.E. Overturf, R.A. Van Konynenburg, R.D. McCright, Gamma radiation effects on corrosion - I. Electrochemical mechanisms for the aqueous corrosion processes of austenitic stainless steels relevant to nuclear waste disposal in tuff, *Corros. Sci.*, 26 (1986) 577–590.
- [19] M. Behazin, M.C. Biesinger, J.J. Noël, J.C. Wren, Comparative study of film formation on high-purity Co and Stellite-6: Probing the roles of a chromium oxide layer and gamma-radiation, *Corros. Sci.*, 63 (2012) 40–50.
- [20] K. Daub, X. Zhang, J.J. Noël, J.C. Wren, Effects of γ -radiation versus H₂O₂ on carbon steel corrosion, *Electrochim. Acta*, 55 (2010) 2767–2776.
- [21] Å. Björkbacka, S. Hosseinpour, M. Johnson, C. Leygraf, M. Jonsson, Radiation induced corrosion of copper for spent nuclear fuel storage, *Radiat. Phys. Chem.*, 92 (2013) 80–86.
- [22] R.J. Wood, J.W.T. Spinks, *An Introduction to Radiation Chemistry*, 3rd Ed., Wiley-Interscience, New York, 1990.
- [23] H. Heli, H. Yadegari, Nanoflakes of the cobaltous oxide, CoO : Synthesis and characterization, *Electrochim. Acta*, 55 (2010) 2139–2148.
- [24] I. Kelpšaitė, J. Baltrušaitis, E. Valatka, Electrochemical deposition of porous cobalt oxide films on AISI 304 tube steel, *Mater. Sci.*, 17 (2011) 236–243.
- [25] Y. Zhu, H. Li, Y. Koltypin, A. Gedanken, Preparation of nanosized cobalt hydroxides and oxyhydroxide assisted by sonication, *J. Mater. Chem.*, 12 (2002) 729–733.
- [26] S.-L. Chou, J.-Z. Wang, H.-K. Liu, S.-X. Dou, Electrochemical deposition of porous Co(OH)₂ nanoflake films on stainless steel mesh for flexible supercapacitors, *J. Electrochem. Soc.*, 155 (2008) A926–A929.
- [27] M. Dinamani, P.V. Kamath, Electrocatalysis of oxygen evolution at stainless steel anodes by electrosynthesized cobalt hydroxide coatings, *J. Appl. Electrochem.*, 30 (2000) 1157–1161.

- [28] A. Gulino, G. Fiorito, I. Fragalà, Deposition of thin films of cobalt oxides by MOCVD, *J. Mater. Chem.*, 13 (2003) 861–865.
- [29] A. Foelske, H.-H. Strehblow, Structure and composition of electrochemically prepared oxide layers on Co in alkaline solutions studied by XPS, *Surf. Interface Anal.*, 34 (2002) 125–129.
- [30] D. Klissurski, V. Rives, High-temperature superconductors in catalysis, *Appl. Catal. A Gen.*, 109 (1994) 1–44.
- [31] J. Chen, X. Wu, A. Selloni, Electronic structure and bonding properties of cobalt oxide in the spinel structure, *Phys. Rev. B.*, 83 (2011) 245204.
- [32] D. Marijan, M. Gojic, Electrochemical study of the chromium electrode behaviour in borate buffer solution, *J. Appl. Electrochem.*, 32 (2002) 1341–1346.
- [33] G. Sandronet, G. Valeriot, M. Cattit, Electronic, magnetic and crystal structure by theoretical methods of Cr_2O_3 , 1. *Phys. Chem Solids*, 57 (1996) 1735–1741.
- [34] R. Cheng, B. Xu, C.N. Borca, A. Sokolov, C.-S. Yang, L. Yuan, Characterization of the native Cr_2O_3 oxide surface of CrO_2 , *Appl. Phys. Lett.*, 79 (2001) 3122–3124.
- [35] C.C. Lin, A review of corrosion product transport and radiation field buildup in boiling water reactors, *Prog. Nucl. Energy*, 51 (2009) 207–224.
- [36] P.S. Liu, K.M. Liang, High-temperature oxidation behavior of the Co-base superalloy DZ40M in air, *Oxid. Met.*, 53 (2000) 351–360.
- [37] U. Lüders, F. Sánchez, J. Fontcuberta, Initial stages in the growth of {111}-faceted CoCr_2O_4 clusters: mechanisms and strained nanometric pyramids, *Appl. Phys. A Mater. Sci. Process*, 79 (2004) 93–97.
- [38] D. Friebel, M. Bajdich, B.S. Yeo, M.W. Louie, D.J. Miller, H. Sanchez Casalongue, On the chemical state of Co oxide electrocatalysts during alkaline water splitting., *Phys. Chem. Chem. Phys.*, 15 (2013) 17460–17467.
- [39] C.F. Baes, *The Hydrolysis of Cations*, 2nd Ed., Wiley, New York, 1986.
- [40] J. Chivot, L. Mendoza, C. Mansour, T. Pauporté, M. Cassir, New insight in the behaviour of Co– H_2O system at 25–150 °C, based on revised Pourbaix diagrams, *Corros. Sci.*, 50 (2008) 62–69.
- [41] Y. Hai-Xia, X.H.-Bin, Z. Yi, Z. Shi.-Li, G. Y.-Ying Potential pH diagrams of Cr– H_2O system at elevated temperatures, *Trans. Nonferrous Met. Soc. China*, 20 (2010) s26–s31
- [42] A. Bewick, C. Gutiérrez, G. Larramona, C. Gutierrez, An in-situ IR spectroscopic study of the anodic oxide film on cobalt in alkaline solutions, *J. Electroanal. Chem.*, 333 (1992) 165–175.
- [43] W.A. Badawy, Electrochemical behaviour of cobalt in aqueous solutions of different pH, *J. Appl. Electrochem.*, (2000) 693–704.
- [44] W.K. Behl, J.E. Toni, Anodic oxidation of cobalt in potassium hydroxide, *J. Electroanal. Chem.*, 31 (1971) 63–75.
- [45] U. Malayoglu, A. Neville, Mo and W as alloying elements in Co-based alloys—their effects on erosion–corrosion resistance, *Wear*, 259 (2005) 219–229.
- [46] V. Kuzucu, M. Ceylan, H.C. Aksoy, Microstructure and phase analyses of Stellite 6 plus 6 wt .% Mo alloy, *J. Materials Process. Technol.*, 69 (1997) 257–263.

- [47] G. Michel, P. Berthod, M. Vilasi, S. Mathieu, P. Steinmetz, Protection of cobalt-based refractory alloys by chromium deposition on surface, *Surf. Coatings Technol.*, 205 (2011) 5241–5247.
- [48] J.-N. Aoh, J.-C. Chen, On the wear characteristics of cobalt-based hardfacing layer after thermal fatigue and oxidation, *Wear*, 250 (2001) 611–620.
- [49] P. Berthod, P. Lemoine, J. Ravoux, High-temperature microstructures of ternary Co-30wt.% Cr-based alloys over the [0–2.0wt.%] carbon range, *J. Alloys Compd.*, 467 (2009) 227–234.
- [50] F. Rosalbino, G. Scavino, Corrosion behaviour assessment of cast and HIPed Stellite 6 alloy in a chloride-containing environment, *Electrochim. Acta*, 111 (2013) 656–662.
- [51] J.-C. Shin, J.-M. Doh, J.-K. Yoon, D.-Y. Lee, J.-S. Kim, Effect of molybdenum on the microstructure and wear resistance of cobalt-base Stellite hardfacing alloys, *Surf. Coatings Technol.*, 166 (2003) 117–126.
- [52] M.X. Yao, J.B.C. Wu, Y. Xie, Wear, corrosion and cracking resistance of some W- or Mo-containing Stellite hardfacing alloys, *Mater. Sci. Eng. A*, 407 (2005) 234–244.
- [53] M.X. Yao, J.B.C. Wu, Y. Xie, Wear, corrosion and cracking resistance of some W- or Mo-containing Stellite hardfacing alloys, *Mater. Sci. Eng. A*, 407 (2005) 234–244.
- [54] F.P. Fehlner, N.F. Mott, Low-temperature oxidation, *Oxid. Met.*, 2 (1970) 59–99.
- [55] E.C.C. Baly, W.P. Pepper, C.E. Vernon, A theory of formation of protective oxide film on metals, *Trans. Faraday Soc.*, 35 (1939) 1175–1177.
- [56] C.C. Lin, C.Y. Chao, D.D. Macdonald, A point defect model for anodic passive films, *J. Electrochem. Soc.*, 128 (1981) 1194–1198.
- [57] N.F. Mott, The theory of the formation of protective oxide films on metals-III, *Trans. Faraday Soc.*, 43 (1946) 429–434.
- [58] N. Cabrera, Theory of the oxidation of metals, *Rep. Prog. Phys.*, 12 (1949) 163–184.
- [59] D.D. Macdonald, The history of the Point Defect Model for the passive state: A brief review of film growth aspects, *Electrochim. Acta*, 56 (2011) 1761–1772.
- [60] C. Wagner, Theoretical analysis of the diffusion processes determining the oxidation rate of alloys, *J. Electrochem. Soc.*, 99 (1952) 369–380.
- [61] D.D. Macdonald, The Point Defect Model for the passive state, *J. Electrochem. Soc.*, 139 (1992) 3434.
- [62] M. Bojinov, Modelling the formation and growth of anodic passive films on metals in concentrated acid solutions, *J. Solid State Electrochem.*, (1997) 161–171.
- [63] B. Diawara, Y.-A. Beh, P. Marcus, Nucleation and growth of oxide layers on stainless steels (FeCr) using a virtual oxide layer model, *J. Phys. Chem., C*, 114 (2010) 19299–19307.
- [64] K. Leistner, C. Toulemonde, B. Diawara, A. Seyeux, P. Marcus, Oxide film growth kinetics on metals and alloys:II. Numerical simulation of transient behavior, *J. Electrochem. Soc.*, 160 (2013) C197–C205.
- [65] CRC Handbook of Chemistry and Physics, CRC Press, Cleveland, Ohio, 1978.
- [66] D. Janik, I. Janik, D.M. Bartels, Neutron and beta/gamma radiolysis of water up to supercritical conditions. 1. beta/gamma yields for H₂, H(·) atom, and hydrated electron., *J. Phys. Chem. A*, 111 (2007) 77–86.

- [67] J.R. Farhataziz, *Radiation Chemistry. Principles and Applications*, VCH Publishers, Weinheim, 1987..
- [68] D.F. Sangster, J.H. O'Donnell, *Principles of Radiation Chemistry*, in: American Elsevier Publishing Co., New York, 1970.
- [69] I.G. Draganic, *The Radiation Chemistry of Water*, Academic Press, New York, 1971.
- [70] J.C. Wren, *Steady-State Radiolysis: Effects of Dissolved Additives*, in: B.J.M. , C.M. Wai (Ed.), *Nucl. Energy Environ., ACS Symposium Series*, 2010 pp. 271–295.
- [71] G.V. Buxton, *Radiation Chemistry*, in: J.B. M. Spothem-Maurizot, M. Mostafavi, T. Douki (Ed.), *EDP Science, France*, 2008.
- [72] A.J. Elliot, D.M. Bartel, *AECL Report, 153127160450001*, Chalk River, Canada, 2009.
- [73] W.E. Clark, *The effect of gamma irradiation on the potential behavior of platinum and stainless steel electrodes*, *J. Electrochem. Soc.*, 105 (1958) 483–485.
- [74] K.S. Fujita, N.C. Matsuura, *Radiation-induced potential difference between electrodes with and without gamma rays*, *Radiat. Phys. Chem.*, 49 (1997) 357–362.
- [75] R.H. Lamoreaux, S. Jose, D. Cubicciotti, *Contributions of the oxide layer to the corrosion potential of stainless steel under nuclear reactor conditions H₂ only*, *J. Electrochem. Soc.*, 140 (1993) 2197–2205.
- [76] R.S. Lillard, G. Vasquez, *The inhibition of pitting corrosion in stainless steel 304L during proton irradiation*, *J. Electrochem. Soc.*, 155 (2008) C162–C168.
- [77] A.N. Scott, *Electrochemical corrosion potential of carbon steel feeder pipes in a Canadian deuterium uranium reactor generating station under return-to-service conditions*, *Corrosion*, 65 (2009) 49–60.
- [78] W.H. Hocking, D.H. Lister, *Corrosion of Stellite-6 in lithiated and borated high-temperature water*, *Surf. Interface Anal.*, 11 (1988) 45–59.
- [79] C. Maffiotte, M. Navas, M.L. Casta, *XPS characterization of oxide films formed in cobalt-based alloys during corrosion tests at high temperature*, *Surf. Interface Anal.*, 166 (2000) 161–166.
- [80] W.H. Hocking, F.W. Stanchell, E. McAlpine, D.H. Lister, *Mechanisms of corrosion of Stellite-6 in lithiated high temperature water*, *Corros. Sci.*, 25 (1985) 531–557.
- [81] N.I.Y. Hemmi, Y. Uruma, *General corrosion of materials water under conditions simulated primary*, *J. Nucl. Sci. Technol.*, 455 (1994) 443–455.
- [82] N.S. McIntyre, D. Zetaruk, E.V. Murphy, *X-ray photoelectron spectroscopic study of the aqueous oxidation of Stellite-6 alloy*, *Surf. Interface Anal.*, 1 (1979) 105–110.
- [83] X. Zhang, Y. Li, N. Tang, E. Onodera, A. Chiba, *Corrosion behaviour of CoCrMo alloys in 2 wt.% sulphuric acid solution*, *Electrochim. Acta*, 125 (2014) 543–555.
- [84] M. Reyes, A. Neville, *Mechanisms of erosion-corrosion on a cobalt-base alloy and stainless-steel UNS S17400 in aggressive slurries*, *J. Mater. Eng. Perform.*, 10 (2001) 723–730.
- [85] P. Bouniol, A. Aspart, *Disappearance of oxygen in concrete under irradiation: the role of peroxides in radiolysis*, *Cem. Concr. Res.*, 28 (1998) 1669–1681.
- [86] R.J. Winsley, N.R. Smart, A.P. Rance, P.A.H. Fennell, B. Reddy, B. Kursten, *Further studies on the effect of irradiation on the corrosion of carbon steel in alkaline media*, *Corros. Eng. Sci. Technol.*, 46 (2011) 111–116.

- [87] C.M.N. Fujita, Evaluation of the potential difference induced between platinum electrodes with and without gamma-ray irradiation, *Radiat. Phys. Chem.*, 50 (1997) 457–463.
- [88] S. Sunder, N.H. Miller, D.W. Shoesmith, Corrosion of uranium dioxide in hydrogen peroxide solutions, *Corros. Sci.*, 46 (2004) 1095–1111.
- [89] G. Bellanger, Behaviour of 316 Ti stainless steel in deuterium oxide with chloride, *J. Mater. Sci.*, 2 (1997) 4355–4376.
- [90] E. Leoni, C. Corbel, V. Cobut, D. Simon, D. Féron, M. Roy, Electrochemical behaviour of gold and stainless steel under proton irradiation and active Redox couples, *Electrochim. Acta*, 53 (2007) 495–510.
- [91] M.A. Nejad, M. Jonsson, Reactivity of hydrogen peroxide towards Fe_3O_4 , Fe_2CoO_4 and Fe_2NiO_4 , *J. Nucl. Mater.*, 334 (2004) 28–34.
- [92] T.M Ahn, P. Soo, Corrosion of low-carbon cast steel in concentrated synthetic groundwater at 80 to 150°C, *Waste Manag.*, 15 (1995) 471–476.
- [93] R.S. Glass, W.H. Yunker, Long-term corrosion behaviour of copper-base materials in a gamma irradiated environment. In: Bates, J.K., Seefeldt, W.B. (Eds.). *Scientific Basis for Nuclear Waste Management: Symposium held in Boston, Massachusetts, USA, 1 – 4 December 1986* pp. 579–590.
- [94] Å. Björkbacka, S. Hosseinpour, C. Leygraf, M. Jonsson, Radiation induced corrosion of copper in anoxic aqueous solution, *Electrochem. Solid-State Lett.*, 15 (2012) C5–C7.

CHAPTER 3

Experimental Techniques and Procedures

3.1 ELECTROCHEMICAL TECHNIQUES

A series of electrochemical experiments along with the surface analyses were used to develop a mechanistic understanding of the aqueous corrosion kinetics of Stellite-6. In this chapter the experimental techniques and procedures that were used are described.

3.1.1 Electrochemical Cell

A standard three-electrode electrochemical cell design was used in this study, consisting of a working electrode (WE), a counter electrode (CE) and a reference electrode (RE), connected to a potentiostat to control the potential and measure the current. The cell used in all electrochemical experiments is shown in Figure 3.1. In the electrochemical cell the current of the reaction under investigation passes between the WE (the electrode of interest, in this case, pure Co or Stellite-6) and the CE. The CE should have high activity, negligible by-product production and a larger surface area compared to the working electrode. For these reasons platinum mesh is a common choice for the CE and was used in this work. The RE electrode is a stable electrode of known potential against which the potential of the WE can be controlled or measured. In the potentiostat, the WE and RE are connected through a circuit with a high impedance voltmeter that ensures negligible current flows through the external measurement circuit between the WE and RE [1].

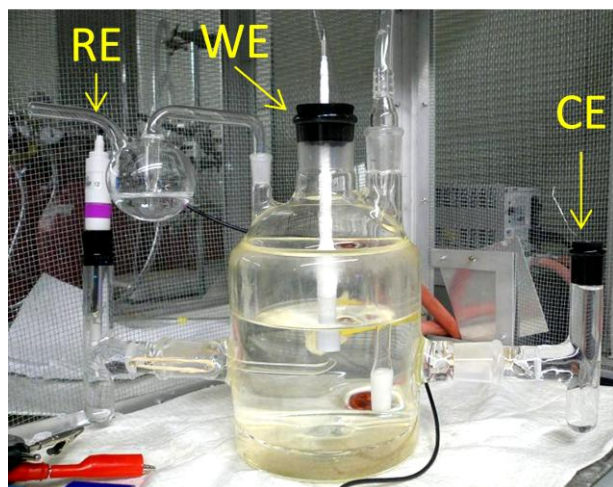


Figure 3.1: Standard three-electrode electrochemical cell.

3.1.2 Cyclic Voltammetry

Cyclic voltammetry (CV) is the most widely used technique to study the anodic and cathodic processes that occur at an electrode surface as a function of an applied potential. In this technique, the current density is monitored while the working electrode potential is swept between an initial potential and a final potential and back, Figure 3.2.

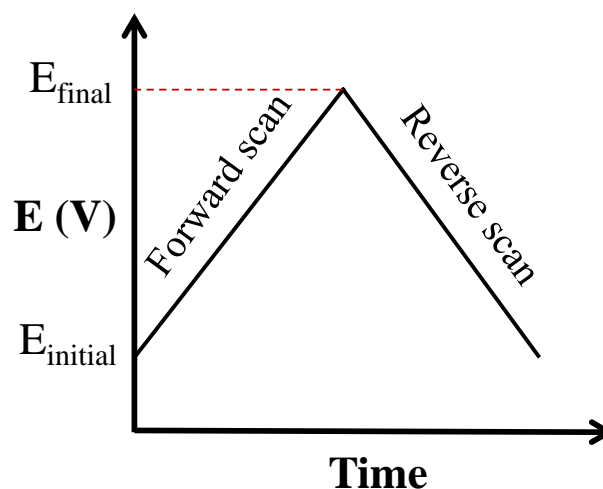


Figure 3.2: The potential-time profile applied in a cyclic voltammetry experiment.

This cycle can be repeated any number of times. The initial and final vertex potentials are chosen to be within the water stability region (above the potential of water reduction and below the potential of water oxidation). These limits depend on the pH of a water solution and can shift by ± 59 mV per pH unit. The measured current density at any point in a scan shows the net charge transfer occurring on the working electrode at the applied potential. This provides information about the sequence of electrochemical oxidation and reduction reactions occurring on the WE. The current response may depend on the scan rate and changes to the scan rate may provide information on the relative contribution to the current of different reactions [2]. Also, changes to the final potential can provide information on the coupling of oxidation and reduction processes. In fact, it is a way to check on the presence of a reduction peak that corresponds to a specific oxidation peak.

3.1.3 Potentiostatic Polarization

In a potentiostatic polarization experiment a constant external potential, E_{APP} , with respect to the reference electrode, is applied to the working electrode, and is held for a desired length of time while the resulting current flow is measured. The value of the applied potential with respect to E_{CORR} will determine the direction of electron flow, thereby allowing either anodic or cathodic reactions to be studied. During anodic polarization the time-dependent behaviour of the current can often provide insight into processes such as the oxide film growth mechanism. Under potentiostatic polarization, the measured current will have a unique value if the coupled redox half reactions remain the same due to the fact that i and E_{APP} are related via the Butler-Volmer equation as explained in Chapter 2. The change in current with time also provides insight into the changes occurring on the working electrode surface as the system approaches steady state.

3.1.4 Electrochemical Impedance Spectroscopy

The electrochemical impedance spectroscopy (EIS) method is useful in characterizing oxide layer properties. However, analysis of EIS data is more complicated than the electrochemical techniques described above. Oxide characterization includes the determination of the polarization resistance (R_p), capacitive (C_{eff}), inductive, and diffusive components of the oxide as an electric circuit component, and the rates of charge transfer at various interfaces [3]. An electrical interface is rarely purely resistive or capacitive in nature, but instead a combination of those two properties. Electrochemical impedance spectroscopy permits the analysis of alternating current (AC) impedance data based on modeling of an

equivalent electrical circuit. EIS involves application of a small AC potential oscillation (typically 10 mV in amplitude) to an applied potential (E_{app} or E_{corr}) and measurement of the amplitude, I_0 , and phase shift Φ of the output AC current, as illustrated in Figure 3.3,

$$E_{AC} = E_0 \sin(\omega t) + E_{APP} \text{ (or } E_{corr}) \quad (3.1)$$

$$I_{AC} = I_0 \sin(\omega t + \Phi) \quad (3.2)$$

where ω is the angular frequency, E_0 is the maximum amplitude of the sinusoidal potential, I_0 is the current amplitude and Φ is the phase shift. The applied AC voltage is small so that the system is not disturbed from a linear relationship, Figure 3.4.

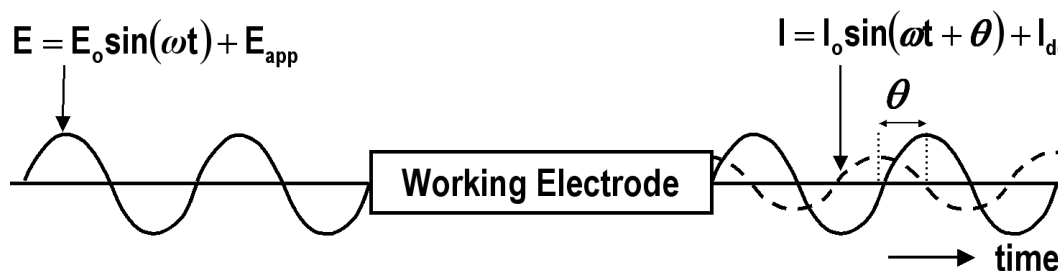


Figure 3.3: Schematic of the applied sinusoidal potential and the current response for electrochemical impedance spectroscopy. The parameters are defined in the text.

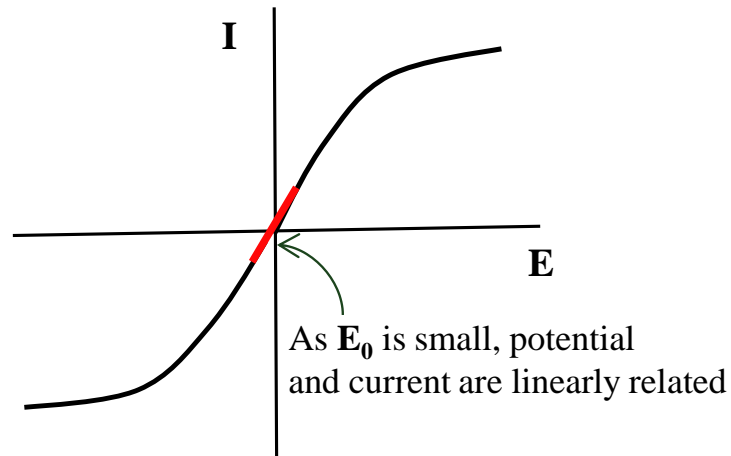


Figure 3.4: Schematic of the linear current-potential response measured when a small +/- E_0 is applied in electrochemical impedance spectroscopy for a corrosion reaction occurring at steady state.

For electrochemical purposes, resistive behaviour in a system is often related to the resistance of an oxide film, or a charge transfer process at an interface. The current passing through a resistor, with a resistance R_x , can be calculated from Ohm's law,

$$i = \frac{\Delta E}{R_x} \quad (3.3)$$

where i is the current and ΔE is the potential drop across the resistance. The impedance, $Z(\omega)$, of the system is a function of the frequency of the sinusoidal potential input and the measured sinusoidal current.

$$Z(\omega t) = \frac{E_0 \sin(\omega t)}{I_0 \sin(\omega t + \phi)} \quad (3.4)$$

If the current is completely in-phase with the potential ($\phi = 0^\circ$) it means that the electrochemical response is purely resistive whereas an out-of-phase current output ($\phi = -90^\circ$)

indicates that electrochemical response is purely capacitive. The measured current for a capacitor is,

$$\begin{aligned} i &= C \frac{dE}{dt} = \frac{d}{dt} (CE_0 \sin(\omega t)) = C E_0 \frac{d \sin(\omega t)}{dt} \\ &= CE_0 \omega \cos(\omega t) = I_0 \sin\left(\omega t - \frac{\pi}{2}\right) \end{aligned} \quad (3.5)$$

where C is the capacitance. The impedance is expressed as a combination of real, $Z'(\omega)$, and imaginary, $Z''(\omega)$, components,

$$Z(\omega t) = \frac{E_0 \sin(\omega t)}{I_0 \sin(\omega t + \phi)} = Z'(\omega t) - jZ''(\omega t) \quad \text{where } j^2 = -1 \quad (3.6)$$

The resistance, R_x is the real part of the impedance and the capacitance is related to the imaginary part of the total impedance.

$$Z'(\omega t) = R_x \text{ and } Z''(\omega) = \frac{1}{\omega C} \quad (3.7)$$

The absolute impedance value, $|Z(\omega)|$, can be obtained from

$$|Z(\omega t)|^2 = Z(\omega) \cdot Z(\omega)^* = Z'(\omega)^2 + Z''(\omega)^2 = \frac{R_x^2 + \omega^2 C^2}{\omega^2 R_x^2 C^2} \quad (3.8)$$

and the phase angle is given by,

$$\phi = \arctan \frac{Z''(\omega)}{Z'(\omega)} = \frac{1}{\omega R_x C} \quad (3.9)$$

The relationship of the phase angle to $|Z(\omega)|$, R and C in the complex plane is schematically shown in Figure 3.5.

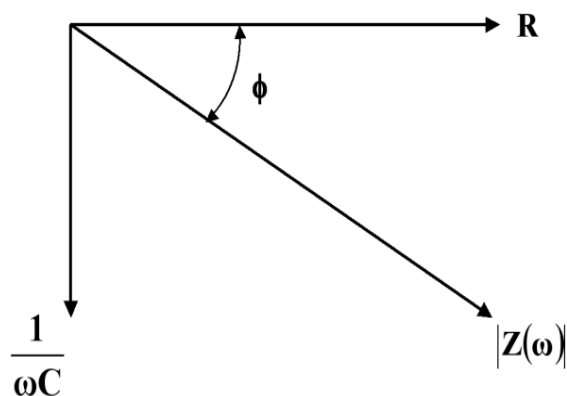


Figure 3.5: Relationship of the real and imaginary components of impedance in a series one-RC circuit.

The impedance results are usually graphed as a Nyquist plot or a Bode plot. For a Nyquist plot, the real impedance component is plotted against the imaginary impedance component. The resulting graph can often be extrapolated to form a semicircle as shown in Figure 3.6a. A Bode plot is composed of two graphs: a plot of the log of the absolute value of the impedance vs. the log of the applied frequency, and a plot of the phase angle vs. the log of the frequency, as shown in Figure 3.6b.

The EIS data is normally interpreted in terms of an equivalent electrical circuit which contains the resistive and capacitive elements of the system (normally the oxide layer(s) under examination). The equivalent circuits shown in Figure 3.7a and 3.7b contain electrical components that correspond to one time constant and two time constants, respectively. In the log $|Z|$ versus log frequency plot, the impedance modulus at high and low frequencies is constant and independent of frequency. At the high frequency end, the response belongs to R_S , while at the low frequency end the response is a sum of the resistive elements ($R_S + R_{CT}$)

[4]. The capacitance can be determined where the slope of the line equals -1 . A single resistor, R_s , is used to account for the resistance to current flow in the test solution, while the resistive element, R_1 , is the resistance associated with the oxide film. The capacitance, C_1 , is associated with the surface oxide film, and represents the charge storage capacity across that film. Constant phase elements (CPE) are commonly used in place of capacitors to account for the non-ideal nature of an oxide film. These non-idealities include differences in film thickness, dielectric constants and defect densities.

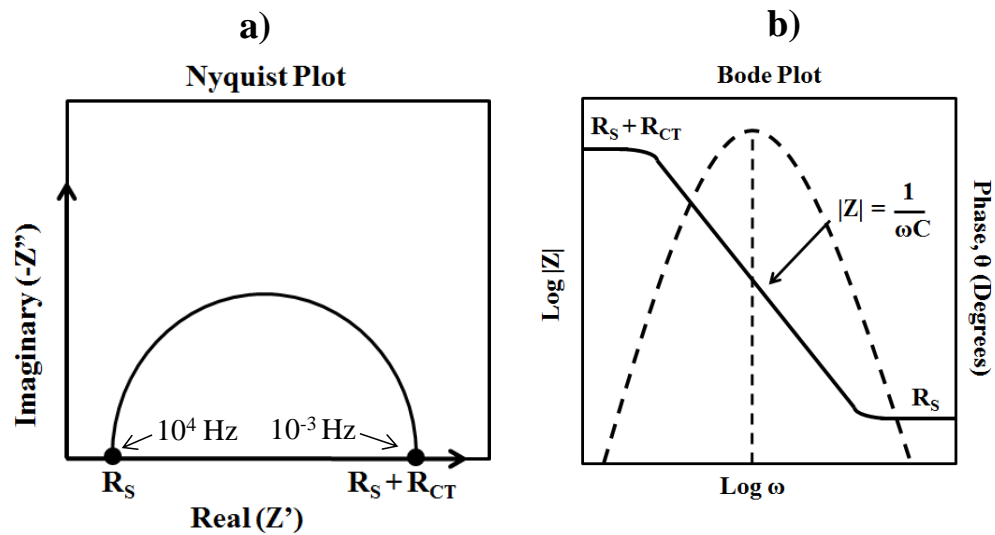


Figure 3.6: EIS data presentation: (a) Nyquist plot and (b) Bode plot.

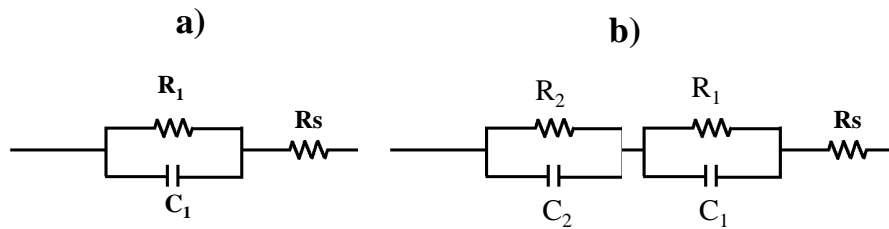


Figure 3.7: Equivalent circuits containing: a) one time constant and b) two time constants.

The impedance of a CPE is defined by

$$Z_{\text{CPE}} = \frac{1}{Q(j\omega)^\alpha} \quad (3.10)$$

Where ω is an angular frequency ($\omega = 2\pi f$). Alpha is a parameter that varies between 1 and 0. When $\alpha = 1$, the CPE is equivalent to a capacitor and $Q = C$. When $\alpha = 0$, the CPE is equivalent to a resistor and $Q = R^{-1}$. At intermediate values of α , the CPE is a phenomenological term with no simple physical justification. It is clear that the CPE parameter Q cannot represent a simple capacitance when $\alpha < 1$. The effective capacitance associated with a CPE can be expressed using the equation derived by Brug et al. [5],

$$C_{\text{eff}} = \left[Q \left(\frac{1}{R_x} + \frac{1}{R_s} \right)^{\alpha-1} \right]^{\frac{1}{\alpha}} \quad (3.11)$$

3.2 SURFACE ANALYSIS

3.2.1 Scanning Electron Microscopy

Scanning electron microscopy (SEM) is used for examination and analysis of microstructure morphology. A high resolution beam of electrons is directed onto the sample surface and the reflected electron intensity is measured and displayed on a cathode-ray screen to produce an image. The resolution of an image taken by SEM is much higher than that of an optical microscope, and images with a much greater depth of field are formed. Samples are located in a vacuum chamber in order to give both incident and resulting scattered electrons free passage from the source to the sample and from the sample to the detector. The incident electrons typically have an energy ranging from a few hundred eV to 40 keV. They are focused by one or two condenser lenses into a beam with a very fine focal spot, typically sized from 0.4 to 5 nm in diameter. The beam passes through pairs of scanning coils or pairs of deflector plates which deflect the beam either horizontally or vertically so that a raster scan can be used to image a rectangular area of the sample [6,7]. When the incident electron beam hits the surface, scattering and absorption cause energy loss of the incident beam within a certain volume of the sample, known as the interaction volume. This volume is dependent on the beam energy, and the atomic number and density of the atoms in the sample. Within this interaction volume, energy exchange between the beam and the sample takes place. High energy electrons from elastic scattering and lower energy secondary electrons formed by inelastic scattering can be detected. After suitable

amplification the detected electrons can be used to modulate the intensity of the scanning image on display video screen.

When a sample surface is subjected to a focused beam of electrons, various processes such as elastic and inelastic scattering can occur. Incident electrons can interact with the atoms on the surface of the sample and eject secondary electrons and photons (characteristic X-rays). These electrons are lower in energy than those in the incident beam (inelastic scattering), and only arise from the top few nanometers of the sample surface. Measurements of secondary electrons are used to study the sample topography and morphology. Due to varying distances from the detector, secondary electrons from areas of higher points on the sample surface are more likely to be detected than electrons from lower points. The varying signal strengths of the secondary electrons results in a brightness contrast in the image that gives the micrograph depth perspective.

Characteristic X-rays are used for the elemental analysis. This technique is called energy dispersive X-ray spectrometry (EDX). Qualitative analysis involves the identification of the lines in the spectrum and is fairly straightforward owing to the simplicity of X-ray spectra [8].

Electrons from the elastic scattering of the beam with the specimen are called backscattered electrons. The escape depth of backscattered electrons can be greater than that of secondary electrons and consequently resolution of surface topographical characteristics can suffer. However, backscattered electrons have the advantage over secondary electrons that they are sensitive to the atomic mass of the nuclei they scatter from [6]. As a result,

heavier elements which backscatter more efficiently appear brighter than lighter elements in a backscattered electron image. The combined use of both secondary and backscattered electron imaging modes provides valuable information not typically available through either imaging method alone.

Secondary electrons and backscattered electrons are commonly used for imaging samples: secondary electrons are most valuable for showing morphology and topography on samples and backscattered electrons are most valuable for illustrating contrasts in composition in multiphase samples

3.2.2 X-Ray Photoelectron Spectroscopy

X-ray photoelectron spectroscopy (XPS) is a quantitative spectroscopic technique that can measure the elemental composition, chemical state, and electronic state of the elements within the first 1–30 monolayers of a surface. Because XPS only measures the properties of a few nm of a surface, it can be used to determine elemental composition as a function of depth by combining it with ion etching to progressively remove surface layers. Spectra are obtained by irradiating a sample with X-rays of known energy, $h\nu$, and causing photoelectrons, a core electron, to be emitted from the sample surface. The kinetic energies (KE) of the photoelectrons are related to the ionization energy (or binding energy, BE) of a particular atom and the work function of the spectrometer, Φ_{sp} , (typically 4-5 eV) by equation 3.12 [9],

$$KE = h\nu - BE - \Phi_{sp} \quad (3.12)$$

Since the binding energy is characteristic of the atom from which it was ejected, measurements of the photoelectron energy and can be used to identify all elements in the periodic table with the exception of He and H. A typical XPS spectrum is a plot of the measured photoelectron intensity as a function of the kinetic energy of the electrons detected. Each element produces a set of XPS peaks or lines at characteristic binding energy values. These peaks correspond to ejection of electrons from different orbitals of an atom and the binding energies correspond to energies of those orbitals (Figure 3.8). The peak locations and areas can be used (with appropriate sensitivity factors) to determine the composition of the surface. The shape of each peak and the binding energy can be slightly altered by the chemical environment of the emitting atom as well (e.g., oxidation state) [10]. The sizes of the peaks are directly related to the amount of a particular element within the sample volume that is irradiated.

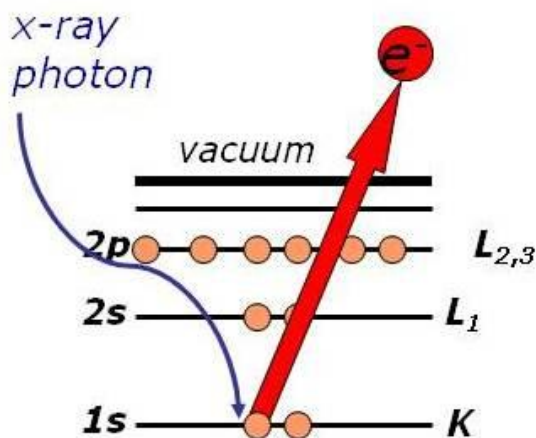


Figure 3.8: Schematic demonstrating the principles of XPS and the ejection of a photoelectron.

3.2.3 Auger Electron Spectroscopy

Auger electron spectroscopy (AES) is one of the most commonly used analytical techniques to measure the chemical composition of the first few monolayers of a given surface. It can have a sensitivity on the order of 0.1 atomic % and a spatial resolution on the order of 10 nm [7]. Auger spectroscopy uses a three-electron process (Figure 3.9). This process is typically initiated by ejection of a core electron of an atom by incident high-energy electrons (typically with energy between 3 and 30 keV). The vacancy leaves the atom in an electronically excited state. The excited atom can lose energy in one of two ways. Firstly, an electron from a higher energy orbital drops down to fill the vacancy. This is accompanied by either the ejection of a photon of the appropriate energy, or by the ejection of another electron. Since the differences in energies of the orbitals involved are typically high, the ejected photon has a high energy (in the X-ray region). The measurement of these X-rays is known as X-ray fluorescence (XRF) spectroscopy. The kinetic energy of an ejected secondary electron (a so-called Auger electron) is also characteristic of the source atom. The Auger electron energy (E_{Auger}) is related to the electronic orbital energies of an atom by,

$$E_{\text{Auger}} = BE_b - E_b(L_1) - E_b(L_{2,3}) \quad (3.13)$$

where BE_b is the binding energy of the 1s orbital (core electron), while $E_b(L_1)$ and $E_b(L_{2,3})$ are the binding energies of the first and second outer orbitals, respectively. Since the atomic energy levels are characteristic of an atom, measurement of the energies of the X-rays and the Auger electrons can determine the atoms that are present. As well, like XPS, the Auger

X-ray and electron energies can be influenced by the chemical environment of the atom and give information on properties like the oxidation state.

Similar to XPS, Auger spectroscopy can be used to analyze elemental composition as a function of depth by combining it with surface etching. For this technique bombardment with a well-focused ion beam (Ar^+) to remove successive surface layers is used. After ablation each layer is analyzed for the individual components [9]

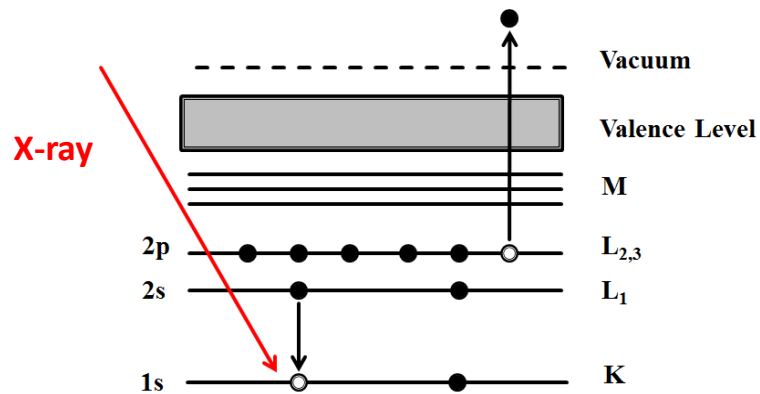


Figure 3.9: Schematic demonstrating the principles of AES and the ejection of an Auger electron.

3.2.4 Inductively-Coupled Plasma Mass Spectrometry

Inductively-coupled plasma mass spectrometry (ICP-MS) combines a high temperature ICP (inductively-coupled plasma) source with a mass spectrometer to determine the levels of trace elements in a sample [11]. An ICP-MS system can be dissected into four main processes: (1) sample introduction and aerosol generation, (2) ionization by an argon plasma source, (3) mass discrimination, and (4) ion detection [12]. In the first phase,

digested solutions are introduced by a peristaltic pump and nebulized in a spray chamber. The resultant aerosol particles are carried by a noble gas (normally pure helium) to a plasma region. In the plasma region inductive coupling of energy from a microwave power supply coil heats the gas stream to a temperature sufficiently high to vaporize and ionize the droplets creating a plasma. The ionization inside the plasma produces both simple and complex (polyatomic) ions. These include dissociation products of water and the components of the solutes in a solution sample. The ions produced are extracted from the plasma into a mass spectrometer (frequently a small quadrupole unit). The ionic stream flows through the quadrupole mass spectrometer and is separated based on atomic mass. The selected ions are collected by a detector which provides an output signal. Based on the distribution of the mass fragments that are detected, the composition of the sample can be determined. The magnitude of the signal can be related to the quantity of the different compounds in the sample.

3.3 EXPERIMENTAL PROCEDURES

The following sections describe the general experimental procedures that were used in this work. Unique experimental techniques, procedures, and equipment are described as required in following chapters.

3.3.1 Electrochemical Setup

A standard three-electrode cell, consisting of a reference electrode, a Pt mesh counter electrode and a working electrode, was used. For all experiments conducted outside of the

gamma cell, the reference electrode was a saturated calomel electrode (SCE) (Fisher Scientific) for experiments at $T \leq 50$ °C. An Ag/AgCl electrode was used for unirradiated tests at 50 °C $\leq T \leq 150$ °C. For radiation experiments a Hg/HgO reference electrode (Radiometer Analytical) in a 1.0 M KOH solution was employed. The Hg/HgO electrode has been found to be more resistant to radiation than either the SCE or Ag/AgCl electrodes. It has a potential of 0.112 V versus a standard hydrogen electrode (SHE). All potentials measured in these tests are adjusted to the SCE scale (0.242 V vs. SHE).

We did not control the temperature during the electrochemical tests and it likely varied within ± 5 °C of the nominal temperature of 25 °C. Corrosion experiments on the bench top were done at temperatures closer to 21 °C, while tests in the gamma cell were at a slightly higher temperature (up to approximately 30 °C), because the temperature is slightly elevated inside the gammacell by the radioactive decay of ^{60}Co .

The working electrodes were either Stellite-6 or pure Co. The Stellite-6 was purchased from Metal Samples Company and had a composition (in wt.%) of Cr, 27.62, Mo, 0.41, W, 4.07, Si, 1.07, C, 1.42, Ni, 2.62, Fe, 2.92, Mn, 0.27, and balance Co. The high-purity cobalt (99.95% purity) was purchased from Metal Sample Company.

A 10-mm diameter Stellite-6 rod was cut into cylindrical pieces. For the aqueous corrosion studies the coupons were 3 mm thick and 9 mm in diameter, giving each coupon a total surface area of 2.12 cm², and for the electrochemical studies the electrode was set in an epoxy resin within a polytetrafluoroethylene (PTFE) cylinder so that only the flat front face (0.636 cm²) was exposed to the electrolyte solution in the cell. Prior to each experiment, the

working electrode was polished manually with 400 and 600 grit silicon carbide papers. This was followed by polishing on a Texmet microcloth (Buehler) with a 1 μm MetaDi Supreme diamond paste suspension (Buehler) and lastly sonication in an acetone/methanol mixture for 5 min to remove polishing residues.

A Solartron potentiostat (either model 1480 or 1287) and a Solartron model 1252 frequency response analyzer were used in all electrochemical measurements. Corrware™ and Zplot™ software (Scribner and Associates) were used for experiment control and data analysis. EIS was performed by applying a 10 mV sinusoidal potential stimulus, either at E_{corr} (for corrosion tests) or at E_{APP} (for potentiostatic tests). The frequency was varied over the range from 10^4 Hz to 10^{-2} Hz or 10^{-3} Hz. A backward scan (from 10^{-3} Hz to 10^4 Hz) was also acquired to verify that the electrode surface remained at steady state over the course of the EIS measurement.

3.3.2 Surface analysis instrumentation

The surfaces of test coupons or working electrodes were analyzed by SEM, XPS, and AES after each electrochemical experiment or corrosion test. A Hitachi S-4500 field emission SEM equipped with a quartz X-ray energy dispersive X-ray spectroscopy (EDX) system, operating in high-resolution mode, was used to examine the morphology and quantitative analysis of surfaces. The chemical compositions of the surface layers were determined from XPS spectra acquired using a KRATOS Axis Nova spectrometer using monochromatic Al K(α) radiation and operating at 210 W, with a base pressure of 10^{-8} Pa. The analysis depth of this instrument was approximately 9 nm. The analysis spot size was

typically $400\ \mu\text{m} \times 700\ \mu\text{m}$ and both low-resolution (or survey spectra) and high-resolution spectra were obtained. The survey spectra were recorded with a pass energy of 160 eV to verify spatial composition and cleanliness. High-resolution spectra (pass energy of 20 eV) were obtained for the regions of Co 2p (binding energy ~ 780 eV), Cr 2p (~ 574 eV), O 1s (~ 530 eV), and C 1s (calibration set point of 284.8 eV from adventitious carbon) [10]. The high resolution spectra were deconvoluted using standard peaks generated from reference materials. All XPS spectral analyses were performed using CasaXPS software (version 2.3.14).

AES combined with argon ion sputtering provided a depth profile of the chemical composition of surface oxides. Auger spectra were obtained using a Phi 660 AES instrument with excitation energy of 5 keV and sputtering was accomplished using an Ar^+ ion beam. The AES scans for Co, Cr, Ni, W, C, and O were performed as a function of sputter time. The AES intensities were calibrated using standard samples under the same sputtering conditions to convert the measured intensities into mole fractions and the sputter time into sputter depth. The sputter rate used for this study was $9\ \text{nm}\cdot\text{min}^{-1}$ for thin oxides and $30\ \text{nm}\cdot\text{min}^{-1}$ for thicker oxides.

3.3.3 Solution Analysis

Samples of the solutions of each corrosion test (7 ml) were collected in glass containers with plastic caps for solution analysis. ICP-MS was used to measure the amount of dissolved Co and Cr in solution after each corrosion test. The detection limits of the ICP

mass spectrometer for Cr and Co were $50 \mu\text{g}\cdot\text{L}^{-1}$ and $0.2 \mu\text{g}\cdot\text{L}^{-1}$, respectively. The pHs of the solutions also were measured after each experiment.

3.4 REFERENCES

- [1] K.J. Vetter, *Electrochemical Kinetics*. Academic Press, New York, 1967.
- [2] J. Wang, *Analytical Electrochemistry*, 2nd ed., New York, 2000.
- [3] E. Barsoukov, *Impedance Spectroscopy Theory, Experiment, and Applications*, 2nd ed., John Wiley & Sons, 2005.
- [4] M.E. Orazem, *Electrochemical Impedance Spectroscopy*, J. Wiley & Sons, 2008.
- [5] G.J. Brug, A.L.G. van den Eeden, M. Sluyters-Rehbach, The analysis of electrode impedances complicated by the presence of a constant phase element, *J. Electroanal. Chem.*, 176 (1984) 275–295.
- [6] R.F. Egerton, *Physical Properties of Electron Microscopy: An Introduction to TEM, SEM and AEM*, Springer, New York, 2005.
- [7] D.J. O'Connor, B.A. Sexton, *Surface Analysis Methods in Materials Science*, 2nd ed., Springer, New York, 2003.
- [6] R.F. Egerton, *Physical Properties of Electron Microscopy: An Introduction to TEM, SEM and AEM*, Springer, New York, 2005.
- [8] D.C. Bell, A.J. Garratt-Reed, *Energy Dispersive X-ray Analysis in the Electron Microscope*, Springer, New York, 2003.
- [9] J.T. Grant, Analysis of Surfaces and Thin Films by Using Auger Electron Spectroscopy and X-ray Photoelectron Spectroscopy, *J. Korean Phys. Soc.*, 51 (2007) 925–932.
- [10] M.C. Biesinger, B.P. Payne, A.P. Grosvenor, L.W.M. Lau, A.R. Gerson, R.St.C. Smart, Resolving surface chemical states in XPS analysis of first row transition metals, oxides and hydroxides: Cr, Mn, Fe, Co and Ni, *Appl. Surf. Sci.*, 257 (2011) 2717–2730.
- [11] F. Vanhaecke, *Isotopic Analysis*, John Wiley & Sons, Weinheim, 2012.
- [12] A. Montaser, *Inductively Coupled Plasma Mass Spectrometry*, John Wiley & Sons, Hoboken, 1998.

CHAPTER 4

Comparative Study of Film Formation on Pure Co and Stellite-6: Probing the Roles of a Chromium Oxide Layer and Gamma-Radiation¹

4.1 INTRODUCTION

Corrosion kinetics in water depends on the aqueous redox conditions, and the composition and morphology of an oxide layer on the alloy surface. Although Stellite-6 is known to be highly corrosion resistant [1,2], its corrosion behaviour in the presence of ionizing radiation has not been well established. The limited information on oxide formation of Co-based alloys [3,4], and in particular Stellite-6 [1,5–8], as a function of aqueous conditions makes it difficult to assess the corrosion susceptibility of this alloy in the transient aqueous environments present in a reactor coolant system.

While the corrosion of pure Co has been studied extensively [9–14], there is still a lack of a detailed room temperature information on the oxide film growth and conversion as a function of potential at pH 10.6. In this chapter oxide formation and conversion on Stellite-6 and Co in water at pH 10.6 and room temperature were studied as a function of electrode

¹ A version of Chapter 4 has been published: M. Behazin, M.C. Biesinger, J.J. Noël, J.C. Wren, Comparative study of film formation on pure Co and stellite-6: Probing the roles of a chromium oxide layer and gamma-radiation, Corrosion Science, 63 (2012) 40–50.

potential under both potentiodynamic and potentiostatic conditions. Knowledge gained from a study of corrosion on pure Co aids in the interpretation of the anodic oxidation processes occurring on the Stellite-6 alloy. The pH value chosen is that maintained in the coolant water in CANDU[®] reactor coolant (pH measured at 25 °C). This pH is an interesting choice for corrosion studies because the solubility of cobalt oxide species is at a minimum near this pH [13,15]. Consequently, oxide formation is preferred over metal dissolution during corrosion and, hence, oxide formation can be studied more easily. Corrosion potential (E_{corr}) measurements, cyclic voltammetry, and electrochemical impedance spectroscopy (EIS) were used to study the corrosion kinetics. The oxide films formed on the metals were examined using scanning electron microscopy (SEM) and X-ray photoelectron spectroscopy (XPS).

4.2 EXPERIMENTAL

The two materials studied in this work are pure cobalt (99.95% purity and henceforth identified only as Co) and Stellite-6 (Metals Samples Company). Electrodes prepared from the metals had a flat, circular face, with a surface area of 10 mm² in the case of Stellite-6 and 12.5 mm² in the case of Co. Prior to each experiment the coupon surface was abraded manually with 400, 600, and then 1200 grit SiC papers, polished with 1 µm MetaDi Supreme diamond paste suspension (Buehler) on Texmet microcloth (Buehler), and then finally sonicated in an acetone/methanol mixture for 5 min to remove surface residues. The polished coupons were then sealed within multiple layers of polyolefin heat shrink tubing, leaving only the polished face exposed to the electrolyte solution. SEM images of as-prepared Co and Stellite-6 electrode surfaces are presented in Figure 4.1. The Stellite-6

images show the presence of two distinct phases: a chromium-rich phase (dark areas) and a cobalt-rich phase (light areas).

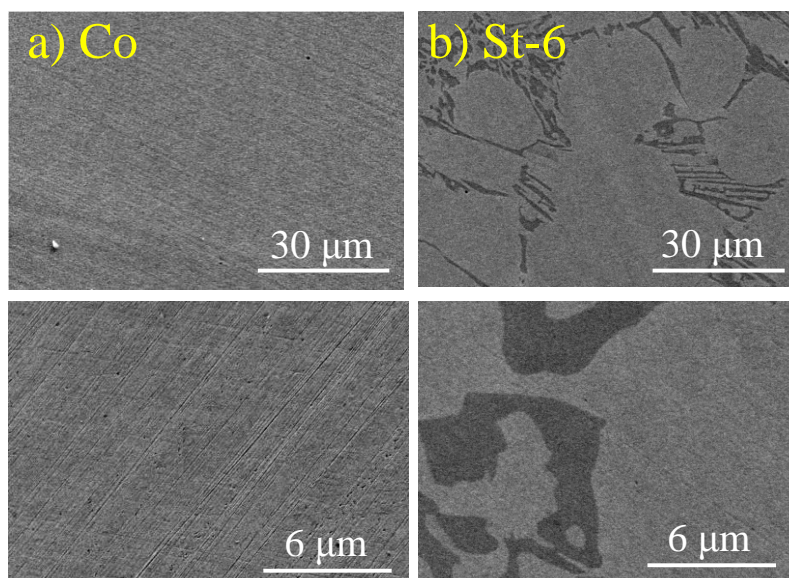


Figure 4.1: SEM images of the surfaces of freshly prepared Co on the left hand panels and freshly prepared Stellite-6 on the right hand panels. Two magnification scales are used to show the degree of surface uniformity.

4.2.1 Solutions

All experiments were conducted at room temperature in Ar-sparged 0.01 M sodium borate solutions. The de-aerated solutions were prepared using reagent grade $\text{Na}_2\text{B}_4\text{O}_7$ (Caledon Laboratories Ltd.) and water purified using a NANOpure Diamond UV ultra-pure water system (Barnstead International) with a resistivity of 18.2 $\text{M}\Omega$ cm. A pH of 10.6 was obtained by adding appropriate amounts of 1 M NaOH (Caledon Laboratories Ltd.) solution

to the borate solution. The pH was measured prior to each experiment using an Accumet AB15 pH meter with standard size glass body combination electrode (Accumet 13-620-530).

4.2.2 Radiation source

All irradiation experiments were conducted in an MDS Nordion Gammacell 220 Excel Cobalt-60 irradiator. The electrochemical cell was positioned inside the gamma cell sample chamber and the chamber was lowered into the irradiation zone, a cylindrical cavity surrounded by 11 tubular pencils containing ^{60}Co . The absorbed radiation dose rate in the cavity during the period of experimentation was $5.5 \text{ kGy}\cdot\text{h}^{-1}$.

4.2.3 Procedure

A Solartron model 1480 multistat and a Solartron model 1255 frequency response analyzer were used in all electrochemical measurements. CorrwareTM and ZplotTM software (Scribner Associates) were used for experiment control, data acquisition and analysis. Electrochemical impedance spectroscopy (EIS) was performed by applying a sinusoidal potential stimulus of 10 mV amplitude on the DC bias potential used in the potentiostatic polarization, over a frequency range of 10^{-3} to 10^4 Hz.

Before each experiment the electrolyte solution was Ar-purged for at least 30 min. The freshly prepared working electrode was then cathodically cleaned at $-1.1 \text{ V}_{\text{SCE}}$ for 5 min. For tests performed under each set of water conditions, a series of three electrochemical tests was performed on each material: (1) corrosion potential measurement, (2) cyclic voltammetry, and (3) potentiostatic polarization measurement. During the potentiostatic

polarization tests, the current response was monitored as a function of time and EIS spectra were periodically recorded. At the end of each potentiostatic test, the electrode was removed from the cell, dried with Ar gas, and stored in a leak-tight vial. The electrode handling was performed in an Ar-purged glove box to minimize air oxidation and electrode contamination prior to surface analysis. Later the electrode was transferred in a sealed container and the electrode surface was analyzed by either SEM or XPS.

4.3 RESULT AND DISCUSSION

4.3.1 Corrosion Potentials under γ -irradiation

Figure 4.2 shows the effect of γ -irradiation on the E_{corr} of the Co and Stellite-6 electrodes. In the absence of radiation, the E_{corr} of both materials is established quickly (in ~ 20 min) and this value then trends very slowly and steadily upward, increasing from $-0.7 V_{\text{SCE}}$ to $-0.6 V_{\text{SCE}}$ over 14 h on the Co electrode; a similar increase is observed for Stellite-6, but with E_{corr} about 0.12 V more positive. When the corroding system is exposed to γ -radiation, E_{corr} reaches different, higher values (increasing from $-0.7 V_{\text{SCE}}$ to $0.08 V_{\text{SCE}}$ for Co and increasing from $-0.48 V_{\text{SCE}}$ to $0.12 V_{\text{SCE}}$ for Stellite-6). It takes longer to reach the higher steady-state values (~ 1 h for Stellite-6 and ~ 3 h for Co), but once reached, the E_{corr} values remain constant with time.

The rate of metal oxidation depends on the potential difference between E_{corr} and the equilibrium potential of the metal redox reaction. Since the corrosion potential is a function of both anodic and cathodic reaction rates, changes in aqueous redox environment as well as

changes in the oxide film can change the corrosion potential. When exposed to ionizing radiation a small fraction of water decomposes to create a range of redox active species (gamma radiation absorbed directly by a metal coupon dissipates as heat). This is the reason for the changes in E_{corr} seen in Figure 4.2

The impact of ionizing radiation on E_{corr} for Co and Stellite-6 is consistent with the observations of this impact on other alloys. Gamma-irradiation has been shown to increase E_{corr} from $-0.65 \pm 0.05 \text{ V}_{\text{SCE}}$ to $0.0 \pm 0.1 \text{ V}_{\text{SCE}}$ on carbon steel [16] and from $-0.4 \pm 0.1 \text{ V}_{\text{SCE}}$ to $0.05 \pm 0.05 \text{ V}_{\text{SCE}}$ on stainless steel [17], at pH 10.6 and room temperature. Previous studies on carbon steel [16,18,19] have shown that γ -irradiation affects the corrosion process primarily by producing redox active species (such as H_2O_2) in the aqueous phase. Oxide formation and conversion on Co and Stellite-6 were investigated as a function of potential under potentiodynamic (using cyclic voltammetry) and potentiostatic conditions over a potential range that encompasses the E_{corr} values observed in the absence and presence of radiation.

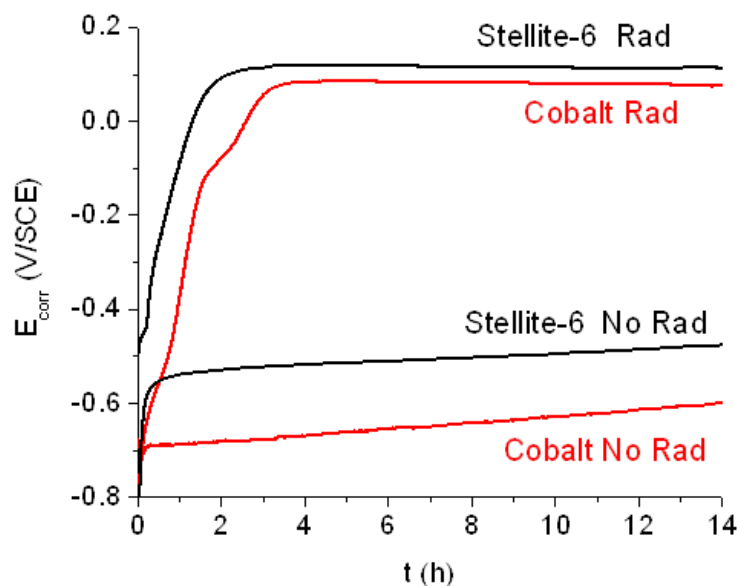


Figure 4.2: E_{corr} as a function of time recorded on Co and Stellite-6 electrodes in an Ar-purged borate solution at pH 10.6 and room temperature, in the presence and absence of γ -irradiation.

4.3.2 Oxide formation and conversion under potentiodynamic conditions

Cyclic voltammetry (CV) was performed to establish characteristic potential ranges for the oxides that can be formed on Co and Stellite-6 under potentiodynamic conditions. The growth rate of the oxide layer in each potential region, as defined in this CV study, was then investigated in detail under potentiostatic conditions (see section 4.3.3). To aid in the assignment of the current peaks seen in the cyclic voltammograms, the thermodynamic equilibrium potentials (E_{eq}) for the redox reactions of cobalt and chromium species at pH 10.6 were calculated from reported standard potentials for the species [20]. These potentials are shown using vertical lines in Figure 4.3. In addition to thermodynamic constraints,

reaction kinetics can control oxide formation. Since the potential scan rate can alter the time available for a given reaction, differences observed in potentiodynamic and potentiostatic studies provide information on the role of kinetics on oxide formation.

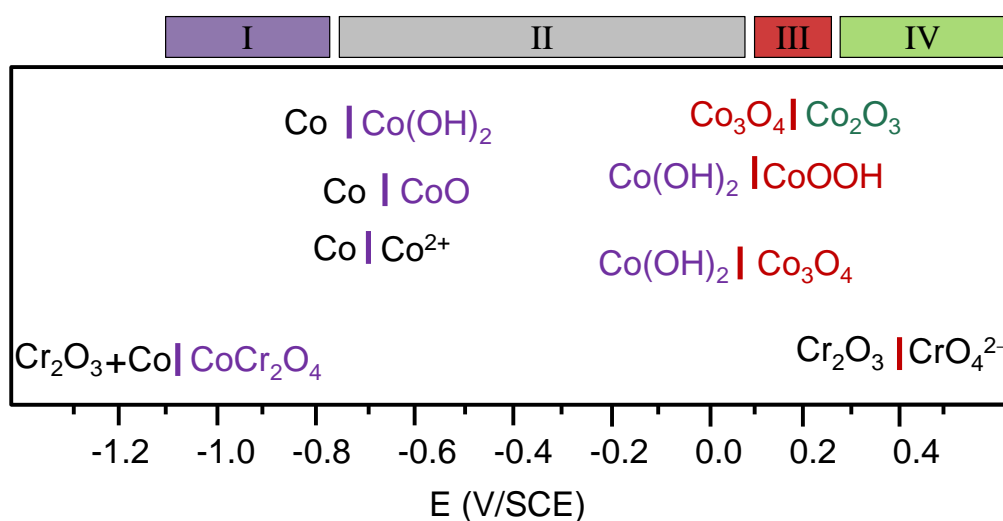
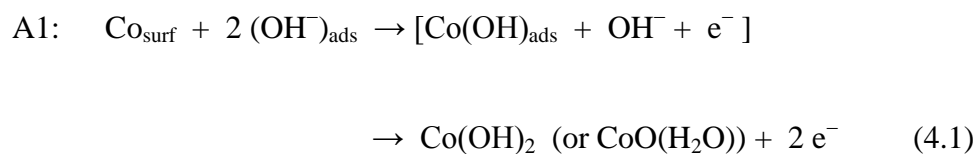


Figure 4.3: Calculated equilibrium potentials for various redox reactions (at $\text{pH}_{25^\circ\text{C}} 10.6$) are indicated by vertical lines. The coloured bar at the top indicates the potential regions for Co oxidations.

Assignments of the current peaks in cyclic voltammograms for pure Co

Cyclic voltammograms recorded on a Co electrode are shown in Figure 4.4. The overlapping anodic peaks labeled A1 (-0.7 to -0.6 V_{SCE}) and A2 (-0.5 V_{SCE}) can both be attributed to the oxidation of Co to Co^{II} oxide/hydroxide ($\text{CoO}/\text{Co}(\text{OH})_2$). There are two pathways for the oxidation of Co to Co^{II} . Peak A1 lies below the E_{eq} for the oxidation of Co in the bulk metal to $\text{Co}(\text{OH})_2$ and is assigned to an oxidation process involving Co in a few surface monolayers:



Peak A2 appears at potentials higher than the E_{eq} and it is assigned to the process:

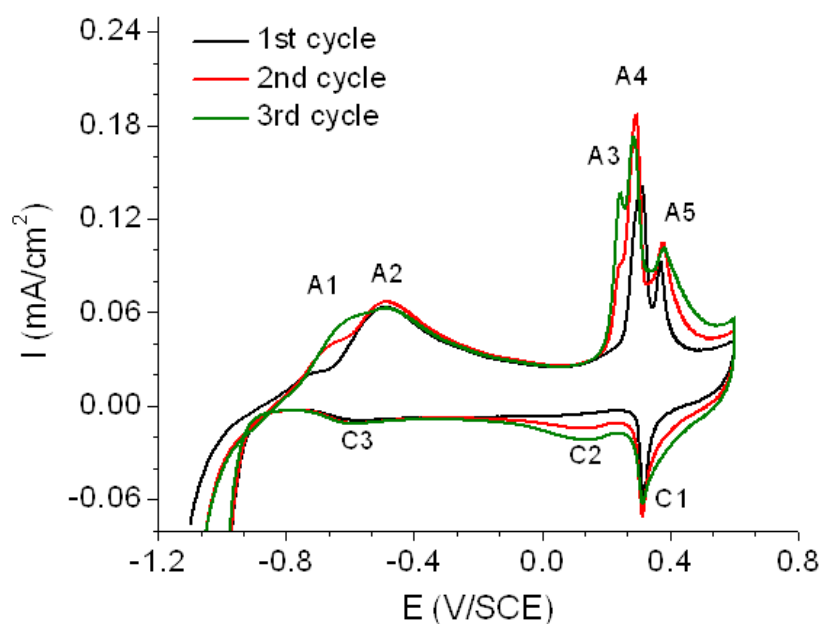
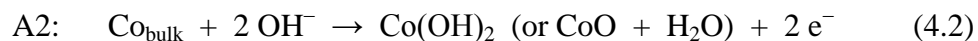
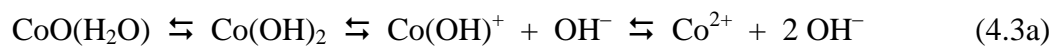


Figure 4.4: Cyclic voltammograms obtained on Co. The CVs were recorded at a scan rate of $5 \text{ mV}\cdot\text{s}^{-1}$.

The Co^{II} species at, or very near, the metal surface will be hydrated. The hydrated Co^{II} is in acid-base equilibrium with hydroxides:



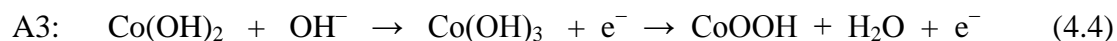


The hydrated species can dissolve from the metal/oxide interface and diffuse into the aqueous phase or precipitate (and/or condense) back onto the metal to form a solid CoO/Co(OH)₂ film. Once a solid phase film is formed, reaction 4.2 may continue by the injection of Co^{II} into the oxide phase at the metal/oxide interface. This is balanced by injection of OH⁻ (or O²⁻) into the oxide phase at the oxide/water interface.

Peak A2 is located at a higher potential because there is a slight barrier to overcome to oxidize the Co atoms in the bulk metal. This barrier is independent of the oxide surface state and we observe that the magnitude of peak A2 is independent of the number of CVs that have been performed on a sample. On the other hand, the magnitude of peak A1 increases with scan-cycle number. This behaviour can be attributed to a process associated with Co at the metal surface where the reactive surface area and number of reactive sites are modified by the potential history of the metal.

The growth of the Co^{II} oxide/hydroxide layer passivates the surface and the current decreases. At potentials above 0.1 V_{SCE}, where the oxidation of Co^{II} to either Co₃O₄ or CoOOH is thermodynamically allowed, the current increases again. The anodic formation of CoOOH should be kinetically more favored than formation of Co₃O₄ since it requires less structural rearrangement of the oxide; it only requires dehydration following the oxidation of Co^{II} to Co^{III} in the hydroxide form. Thus, peak A3 (Figure 4.4) is assigned to the oxidation of hydrated Co(OH)₂ to CoOOH at or near the oxide/water interface (reaction 4.4). Peak A4,

located at a slightly higher voltage, is attributed to the conversion of CoO/Co(OH)₂ in the bulk solid phase to a mixed Co^{II/III} oxide (Co₃O₄) (reaction 4.5):



Peak A3 is barely visible on the first CV scan and increases in intensity with scan-cycle number. The height of peak A3 is initially low because reaction (4.5) will be limited to conversion of a hydrated surface layer. The surface coverage and/or thickness of this layer increases with scan cycle as reaction 4.1 becomes more important.

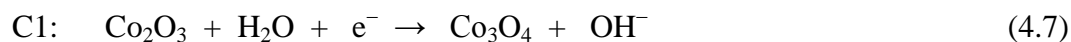
Alternative assignments of peaks A3 and A4 could be made to the oxidation of two different solid phases of Co(OH)₂ that are known to exist: α -Co(OH)₂, which consists of four ordered Co(OH)₂ layers followed by one less-ordered Co(OH)₂ layer, and β -Co(OH)₂, which has an ordered CdI₂ structure in which the anions form a cubic close-packed structure while the cations occupy all of the octahedral interstices [18]. Feitknecht observed that α -Co(OH)₂ was susceptible to oxidation to CoOOH and that this oxidation occurred topochemically without the formation of a new phase and a requirement for nucleation phenomena [21]. Foelske and Strehblow [9] later suggested that intercalated water may be responsible for the ~ 3.4 Å larger c-axis in the α -Co(OH)₂ crystal lattice than in the β -Co(OH)₂ crystal lattice. We do not believe that oxidation of two different Co(OH)₂ phases is important in our system. The oxidation of α -Co(OH)₂ to CoOOH should be fast since it only requires that a proton leave the intercalated water layer and this is consistent with the presence of reaction 3.5. The

presence of Co_3O_4 in the oxide layer grown at potentials $> 0.1 \text{ V}_{\text{SCE}}$ was determined by XPS (see below) and this confirms that reaction 4.5 is also occurring.

At a higher potential ($0.4 \text{ V}_{\text{SCE}}$) an additional peak, A5, is observed. The height of this peak behaves similarly to peak A4 as a function of scan-cycle number, but peak A5 broadened with increased cycling and its corresponding reduction peak, C1, showed near reversible behaviour. Peak A5 is assigned to the conversion of the $\text{Co}^{\text{II/III}}$ oxide (Co_3O_4) to a Co^{III} oxide (Co_2O_3):



The reduction peaks C1 and C2 are assigned to reactions 4.7 and 4.8, respectively:



The near reversibility of peaks A5 and C1 suggests that kinetically facile oxidation and reduction of Co^{II} and Co^{III} is occurring in the oxide lattice. Crystalline Co_3O_4 has a normal spinel structure with Co^{III} occupying the octahedral sites and Co^{II} the tetrahedral sites [10]. Similar reversible oxidation/reduction behaviour has been observed for the conversion between Fe_3O_4 and $\gamma\text{-Fe}_2\text{O}_3$, both of which share a spinel structure (inverse spinel for magnetite) [22]. The broadening of peaks A5 and C1 with increasing scan-cycle number can be attributed to an increase in the reactive surface sites as the cycling increases.

Peak C3 was observed only when the upper scan limit of a CV was higher than $0.1 V_{SCE}$ and, hence, the assignment of this peak to the reduction of Co^{II} species is ruled out. Rather, this peak is assigned to the reduction of $CoOOH$ to $Co(OH)_2$:



This assignment is consistent with the study by Behl et al. [11] which showed that the oxidation of $Co(OH)_2$ to $CoOOH$ occurs readily, but the reduction of $CoOOH$ to $Co(OH)_2$ is very slow. In summary, the CV results show three potential regions of anodic oxidation of Co at pH 10.6:

Region I ($E < -0.7 V_{SCE}$): This region lies below the equilibrium potential for the Co to $CoO/Co(OH)_2$ reaction and no bulk Co oxidation is observed (or expected) in this region.

Region II ($-0.7 V_{SCE} < E < 0.1 V_{SCE}$): Oxidation of Co in the bulk metal phase is limited to the formation of $CoO/Co(OH)_2$.

Region III ($E > 0.1 V_{SCE}$): Oxidation of Co to Co^{II} oxide/hydroxide continues but the Co^{II} formed is also further oxidized to less soluble $Co^{II/III}$ and/or Co^{III} oxides/hydroxides.

The division of the oxidation processes into three potential regions is in good agreement with previous studies on Co oxidation in a mildly basic solution (pH range of 9.3 to 12) [9,12,13]. Those studies also concluded that two types of passive layers are formed in alkaline solutions, a layer formed at low potentials that consists of CoO and a layer formed at high potentials that consists of $CoOOH$ and Co_3O_4 on top of an inner layer of CoO [9,12].

The corrosion potential of Co without ionizing radiation present was found to be in the range -0.7 to -0.6 V_{SCE} during the time scale of our experiments (Figure 4.2), values at or slightly higher than the transition potential between Regions I and II (the transition potential is the equilibrium potential for the Co to CoO/Co(OH)₂ reaction). In contrast, E_{corr} with $5.5 \text{ kGy}\cdot\text{h}^{-1}$ ionizing radiation present (0.08 V_{SCE} as shown in Figure 4.2) is at the transition potential between Regions II and III.

Assignments of the current peaks in cyclic voltammograms on Stellite-6

Cyclic voltammograms recorded on Stellite-6 are shown in Figure 4.5; two different scan ranges were used, -1.1 V_{SCE} to 0.1 V_{SCE} and -1.1 V_{SCE} to 0.6 V_{SCE} . Also shown in Figure 4.6a is the first cycle of a CV performed on Co for comparison. Since chromium is a major secondary element in Stellite-6 we also recorded a CV on pure chromium to ensure a more accurate assignment of the current peaks on Stellite-6. The CVs recorded on pure chromium and Stellite-6 at two different vertex potentials are shown in Figure 4.6.

The first anodic peak (labeled A1(St-6) for Stellite-6) in Figure 4.5a appears at a much lower potential than the first peak seen on Co (A2(Co)). At this potential, Co oxidation to Co^{II} oxide/hydroxide is not thermodynamically allowed. However, the equilibrium potentials for the oxidation of Cr to Cr^{III} (CrOOH and Cr₂O₃) lie below -1.4 V_{SCE} . The Stellite-6 surface is initially covered by a thin, air-formed Cr^{III} oxide and this oxide is not completely removed during the electrode cathodic treatment before the first CV. Peak A1(St-6) can therefore be attributed to the oxidative injection of Co^{II} into the chromium

oxide layer, leading to conversion of that layer to cobalt chromite, CoCr_2O_4 . This is followed by formation of a Co^{II} oxide/hydroxide outer layer at higher potentials:

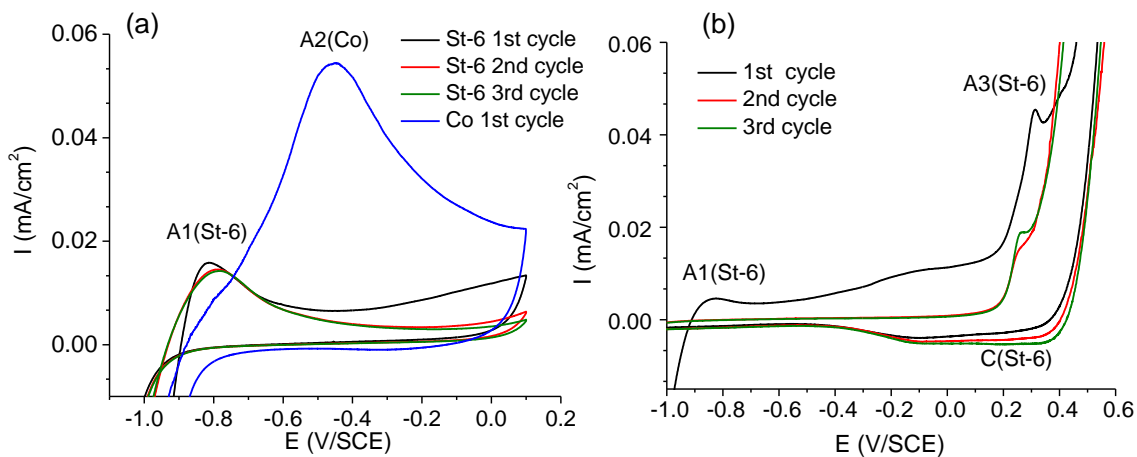


Figure 4.5: Cyclic voltammograms recorded on Stellite-6 for two potential scan ranges: (a) $-1.1 \text{ V}_{\text{SCE}}$ to $0.1 \text{ V}_{\text{SCE}}$ and (b) $-1.1 \text{ V}_{\text{SCE}}$ to $0.6 \text{ V}_{\text{SCE}}$. The first cycle of a CV recorded on Co is also shown in Figure 4.5a for comparison.

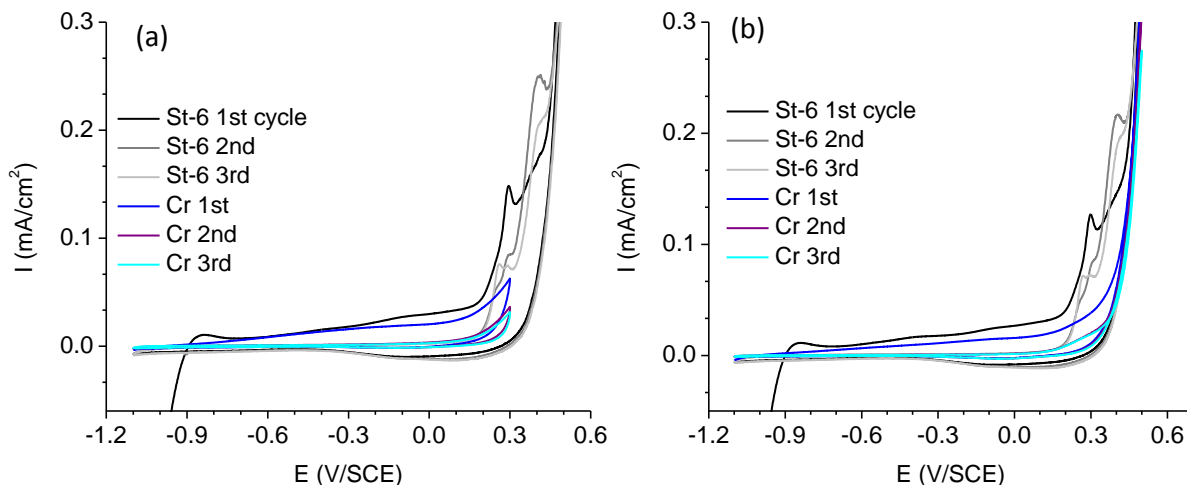


Figure 4.6: Cyclic voltammograms recorded on pure chromium for two potential scan ranges and compared with Stellite-6: (a) $-1.1 V_{SCE}$ to $0.3 V_{SCE}$, and (b) $-1.1 V_{SCE}$ to $0.6 V_{SCE}$.

Chromium oxide, Cr_2O_3 , being a p-type semi-conductor with a large band gap of 3 eV [23], is ionically insulating at low potentials and, therefore, its presence should significantly impede the further oxidation of an underlying metal. However, the air-formed chromium oxide is known to be defective [23] and the Co^{II} ion is thermodynamically stable in a chromite at potentials above $-1.1 V_{SCE}$ (Figure 4.3). When the Cr^{III} oxide layer is saturated with Co^{II} and a potential greater than $-0.7 V_{SCE}$ is applied, additional Co^{II} can migrate through the oxide layer to the chromite/water interface where it can be hydrated and subsequently condense to grow an outer layer of $CoO/Co(OH)_2$ or diffuse into the aqueous phase. Consequently, we see the presence of both $CoCr_2O_4$ and $CoO/Co(OH)_2$ in an oxide potentiostatically grown at $-0.7 V_{SCE}$ (see XPS results below).

The presence of a CoCr_2O_4 layer adds a barrier to cation migration that is not present in pure Co and this explains why the electrochemical reactivity of the Stellite-6 surface is much lower than that of the Co surface (lower anodic current densities) at potentials $> -0.6 V_{\text{SCE}}$ (see further discussion below).

With an upper scan limit of $0.1 V_{\text{SCE}}$, the onset of peak A1(St-6) appears at a lower potential in the first cycle than in subsequent cycles (Figure 4.5a). Stable Cr_2O_3 has a corundum crystal structure while stable CoCr_2O_4 has a spinel structure [24]. Injection of Co into the Cr_2O_3 oxide lattice requires energy sufficient to induce the required changes to the oxide lattice structure. When the upper limit of the potential scan is increased to $0.6 V_{\text{SCE}}$, the anodic current density seen near $-0.7 V_{\text{SCE}}$ is much reduced in the second and higher number CV cycles compared to that seen in the first cycle (Figure 4.5b). This is because of changes to the chromium oxide that occur at higher potentials. At potentials $> 0.3 V_{\text{SCE}}$, Cr^{III} can oxidize to Cr^{VI} . The Cr^{VI} can readily dissolve in the water [25] and this removes the chromite layer. A more coherent and compact Cr_2O_3 oxide layer than the initial defective Cr_2O_3 layer forms after the first CV cycle and this more insulating layer inhibits Co^{II} migration. Consequently, the Stellite-6 CV cycles over the potential range -1.1 to $0.6 V_{\text{SCE}}$ are very different for cycle 1 and subsequent CV cycles, and the latter do not show any further anodic current at low voltages.

The CV of Stellite-6 in Figure 4.5b shows that the anodic current increases again at potentials above $-0.6 V_{\text{SCE}}$ (first cycle) and above $0.2 V_{\text{SCE}}$ for subsequent cycles. In the potential range $-0.6 V_{\text{SCE}}$ to $0.1 V_{\text{SCE}}$, the growth of the outer $\text{CoO}/\text{Co}(\text{OH})_2$ layer continues.

The anodic current in this region increases nearly linearly with potential during the scan and this is attributed to a linear growth in the thickness of the outer CoO/Co(OH)_2 layer. The impact of the increasing potential is balanced by a commensurate increase in the ohmic resistance of the oxide layer as it thickens. As the potential is scanned above $-0.2 \text{ V}_{\text{SCE}}$, the current stays nearly constant with potential and this behaviour is attributed to control of the reaction rate by diffusion of OH^- in the water to the oxide/water surface. No anodic current is seen in this potential region for scan cycles greater than 1 because of the presence of the insulating Cr_2O_3 oxide layer.

It can be observed in Figure 4.6 that the oxidation peaks seen on Stellite-6 did appear on pure chromium cycles. Therefore, we can conclude that the increase in anodic current at peak A3 is due to the oxidation of cobalt species, see reactions (4.5), (4.6) and (4.7). The rates of these reactions are much slower on Stellite-6 than on Co due to the presence of the cobalt chromite in the oxide.

At potentials above $0.2 \text{ V}_{\text{SCE}}$, where Cr^{III} can be easily oxidized to highly soluble Cr^{VI} the anodic current increases rapidly with potential [25]. In this high potential region, the oxidative dissolution of chromium dominates the anodic current behaviour. On the return CV sweep, the reduction current begins to flow almost immediately and is distributed over a very wide potential range, down to about $-0.3 \text{ V}_{\text{SCE}}$ (peak C(St-6)). This broad cathodic feature probably comprises the processes included in peaks C1 and C2 on Co (Figure 4.4), but the separation into two peaks is lost, perhaps due to the influence of chromium oxides on

the film conversion kinetics [3] and also the reduction of any Cr^{VI} species that were retained in the oxide film during the anodic CV sweep.

In summary, the CV results for Stellite-6 show that oxidation behaviour can be divided into four potential regions at pH 10.6. These regions are almost identical to the regions identified for Co oxidation (with the differences in the transition potential between Region I and Region II matching the differences in the values of E_{corr} for the metals. Stellite-6 has an extra region at high potentials to account for Cr oxidation.

Region I ($-0.8 V_{\text{SCE}} < E < -0.6 V_{\text{SCE}}$): In this region the oxidation of Co to Co^{II} converts the pre-existing chromium oxide layer to cobalt chromite.

Region II ($-0.5 V_{\text{SCE}} < E < 0.0 V_{\text{SCE}}$): The oxidation of Co to Co^{II} continues. When the chromite layer becomes saturated with Co^{II} , CoO/Co(OH)_2 is formed at the oxide/water interface. The rate of anodic oxidation in this region is much lower on Stellite-6 than on Co.

Region III ($0.0 V_{\text{SCE}} < E < 0.2 V_{\text{SCE}}$): In this region Co^{II} oxide/hydroxide is continuously formed and it is also further oxidized to less soluble $\text{Co}^{\text{II/III}}$ and/or Co^{III} oxides/hydroxides.

Region IV ($E > 0.2 V_{\text{SCE}}$): The oxidative dissolution of chromium becomes the dominant anodic process.

As for the cobalt system, the E_{corr} of Stellite-6 without ionizing radiation present is about $-0.47 V_{\text{SCE}}$, a value slightly higher than the transition potential between Regions I and II, whereas with ionizing radiation present E_{corr} is about $0.12 V_{\text{SCE}}$, a value at the transition potential between Regions II and III.

4.3.3 Oxide Formation and Conversion under Potentiostatic Conditions

Oxide formation was studied under potentiostatic conditions at three potentials, -0.7 , -0.2 and 0.2 V_{SCE} for both Co and Stellite-6. These potentials were chosen based on the electrochemical reactivity seen in CV scans. Additional potentiostatic experiments were carried out on Stellite-6 at a number of applied potentials in the range 0.1 V_{SCE} to 0.4 V_{SCE} . In the potentiostatic experiments a desired potential, E_{APP} , was applied immediately after cathodically stripping the electrode at -1.1 V_{SCE} for 5 min. The current was monitored as a function of time (typically up to 2 d) to obtain kinetic information on anodic oxidation processes occurring on the Co and Stellite-6 surfaces. Electrochemical impedance spectra (EIS) were recorded periodically during a potentiostatic test to characterize the oxide films that were formed. Upon the conclusion of each experiment, the electrode was removed from the electrochemical cell and the surface was characterized using XPS. The XPS analysis provides information on the state of the metal surface after extended oxidation, and the current vs. time plots and EIS spectra provide information on the film growth kinetics. The EIS spectra were modeled using electric equivalent circuits to derive the resistance and capacitance of the electrochemical systems. The XPS spectra were deconvoluted using standard reference spectra to determine the chemical composition and oxidation states of the metal atoms in the oxide layers.

The results of EIS measurements and analyses are discussed first because this aids in discussion of the other results. Representative EIS spectra, recorded on Stellite-6 during polarization at 0.2 V_{SCE} , are shown in a Bode plot in Figure 4.6. The EIS spectra obtained

during potentiostatic polarization at $-0.2 V_{SCE}$ and $0.2 V_{SCE}$ were analyzed using a modified Randles electric equivalent circuit model to extract the capacitive and resistive characteristics of the films formed on the surfaces. An electric equivalent circuit analysis of the EIS obtained at $-0.7 V_{SCE}$ was not performed due to the large water reduction currents observed for both Co and Stellite-6 surfaces at this voltage.

In our work, the Co and Stellite-6 surfaces contain several oxide phases that are not distinct and, hence, their individual RC components are not easily separated. Thus, a simple Randles-type circuit consisting of one RC (resistor-capacitor) component in series with the resistance of the solution, R_s , was used to model the oxide layer as a whole. A constant phase element (CPE) was used in place of the capacitor for the EIS analysis. A more complex equivalent circuit model could be used but, since there is no unique solution to a least squares fit to our EIS data, this was not done.

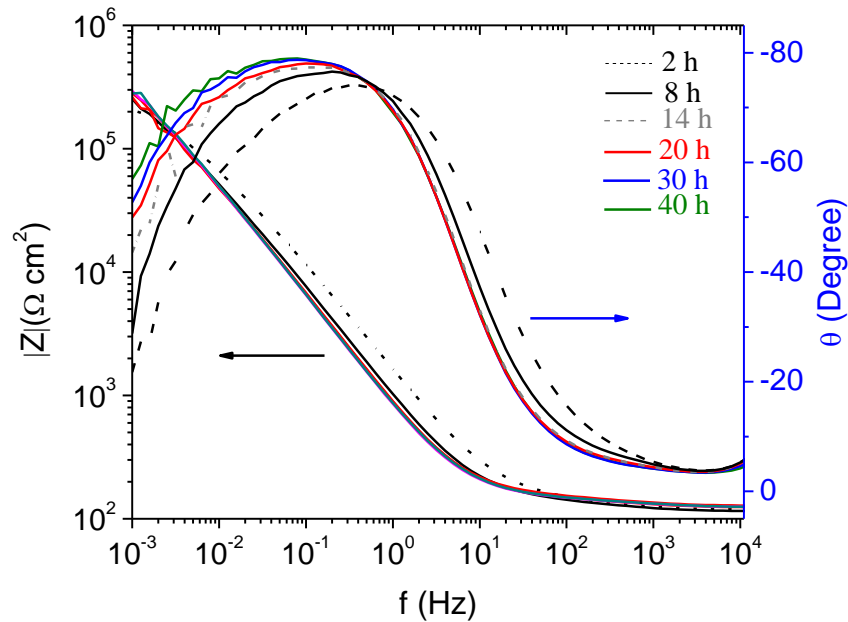


Figure 4.7: Electrochemical impedance spectra recorded at various times during film growth at 0.2 V_{SCE} on Stellite-6: Bode plots of the impedance magnitude and phase angle.

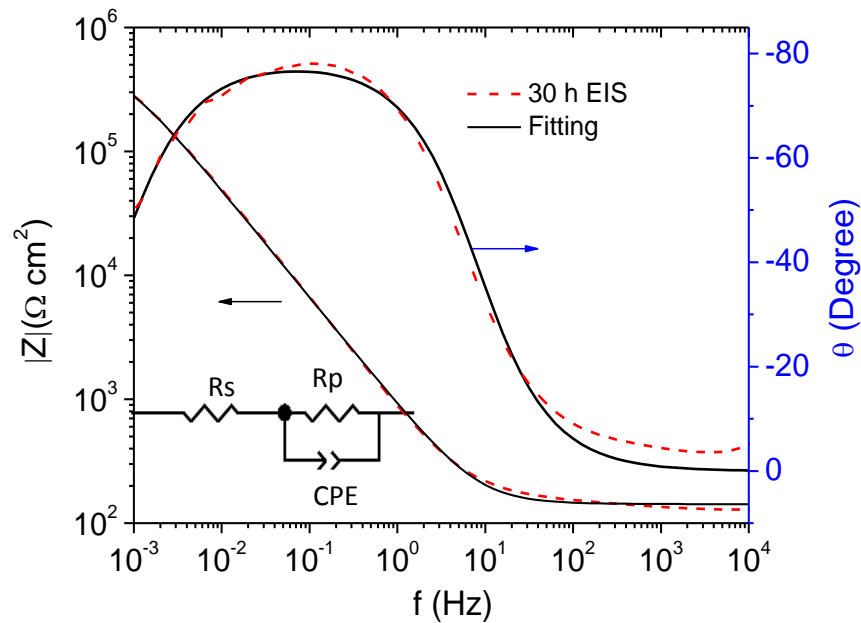


Figure 4.8: Electrochemical impedance spectra recorded at various times during film growth at 0.2 V_{SCE} on Stellite-6: Bode plots of an example of a model fit to an experimental spectrum. The equivalent circuit used for the EIS analysis is shown inset.

The Randles-type circuit provides a good fit to our EIS data, as shown in Figure 4.8. The CPE accounts for non-idealities (i.e., frequency dispersion) in the capacitive response of the system. The exponent of the CPE, α , derived from fitting this circuit model to the data, was in the range of 0.8 to 0.85, indicating that the electrode possessed a very capacitor-like interface (a value of 1 applies to a pure capacitor). The CPE parameters were converted to capacitance values using the method of Brug et al. [26]. The resistance and capacitance values obtained from fitting the EIS data are shown in Figure 4.9. Although the polarization (or system) resistance, R_p , is theoretically composed of a film resistance, R_{film} , and an interfacial charge transfer resistance, R_{ct} , in series with one another, the equivalent circuit analysis of the EIS data could not resolve the contributions of R_{film} and R_{ct} or those of different oxide films, so the additive polarization resistance R_p is plotted in Figure 4.9.

X-ray photoelectron spectroscopy (XPS) was used to characterize the chemical states of Co and Cr in the oxide films. Both low resolution (or survey) spectra and high resolution spectra in the Co 2p, Cr 2p, and O 1s regions were used. The ratio of Co to Cr in the Stellite-6 films was obtained from the relative areas of the Co 2p peak at 780 eV and the Cr 2p peak at 574 eV in the survey spectra. To determine the oxidation state(s) of Co atoms in a film, high resolution spectra of the Co 2p band were deconvoluted using reference spectra for single-phase Co^0 , $\text{Co}(\text{OH})_2$, CoO , Co_3O_4 , CoOOH , and CoCr_2O_4 (with binding energies of 778.1 eV, 780.4 eV, 780.0 eV, 779.6 eV, 780.1 eV and 778.8 eV, respectively) [21]. A representative high resolution spectrum of the Co 2p band and its deconvolution into oxide contributors is shown in Figure 4.10 for a film grown at 0.15 V_{SCE} on Stellite-6. Some of the

reference spectra contain multiple peaks, for example, the CoOOH spectrum is composed of multiple peaks as shown in the inset of Figure 4.10.

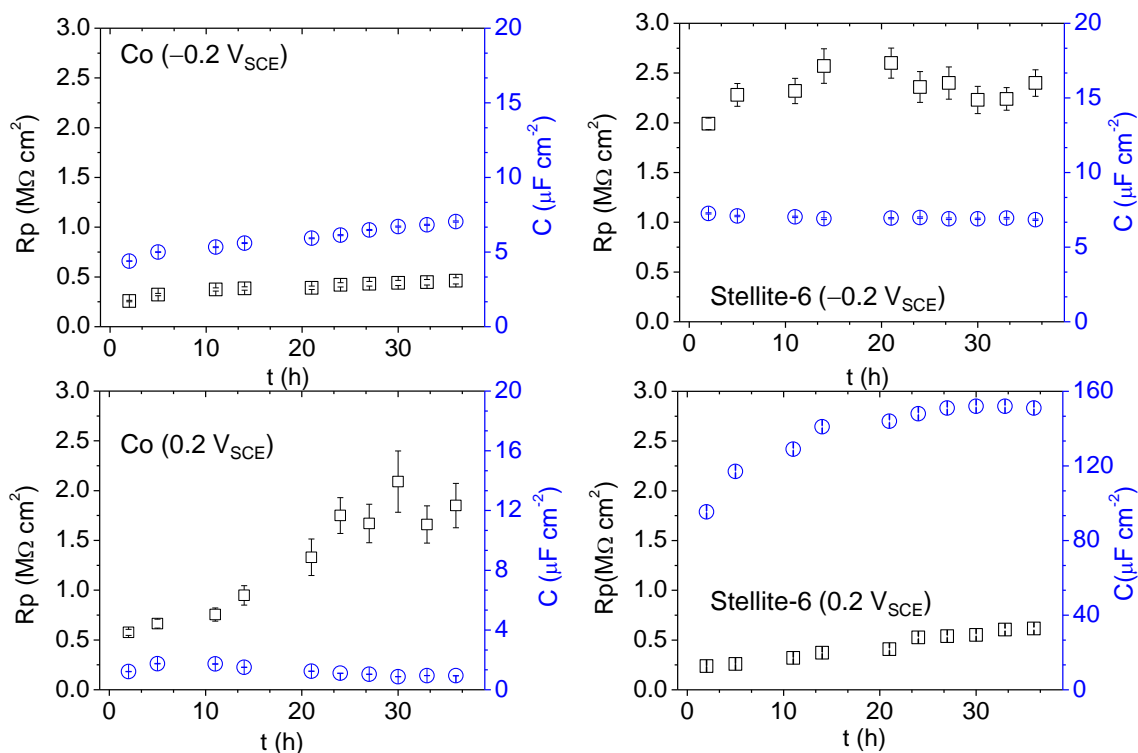


Figure 4.9: Polarization resistance (\square) and capacitance (\circ) as a function of time during potentiostatic film growth at $-0.2 \text{ V}_{\text{SCE}}$ (upper figures) and $0.2 \text{ V}_{\text{SCE}}$ (lower figures) on Co and Stellite-6. The resistance and capacitance values were obtained from fits to EIS spectra using the equivalent circuit model shown in the inset of (b). The error bars include only the model-fitting errors which in most cases are smaller than the sizes of the symbols representing the data.

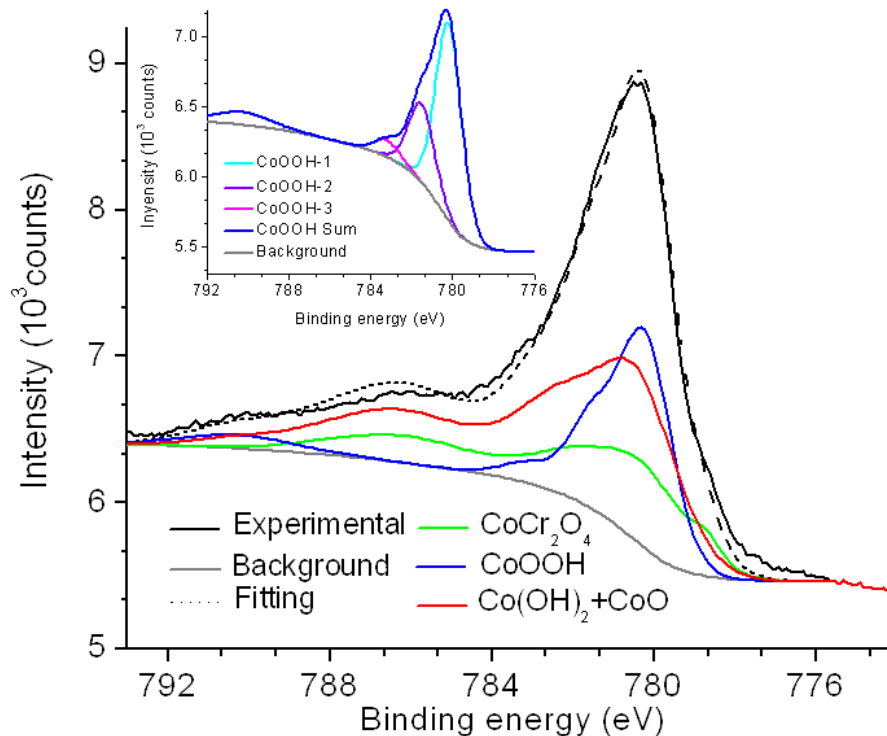


Figure 4.10: High resolution XPS spectrum of the Co 2p band (and its deconvoluted components) for a film grown at 0.15 V_{SCE} on Stellite-6. The inset shows that the CoOOH spectrum consists of multiple peaks.

For Cr speciation, high resolution spectra of the Cr 2p (~ 575 eV) region were deconvoluted using reference spectra for single-phase Cr⁰, Cr₂O₃, CoCr₂O₄, and Cr(OH)₃ (binding energies of 574.2 eV, 575.7 eV, 575.2 eV and 577.3 eV, respectively) [21,27]. The deconvolution of an XPS band using multiple-peak reference spectra with a Shirley-type background subtracted has previously been successfully applied to cobalt oxide samples by Biesinger et al. [21]. In fitting the measured spectra, a weighted-composite peak was constructed and compared with the observed peak, see Figure 4.10. Commercial software (CASAXPS®) was used for the fitting analysis. The weighting factors correspond to the

relative concentrations of each species in an oxide film. The results of the XPS fitting analysis for films grown on pure Co and Stellite-6 are summarized in Figure 4.11 and 4.12, respectively. Note that in Figure 4.11a only the fractions of Co metal and Co_3O_4 in the Co 2p peak are shown. The dominant contributor at all potentials (balance $\text{Co}(\text{OH})_2$) is not shown in order to present the contributions of the two minor components of the Co oxide film more clearly.

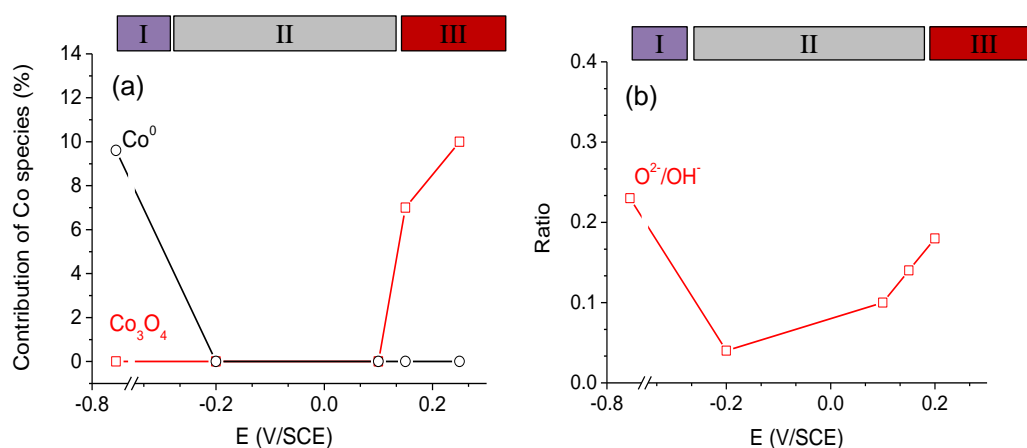


Figure 4.11: Speciation on the surface of Co as a function of applied potential determined by XPS analysis: (a) Co oxides and (b) $\text{O}^{2-}/\text{OH}^-$.

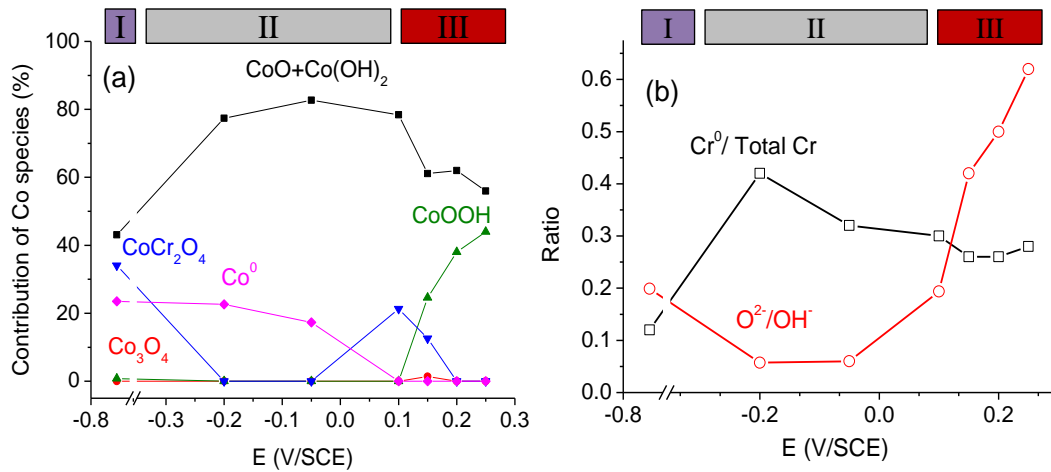


Figure 4.12: Speciation on the surface of Stellite-6 as a function of applied potential determined by XPS analysis: (a) Co oxides and (b) ratios of metallic Cr/total Cr and O^{2-}/OH^- .

4.3.3.1 Film Growth on Cobalt

4.3.3.1.1 Film Growth at $-0.7 V_{SCE}$

The time dependent behaviour of current as a function of time at constant potential is shown in the $\log |i|$ versus $\log t$ plots in Figure 4.13. During potentiostatic polarization at $-0.7 V_{SCE}$, the current initially decreases linearly with time (i.e., the slope of the $\log |i|$ vs. $\log t$ plot is -1) but switches in sign from anodic to cathodic at ~ 100 s (Figure 4.13). The linear decrease in the anodic current within the first 100 s indicates that the nature of the oxide formed on Co does not change during this time. This is consistent with growth of a Co^{II} oxide/hydroxide layer at a constant rate at this potential (reaction 3.1). The solubility of $Co(OH)_2$ is at its minimum at pH 11 ($\sim 1 \mu M$) [13,15] and a uniform solid phase of Co^{II}

oxide/hydroxide quickly covers the surface. The current density decreases steadily as the oxide thickens.

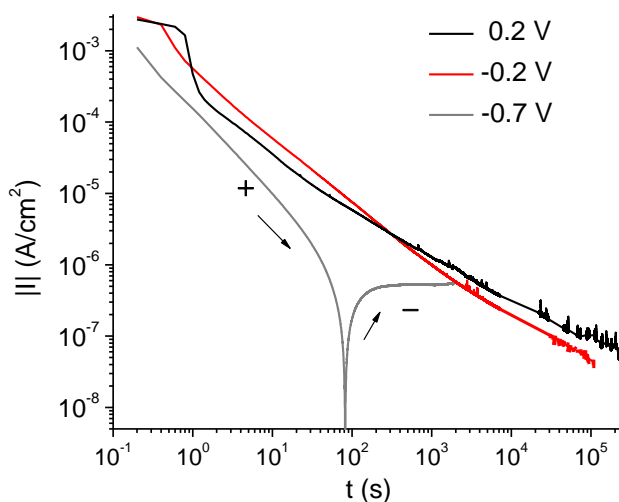


Figure 4.13: Current as a function of time observed during potentiostatic film growth at -0.7 , -0.2 , and 0.2 V_{SCE} , on Co. The + and – signs indicate anodic and cathodic currents, respectively.

At ~ 100 s the current becomes cathodic and its magnitude quickly reaches a steady-state value (constant for the rest of the potentiostatic experiment). Cobalt oxide/hydroxide is known to be electronically conducting [14]. Although it is a p-type semiconductor it has a small band gap of 2.4 eV and a photocurrent can be easily generated by room fluorescent lighting (the experiments were not conducted in the dark). The negative current is attributed to reduction of aqueous species on this electronically conducting surface, possibly driven by a photo-process. This process is hidden at first by the overriding anodic reaction and only becomes observable when the anodic reaction rate decreases sufficiently. We did not fully

investigate the contribution of a photocurrent, but limited tests in a darkened laboratory showed a reduction in the cathodic current level.

The XPS analysis of the film formed at $-0.7 \text{ V}_{\text{SCE}}$ (Figure 4.11a) shows a substantial contribution of metal atoms (Co^0) to the Co 2p peak ($\sim 10\%$). This component comes from the bulk metal that underlies the surface oxide and indicates that the oxide film is less than 10 nm thick (the depth analysis range of the XPS instrument). The remaining contribution to the Co 2p band is from $\text{CoO}/\text{Co}(\text{OH})_2$. Analysis of the high resolution O 1s peak shows a high contribution from OH^- (Figure 4.11b) indicating that Co^{II} is present mostly in the hydroxide form ($\text{Co}(\text{OH})_2$).

4.3.3.1.2 Film growth at $-0.2 \text{ V}_{\text{SCE}}$

During potentiostatic polarization at $-0.2 \text{ V}_{\text{SCE}}$, the current is initially high ($\sim 3 \text{ mA}\cdot\text{cm}^{-2}$) and remains nearly constant for a very short duration (Figure 4.13). The current then drops abruptly and subsequently decreases linearly with time from this new, lower current level to reach a very low value of $60 \text{ nA}\cdot\text{cm}^{-2}$ after $\sim 10^5 \text{ s}$ ($\sim 1 \text{ d}$). At this potential the rate of Co to Co^{II} oxidation at the metal/water interface is initially very high due to a large overpotential. The short duration of this high term current can be attributed to the fact that the oxidation of Co to Co^{II} is limited not by the rate of interfacial charge transfer but by the rate of diffusion of charged species (metal cations and aqueous ions, H^+ and OH^-) through the Helmholtz or double layer (or the interfacial region). The rate of movement of charged species through the double layer depends on the electric field potential gradient

across the layer. Injection of a large amount of Co^{II} can result in a significant iR drop across into the interfacial region and can slow down the diffusion of the charged species [28].

When the concentration of Co^{II} species in the interfacial region reaches its solubility limit, the Co^{II} species precipitate and condense into a solid phase oxide/hydroxide. With this solid film present the oxidation rate is limited by the rates of interfacial charge transfer and/or ion transport through the oxide. Thus, the rapid formation of a uniform layer of Co^{II} oxide/hydroxide causes a sudden drop in the current.

Once a uniform coherent oxide layer is formed, the anodic oxidation rate of Co to Co^{II} is determined by the rate of interfacial charge transfer at the metal/oxide and oxide/water interfaces and the rate of Co ion migration through the oxide layer. The Co^{II} produced can either be incorporated into the growing the oxide layer or be transported to the oxide/water interface where it can be hydrated and dissolve into the aqueous phase. The linear decrease in the anodic current with time suggests the current is mainly due to oxide growth and that the dissolution current is small. As the oxide layer thickens anodic oxidation slows and the anodic oxidation rate approaches the rate of dissolution of the Co cation from the oxide surface. The system eventually reaches a steady-state balance between the rates of Co oxidation and Co dissolution and the oxide layer no longer grows. As expected, at long times the anodic current is higher for the higher applied potential.

The current on an electrode during the linear decrease period was about an order of magnitude higher during polarization at $-0.2 \text{ V}_{\text{SCE}}$ than that seen at $-0.7 \text{ V}_{\text{SCE}}$ (Figure 4.12). This higher current can support the growth of a thicker film. This is consistent with the XPS

results (Figure 4.10a) which show the presence of a thicker Co^{II} oxide/hydroxide layer on an electrode treated at $-0.2 \text{ V}_{\text{SCE}}$ compared to the layer on an electrode treated at $-0.7 \text{ V}_{\text{SCE}}$.

The equivalent electric circuit analysis of the EIS taken at $-0.2 \text{ V}_{\text{SCE}}$ (Figure 4.9) yielded a polarization resistance value that is relatively low (initially $\sim 0.2 \text{ M}\Omega\cdot\text{cm}^2$ and increasing to a steady-state value of $\sim 0.5 \text{ M}\Omega\cdot\text{cm}^2$ after 2 h). The increase in R_p is accompanied by a decrease in the system capacitance from $\sim 7 \mu\text{F}\cdot\text{cm}^{-2}$ to $\sim 4 \mu\text{F}\cdot\text{cm}^{-2}$. The increase in resistance can be caused by either a thickening of an oxide film or the conversion of an existing film to a more insulating oxide. The increase in capacitance can be caused by either a decrease in film thickness, an increase in electrode surface area, or an increase in the dielectric constant of the oxide film. The XPS results (Figure 4.11a) show that only $\text{CoO}/\text{Co}(\text{OH})_2$ is present (within the analysis depth of 10 nm). The increase in resistance is attributed to the thickening of this oxide and the increase in capacitance is attributed to an increase in the active electrode surface area as the oxide grows. An SEM image of the surface (not presented) shows the presence of a filiform layer. This physical structure has an active surface area that is much larger than the geometric area of the electrode coupon. Growth of this type of structure is consistent with an increase in the active surface area of a $\text{CoO}/\text{Co}(\text{OH})_2$ oxide layer.

4.3.3.1.3 Film growth at $+0.2 \text{ V}_{\text{SCE}}$

The current observed during polarization at $0.2 \text{ V}_{\text{SCE}}$ shows similar behaviour to the current observed at $-0.2 \text{ V}_{\text{SCE}}$ (Figure 4.13). The initial current is the same, but the duration of near constant current lasts longer at $0.2 \text{ V}_{\text{SCE}}$. This short-term behaviour is attributed to

the same phenomena discussed above for the polarization at $-0.2 V_{SCE}$. The current remains constant longer at a higher potential because the diffusion of charged species through the double layer will be prolonged by the higher potential gradient in the interfacial region. The larger current drop at $0.2 V_{SCE}$ than at $-0.2 V_{SCE}$ is attributed to the formation of a thicker oxide at this potential as more Co^{II} species accumulate in the oxide layer over the longer cation diffusion period.

Following a sudden initial current drop, the current decreases linearly. Again, this is consistent with the growth of a thicker oxide layer. However, the current at $0.2 V_{SCE}$ actually drops below the current seen at $-0.2 V_{SCE}$ for some time, but then the situation reverses after ~ 500 s. The XPS results (Figure 4.11) show that the oxide layer formed at $0.2 V_{SCE}$ consists of both Co^{II} oxide/hydroxide and Co_3O_4 while the film formed at $-0.2 V_{SCE}$ consists of only $CoO/Co(OH)_2$. We attribute the lower current at $0.2 V_{SCE}$ at intermediate times to the early growth of a thicker oxide film. At longer times the current at $0.2 V_{SCE}$ becomes greater than that at $-0.2 V_{SCE}$ as the oxidation of Co^{II} to Co_3O_4/Co_2O_3 contributes more to the total current. The Co 2p band in the XPS spectra was successfully deconvoluted without any contribution from Co_2O_3 . The reference spectrum of this oxide was not available and, hence, it was not included in the XPS deconvolution. The oxidation of Co_3O_4 to Co_2O_3 is kinetically facile at potentials above the equilibrium potential for the redox pair ($0.23 V_{SCE}$, shown in Figure 4.3). However, since Co_2O_3 is both insulating and insoluble, it will form a very thin outer layer on the oxide surface. It is unsurprising that its omission in the Co 2p band deconvolution was not a problem.

At 0.2 V_{SCE}, the polarization resistance is initially low ($\sim 0.5 \text{ M}\Omega\cdot\text{cm}^2$) at 2 h, but it increases steadily with time, reaching a value of $\sim 2 \text{ M}\Omega\cdot\text{cm}^2$ after 30 h (Figure 4.9). The rate of increase is slow in the first 10 h while the dominant anodic process is conversion of CoO/Co(OH)₂ to Co₃O₄. However, at longer times the resistance increases more rapidly due to the conversion of the Co₃O₄ to more insulating and less soluble Co₂O₃. At the same time, the capacitance shows only slight decreases.

4.3.3.2 Film Growth on Stellite-6

4.3.3.2.1 Film growth at $-0.7 \text{ V}_{\text{SCE}}$

At $-0.7 \text{ V}_{\text{SCE}}$, the current behaviour observed on Stellite-6 is very similar to that on Co (Figure 4.14); the current decreases nearly linearly with time and it switches from anodic to cathodic at $\sim 300 \text{ s}$. The current during potentiostatic polarization on Stellite-6 is, however, about an order of magnitude lower than the current seen on Co under the same conditions. This is opposite to the current behaviour observed during a CV scan; the current at $-0.7 \text{ V}_{\text{SCE}}$ is higher on Stellite-6 than on Co. The current observed at this potential during the CV scan corresponds to the oxidation of Co to Co^{II} to form cobalt chromite. During long-term polarization the conversion of the pre-existing thin layer of Cr^{III} oxide to CoCr₂O₄ is completed in a very short time and the current at longer times is due to anodic oxidation of Co to form a Co^{II} oxide/hydroxide layer. The current due to the latter anodic process is lower on Stellite-6 than on Co at long times because of the presence of a passive inner layer of chromite on Stellite-6. Water reduction also occurs on Stellite-6 but the reduction current is lower than on Co because of the presence of the passive chromite layer. Cobalt chromite is

also a p-type semiconductor but it has a higher a band gap (3.4 eV) [24] than the band gap of $\text{Co}(\text{OH})_2$ (2.4 eV).

The XPS analysis results for the Stellite-6 at $-0.7 \text{ V}_{\text{SCE}}$ (Figure 4.12) show that Co^{II} is present mainly as cobalt chromite (CoCr_2O_4) and to a smaller extent as Co^{II} oxide/hydroxide. The presence of Co^0 in the high resolution Co 2p band indicates that the film formed at $-0.7 \text{ V}_{\text{SCE}}$ is very thin ($< 10 \text{ nm}$).

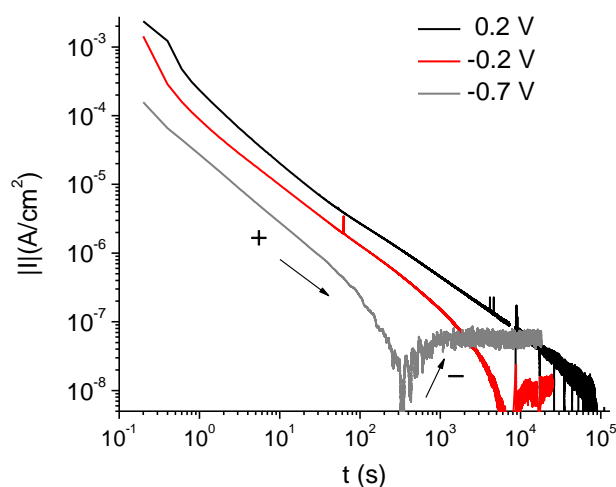


Figure 4.14: Current as a function of time observed during potentiostatic film growth at -0.7 , -0.2 , and $0.2 \text{ V}_{\text{SCE}}$, on Stellite-6. The + and - signs indicate anodic and cathodic currents, respectively.

4.3.3.2.2 Film growth at $-0.2 \text{ V}_{\text{SCE}}$

The current at $-0.2 \text{ V}_{\text{SCE}}$ shows a linear decrease with time (Figure 4.14). It reaches a very small value before the net current ($\sim 10^{-8} \text{ A}\cdot\text{cm}^{-2}$) becomes cathodic after $\sim 2 \text{ h}$. Since this cathodic current is very low, it could be generated by several processes, all of which are

slow. Potential contributors include water reduction and reduction of trace dissolved oxygen in the alloy, possibly assisted by photo-induced reactions. The oxidative conversion of the pre-existing chromium oxide layer to a cobalt chromite layer occurs early and the linear behaviour of the current vs. time is attributed to steady growth of CoO/Co(OH)_2 . The current at $-0.2 \text{ V}_{\text{SCE}}$ is about an order of magnitude higher than the current at $-0.7 \text{ V}_{\text{SCE}}$ and this is consistent with the growth of a thicker outer layer of Co^{II} oxide/hydroxide at this potential.

The XPS analysis results (Figure 4.12) are also consistent with a thicker growth of CoO/Co(OH)_2 on an inner chromite layer. The XPS Co 2p spectrum is dominated by the CoO/Co(OH)_2 contribution for films grown at $-0.2 \text{ V}_{\text{SCE}}$ (and at $-0.1 \text{ V}_{\text{SCE}}$, a potential which is also in potential Region II) and the chromite contribution is below the XPS detection level. However, the metal Co^0 peak still contributes to the Co 2p band, indicating that the oxide layer is still $<10 \text{ nm}$ at this potential.

The EIS analysis of the film growth at $-0.2 \text{ V}_{\text{SCE}}$ (Figure 4.9) shows that the polarization resistance is $2.0 - 2.5 \text{ M}\Omega\cdot\text{cm}^2$ and is relatively independent of time. This is consistent with the presence of a passive chromite layer on Stellite-6. The resistance is already high at the time of the first EIS measurement (2 h) due to the presence of this layer. The resistance increases only slightly with time (from 2.0 to $2.5 \text{ M}\Omega\cdot\text{cm}^2$) and the capacitance remains nearly constant at $\sim 6 \mu\text{F}\cdot\text{cm}^{-2}$, which attests to the steady-state nature of the outer Co^{II} oxide/hydroxide layer.

4.3.3.2.3 Film growth in potential range of 0.1 to 0.4 V_{SCE}

Since the electrochemical reactivity of Stellite-6 is high at potentials $> 0.1 V_{SCE}$ (Figure 4.5b) and E_{corr} increases to a value greater than $0.1 V_{SCE}$ when radiation is present (Figure 4.2), the anodic oxidation and dissolution of Stellite-6 was explored at a number of potentials within potential Regions III and IV. The potentiostatic polarization results are shown in Figure 4.15. At all potentials $> 0.1 V_{SCE}$ the current initially decreases nearly linearly with time. However, after about 10 to 100 s the rate of current decrease slows and becomes non-linear. The slowing of the current decrease occurs faster with higher applied potentials. This change in behaviour indicates the presence of more than one anodic process. Candidates include metal cation dissolution or further oxidation of an oxide that has already formed. At $0.4 V_{SCE}$ the current on Stellite-6 reaches a constant value after only ~ 10 s. The magnitude of this current ($30 \mu A \cdot cm^{-2}$) approaches a value expected for an aqueous diffusion-limited process at the electrode surface. At this potential, oxidation of insoluble Cr^{III} oxide to highly soluble Cr^{VI} oxide species is allowed and the high steady-state current at long times is attributed to this oxidation and chromium dissolution. This explanation is consistent with a potential dependent rate for chromium oxidation [25].

The presence of $CoOOH$ in films grown at potentials $> 0.1 V_{SCE}$ was found by the XPS (Figure 4.12a). The fraction of $CoOOH$ in the outer layer increases, while the fraction of $CoO/Co(OH)_2$ decreases, with an increase in the applied potential. The ratio of Co/Cr in the surface oxide also increases in this potential region, consistent with the loss of Cr from the oxide surface. No Co metal component of the $Co 2p$ band was found showing that the

oxides grown in this potential region are thicker than 10 nm despite the high rate of Cr dissolution. Comparison of the XPS results for Co and Stellite-6 (Figure 4.11a and 4.12a) shows that the Co^{III} species formed at potentials $> 0.1 \text{ V}_{\text{SCE}}$ on Stellite-6 is mainly CoOOH while it is mainly Co_3O_4 on Co. The presence of the chromite-like inner layer on Stellite-6 means that Co^{II} reaches the oxide/water interface at a slower rate and all of this Co^{II} can be subsequently oxidized to Co^{III} through the kinetically favored formation of CoOOH . As discussed for reactions (4.5) and (4.6) in section 4.3.2.1, the oxidation of $\text{Co}(\text{OH})_2$ to CoOOH should be faster than the oxidation of $\text{Co}(\text{OH})_2$ to Co_3O_4 .

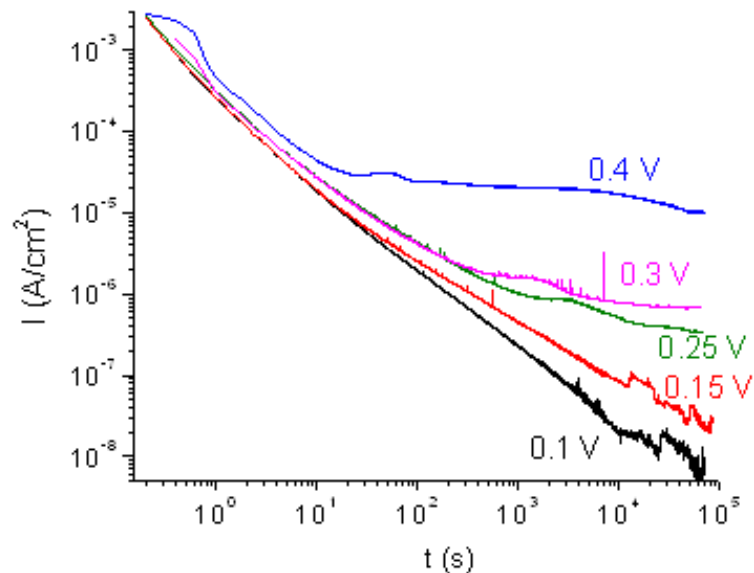


Figure 4.15: Current as a function of time observed during potentiostatic film growth at 0.1, 0.15, 0.25, 0.3 and 0.4 V_{SCE} on Stellite-6.

At 0.2 V_{SCE} the polarization resistances of the Stellite-6 films are lower and the capacitances are higher than the corresponding values derived for films grown at $-0.2 \text{ V}_{\text{SCE}}$.

At $0.2 V_{SCE}$ the Cr^{III} can begin to oxidize to Cr^{VI} rendering the oxide film somewhat less protective and decreasing its resistivity. The capacitance of the film ($\sim 150 \mu F \cdot cm^{-2}$) is independent of time and is an order of magnitude higher than that expected for a double-layer capacitance [3]. Since a potential of $0.2 V_{SCE}$ is high enough to drive cobalt oxidation and since the oxide layer on Stellite-6 at this potential has a mix of metal cation oxidation states, any change in the relative population of species in each oxidation state would change the net surface charge. For example, the oxidation of Co^{II} to Co^{III} can attract more OH^{-} to the oxide surface whereas the reduction of Co^{III} to Co^{II} repulses OH^{-} . This is equivalent to adsorbing and desorbing a high surface coverage of ions and leads to the storage of a large amount of charge in an extremely thin layer in the interfacial region. This is often referred to as pseudo-capacitance and is the probable explanation for the observed high capacitance value [29].

4.4 CONCLUSIONS

At pH 10.6 and room temperature, gamma-irradiation at a dose rate of $5.5 \text{ kGy} \cdot \text{h}^{-1}$ increases the corrosion potential from $-0.7 V_{SCE}$ to $0.08 V_{SCE}$ on pure Co and from $-0.48 V_{SCE}$ to $0.12 V_{SCE}$ on Stellite-6. The corrosion behaviour of Co and Stellite-6 can be divided into a number of potential regions and the presence of ionizing radiation shifts the corrosion potential from the transition between potential Regions I and II to the transition between potential Regions II and III for both metals. The transition from Region I to II occurs near $-0.7 V_{SCE}$, the equilibrium potential for Co to $CoO/Co(OH)_2$ oxidation, while the transition from Region II to III occurs at $\sim 0.1 V_{SCE}$, the equilibrium potential for $CoO/Co(OH)_2$ conversion to mixed $Co^{II/III}$ or Co^{III} oxides/hydroxides.

Due to the presence of a thin, defective Cr^{III} oxide layer on Stellite-6, the oxidation of Co to Co^{II} starts at a lower potential on Stellite-6 than on Co. The Co^{II} produced at potentials lower than $-0.7 V_{SCE}$ is incorporated into the Cr^{III} oxide layer on Stellite-6 and forms cobalt chromite (CoCr₂O₄). The chromite layer on Stellite-6 also suppresses the electrochemical reactivity of this alloy at higher potentials. The same cobalt oxidation reactions occur on Stellite-6 as on Co, but at much slower rates for a given potential. Gamma-irradiation increases the corrosion potential of both metals to a range where the rate of oxidation of Co to Co^{II} increases. This Co^{II} can further oxidize to form less soluble Co^{III} species. The competition of these two reactions (oxidation of Co to Co^{II} and oxidation of Co^{II} to Co^{III}) determines the net effect of gamma radiation on the rate of Co dissolution from Stellite-6. Solution pH and temperature have a strong influence on oxide solubilities.

4.5 REFERENCES

- [1] W.H. Hocking, D.H. Lister, Corrosion of Stellite-6 in lithiated and borated high-temperature water, *Surf. Interface Anal.*, 11 (1988) 45–59.
- [2] N.S. McIntyre, D. Zetaruk, E.V. Murphy, X-ray photoelectron spectroscopic study of the aqueous oxidation of Stellite-6 alloy, *Surf. Interface Anal.*, 1 (1979) 105–110.
- [3] M. Metikoš-Huković, R. Babić, Passivation and corrosion behaviours of cobalt and cobalt–chromium–molybdenum alloy, *Corros. Sci.*, 49 (2007) 3570–3579.
- [4] R.W.-W. Hsu, C.-C. Yang, C.-A. Huang, Y.-S. Chen, Electrochemical corrosion studies on Co–Cr–Mo implant alloy in biological solutions, *Mater. Chem. Phys.*, 93 (2005) 531–538.
- [5] P.D. Wood, H.E. Evans, C.B. Ponton, Investigation into the wear behaviour of Stellite 6 during rotation as an unlubricated bearing at 600°C, *Tribol. Int.*, 44 (2011) 1589–1597.
- [6] L. Benea, P. Ponthiaux, F. Wenger, J. Galland, D. Hertz, J.Y. Malo, Tribocorrosion of Stellite 6 in sulphuric acid medium: electrochemical behaviour and wear, *Wear*, 256 (2004) 948–953.
- [7] W.H. Hocking, F.W. Stanchell, E. McAlpine, D.H. Lister, Mechanisms of corrosion of Stellite-6 in lithiated high temperature water, *Corros. Sci.*, 25 (1985) 531–557.

- [8] F. Rosalbino, G. Scavino, Corrosion behaviour assessment of cast and HIPed Stellite 6 alloy in a chloride-containing environment, *Electrochim. Acta*, 111 (2013) 656–662.
- [9] A. Foelske, H.H. Strehblow, Structure and composition of electrochemically prepared oxide layers on Co in alkaline solutions studied by XPS, *Surf. Interface Anal.*, 34 (2002) 125–129.
- [10] M. Pontinha, S. Faty, M.G. Walls, M.G.S. Ferreira, M. Da Cunha Belo, Electronic structure of anodic oxide films formed on cobalt by cyclic voltammetry, *Corros. Sci.*, 48 (2006) 2971–2986.
- [11] W.K. Behl, J.E. Toni, Anodic oxidation of cobalt in potassium hydroxide, *J. Electroanal. Chem.*, 31 (1971) 63–75.
- [12] W.A. Badawy, Electrochemical behaviour of cobalt in aqueous solutions of different pH, *J. Appl. Electrochem.*, (2000) 693–704.
- [13] T. Ohtsuka, N. Sato, Anodic oxide film on cobalt in weakly alkaline solution, *J. Electroanal. Chem.*, 147 (1983) 167–179.
- [14] A. Gulino, G. Fiorito, I. Fragalà, I. Fragala, Deposition of thin films of cobalt oxides by MOCVD, *J. Mater. Chem.*, 13 (2003) 861–865.
- [15] C.F. Baes, *The Hydrolysis of Cations*, 2nd ed., Wiley, New York, 1986.
- [16] K. Daub, X. Zhang, J.J. Noël, J.C. Wren, Effects of γ -radiation versus H_2O_2 on carbon steel corrosion, *Electrochim. Acta*, 55 (2010) 2767–2776.
- [17] Q.W. Knapp, J.C. Wren, Film formation on type-316L stainless steel as a function of potential: Probing the role of gamma-radiation, *Electrochim. Acta*, 80 (2012) 90–99.
- [18] K. Daub, X. Zhang, L. Wang, Z. Qin, J.J. Noël, J.C. Wren, Oxide growth and conversion on carbon steel as a function of temperature over 25 and 80 °C under ambient pressure, *Electrochim. Acta*, 56 (2011) 6661–6672.
- [19] K. Daub, X. Zhang, J.J. Noël, J.C. Wren, Gamma-radiation-induced corrosion of carbon steel in neutral and mildly basic water at 150 °C, *Corros. Sci.*, 53 (2011) 11–16.
- [20] M. Pourbaix, *Atlas of Electrochemical Equilibria in Aqueous Solution*, Oxford, New York, 1966.
- [21] M.C. Biesinger, B.P. Payne, A.P. Grosvenor, L.W.M. Lau, A.R. Gerson, R. St.C. Smart, Resolving surface chemical states in XPS analysis of first row transition metals, oxides and hydroxides: Cr, Mn, Fe, Co and Ni, *Appl. Surf. Sci.*, 257 (2011) 2717–2730.
- [22] L.J. Oblonsky, T.M. Devine, A surface enhanced Raman spectroscopic study of the passive films formed in borate buffer on iron, nickel, chromium and stainless, *Corros. Sci.*, 37 (1995) 17–41.
- [23] R. Cheng, B. Xu, C.N. Borca, A. Sokolov, C.-S. Yang, L. Yuan, Characterization of the native Cr_2O_3 oxide surface of CrO_2 , *Appl. Phys. Lett.*, 79 (2001) 3122–3124.
- [24] U. Lüders, F. Sánchez, J. Fontcuberta, Initial stages in the growth of {111}-faceted $CoCr_2O_4$ clusters: mechanisms and strained nanometric pyramids, *Appl. Phys. A Mater. Sci. Process.*, 79 (2004) 93–97.
- [25] D. Marijan, M. Gojic, Electrochemical study of the chromium electrode behaviour in borate buffer solution, *J. Appl. Electrochem.*, 32 (2002) 1341–1346.

- [26] G.J. Brug, A.L.G. Van den Eeden, M. Sluyters-Rehbach, The analysis of electrode impedances complicated by the presence of a constant phase element, *J. Electroanal. Chem.*, 176 (1984) 275–295.
- [27] M.C. Biesinger, C. Brown, J.R. Mycroft, R.D. Davidson, N.S. McIntyre, X-ray photoelectron spectroscopy studies of chromium compounds, *Surf. Interface Anal.*, 36 (2004) 1550–1563.
- [28] G.T. Burstein, A.J. Davenport, The current-time relationship during anodic oxide film growth under high electric field, *J. Electrochem. Soc.*, 136 (1989) 936–941.
- [29] T. Nishimura, H. Katayama, K. Noda, Effect of Co and Ni on the corrosion behavior of low alloy steels in wet/dry environments, *Corros. Sci.*, 42 (2000) 1611–1621.

CHAPTER 5

Combined Effects pH and γ -Irradiation on Corrosion of Stellite-6²

5.1 INTRODUCTION

The electrochemical studies at room temperature and pH 10.6 (Chapter 4) showed that the corrosion potential of Stellite-6 increased by roughly 0.4 V in the presence of gamma irradiation. The increase in corrosion potential resulted in a dramatic increase in the Co^{II} content in the oxide as well a slight contribution of Co^{III} . The changes in potential and oxide composition were attributed to the formation of H_2O_2 via water radiolysis.

It is well understood that aqueous corrosion kinetics are significantly influenced by water chemistry conditions that include pH, temperature, and the presence of redox-active aqueous species. However there are still some uncertainties about the combined effect of pH and ionizing radiation on the corrosion mechanism. Some studies of radiation-assisted corrosion have focused primarily on the direct interaction of radiation particles (mostly neutrons and protons) with the metal (or alloy) phase. These interactions lead to metallurgical changes such as increases in the alloy defect density, atomic displacement and element segregation in the metal (or oxide) phase [11].

²A version of Chapter 5 has been published: M. Behazin, J.J. Noël, J.C. Wren, Combined effect of pH and γ -irradiation on corrosion of Stellite-6, *Electrochimica Acta*, 134 (2014) 399–410.

Some of the other corrosion studies on Co-based alloys have been performed in extremely acidic or basic solutions at room temperature [22], in a chloride-containing and saline environment at room temperature [23,24], in a 2 wt.% sulphuric acid solution [25], and also in mildly basic water (pH 10) at 285 °C [26]. However, it is difficult to separate the effects of individual parameters or to extrapolate the corrosion rate obtained under one set of conditions to another set of conditions, since individual solution parameters can affect the film growth and metal dissolution rates differently.

This chapter examines the effects of pH and γ -radiation at room temperature. For this study, we have performed two sets of experiments at pH 6.0, pH 8.4, and pH 10.6. The first set of experiments involves 3-d long corrosion tests using Stellite-6 coupons in sealed vials with analysis of the changes on the coupon surfaces by scanning electron microscopy (SEM), X-ray photoelectron spectroscopy (XPS) and Auger electron spectroscopy (AES), and measurement of the dissolved metal loss using inductively coupled plasma mass spectrometry (ICP-MS). The second set of experiments involves corrosion potential (E_{corr}) measurements and potentiostatic polarization tests as a function of the applied potential (E_{APP}).

5.2 EXPERIMENTAL

5.2.1 Solution Preparation

All solutions were prepared with water purified using a NANO pure Diamond UV ultra-pure water system from Barnstead International to remove organic and inorganic

impurities; this water had a resistivity of 18.2 M Ω cm. The 10 mM borate electrolyte solutions were prepared using reagent grade Na₂B₄O₇·10H₂O (Caledon Laboratories Ltd.) (for pH 10.6 and 8.4 solutions) or with reagent grade H₃BO₃ (Caledon Laboratories Ltd.) (for pH 6.0 solutions). The pH was adjusted to 10.6 by dropwise addition of reagent grade 1 M NaOH (Caledon Laboratories Ltd.), to 8.4 by dropwise addition of 0.5 M boric acid, or to 6.0 by dropwise addition of 0.01 M NaOH. The solution preparation methods were chosen in order to maintain a similar ionic strength in solutions with different pH.

Irradiation experiments were performed inside an MDS Nordion Gammacell 220 Excel Cobalt-60 irradiator which provided a dose rate of 5.5 kGy·h⁻¹ at the time of these experiments.

5.2.2 Aqueous Corrosion Experiments

The aqueous corrosion experiments were performed using coupons in sealed quartz vials. The test coupons were placed on a quartz pedestal attached to the bottom of the vial, in order to suspend the coupons and avoid crevice formation. The test vials were prepared inside an Ar-purged glove box where the oxygen concentration was maintained at a low level (typically less than 0.4 ppm at room temperature). Once a coupon was placed on the pedestal, 7 mL of electrolyte solution was added to the vial to fully immerse the coupon. The ratio of the coupon surface area to the water volume was thus 0.265 cm²·mL⁻¹ in all of the aqueous corrosion tests. Each vial was then sealed using an aluminum crimp cap with a PTFE silicone septum to provide a vacuum tight seal and ensure no loss of gas during a test.

All of the aqueous corrosion tests, with and without irradiation, were conducted for 72 h (3 d). This duration allowed sufficient time for corrosion to develop different oxide films as a function of pH. Following corrosion tests, the vials were opened and the coupons were removed, dried in flowing argon gas, and stored in a glove box for further surface analyses. The solutions were also analyzed for pH and their dissolved metal content. The pH was measured with an Accumet® Basic AB15 pH meter. During the course of the radiation exposure experiments, the pH decreased from 10.6 to 9.94, 8.4 to 8.22, or 6.0 to 5.25, depending on the starting pH. The pH change of the un-irradiated solutions was negligible.

5.3 AQUEOUS CORROSION TESTS

5.3.1 SEM Results

The SEM images of Stellite-6 coupon surfaces corroded for 3 d at three different pH values are shown in Figure 5.1. The SEM images of a freshly polished surface at two different magnifications are shown to illustrate different aspects of the surface morphology. The images of the fresh surface show two regions of differing brightness, corresponding to the two main alloy phases in Stellite-6; the dark area is enriched in Cr, which favours a hexagonal closed-packed phase structure, whilst the light area is enriched in Co and has a face-centered cubic phase structure [2].

The surfaces corroded at the two lower pH values in the presence of radiation are smooth and the two phases of the alloy are still clearly visible. The coupons corroded without irradiation at these pHs show similar morphology and hence are not shown. These

results indicate that the oxides present on the surfaces exposed to solutions at pH 6.0 and 8.4, with and without irradiation, are very thin.

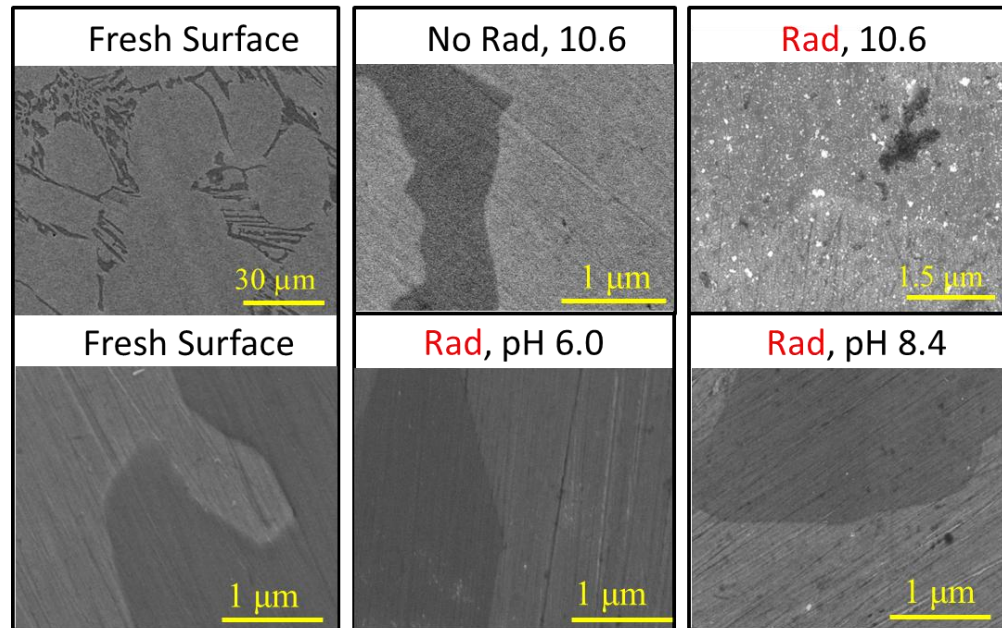


Figure 5.1: SEM images of Stellite-6 coupons corroded under different conditions: freshly polished, at pH 10.6 without and with irradiation (Rad), and at pH 6.0 and pH 8.4 with irradiation.

The effect of γ -irradiation on the morphology of Stellite-6 corroded at pH 10.6, where the solubility of Co(OH)_2 is near its minimum [27,29], is more interesting. The surface corroded at pH 10.6 without irradiation still shows the Co-rich and Cr-rich phases, but the sharp polishing lines that are seen on the freshly prepared surface become blurred, indicating that the surface is uniformly covered by an oxide film. The surface corroded at pH 10.6 with irradiation still shows blurred images of both the Co-rich and Cr-rich phases, indicating a uniform inner oxide film, but there are also oxide particulates (white crystallites) present that

are evenly distributed on top of the inner oxide film. The even distributions of the inner oxide layer and the outer particulates show no evidence of preferential growth of oxide/hydroxide on either the Cr-rich or the Co-rich phase. The results suggest that corrosion of Stellite-6 at pH 10.6 occurs uniformly, both with or without irradiation, but under γ -irradiation it leads to formation of a different type(s) of oxide.

5.3.2 XPS Results

To obtain the chemical composition of the surface oxide layer, high-resolution XPS spectra of the Co 2p and Cr 2p bands were deconvoluted using reference samples of pure-phase metals and oxides [28]. The values for binding energies of different Co oxides are those previously mentioned in Chapter 4. Some of the reference spectra contain multiple peaks. A representative high-resolution Co 2p band from one XPS spectrum and its deconvolution into the bands of the contributors to the spectrum are shown in Figure 5.2.

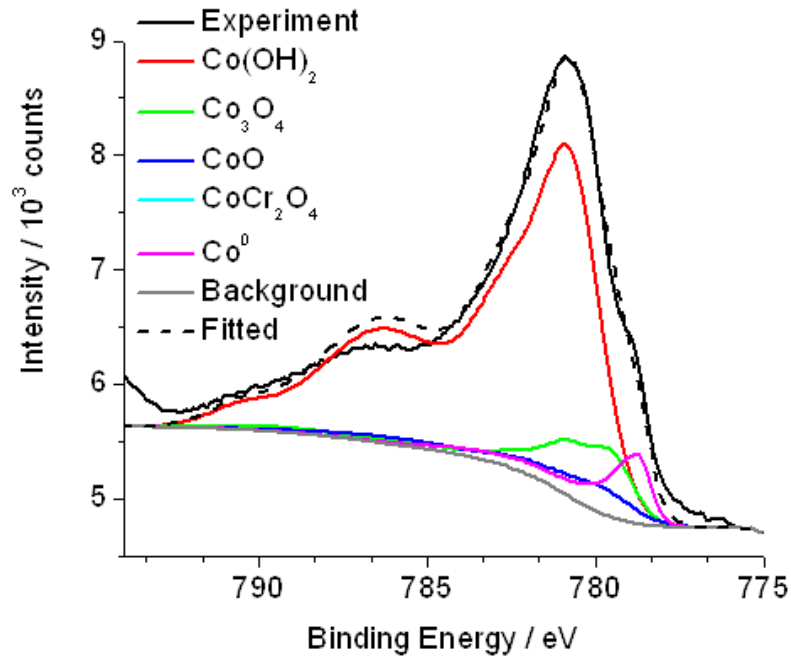


Figure 5.2: High resolution XPS spectrum of the Co 2p band region and its deconvoluted components for a coupon irradiated at pH 10.6.

The XPS analysis results are presented in Table 5.1. For the samples corroded in the absence of radiation, the contribution of the metallic component, Co^0 , to the Co 2p band decreases with increasing pH, from 92% to 19% (Table 5.1). A smaller Co^0 contribution indicates the presence of a thicker oxide. On the un-irradiated samples, the oxide component is present only as Co^{II} ; that is, no species containing Co^{III} was present. The Co^{II} oxide is present mostly as $\text{Co}(\text{OH})_2$. On any metal surface corroded in water the outermost oxide layer should be in the form of metal hydroxides. (Depending on the stability of the hydroxide, an inner layer may be in dehydrated form, a metal oxide.) The large fraction of Co^{II} seen as $\text{Co}(\text{OH})_2$ mostly reflects the presence of a thin Co^{II} layer. This also explains the

relatively large fraction of Co^{II} oxide on the fresh samples attributable to the adsorbed water. At pH 10.6, where a thicker oxide is present, a small fraction of the Co^{II} is present as chromite (CoCr_2O_4). The amount of these species is negligible at lower pH.

Table 5.1: Cobalt speciation in the top 9 nm layer as determined by XPS analysis at 25 °C.

Co Species	Fresh Surface %	pH _{25°C} 10.6		pH _{25°C} 8.4		pH _{25°C} 6.0	
		No Rad %	Rad %	No Rad %	Rad %	No Rad %	Rad %
Co^0	61	19	1	77	47	92	73
CoCr_2O_4	4	14	17	0	0	0	0
$\text{Co}(\text{OH})_2$	35	67	51	23	8	8	3
Co_3O_4	0	0	8	0	36	0	22
CoOOH	0	0	23	0	9	0	2

On the irradiated coupons, the Co^0 contribution to the Co 2p band intensity also decreases with increasing pH, indicating that a thicker oxide is formed at a higher pH. At pH 10.6, the contribution of Co^0 to the XPS spectra is negligible, showing that the oxide layer is at least 9 nm thick (the instrument analysis depth). On the irradiated samples at all pH values, the Co 2p band contains contributions from both Co^{II} and Co^{III} . Due to the thinness of the oxide layers at low pH, the oxide compositions determined by XPS for those samples have large uncertainties. Nevertheless, the XPS analyses consistently reveal a higher Co^{III} fraction in the oxides of coupons corroded in the presence of radiation than on those corroded in the absence of radiation, at all pH values. These results indicate that the solution environment becomes more oxidizing under γ -irradiation as was discussed in Chapter 4.

5.3.3 AES Results

The variation of the elemental composition of the surface oxide layer with depth was investigated by AES depth profiling. Figure 5.3 shows the atomic percentages of all of the elements present on the surface as a function of sputtered depth obtained for two extreme cases: pH 6.0 without irradiation (Figure 5.3a), and pH 10.6 with irradiation (Figure 5.3b).

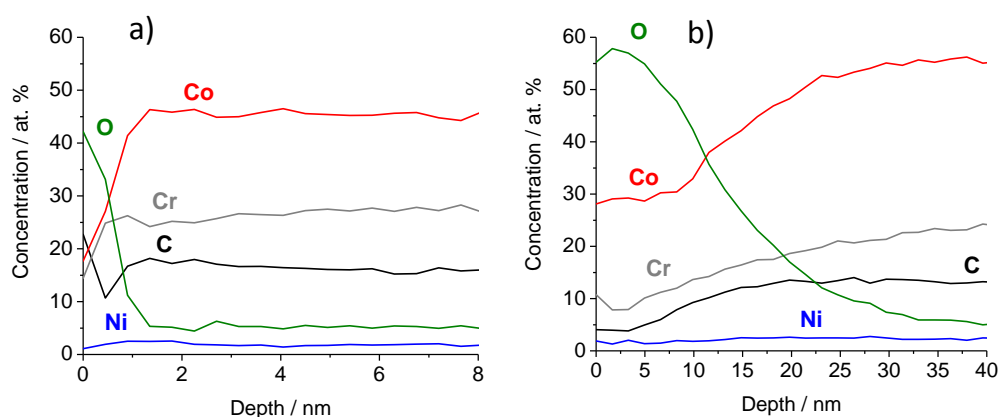


Figure 5.3: Depth profiles of the elements determined by AES of Stellite-6 coupons corroded for 3 d (a) at pH 6.0 without irradiation and (b) irradiated at pH 10.6.

The atomic percentage of each element in this figure is the atomic ratio of the element to the sum of all of the elements present at the depth. The results show that the outermost surface composition (at a nominal depth of 0 nm) is easily affected by carbon or by the adsorbed hydrated species. Thus, the data at 0 nm are not very meaningful. The AES data show that the atomic % of oxygen decreases with depth. This change in atomic percentage can obscure any changes in the characteristics of the oxides of the main elements, Co and Cr.

To observe more clearly the degree of oxidation of the two main alloying components and their relative abundance in the oxide, the AES data are presented as the ratios of $O/(Co + 1.5 Cr)$ and $Co/(Co+Cr)$, as a function of sputtered depth, in Figure 5.4. Plotting the ratio of O to $(Co + 1.5 Cr)$ implies that we are comparing the composition of the oxide present on the alloy surface with one that is either a 1:1 mixture of CoO and Cr_2O_3 or one that is $CoCr_2O_4$ (chromite).

The depth profiles of $O/(Co + 1.5 Cr)$ in Figure 5.4a show that the oxide films on the samples corroded without irradiation are all very thin (less than 4 nm thick). Nevertheless, the oxide shows a small pH dependence; the $O/(Co + 1.5 Cr)$ ratio decreases to zero at ~ 1.0 nm, 2.0 nm and 3.5 nm at pH 6.0, 8.4 and 10.6, respectively. The oxygen-oxygen distances in the metal oxide lattices range from 0.289 to 0.292 nm [30]; for example, the O-O bond in $Co(OH)_2$ is reported to be 0.289 nm [31]. The oxide thickness on the un-irradiated samples is thus comprised of only 3 – 10 oxide molecular layers. Even in this thin oxide layer, the depth profile of the ratio of $O/(Co + 1.5 Cr)$ is strongly correlated with the depth profile of the $Co/(Co+Cr)$ ratio.

Surfaces corroded in the absence of radiation

On the samples corroded at pH 6.0 and 8.4 without irradiation, the $O/(Co + 1.5 Cr)$ ratios decrease exponentially from ~ 0.5 to 0 with depth. The $Co/(Co+Cr)$ ratios decrease from ~ 0.55 and 0.62 from ~ 0.5 to 0 with depth and then increase to a maximum value of 0.62 – 0.7. The depth profiles of $Co/(Co+Cr)$ obtained at different pHs are shifted by one unit of the y-axis up or down in Figure 5.4 to show the depth dependence of this ratio more

clearly for the different pH values. In an oxide layer that is less than 9 nm thick both the oxide and the underlying alloy contribute to the elemental composition determined by AES, with the alloy phase contributing more at a greater sputter depth. The maximum in $\text{Co}/(\text{Co}+\text{Cr})$ occurs at a depth where $\text{O}/(\text{Co}+1.5 \text{ Cr})$ reaches zero. This behaviour suggests that there is a Co^{II} gradient across the thin initial Cr_2O_3 layer from a lowest concentration at the oxide/water interface to a highest concentration at the oxide/alloy interface. Below this point, where the oxygen content is negligible, the $\text{Co}/(\text{Co}+\text{Cr})$ ratio decreases until it reaches a constant value which corresponds to ratio of the bulk alloy (1.8 for Stellite-6) with an uncertainty of ± 0.2 as determined by AES.

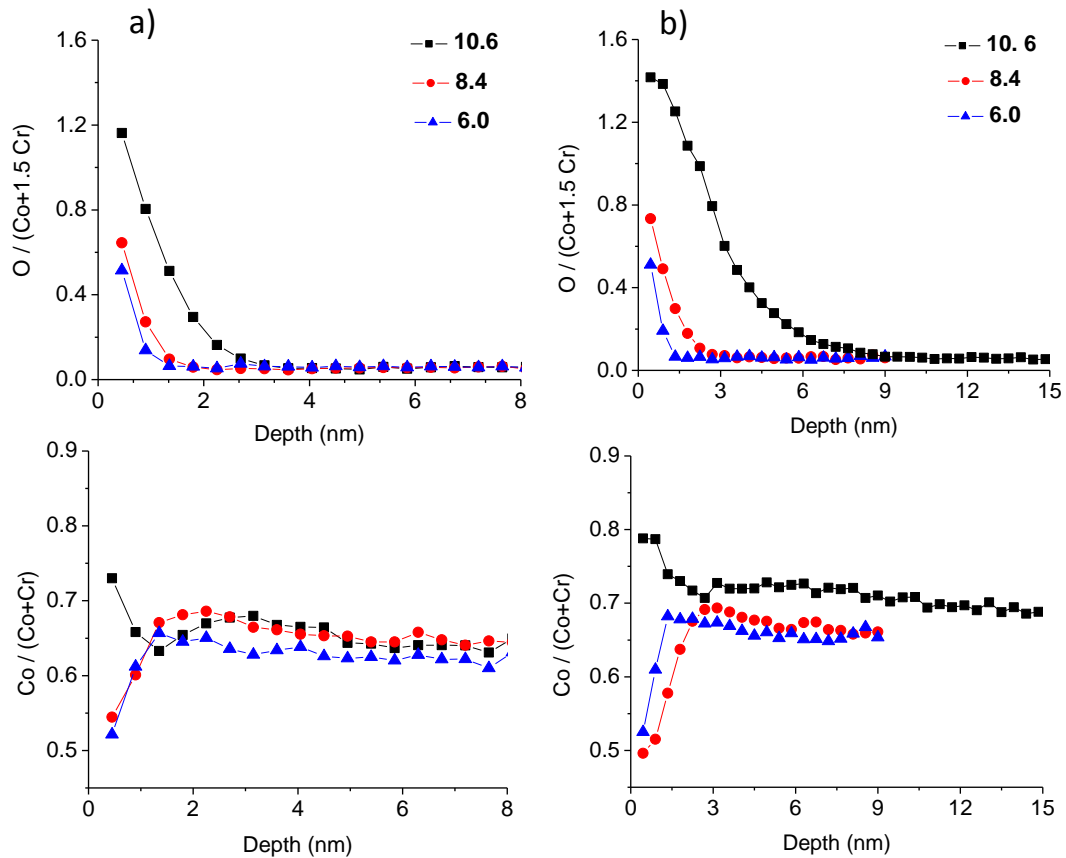


Figure 5.4: Depth profiles of $O/(Co+1.5 Cr)$ and $Co/(Co+Cr)$ on coupons corroded at different pHs: 10.6 (—■—), 8.4 (—●—), and 6.0 (—▲—). The left panels (a) present the results obtained in the absence of radiation and the right panels (b) present the results obtained in the presence of radiation.

On the samples corroded at pH 10.6 without irradiation, the oxide layer is thicker and $O/(Co + 1.5 Cr)$ is initially high (> 1.2). Over the depth range of 0 nm to 1.5 nm where $O/(Co + 1.5 Cr)$ is greater than 0.5, the $Co/(Co+Cr)$ ratio is also higher than that of the bulk alloy. In this region both ratios decrease with depth, a trend opposite to that observed at the two lower pH values. Further into the oxide (depth > 1.5 nm) the depth profiles of $O/(Co +$

1.5 Cr) and $\text{Co}/(\text{Co}+\text{Cr})$ show the same behaviour as that observed for the oxides formed at the low pH values; $\text{O}/(\text{Co} + 1.5 \text{ Cr})$ decreases from 0.5 to zero while $\text{Co}/(\text{Co}+\text{Cr})$ increases to a maximum of about 0.75, followed by a decrease to the bulk alloy value of 0.65. The decreases in both $\text{O}/(\text{Co} + 1.5 \text{ Cr})$ and $\text{Co}/(\text{Co}+\text{Cr})$ within the first 1.5 nm suggest that there is a larger contribution of cobalt oxide than chromium oxide to the oxide at the outer surface, and a $\text{O}/(\text{Co} + 1.5 \text{ Cr})$ ratio greater than 1.0 suggests that the cobalt oxide near the surface is in the form of $\text{CoO}/\text{Co}(\text{OH})_2$. This oxide is absent from the surfaces corroded at the lower pH values. At pH 6.0 and 8.4, the $\text{Co}/(\text{Co}+\text{Cr})$ ratio is initially about half that of the bulk alloy. There is a lower Co content (or a higher Cr content) near the surface than one would find in the bulk alloy. A similar observation for the oxides formed on other Cr alloys (such as stainless steels and nickel alloys) is often interpreted as being due to Cr migration to the surface as a precursor to Cr dissolution [32,33]. Our XPS, AES and ICP-MS results (as well as the electrochemical analyses to be discussed later) indicate that a low $\text{Co}/(\text{Co}+\text{Cr})$ ratio at the surface of coupons corroded at the two lower pH values is a result of cobalt dissolution during corrosion. Figure 5.3a shows that the Cr, C and Ni fractions increase similarly with depth near the surface, while that of Co increases very rapidly and this is consistent with a loss of Co to the solution. Interestingly, all of the surfaces show a region with a $\text{Co}/(\text{Co}+\text{Cr})$ value that is slightly higher than the bulk alloy value and this ratio is highest when $\text{O}/(\text{Co} + 1.5 \text{ Cr})$ is zero. A higher $\text{Co}/(\text{Co}+\text{Cr})$ value than that of the bulk alloy suggests that some chromium depletion has occurred in this region. This might have occurred during the formation of the initial, thin air-formed chromium oxide layer. The chromium depletion can be seen clearly in Figure 5.3b.

Surfaces corroded in the presence of radiation

A thicker oxide is formed under irradiation, and the effect of pH on the oxide thickness is more pronounced on the irradiated samples (see Figure 5.4b). At pH 6.0, γ -irradiation has a negligible effect on oxide formation; the depth profiles of O/(Co + 1.5 Cr) on the surfaces exposed to pH 6.0 solution with and without irradiation are nearly identical (Figure 5.4a and Figure 5.4b). Had irradiation increased the rate of cobalt oxidation, this oxidation would have resulted in cobalt dissolution rather than oxide growth, see further discussion below.

On the coupons irradiated at pH 8.4, Co/(Co+Cr) is initially constant (at ~1.0) until O/(Co + 1.5 Cr) decreases to ~0.5 at a depth of ~3 nm. At depths > 4 nm, Co/(Co+Cr) increases with depth while O/(Co + 1.5 Cr) decreases from 0.5 to 0.0. This qualitative relationship between the depth dependences of Co/(Co+Cr) and O/(Co + 1.5 Cr) is the same as that observed on an un-irradiated coupon. However O/(Co + 1.5 Cr) decreases less steeply with depth on the irradiated coupon than on the un-irradiated coupon. This indicates that significant cobalt dissolution has occurred and that the chromium oxide has become more saturated with Co^{II} (and possibly converted to CoCr₂O₄ and Co(OH)₂ at the outer layer) on the Stellite-6 coupons corroded at pH 8.4 under irradiation.

The O/(Co + 1.5 Cr) and Co/(Co+Cr) ratios on the surfaces corroded at pH 10.6 with irradiation show distinctly different depth profiles from those observed under other conditions. The Co/(Co+Cr) ratio near the surface (< 3 nm) is nearly constant and approximately twice that of the bulk alloy. The corresponding O/(Co + 1.5 Cr) ratio is also

high (~1.4). The high Co/(Co+Cr) ratio indicates that the oxygen in the outermost layer is mainly bound to cobalt, and the high O/(Co + 1.5 Cr) ratio indicates that the cobalt oxide is in the form of a hydrated species, Co(OH)₂ or CoOOH, consistent with the XPS results. At depths of 4 nm – 9 nm, both Co/(Co+Cr) and O/(Co + 1.5 Cr) decrease until the O/(Co + 1.5 Cr) ratio reaches 1.0 at ~9 nm. This behaviour is attributed to a gradual change in the nature of the oxide from mostly Co(OH)₂ to mostly CoO. The high Co/(Co+Cr) and O/(Co + 1.5 Cr) ratios of this region also suggest that no significant cobalt dissolution occurred during oxidation and the oxidized cobalt was incorporated into the oxide layer.

5.3.4 ICP-MS Results

The amount of Co dissolved into the solution after each 3-d exposure experiment was determined by ICP-MS; see results in Table 5.2. The Co level in the corrosion test solutions was below the instrument detection limit (0.2 µg·L⁻¹) after tests at all three pHs in the absence of radiation. For the coupons corroded in the presence of radiation, the Co level was below the detection limit at pH 10.6, while it was 5 µg·L⁻¹ and 6 µg·L⁻¹ at pH 8.4 and 6.0, respectively. These levels are below the Co^{II} solubility limits at these pH values [29]. The most cobalt dissolution occurred at pH 6.0 where the thinnest oxide layer was observed. Cobalt dissolution was negligible at pH 10.6 where Co^{II} solubility is near its minimum [27,29] and the thickest oxide was observed.

Table 5.2: Dissolved cobalt content after 3-d corrosion.

Cobalt content at 25 °C ($\mu\text{g}\cdot\text{L}^{-1}$)		
pH	No Rad	Rad
6.0	< DL ¹	6.0
8.4	< DL	5.0
10.6	< DL	< DL

1. Detection limit

5.3.5 Summary of the Corrosion Study

Corrosion of Stellite-6 in a deaerated solution with and without radiation involves mainly cobalt oxidation. Negligible chromium oxidation occurs. The cobalt oxidation results in either dissolution or oxide growth, or both. In the absence of radiation, the total cobalt oxidation, the sum of dissolution and oxide growth, is small. Gamma-irradiation increases the cobalt oxidation at all three pH values. At pH 6.0 the oxidized cobalt is mainly dissolved into solution, whereas at pH 10.6, where Co^{II} solubility is near its minimum, the oxidation of cobalt results mainly in oxide growth.

5.4 ELECTROCHEMICAL EXPERIMENTS

The coupon corrosion study clearly demonstrates that γ -irradiation has a significant effect on Stellite-6 corrosion and that the effect varies with pH. To obtain kinetic information, E_{corr} measurements in the absence or presence of radiation and potentiostatic polarization experiments were performed.

5.4.1 Corrosion Potential Measurements

Figure 5.5 shows the corrosion potential (E_{corr}) measured on a Stellite-6 working electrode during corrosion in the absence and presence of radiation. No E_{corr} measurements were performed at pH 6.0 with irradiation because a reference electrode that is stable under both acidic and irradiation conditions could not be found. The measurements at higher pHs show that γ -irradiation has a big impact on E_{corr} . In the absence of radiation E_{corr} quickly rises to a (pseudo-) steady-state value, ranging from $-0.6 V_{\text{SCE}}$ to $-0.5 V_{\text{SCE}}$ depending on pH. In the presence of radiation E_{corr} rises to approximately $-0.45 V_{\text{SCE}}$ within a few min followed by a slower increase before reaching a steady state value near $0.1 V_{\text{SCE}}$. The rate of increase is faster at pH 10.6 than at pH 8.4. To explain the change in E_{corr} with time requires an understanding of the oxidation kinetics as a function of potential, as provided in Section 5.5.

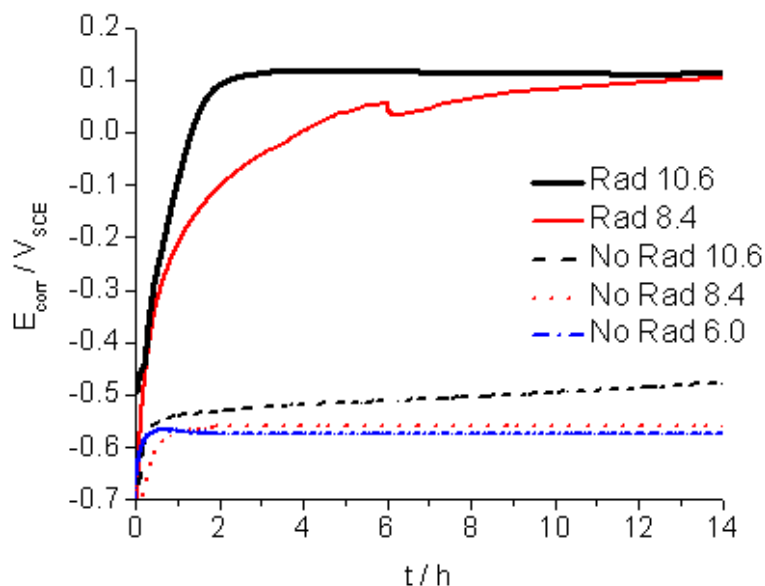


Figure 5.5: E_{corr} as a function of time recorded on the Stellite-6 electrodes with (—) and without (----) γ -irradiation at different pHs.

5.4.2 Potentiostatic Polarization Experiments

5.4.2.1 Long-term steady-state current behaviour

To obtain the cobalt oxidation rate as a function of an E_{corr} that is changing with time a series of potentiostatic polarization experiments were performed at fixed potentials (E_{APP}) in a range encompassing the E_{corr} values observed with and without irradiation. The current is a direct measure of the rate of electrochemical redox reactions occurring on the working electrode, but the current density, i , that we measured on Stellite-6 in our tests, particularly at long times, is very small ($< 0.05 \mu\text{A}\cdot\text{cm}^{-2}$) and barely above the background noise level. The signal-to-noise ratio is improved by measuring the total charge accumulated as a function of

time. The slope of the rate of change of the charge $i = dQ/dt$ is then used to provide a more accurate current value, particularly at long times when the system is at steady state. The polarization experiments were performed at three pH values are shown in Figure 5.6.

At E_{APP} below about $-0.2 V_{SCE}$ (at pH 8.4) the long-term behaviour of Q shows a near-linear decrease with time; that is, the net current after about 1 h is cathodic and nearly constant. This steady-state current, i_{SS} , is present at all pH values, albeit at different levels. A cathodic current indicates that Stellite-6 can support electrolytic reduction of water to H_2 at these potentials. In an electrochemical cell, metal oxidation typically occurs on the alloy working electrode while reduction of aqueous species typically occurs on the counter electrode. However, in our tests electrolytic water reduction is efficient on the Stellite-6 working electrode at low applied potentials, despite the presence of a presumably passive oxide layer on the metal (initially Cr_2O_3 and later $CoCr_2O_4$ and/or $Co(OH)_2$). Note that these oxides are p-type semiconductors with band gaps of 4.7-5.0, 3.4 and 2.4 eV, respectively [34–36].

The presence of a steady-state cathodic current shows that while these oxides may be passive in terms of ionic conductivity, they do not suppress electronic conductivity. Due to the water reduction process, the rate of cobalt oxidation occurring at the same time (the anodic current component) cannot be extracted from the net measured current. For the same reason, electrochemical impedance spectra (EIS) performed at $E_{APP} \leq -0.2 V_{SCE}$ did not provide meaningful information on the oxide film resistance. Nevertheless, since the rates of cobalt oxidation and water reduction depend on the thickness of the oxide layer that is

present, the net current provides useful information on oxide growth kinetics. A kinetic analysis that is relevant to the current study is presented here.

The time-dependent behaviour of Q measured during potentiostatic polarization shows that there are potential regions with different characteristics associated with the short-term behaviour of Q and the slope of $\log |i_{SS}|$ vs E_{APP} with time (Figure 5.6). At pH 8.4 these potential regions are:

Region 0 ($E \leq -0.8 V_{SCE}$). In this region there is only a cathodic current, indicating that the surface is electronically conductive and that the potential on the surface is not high enough for metal oxidation. The log of the cathodic current ($\log |-i_{SS}|$) decreases linearly with E_{APP} .

Region I ($-0.8 V_{SCE} < E_{APP} \leq -0.6 V_{SCE}$). In this region Q is initially positive and small. The duration of positive Q increases with E_{APP} , the steady-state current is cathodic, and $\log |-i_{SS}|$ decreases linearly with E_{APP} with a Tafel slope of approximately $-160 \text{ mV} \cdot \text{dec}^{-1}$.

Region II ($-0.5 V_{SCE} \leq E_{APP} \leq -0.2 V_{SCE}$). In this region the initial increase in Q is nearly independent of E_{APP} , the steady-state current remains cathodic and its magnitude decreases with increasing E_{APP} . There is a discontinuity in the decrease in $\log |-i_{SS}|$ at the boundary between Regions I and II.

Region III ($-0.1 V_{SCE} \leq E_{APP} \leq +0.2 V_{SCE}$). In this region there is an initial sharp rise in Q and a subsequent slower increase in Q that depends on E_{APP} . The $\log |-i_{SS}|$ does not show a linear relationship with E_{APP} . At $E_{APP} > -0.2 V_{SCE}$ $|i_{SS}|$ becomes very small because the

potential is too high to support water reduction but too low to support metal oxidation as the oxide layer thickens with time.

Region IV ($+0.2 V_{SCE} \leq E_{APP}$). In this region, after an initially rapid rise, Q continues to increase with time at a slower rate and the current, i_{SS} , is positive.

Similar potential regions can be identified from the polarization data obtained at other pHs, but the boundaries of the regions differ by small amounts. The results are summarized in Table 5.3.

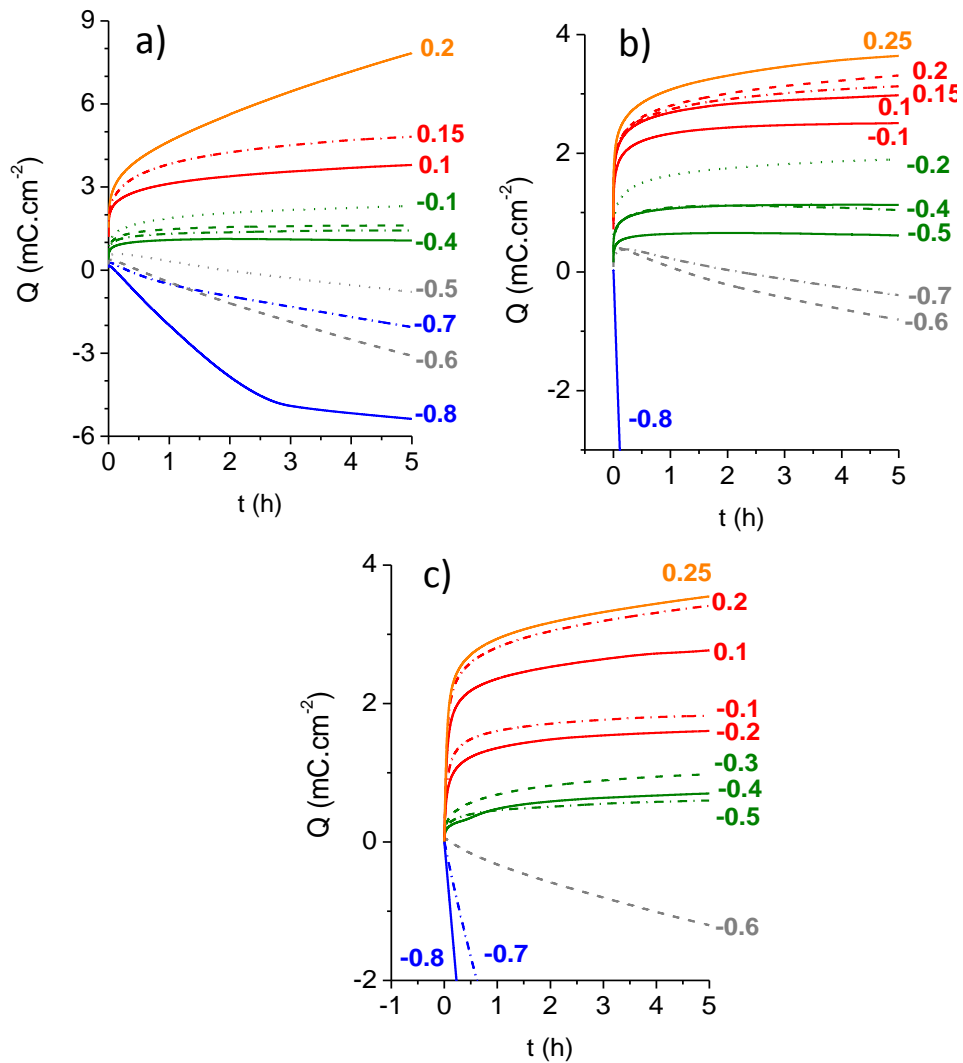


Figure 5.6: Net charge, Q , accumulated as a function of time during potentiostatic polarization at pH a) 10.6, b) 8.4, c) 6.0. The numbers in the figure represent the applied potential, E_{APP} . The Roman numerals represent different oxide growth regions as summarized in Table 5.3. Different colors and styles differentiate four regions.

Table 5.3: Summary of the potentiostatic polarization experiments.

Potential Region	0 and I		II	III
Potential Range (V_{SCE})				
pH 6.0	$-0.60 < E \leq -0.20$	ND ¹	$-0.50 \leq E \leq -0.30$	$-0.2 \leq E \leq 0.00$
pH 8.4	$-0.65 < E \leq -0.55$	$-0.80 \leq E \leq -0.60$	$-0.50 \leq E \leq -0.20$	$-0.1 \leq E \leq 0.2$
pH 10.6	ND	$-0.80 \leq E \leq -0.50$	$-0.40 \leq E \leq +0.00$	$+0.1 \leq E \leq 0.2$
Net Results				
Oxidation Products ²	$Co^{2+}(aq)$	$Co^{2+}(aq)$ $CoCr_2O_4$	$Co^{2+}(aq)$ $CoCr_2O_4$ $CoO/Co(OH)_2$	$Co^{2+}(aq)$ $CoCr_2O_4$ $CoO/Co(OH)_2$ $Co_3O_4/CoOOH$ H
Outer Surface (at long times)	Defective Cr_2O_3 with a Co^{II} gradient	$CoCr_2O_4$	$CoO/Co(OH)_2$	$CoO/Co(OH)_2$ $Co_3O_4/CoOOH$ H

1. Not determined due to lack of clear changes in the time-dependent behaviour of Q .

2. The relative yields of different corrosion products depend on pH.

The boundaries of the characteristic potential ranges are typically 0.05 to 0.1 V higher than the electrochemical equilibrium potentials of various cobalt oxidation reactions. The equilibrium potentials, E_{eq} , for those reactions were calculated as a function of pH using thermodynamic data [37] and are shown in Figure 5.7. For the equilibrium potentials involving $Co^{2+}(aq)$, the E_{eq} values of two different concentrations (10^{-9} and 10^{-6} M) are shown since $E_{eq}(Co \rightleftharpoons Co^{2+}(aq))$ may change due to cobalt dissolution as corrosion

progresses. The equilibrium potential for the oxidation of Cr^{III} to soluble Cr^{VI} is higher than $0.25 \text{ V}_{\text{SCE}}$ at pH 10.6, the top end of the E_{corr} range observed in this study, and hence is not included in the figure. A comparison of the potential ranges of the regions (Table 5.3) with the equilibrium potentials (Figure 5.7) indicates that the characteristic dependence of i_{SS} on E_{APP} in each region arises from the nature of the oxide layer formed at the very early stages of polarization.

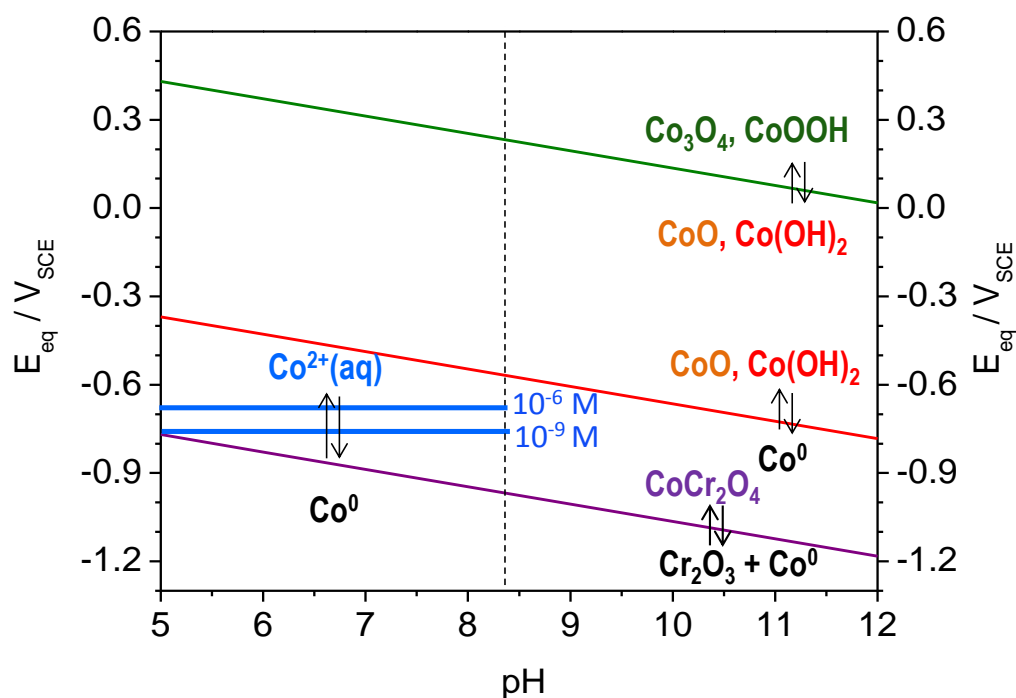


Figure 5.7: Calculated equilibrium potentials for cobalt oxidation reactions at different pH values at $25 \text{ }^{\circ}\text{C}$. In calculating the equilibrium potential for the oxidation to $\text{Co}^{2+}(\text{aq})$, two concentrations of $\text{Co}^{2+}(\text{aq})$ (10^{-6} and 10^{-9} M) were used. Vertical dashed line indicates pH 8.4.

At pH 6.0, where Co^{II} solubility is highest, cobalt oxidation occurs at potentials $> -0.60 \text{ V}_{\text{SCE}}$, close to $E_{\text{eq}}(\text{Co} \rightleftharpoons \text{Co}^{2+}(\text{aq}))$. At pH 6.0, Region II is absent and Region I is

extended to $-0.2 V_{SCE}$ (Table 4.3). At potentials below $-0.2 V_{SCE}$, all of the cobalt oxidation leads to cobalt dissolution since the rate of oxide formation is too slow to compete with the rate of dissolution (see further discussion in Section 4.5). Any measurable oxide formation occurs only at potentials $> -0.2 V_{SCE}$ (Region III) but in this region oxide formation is still at a low rate.

At pH 10.6 where Co^{II} solubility is near its minimum, Region I is not observed, i.e., oxidation requires a potential greater than $-0.6 V_{SCE}$, above which all of the cobalt oxidation leads to oxide formation (Table 3). At potentials below about $-0.5 V_{SCE}$, a value slightly above $E_{eq}(Co \rightleftharpoons CoO/Co(OH)_2)$ (Region II), the oxidation is limited to formation of $CoCr_2O_4$. At higher potentials (Region III) $CoO/Co(OH)_2$ also forms. At potentials higher than $+0.1 V_{SCE}$ (Region IV), oxidation of the Co^{II} oxides to $Co^{II/III}$ and Co^{III} oxides occurs, and oxidation of Cr^{III} to Cr^{VI} occurs at potentials $\geq +0.25 V_{SCE}$, $E_{eq}(Cr^{III} \rightleftharpoons Cr^{VI})$ (not listed in Table 3).

At the intermediate pH value of 8.4 the rate of dissolution is lower than that at pH 6.0 and hence the rate of oxide formation becomes comparable with the rate of dissolution at modest potentials. At potentials between $-0.65 V_{SCE}$ (slightly above $E_{eq}(Co \rightleftharpoons Co^{2+}(aq))$) and $-0.55 V_{SCE}$ (slightly above $E_{eq}(Co \rightleftharpoons CoO/Co(OH)_2)$) all cobalt oxidation leads to dissolution, similar to what was observed in Region I at pH 6.0. In Regions II, III and IV the oxide formation at pH 8.4 is similar in character to that at pH 10.6, but it occurs at a lower rate. The oxidation products and the outer surface formed during polarization at a potential in each region are summarized in Table 5.3.

The results indicate that the long-term behaviour of Q vs. time is closely linked to the type of oxide that is formed under potentiostatic conditions. Once a coherent oxide film is developed, cobalt cation transport through that film is suppressed. Cobalt dissolution requires surface hydration of a cobalt ion from the oxide lattice followed by aqueous diffusion of the hydrated ion into the bulk electrolyte. Consequently, the dissolution rate over the long term depends strongly on the type of oxide on the outer surface and its ability to be hydrolysed. Oxide formation can take a long time, during which the rate of metal dissolution may be very different from that at a long-term steady state. The dissolution occurring during the transient period can be substantial and the duration of this transient period depends strongly on pH and the presence of radiation.

5.4.2.2 Short-term current behaviour

The influence of pH on the current can be seen in Figure 5.8 where the polarization results are presented in $\log i$ versus $\log t$ plots to show the short-term behaviour more clearly. As noted above, the oxidation kinetics during the initial transient period are affected by water reduction at $E_{APP} \leq -0.2 V_{SCE}$. Thus, only the results obtained at $E_{APP} \geq 0.0 V_{SCE}$ are presented in Figure 5.8. The current observed in the first 1 s is affected by the initial charge distribution on the working electrode surface (more pronounced at higher pHs due to faster accumulation of metal cations) and hence, is not considered. At pH 8.4 and 10.6, the magnitude of the current decreases nearly linearly for longer than one hour (the slope of $\log i$ vs $\log t$ is about -1), indicating the growth of a passive oxide. At pH 6.0, the current is initially high and nearly constant with time before it decreases sharply to reach a lower

steady-state value. As discussed above, the current values at these times can be obtained better from a Q vs. t plot.

The initially constant current at pH 6.0 suggests that cobalt oxidation is not impeded at first. The high current values show that the rate of cobalt dissolution from the initially defective Cr_2O_3 layer is high at this pH. Due to the high dissolution rate, the surface changes its oxide characteristics slowly, if at all, and the current is nearly constant with time. Nevertheless, a small fraction of the cobalt oxidation leads to oxide formation, albeit at a slow rate. The slow oxide formation causes the very slow decrease in current that is seen. The sharp decrease in current that follows the nearly constant current period can then be attributed to the eventual formation of a uniform and compact passivating layer of Co^{II} oxides (CoCr_2O_4 and/or $\text{CoO}/\text{Co}(\text{OH})_2$). This explains why the duration of the period with nearly constant current is shorter at a higher E_{APP} ; the protective oxide is formed faster at higher potentials. The final steady-state current, i_{SS} , represents the dissolution current from a Co^{II} -covered Stellite-6 surface. At pH 6.0, in high E_{CORR} environments, cobalt dissolution from the initially defective Cr_2O_3 -covered surface at early stages of corrosion contributes significantly to the total amount of dissolved cobalt.

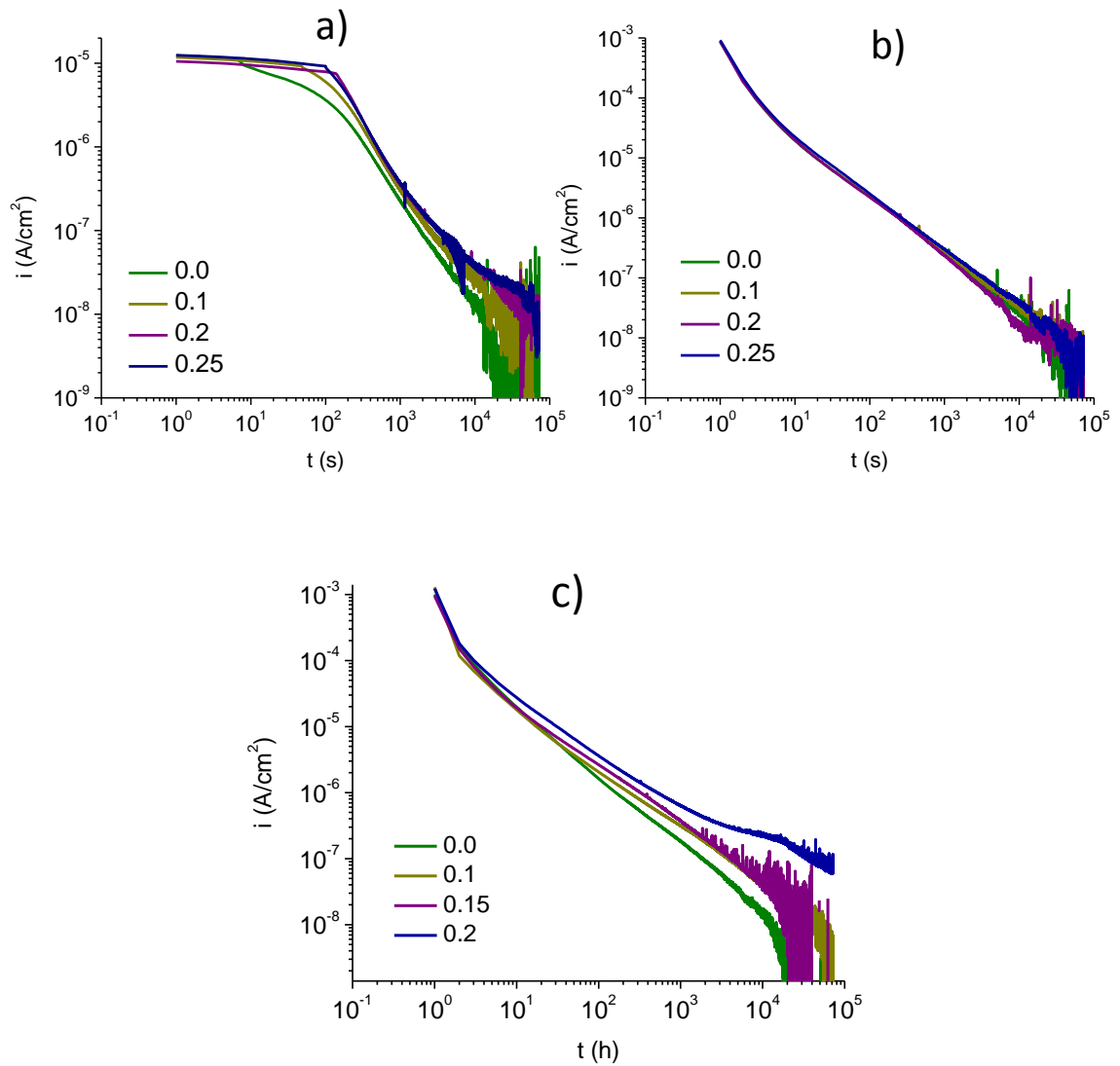


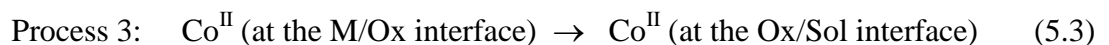
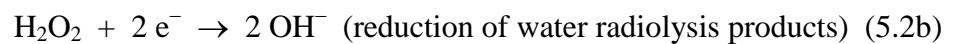
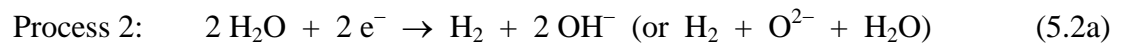
Figure 5.8: Current density observed as a function of time during potentiostatic polarization at $E_{APP} > 0.0$ V_{SCE} at a) pH 6.0, b) pH 8.4, and c) pH 10.6.

5.5 CORROSION KINETIC MECHANISM

5.5.1 General Corrosion Kinetic Mechanism

Aqueous corrosion is an electrochemical process involving two redox half-reactions, metal oxidation coupled with reduction of an aqueous species [38,39]. In the presence of a uniform oxide layer, the metal oxidation occurs at the metal/oxide (M/Ox) interface (referred to as Process 1) whereas the reduction of aqueous species occurs at the oxide/solution (Ox/Sol) interface (Process 2). In order to complete the electrochemical reaction, a net flux of metal cations must proceed from the M/Ox interface to the Ox/Sol interface (Process 3). The metal cations can combine with oxygen anions (O^{2-} or OH^-) to form metal oxides or hydroxides (Process 4), or they can dissolve into the solution from the Ox/Sol interface (Process 5) [38,39]. These processes are schematically presented in Figure 5.9.

We can thus propose that corrosion of Stellite-6 with an insoluble but defective chromium oxide layer consists of similar steps:



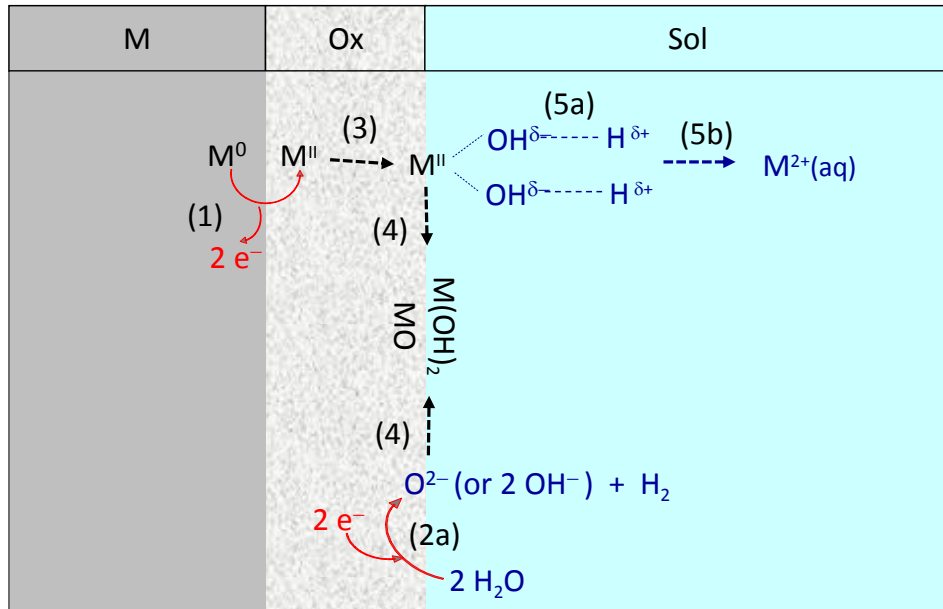
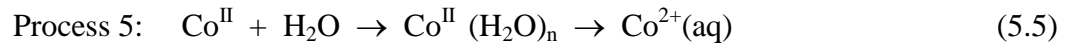


Figure 5.9: Schematic illustration of corrosion reactions in the presence of an oxide layer. Five distinct processes are numbered on the diagram: (1) metal oxidation, (2a) water reduction, (3) mass transport across the existing oxide, (4) oxide growth, and (5a and b) metal cation hydration and dissolution.

Process 4 (sum of reactions 5.4a and 5.4b) and Process 5 occur in parallel, albeit at different rates, whereas Processes 1, 2, 3 and the sum of 4 and 5 occur in series. That is, cobalt dissolution (Process 5) competes with oxide formation (Process 4) whereas the slowest of the process in series dictates the oxidation rate. Process 3 represents the net flux of metal cations from the M/Ox to the Ox/Sol interface. To account for the cation flux through a solid

oxide lattice, many mechanisms, such as transport via interstitials, cation and anion vacancies and electron hopping (or ion exchanges), have been proposed, and these different mechanisms have been incorporated into different corrosion kinetic models, such as a point defect model and a mixed conduction model [32,40–42]. Our experimental data cannot differentiate between the possible options. However, our results are consistent with the expectations arising from macroscopic reaction kinetics and transport rate equations consisting of the elementary steps, and mass and charge balance requirements for the rate equations.

These requirements dictate that (a) the rate of total cobalt oxidation (Process 1) must be equal to the rate of total reduction of aqueous species (Process 2), (b) these electrochemical reaction rates (oxidation and reduction) must be equal to the rate of cobalt cation migration across the oxide layer (Process 3), irrespective of the nature of the migrating species, and (c) these rates must be equal to the sum of the rates of cobalt oxide formation (Process 4) and cobalt dissolution (Process 5). That is, the total rate of reactions in parallel is the sum of those rates, while the slowest process of the reactions in series dictates the oxidation rate. Thus, for corrosion of Stellite-6,

$$\text{Net Rate} = \text{Rate (1)} = \text{Rate (2)} = \text{Rate (3)} = \text{Rate (4)} + \text{Rate (5)} \quad (5.6)$$

where Rate (2) represents the sum of the rates of reactions (2a) and (2b) and Rate (4) represents the sum of the rates of reactions (5.4a) and (5.4b).

The rates of the individual reactions can be described using bulk-phase reaction and transport kinetics. For example, since Processes (1) and (2) are electrochemical reactions

and their rates can be described by corresponding Butler-Volmer equations [38]. The rate of ion transport, Process (3), can be described by a modified Nernst-Planck equation, and so on. Irrespective of these differences, at any given time all the rates must adhere to the mass and charge balance requirements specified in Equation (5.6). An example of the relationships between different rates is schematically presented in Figure 5.10.

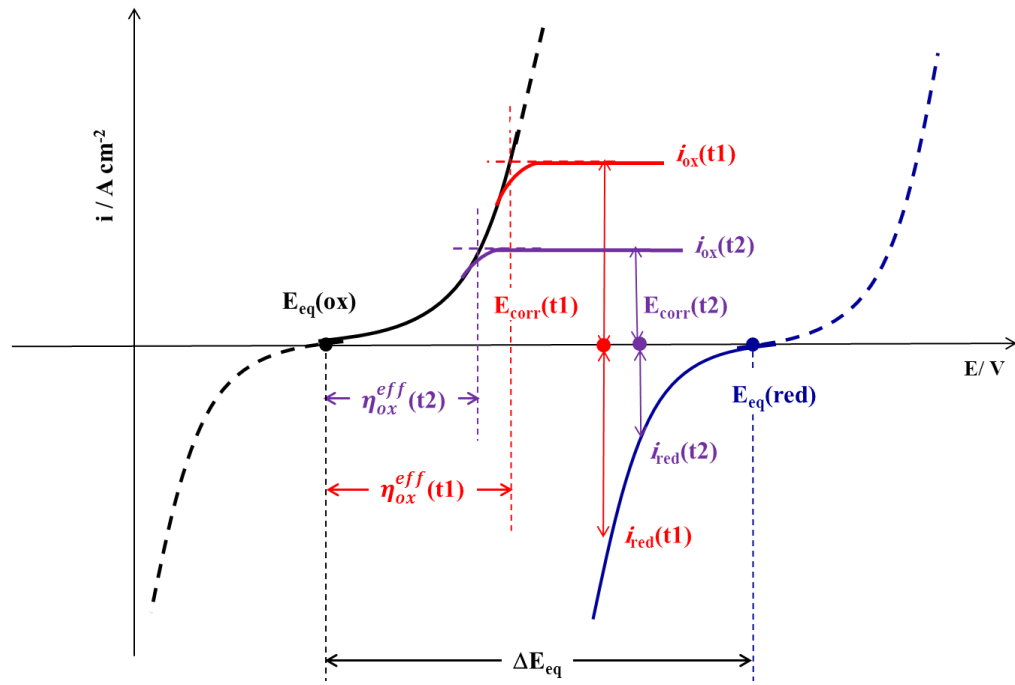


Figure 5.10: Schematic diagram showing the relationship between the energetics and kinetics of the corrosion half-reactions taking place on an oxide-covered metal surface.

In this figure, the rates are represented by currents and only their dependences on potential are considered. The presence of an oxide layer decreases the effective overpotential for oxidation, η_{ox}^{eff} , since charged species must transport across the oxide layer. Since the charge transport rate decreases with oxide thickness, two different rates ($i_{ox}(t1)$ and $i_{ox}(t2)$),

representing two different times, are shown. Figure 5.10 also shows schematically what would happen to E_{corr} when an oxide layer thickens even though the aqueous redox environment does not change. Although Processes (1) and (2) involve the same redox species, as the oxide grows the rate of Process (3) decreases, decreasing $\eta_{\text{ox}}^{\text{eff}}$. This decreases the rate of Process (1) and accordingly the rate of Process (2) must also decrease. This increases E_{corr} , as we observed at pH 10.6 in the absence of radiation. The observed oxide growth and E_{corr} as a function of pH and the oxidation current as a function of E_{APP} during potentiostatic polarization can then be rationalized by how the experimental parameters affect the individual reaction rates, and hence the corrosion rate.

5.5.2 Effects of pH and γ -Radiation on Corrosion Kinetics

5.5.2.1 Effect of pH in the absence of radiation

In the absence of radiation, the aqueous chemical environment in an Ar-purged electrochemical cell does not change as corrosion progresses. No oxidizing chemicals, such as O_2 or H_2O_2 , are introduced into the water phase and the concentrations of dissolved corrosion products are very small due to the large ratio of the solution volume to the Stellite-6 surface area. If there is no change in the surface reactivity (i.e., no change in the nature or thickness of the oxide layer), the corrosion rate and E_{corr} should remain constant with time. Indeed this is what we observe at pH 6.0 and 8.4. At pH 6.0, in the absence of radiation, the E_{corr} value in deaerated solutions is low and lies just above $E_{\text{eq}}(\text{Co} \rightleftharpoons \text{Co}^{2+}(\text{aq}))$ (Process 5). The large Co^{II} solubility at this pH facilitates aqueous diffusion of $\text{Co}^{2+}(\text{aq})$. The cobalt oxidation (Process 1) does not require a large overpotential to keep up with the rate of water

reduction (Process 2a) at this potential. The E_{corr} value is also higher than E_{eq} for the oxidative conversion of Cr_2O_3 to CoCr_2O_4 (reaction 5.4a), but this process requires a physical rearrangement of the oxide structure (chemical bond and solid lattice formation). The potential energy barrier for such a rearrangement makes the oxide formation process slower than the oxidative dissolution of cobalt at room temperature. Thus, at pH 6.0, in the absence of radiation, the oxidized cobalt exclusively takes the dissolution path, i.e., Rate (4a) \ll Rate (5). Under these conditions, Rate (1) = Rate (3) \approx Rate (5), there is no oxide growth and no surface change occurs as corrosion progresses. The rate of cobalt dissolution is, however, small due to a low water reduction rate in deaerated solutions. The value of E_{corr} also remains constant as corrosion progresses (Figure 5.5).

Compared to pH 6.0, cobalt solubility at pH 8.4 is more than two orders of magnitude lower [29] but not negligible. The Co^{II} oxide formation (Process 4) at this pH can compete better with dissolution, particularly at a higher potential. In the absence of radiation, the oxidation rate in deaerated water is still low and cobalt dissolution is still faster than oxide formation. Accordingly, the formation of Co^{II} oxides (as CoCr_2O_4 or $\text{Co}(\text{OH})_2$) is small, consistent with the XPS and AES analyses of the coupons after 3 d of corrosion (Tables 5.1 and 5.2 and Figure 5.4). The E_{corr} value at pH 8.4 is similar to that observed at pH 6.0, close to the upper limit of Region I (Table 5.3), and only slightly higher than $E_{\text{eq}}(\text{Co} \rightleftharpoons \text{Co}^{2+}(\text{aq}))$. The electrochemical potential of deaerated water is not oxidizing enough to put the corroding system into Region II. At pH 10.6, the (pseudo-) steady-state E_{corr} increases slowly, even in the absence of radiation. The slow increase, despite a constant aqueous environment and hence a constant driving force, is thus attributed to oxide growth which makes the surface

increasingly more passive. At pH 10.6, where the Co^{II} solubility is at its minimum (and more than seven orders of magnitude lower than the solubility at pH 6.0), the dissolution rate of Co^{II} (Process 5) is negligible and hence Rate (4) \gg Rate (5), and Rate (1) = Rate (3) \approx Rate (4). This is consistent with the absence of Region I at pH 10.6 (Table 5.3). At pH 10.6, the oxidized cobalt ions can grow a coherent oxide phase. This oxide growth decreases the effective overpotential for oxidation, $\eta_{\text{ox}}^{\text{eff}}$, decreasing the net metal oxidation rate (i_{ox}), and accordingly E_{corr} increases as corrosion progresses (Figure 5.10). We see the growth of a thicker oxide layer at this pH (Figure 5.4) and negligible cobalt dissolution (Table 5.2). The E_{corr} value at this pH is now in Region II where the oxidation of Co to CoCr_2O_4 occurs (Table 5.3).

5.5.2.2 Combined effects of radiation and pH

In the presence of ionizing radiation, ΔE_{eq} increases due to the radiolytic production of redox active species, particularly H_2O_2 . The equilibrium potential for H_2O_2 reduction (reaction 5.2b) is significantly higher than that of water reduction (reaction 5.2a), thus increasing ΔE_{eq} . The increase in ΔE_{eq} leads to an increase in the overpotential, η_{ox} , for cobalt oxidation (Figure 5.9). Under continuous γ -irradiation, water radiolysis products reach pseudo steady state on a very short time scale (within a few ms) [16,18]. Any change in E_{corr} occurring on a minutes to hour time scale is not due to a change in aqueous environment caused by radiation, but is due to slowing interfacial reaction kinetics caused by gradual oxide growth.

Figure 5.5 shows that after an initial jump to a value about $-0.45 V_{SCE}$, E_{corr} increases more slowly at pH 10.6 for about 20 min. The $-0.45 V_{SCE}$ potential is at the boundary between potential Regions II and III (Table 5.3). The near constant potential indicates that the oxidation process involved during this time scale is not limited by an interfacial charge transfer process but by another parameter, such as the limited quantity of Cr_2O_3 that is initially present on the Stellite surface. The pause in the change of E_{corr} with time is attributed to the time required for conversion of Cr_2O_3 to $CoCr_2O_4$. This is also the time required to reach the maximum Q during polarization at potentials in Region II at pH 10.6. Once all of the Cr_2O_3 initially present on the surface has been converted to $CoCr_2O_4$, an outer layer of $CoO/Co(OH)_2$ starts to grow. The growth of these oxides explains the time-dependent behaviour of E_{corr} observed at pH 10.6. After the initial Cr_2O_3 is consumed E_{corr} increases to a final steady-state value of about $+0.1 V_{SCE}$. This final value is at the boundary between Regions III and IV where Co^{II} oxides can convert to $Co^{II/III}$ or Co^{III} oxides, but Cr^{III} cannot oxidize to Cr^{VI} .

The slower increase in E_{corr} at pH 8.4 than at pH 10.6 (Figure 5.5) is due to a higher rate of cobalt dissolution at the lower pH (Process 5). This slows the of $CoCr_2O_4$ and $CoO/Co(OH)_2$ (Process 4). Compared to the coupons corroded in the absence of radiation, the irradiated surfaces at pH 8.4 have a thicker oxide. At pH 6.0, even in the presence of radiation, the rate of cobalt dissolution dominates and oxide formation is negligible.

5.6 CONCLUSIONS

We have performed a comprehensive study of the corrosion of Stellite-6 as a function of pH and solution redox conditions at room temperature. Cobalt oxidation during corrosion leads to two competing processes, oxide growth and cobalt dissolution. The solution redox state affects primarily the net cobalt oxidation rate while pH affects primarily the metal dissolution rate. These are two competing rates and the faster of the two determines the main corrosion pathway. The main pathway at pH 6.0 is dissolution, both in the presence and absence of radiation, whereas the main pathway at pH 10.6 is oxide formation. At pH 8.4, the main pathway is dissolution in the absence of radiation, but oxide formation becomes comparable in rate to cobalt dissolution in the presence of radiation. The presence of ionizing radiation causes the corrosion potential of the system to rise substantially due to radiolytic production of oxidizing species such as H_2O_2 . This increases the total cobalt oxidation rate. At pH 6.0, the increase in oxidation results only in increased cobalt dissolution. At pH 10.6 the presence of radiation leads to formation of a thicker oxide and the dissolution rate remains negligible. These results give us information that can be used to predict Stellite-6 corrosion rates over a range of conditions and, especially, to predict cobalt dissolution rates under different conditions, an ability of particular value to the nuclear industry.

5.7 REFERENCES

- [1] C. Maffiotte, M. Navas, M.L. Casta, XPS characterization of oxide films formed in cobalt-based alloys during corrosion tests at high temperature, *Surf. Interface Anal.*, 166 (2000) 161–166.
- [2] V. Kuzucu, M. Ceylan, H.C. Aksoy, Microstructure and phase analyses of Stellite 6 plus 6 wt.% Mo alloy, *J. Mater. Process. Technol.*, 69 (1997) 257–263.
- [3] W.H. Hocking, F.W. Stanchell, E. McAlpine, D.H. Lister, Mechanisms of corrosion of Stellite-6 in lithiated high temperature water, *Corros. Sci.*, 25 (1985) 531–557.
- [4] U. Malayoglu, A. Neville, Mo and W as alloying elements in Co-based alloys – their effects on erosion–corrosion resistance, *Wear*, 259 (2005) 219–229.
- [5] C.C. Lin, A review of corrosion product transport and radiation field buildup in boiling water reactors, *Prog. Nucl. Energy*, 51 (2009) 207–224.
- [6] W.G. Burns, W.R. Marsh, W.S. Walters, The γ irradiation-enhanced corrosion of stainless and mild steels by water in the presence of air, argon and hydrogen, *Radiat. Phys. Chem.*, 21 (1983) 259–279.
- [7] H.C. Studsvik, M. Ab, Current state of knowledge of water radiolysis effects on spent nuclear fuel, *Corrosion*, 131 (2000) 102–123.
- [8] V. Čuba, R. Silber, V. Můčka, M. Pospíšil, S. Neufuss, J. Bárta, A. Vokál, Radiolytic formation of ferrous and ferric ions in carbon steel – deaerated water system, *Radiat. Phys. Chem.*, 80 (2011) 440–445.
- [9] R.S. Glass, G.E. Overturf, R.A. Van Konynenburg, R.D. McCright, Gamma radiation effects on corrosion – I. Electrochemical mechanisms for the aqueous corrosion processes of austenitic stainless steels relevant to nuclear waste disposal in tuff, *Corros. Sci.*, 26 (1986) 577–590.
- [10] Q.W. Knapp, J.C. Wren, Film formation on type-316L stainless steel as a function of potential: Probing the role of gamma-radiation, *Electrochim. Acta*, 80 (2012) 90–99.
- [11] J. Busby, G. Was, E. Kenik, Isolating the effect of radiation-induced segregation in irradiation-assisted stress corrosion cracking of austenitic stainless steels, *J. Nucl. Mater.*, 302 (2002) 20–40.
- [12] K. Daub, X. Zhang, J.J. Noël, J.C. Wren, Gamma-radiation-induced corrosion of carbon steel in neutral and mildly basic water at 150 °C, *Corros. Sci.*, 53 (2011) 11–16.
- [13] IAEA Nuclear Energy Series, Stress Corrosion Cracking in Light Water Reactors: Good Practices and Lessons Learned, International Atomic Energy Agency, Vienna, 2011.
- [14] B.G. Ershov, A.V. Gordeev, A model for radiolysis of water and aqueous solutions of H₂, H₂O₂ and O₂, *Radiat. Phys. Chem.*, 77 (2008) 928–935.
- [15] J.A. Laverne, OH radicals and oxidizing products in the gamma radiolysis of water, *Radiat.*, 153 (2014) 196–200.
- [16] J.M. Joseph, B.S. Choi, P.A. Yakabuskie, J.C. Wren, A combined experimental and model analysis on the effect of pH and O₂(aq) on γ -radiolytically produced H₂ and H₂O₂, *Radiat. Phys. Chem.*, 77 (2008) 1009–1020.

- [17] P.A. Yakabuskie, J.M. Joseph, J.C. Wren, The effect of interfacial mass transfer on steady-state water radiolysis, *Radiat. Phys. Chem.*, 79 (2010) 777–785.
- [18] J.C. Wren, Steady-State Radiolysis: Effects of Dissolved Additives, in: B.J.M. , C.M. Wai (Ed.), *Nucl. Energy Environ., ACS Symposium Series*, 2010: pp. 271–295.
- [19] K. Daub, X. Zhang, J.J. Noël, J.C. Wren, Effects of γ -radiation versus H_2O_2 on carbon steel corrosion, *Electrochim. Acta*, 55 (2010) 2767–2776.
- [20] W.A. Badawy, Electrochemical behaviour of cobalt in aqueous solutions of different pH, *J. Applied Electrochem.*, 30 (2000) 693–704.
- [21] K. Daub, X. Zhang, L. Wang, Z. Qin, J.J. Noël, J.C. Wren, Oxide growth and conversion on carbon steel as a function of temperature over 25 and 80°C under ambient pressure, *Electrochim. Acta*, 56 (2011) 6661–6672.
- [22] M.X. Yao, J.B.C. Wu, Y. Xie, Wear, corrosion and cracking resistance of some W- or Mo-containing Stellite hardfacing alloys, *Mater. Sci. Eng. A*, 407 (2005) 234–244.
- [23] F. Rosalbino, G. Scavino, Corrosion behaviour assessment of cast and HIPed Stellite 6 alloy in a chloride-containing environment, *Electrochim. Acta*, 111 (2013) 656–662.
- [24] U. Malayoglu, A. Neville, H. Lovelock, Assessing the kinetics and mechanisms of corrosion of cast and HIPed Stellite 6 in aqueous saline environments, *Corros. Sci.*, 47 (2005) 1911–1931.
- [25] X. Zhang, Y. Li, N. Tang, E. Onodera, A. Chiba, Corrosion behaviour of CoCrMo alloys in 2 wt.% sulphuric acid solution, *Electrochim. Acta*, 125 (2014) 543–555.
- [26] N.S. McIntyre, D. Zetaruk, E.V. Murphy, X-ray photoelectron spectroscopic study of the aqueous oxidation of Stellite-6 alloy, *Surf. Interface Anal.*, 1 (1979) 105–110.
- [27] M. Behazin, M.C. Biesinger, J.J. Noël, J.C. Wren, Comparative study of film formation on high-purity Co and Stellite-6: Probing the roles of a chromium oxide layer and gamma-radiation, *Corros. Sci.*, 63 (2012) 40–50.
- [28] M.C. Biesinger, B.P. Payne, A.P. Grosvenor, L.W.M. Lau, A.R. Gerson, R. St. C. Smart, Resolving surface chemical states in XPS analysis of first row transition metals, oxides and hydroxides: Cr, Mn, Fe, Co and Ni, *Appl. Surf. Sci.*, 257 (2011) 2717–2730.
- [29] C.F. Baes, R.E. Mesmer, *The Hydrolysis of Cations*, 2nd ed., Wiley, New York, 1986.
- [30] R.A. Young, A.W. Hewat, Verification of the triclinic crystal structure of kaolinite, *Clays and Clay Minerals*, 36 (1988) 225–232.
- [31] P.A. O'Day, G.A. Parks, G.E. Brown Jr., Molecular structure and binding sites of cobalt(II) surface complexes on kaolinite from X-ray absorption spectroscopy, *Clays and Clay Minerals*, 42 (1994) 337–355.
- [32] B. Beverskog, M. Bojinov, P. Kinnunen, T. Laitinen, K. Mäkelä, T. Saario, A mixed-conduction model for oxide films on Fe, Cr and Fe–Cr alloys in high-temperature aqueous electrolytes – I. Comparison of the electrochemical behaviour at room temperature and at 200 °C, *Corros. Sci.*, 44 (2002) 1923–1940.
- [33] M. Bojinov, A. Galtayries, P. Kinnunen, A. Machet, P. Marcus, Estimation of the parameters of oxide film growth on nickel-based alloys in high-temperature water electrolytes, *Electrochim. Acta*, 52 (2007) 7475–7483.
- [34] A. Gulino, G. Fiorito, I. Fragalà, I. Fragalà, S. Chimiche, Deposition of thin films of cobalt oxides by MOCVD, *J. Mater. Chem.*, 13 (2003) 861–865.

- [35] R. Cheng, B. Xu, C.N. Borca, A. Sokolov, C.S. Yang, L. Yuan, Characterization of the native C_2O_3 oxide surface of CrO_2 , *Appl. Phys. Lett.*, 79 (2001) 3122–3124.
- [36] S. Hong, E. Kim, D.W. Kim, T.H. Sung, K. No, On measurement of optical band gap of chromium oxide films containing both amorphous and crystalline phases, *J. Non. Cryst. Solids*, 221 (1997) 245–254.
- [37] M. Pourbaix, *Atlas of Electrochemical Equilibria in Aqueous Solution*, Oxford, New York, 1966.
- [38] J.O'M. Bockris, A. Reddy, *Modern Electrochemistry 2A: Fundamentals of Electrode Processes*, 2nd Ed., Springer, New York, 1998.
- [39] P. Marcus, *Corrosion Mechanisms in Theory and Practice Corrosion Technology*, 3rd ed., CRC Press, New York, 2011.
- [40] L.F. Lin, C.Y. Chao, A point defect model for anodic passive films, *J. Electrochem. Soc.*, 128 (1981) 1194–1198.
- [41] D.D. Macdonald, S.R. Biaggio, Steady-state passive films interfacial kinetic effects and diagnostic criteria, *J. Electrochem. Soc.*, 139 (1992) 170–177.
- [42] A. Seyeux, V. Maurice, P. Marcus, Oxide film growth kinetics on metals and alloys: I. Physical model, *J. Electrochem. Soc.*, 160 (2013) 189–196.

CHAPTER 6

Corrosion Kinetics on Co-Cr Alloy Stellite-6 under Potentiostatic Polarization at 25 °C Versus 80 °C

6.1 INTRODUCTION

In Chapter 4 we presented the results of a study of the corrosion kinetics on Stellite-6 as a function of electrode potential during potentiostatic polarization at room temperature [1]. The room temperature study focused on the effect of pH on corrosion kinetics and its potential dependence. The work presented in this chapter investigates the effect of temperature on corrosion kinetics. Elevating temperature can increase the rate of solid-state diffusion through an oxide layer as well as the rate of aqueous diffusion of metal cations [2], while a change in pH can have a significant impact on the rate of metal cation dissolution [3,4]. In addition to the mass transport rates, temperature also affects the rates of chemical reactions such as oxide formation and surface hydration [2]. In this work we have focused on corrosion at $\text{pH}_{25^\circ\text{C}} 10.6$ (pH measured at 25 °C) at two different temperatures (25 °C and 80 °C) because the solubility of cobalt oxide species is at a minimum near this pH [4,5]. This is also the pH that is maintained in the reactor coolant system of operating CANDU[®] nuclear reactors. Near $\text{pH}_{25^\circ\text{C}} 10.6$ oxide formation is preferred over metal cation dissolution during corrosion and, hence, the effects of potential and temperature on oxide formation kinetics and the influence of oxide growth on corrosion can be discerned more clearly.

The metal oxidation kinetics on Stellite-6 were followed by monitoring the current on a Stellite-6 electrode during potentiostatic polarization in deaerated water for 5 h. After the polarization, the surfaces of the electrodes were examined by scanning electron microscopy (SEM) and Auger electron spectrometry (AES). The range of potentials studied was from $-0.8 V_{SCE}$ to $+0.2 V_{SCE}$ (at $pH_{25^{\circ}C}$ 10.6). This encompasses a range of corrosion potentials from reducing deaerated water to highly oxidizing water (e.g., that containing H_2O_2 or water exposed to ionizing radiation), while remaining within the water stability range [1,6–9].

6.2 EXPERIMENTAL PROCEDURES

The electrochemistry procedures are similar to the procedures of the experiments described in Chapters 4 and 5. The only change was to include a temperature control capability. The temperature of the solution in the electrochemistry cell was held constant with a cycled water bath and a thermal jacket on the exterior of the electrochemical cell. The SEM and AES analyses were the same as those used for the study on the pH effect on Stellite-6 corrosion at room temperature described in Chapter 5.

6.3 RESULTS AND DISCUSSION

6.3.1 Potentiostatic Polarization Results

The current density, i , on the working electrode is a direct measure of the net rate of oxidation and its time-dependent behaviour provides useful information about the time evolution of the metal oxidation rate as corrosion progresses. The results from the 5-h

potentiostatic polarization experiments at 25 °C and 80 °C are compared in Figures 6.1 and 6.2.

In Figure 6.1 the results are presented as $\log |i|$ vs. $\log t$ (referred to as a $\log |i(t)|$ plot) to show the oxidation kinetics at short times. In Figure 6.2 the results are presented as accumulated charge Q vs. t (referred to as a $Q(t)$ plot) to show the potential dependence of the oxidation kinetic behaviour (time-dependence) over the full polarization period more clearly. As can be seen from Figure 6.1, the current density decreases several orders of magnitude in less than an hour. Due to the large span of the current density, the effect of polarization potential (E_{APP}) on the long-term kinetic behaviour is difficult to observe from the $\log |i(t)|$ plots. The current density at long times is small ($< 1 \mu\text{A}\cdot\text{cm}^{-2}$) and fluctuating with time so the slope of the $Q(t)$ plot provides a more accurate current value ($i(t) = \frac{dQ(t)}{dt}$) at long times when the system is near or at steady state.

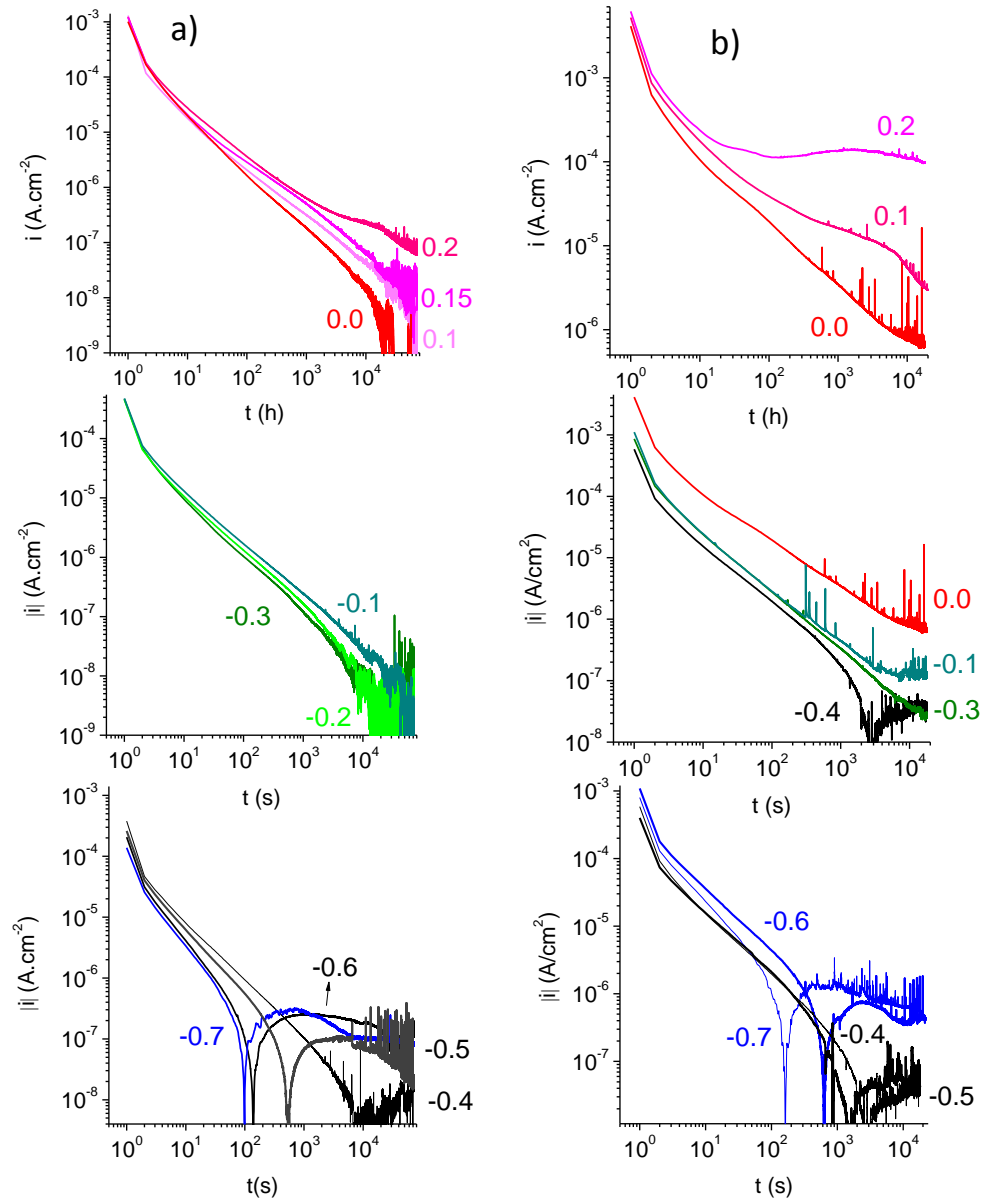


Figure 6.1: Current as a function of time observed during potentiostatic polarization on Stellite-6 at a) 25 °C and b) 80 °C. The Roman numerals correspond to the potential region. The numbers indicate the applied potentials in V_{SCE} .

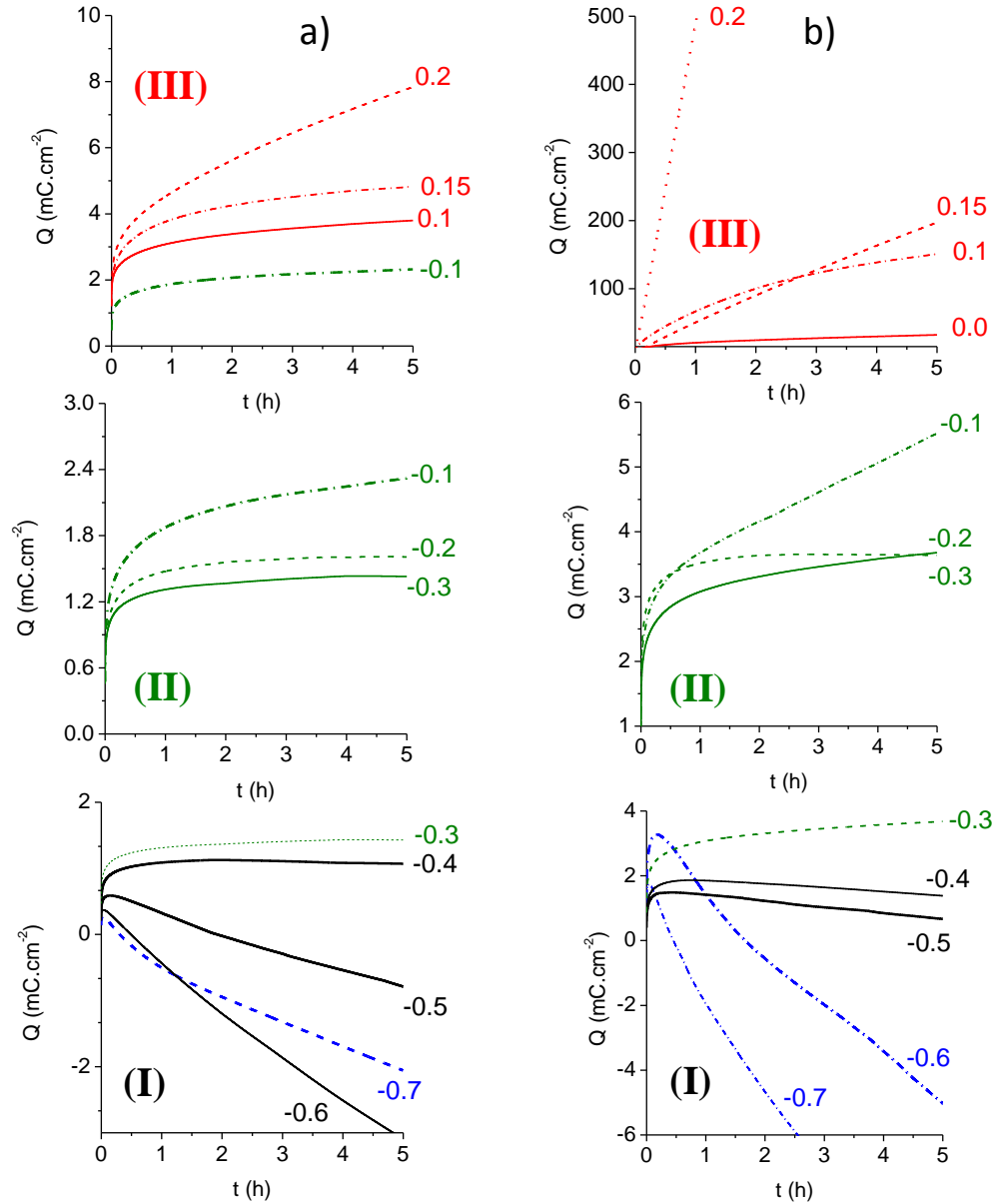


Figure 6.2: Accumulated charge as a function of time observed during potentiostatic polarization on Stellite-6 at a) 25 °C and b) 80 °C. The results are separated based on the oxidation potential regions discussed in the text. The numbers indicate the applied potentials in V_{SCE}.

As described below, at a given temperature the time-dependent behaviour of $\log |i(t)|$ and $Q(t)$ depend on the polarization potential (E_{APP}). There are five characteristic regions of applied potential, each with distinct time dependences. These regions are indicated by using lines with different colours in Figures 6.1 and 6.2. Prior to the discussion on the corrosion behaviour in the individual potential regions it should be noted that at potentials below $-0.4 V_{SCE}$ the net current is initially anodic but then switches to cathodic (Figure 6.1). (The cathodic current appears as the negative slope in the $Q(t)$ plots in Figure 6.2). The presence of a cathodic current at long times indicates that the Stellite-6 working electrode can support electrolytic reduction of water to H_2 at these potentials. The current flows from the CE to the WE and to the solution despite the presence of presumably passive oxides on the Stellite-6 alloy electrode (initially Cr_2O_3 that is later converted to other oxides). This suggests that while these oxides may become passivating in terms of ionic conductivity at these potentials, they do not completely suppress electronic conductivity. Due to this reduction process, the rate of any metal oxidation that may also continue to occur on the working electrode at long times cannot be directly extracted from the measured current at these low potentials. For the same reason, the electrochemical impedance spectroscopy (EIS) analysis performed at $E_{APP} \leq -0.4 V_{SCE}$ did not provide meaningful information on the oxide film resistance. Nevertheless, since the rates of both metal oxidation and water reduction depend on the nature and the thickness of the oxide layer that is being formed, albeit with different dependences, the net current still provides useful information on the type of the oxide that grows and its growth kinetics.

At a given temperature, there are four potential regions in the range from $-0.8 V_{SCE}$ to $+0.2 V_{SCE}$, each having distinctly different short- and long-term characteristics. At a potential below $-0.8 V_{SCE}$, the current becomes cathodic immediately (< 2 s) upon polarization, indicating that there is negligible metal oxidation and hence potentials below $-0.8 V_{SCE}$ are not of interest. The water reduction that is responsible for the cathodic current is not a reduction half-reaction coupled with the metal oxidation during corrosion as discussed in Chapter 3. Hence, the water reduction observed under polarization is referred to as ‘electrolytic’ water reduction.

The observed characteristics of the five oxidation potential regions are summarized in this section. The metal oxidation kinetics in each region are discussed in more detail in Section 6.3.3. While there are the same number of potential regions at both $25\text{ }^{\circ}\text{C}$ and $80\text{ }^{\circ}\text{C}$, the actual potential ranges of these regions sometimes differs for the different temperatures.

Region 0 ($-0.8 V_{SCE} \leq E_{APP} \leq -0.7 V_{SCE}$ at $25\text{ }^{\circ}\text{C}$ and $-0.8 V_{SCE} \leq E_{APP} \leq -0.6 V_{SCE}$ at $80\text{ }^{\circ}\text{C}$): This region is characterized by: (1) increasing short-term $Q(t)$ and $\log |i(t)|$ with E_{APP} , (2) fast conversion from anodic to cathodic current, (3) the magnitude of the cathodic current or of the negative slope of $Q(t)$ having two stages, changing from a high to a low value at a certain time depending on E_{APP} and temperature (e.g., ~ 2.5 h at $-0.8 V_{SCE}$ and $25\text{ }^{\circ}\text{C}$ and ~ 0.3 h at $-0.8 V_{SCE}$ and $80\text{ }^{\circ}\text{C}$), and (4) the cathodic current in the first stage decreasing with E_{APP} while the cathodic current in the second stage is nearly independent of E_{APP} but dependent on temperature.

As discussed in Section 6.3.3, the observed kinetic behaviours are consistent with the corrosion mechanism consisting of Co oxidation to Co^{II} at a very slow rate in this low potential region. This leads mainly to cobalt dissolution ($\text{Co}^{2+}(\text{aq})$) initially. However, some oxidized cobalt is also incorporated, albeit at a very slow rate, into the pre-existing Cr_2O_3 film, converting it to CoCr_2O_4 . The rate of initial oxidation of Co to Co^{II} with the initially present defective Cr_2O_3 film increases with E_{APP} . The defective Cr_2O_3 film also facilitates electrolytic water reduction and, in the presence of this film, the water reduction current decreases with E_{APP} . However, the eventual formation of a uniform layer of CoCr_2O_4 impedes the oxidation of Co to Co^{II} and the electrolytic water reduction. The decrease in water reduction can be seen from the change in the slope of $Q(t)$ (Figure 6.2). The oxidative conversion of Cr_2O_3 to CoCr_2O_4 requires chemical bond formation and occurs at a faster rate at a higher temperature. The decrease in the rate oxidation of Co to Co^{II} following the formation of CoCr_2O_4 can be seen from the progressively smaller increase in the initial $Q(t)$ with E_{APP} . The initial $Q(t)$ in fact decreases even more when E_{APP} increases from a potential in Region 0 to Region I.

Region I ($-0.7 V_{\text{SCE}} < E_{\text{APP}} < -0.4 V_{\text{SCE}}$ at 25 °C and $-0.5 V_{\text{SCE}} \leq E_{\text{APP}} < -0.4 V_{\text{SCE}}$ at 80 °C):

The boundary between Region 0 and this region is based on the sudden change in the potential dependence of short-term $Q(t)$ or $\log |i(t)|$. This change occurs at a potential between $-0.7 V_{\text{SCE}}$ and $-0.4 V_{\text{SCE}}$ at 25 °C and at a potential between $-0.5 V_{\text{SCE}}$ and $-0.4 V_{\text{SCE}}$ at 80 °C. In this potential region, the metal oxidation is limited to the Co oxidation to form $\text{Co}^{2+}(\text{aq})$ and CoCr_2O_4 , the same oxidation that occurs in Region 0. Thermodynamically Regions 0 and I are the same with respect to CoCr_2O_4 stability. As can

be seen in Figure 6.1, the corrosion kinetics in both regions are similar. The distinction between Regions 0 and I is the rate of oxidation and hence the rate of the formation of a uniform layer of CoCr_2O_4 which slows down the further oxidation of Co to Co^{II} . The formation of this layer occurs faster at 80 °C than at 25 °C. At 80 °C $\text{Co}^{2+}(\text{aq})$ also dissolves from CoCr_2O_4 at a faster rate which results in the larger initial anodic current and a larger negative slope at the second stage of $Q(t)$ than is observed at potentials at 25 °C. Because the distinction between Region 0 and Region I is only rate of oxidation we do not distinguish them thermodynamically as you can see in Figure 6.3

Region II ($-0.3 V_{\text{SCE}} \leq E_{\text{APP}} \leq 0.0 V_{\text{SCE}}$ at 25 °C and $-0.3 V_{\text{SCE}} \leq E_{\text{APP}} \leq -0.1 V_{\text{SCE}}$ at 80 °C):

The distinction between Region I and II can be seen from the time-dependent behaviour of $\log |i(t)|$ and $Q(t)$. In Region II, the negative slope of $\log |i(t)|$ shows three time stages at $t > 2$ s (Figure 6.1). These stages are more clearly seen at 80 °C. At this temperature, the negative slope between 2 and ~ 20 s (Stage I) is close to 1.0 and the slope becomes less steep (~ 0.8) between ~ 20 and ~ 1000 s (Stage II), before the current becomes near constant with time (slope ~ 0) (Stage III). At a potential below $-0.5 V_{\text{SCE}}$ all three stages are difficult to discern due to the still large contribution of electrolytic water reduction current at this potential. In this region the current density at all times is higher at a higher E_{APP} , indicating that the rate of metal oxidation increases with E_{APP} . The higher current shows up as a faster increase in $Q(t)$ with time and E_{APP} in Figure 6.2.

The different stages are attributed to different oxide growth stages. Based on reaction thermodynamics and the surface analysis results (discussed in more detail later), Stage I is

attributed to the oxidative conversion of Cr_2O_3 to CoCr_2O_4 and Stage II is attributed to the growth of an outer layer of $\text{Co}(\text{OH})_2$. The latter oxide layer acts as a chemical as well as an electric field potential barrier. Thus, as the oxide layer thickens the Co oxidation to Co^{II} becomes progressively more difficult. That the slopes of $\log |i(t)|$ in these two stages are independent of E_{APP} while the net rate of Co oxidation (i.e., the current density) increases with E_{APP} suggests that the rate of oxide formation is not controlled by electrochemical redox reactions but by a thermal activation process such as chemical bond formation leading to oxide growth.

The near constant anodic current in Stage III indicates that the net rate of Co oxidation to Co^{II} has decreased to a rate that matches the rate of $\text{Co}^{2+}(\text{aq})$ dissolution. At 25 °C the dissolution current is very small at any potential in Region II. At 80 °C the dissolution current is not negligible and increases with E_{APP} , indicating that the rate of Co oxidation controls the dissolution rate. If the rate of metal dissolution is limited by thermal dissolution processes (surface hydration and diffusion) of metal cations from an oxide lattice the rate of dissolution should be nearly independent of E_{APP} . The observed potential dependence thus supports the claim that oxide growth and metal dissolution compete for the oxidized metal [10] at these potentials.

Region III ($0.0 V_{\text{SCE}} < E_{\text{APP}} \leq 0.15 V_{\text{SCE}}$ at 25 and 80 °C): The time dependent behaviour of the current during polarization at a potential in this region also shows different time stages as observed in Region II. These different stages are again more noticeable at 0.1 V_{SCE} and 80 °C (Figure 6.1). The characteristics of Region III, are: (1) Stages I and II are more difficult to

differentiate at higher potentials (a distinct separation is observed at ~ 100 s only at $0.0 V_{SCE}$, the boundary potential of Regions II and III), (2) the current in Stages I and II decreases progressively more slowly with increasing potential before reaching a near constant value (Stage III), but (3) the near constant current stage is followed by a decrease in current in Stage 4. This later decrease in current occurs earlier at a higher E_{APP} .

The decrease in current at long times suggests that conversion of the oxide formed at earlier times to a less soluble and more protective oxide(s) is occurring. Thus, the anodic process in Stage IV is attributed to continuing formation of $Co(OH)_2$ and the oxidative conversion of $Co(OH)_2$ to $Co_3O_4/CoOOH$. Oxidation of Cr^{III} hydroxide, $Cr(OH)_3$ to soluble Cr^{IV} species is also thermodynamically possible. However, such conversion would increase the anodic current rather than decrease the current. The absence of clear separation between Stage I and II in Region III may be due to the fact that at a sufficiently large polarization potential the rate of oxide growth is not controlled by electrochemical redox reactions at the metal/oxide/solution interfaces but thermal processes such as chemical bond formation with incorporation of metal cations and oxygen anions into the oxide lattice growing the oxide and/or surface hydration, and diffusion of metal cations leading to dissolution. At a sufficiently high potential the rate of formation of $Co(OH)_2$ can occur faster than that of $CoCr_2O_4$. This can leave unreacted Cr_2O_3 to be hydrated to form adsorbed $CrOOH$ and $Cr(OH)_3$ and the chromium can be oxidized to soluble Cr^{VI} ions at this potential. A corrosion reaction mechanism in this potential range that can explain the surface analysis results and the amounts of dissolved Co and Cr in the corrosion tests using coupons under γ -irradiation

[6] is discussed in Chapter 5 for the room temperature study and in Chapter 7 for the study at 80 °C).

Region IV ($E_{APP} > 0.2 V_{SCE}$ at 25 and 80 °C): Only at a potential higher than +0.2 V_{SCE} is the rate of oxidation of Cr^{III} to soluble CrO_4^{2-} sufficiently high that it can compete with the Co oxidation. This competition leads to slower coverage of the surface with a protective cobalt oxide layer and the current reaches a constant level very quickly (few seconds), and remains high for a longer period of time. A potential in this region is higher than the corrosion potential that is normally observed even in highly oxidizing solution environments such as those encountered in aerated water or water under γ -irradiation [1,11,12]. At such high potentials water can also oxidize at a substantial rate and hence the corrosion in this potential region was not explored.

6.3.2 Electrochemical Equilibrium Potentials

The boundaries of the potential regions show a correlation with the electrochemical equilibrium potentials, E_{eq} , of the oxidation reactions of the primary and the secondary elements of Stellite-6 (Co and Cr) as shown in Figure 6.3. The equilibrium potentials shown in the figure were calculated for $pH_{25^\circ C}$ 10.6 at 25 °C from the standard reduction potentials of the redox pairs reported in literature [13], as previously described in Chapter 4. The E_{eq} values are shown by vertical lines and the redox couple involved in each equilibrium reaction is given beside each bar. For a given redox couple, oxidation is thermodynamically possible when the applied potential is greater than the corresponding equilibrium potential. The potential ranges where the formations of different oxides are thermodynamically possible are

indicated at the top of Figure 6.3. The equilibrium potentials of the redox pairs at 80 °C are not well established. The equilibrium potentials for the Co and Co(OH)₂ pair, and the Co(OH)₂ and Co₃O₄ pair as a function of pH_T at 75 °C for a Co-H₂O system has been reported [14]. The pH_{25°C} 10.6 measured at 25 °C corresponds to pH_{75°C} 9.4 at 75 °C as pK_w decreases from 14 to 12.8 [15] . The Pourbaix diagram reported in ref. [14] shows the E_{eq} values for the redox pairs Co/Co(OH)₂ and Co(OH)₂/Co₃O₄ at pH_{75°C} differ only by –30 mV compared with E_{25°C}. For example, E_{eq} calculated at 25 for Co/Co(OH)₂ is around –0.8 V_{SCE} whereas it is –0.83 V_{SCE} at 75 °C.

Also shown in bars at the top of Figure 6.3 are the potential regions determined from the potentiostatic polarization results presented above. The ranges of different potential regions determined from the potentiostatic polarization experiments at two different temperatures, 25 °C and 80 °C, are similar. Comparison of the potential regions presented in Figure 6.3 shows that Regions 0/I and II, as determined from the polarization results, are not really shifted with respect to those established by the thermodynamic equilibrium potentials. The same number of potential regions (with similar breadths) as those determined thermodynamically and the presence of distinct stages of different current behaviour at a given E_{APP} suggest that the formation of, or conversion to, different oxides are dictated by the reaction thermodynamics. The presence of such oxide layers is consistent with the surface analysis results discussed below.

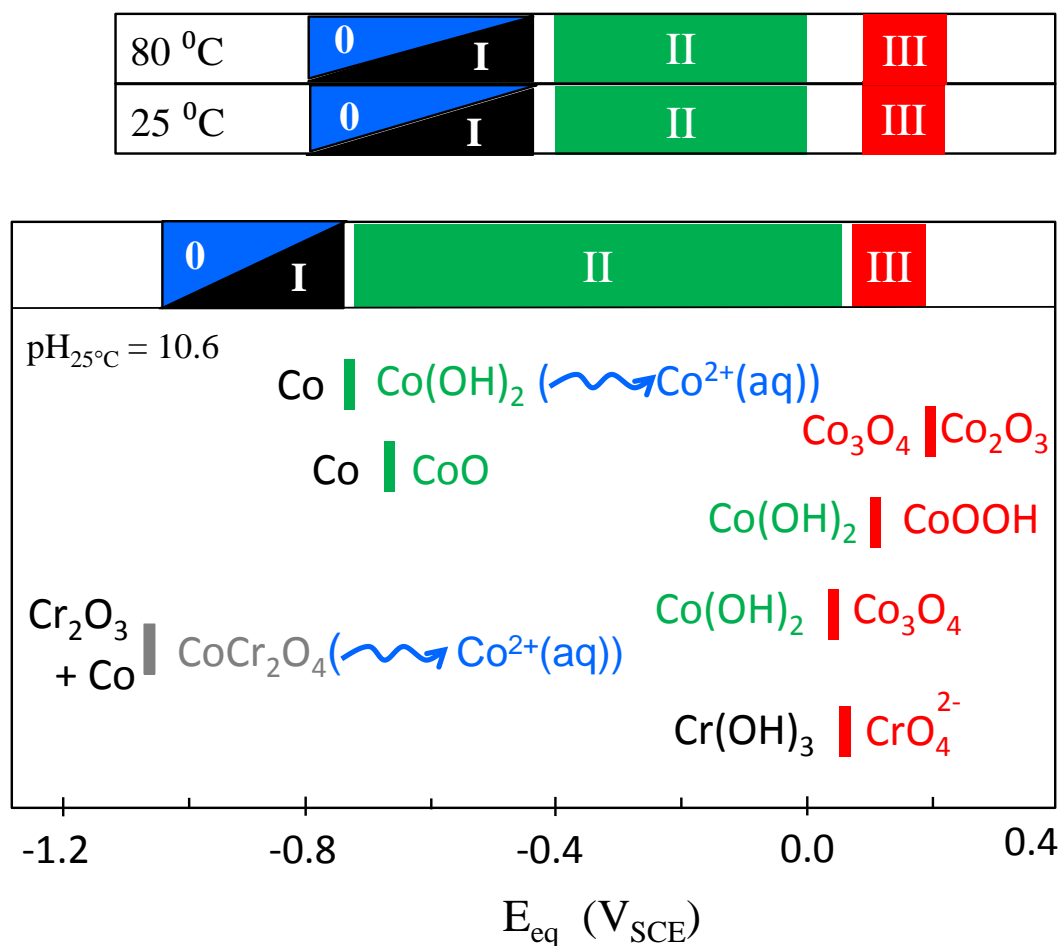


Figure 6.3: Electrochemical equilibrium potentials for the redox reactions of Co and Cr species at $\text{pH}_{25^\circ\text{C}} = 10.6$. The vertical bars show the equilibrium potentials and the corresponding redox pairs are listed on both sides of these bars. The potential ranges where the different oxides are thermodynamically stable are shown in the bar at the top of the graph. Above the graph are two additional bars that show the locations of the potential regions determined from the polarization experiments at 25 °C and 80 °C.

6.3.3 Surface Analyses of Oxides Formed by Potentiostatic Polarization

We have previously reported on analyses of the oxides grown at different potentials at pH 10.6 and 25 °C [1] in Chapter 4. Only the key results from the room temperature study are summarized here for comparison with the results of 80 °C tests. The oxides present on the Stellite-6 electrodes polarized at potentials below 0.1 V_{SCE}, even for times up to 20 h, were very thin and hence the surfaces of these electrodes were analyzed mainly by XPS. We have previously reported on the analysis of the high resolution XPS spectra of the Co 2p bands taken for these surfaces, and the results are reproduced here in Figure 6.4.

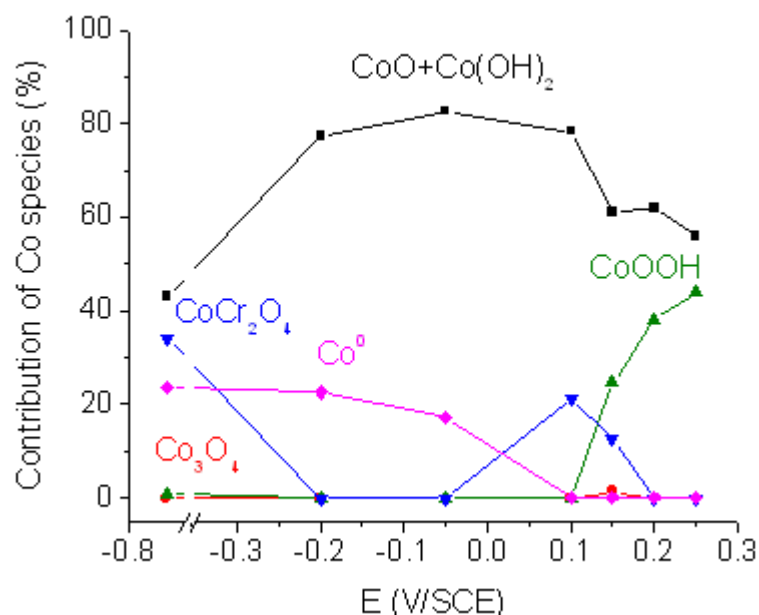


Figure 6.4: Speciation of the cobalt oxide on the surface of Stellite-6 as a function of applied potential determined by XPS analysis at 25 °C.

The XPS analysis results of a surface polarized at a potential below 0.0 V_{SCE} show a metallic Co component in the Co 2p band, indicating that the oxide thickness is less than the XPS analysis depth (< 9 nm). The Co speciation determined by XPS, as a function of E_{APP}, shows that: (1) the oxide present on an electrode polarized at -0.7 V_{SCE} (Region I) is very thin and is mostly in the form of CoCr₂O₄ and Co(OH)₂, (2) the oxide formed at a potential in Region II is mainly in the form of Co(OH)₂ and the oxide layer is thicker on an electrode polarized at a higher potential, and (3) the oxide formed at a potential in Region III (> 0.0 V_{SCE}) contains a significant fraction of cobalt oxides at higher oxidation state, Co₃O₄ and CoOOH in addition to Co(OH)₂. These results are consistent with the oxidation kinetics (current as a function of time) observed during polarization and the type of oxide that can be formed based on reaction thermodynamics as discussed above.

The surfaces of Stellite-6 electrodes polarized at different potentials at 80 °C were analyzed using SEM, XPS, and AES with Ar⁺ sputtering. For these analyses the electrodes were polarized for only 3 h to explore the types of oxide that form at early stages of corrosion. As discussed later in Chapter 7 the longer term (3 d) corrosion of Stellite-6 at different potentials at 80 °C was studied using coupons in leak-tight quartz cells in the absence and presence of radiation. The surfaces of the electrodes polarized at four potentials, -0.7 V_{SCE} (in Region 0/I), -0.4 V_{SCE} and -0.2 V_{SCE} (near the lower and upper limits in Region II), and +0.1 V_{SCE} (in Region III) were examined. The SEM images of these surfaces are shown in Figure 6.5. The XPS analysis as a function of applied potential is shown in Figure 6.6. The AES depth profile analysis results are shown in Figures 6.7 and 6.8.

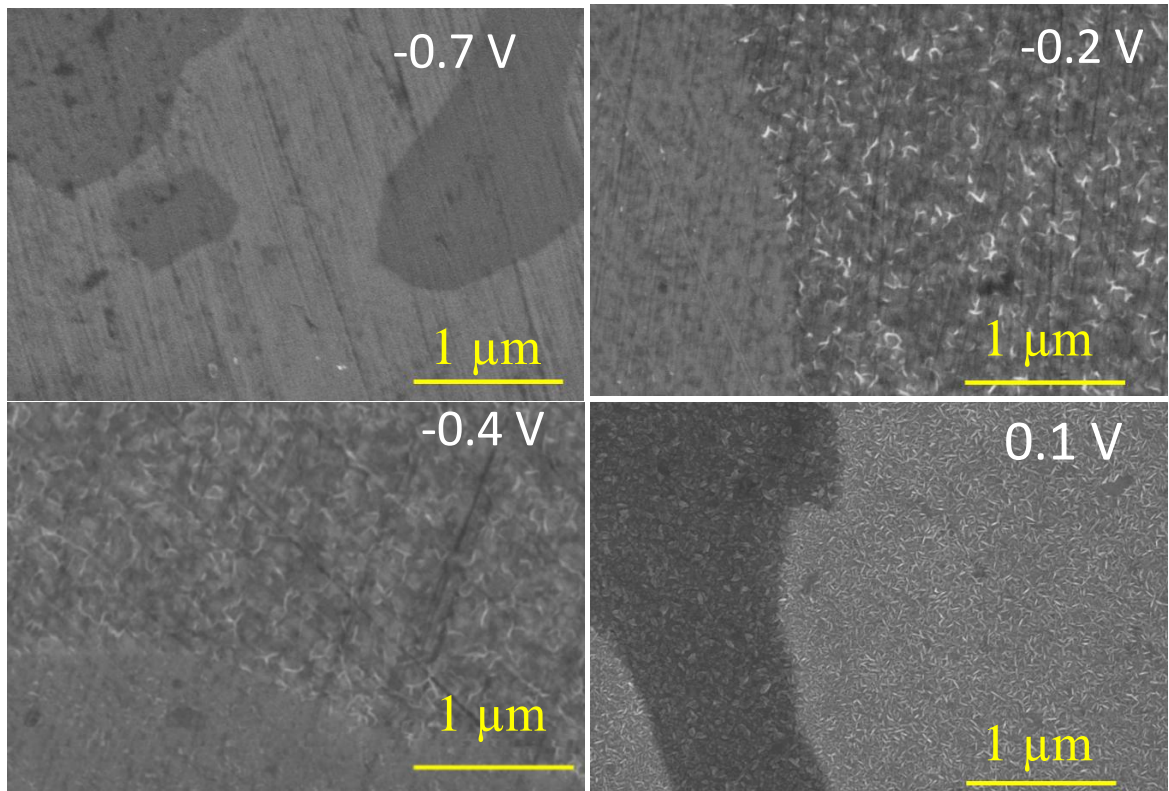


Figure 6.5: SEM images of Stellite-6 surfaces corroded following 3 h polarization at $-0.7 V_{SCE}$, $-0.4 V_{SCE}$, $-0.2 V_{SCE}$, and $0.1 V_{SCE}$ at $pH_{25^{\circ}C} 10.6$ at $80^{\circ}C$.

The SEM image of the electrode polarized at $-0.7 V_{SCE}$ shows a smooth surface with the polish lines still visible (Figure 6.5). The polish lines are, however, duller on this surface compared to those seen on the fresh surface, indicating the presence of a thin film of an oxide, likely that of $CoCr_2O_4$. Images of electrodes polarized at $-0.4 V_{SCE}$ and $-0.2 V_{SCE}$ show that a uniform layer of filament-like oxide has developed mainly on the surface of the

Co-rich phase, and this layer is denser and thicker on the electrode polarized at $-0.2 V_{SCE}$ than at $-0.4 V_{SCE}$. This type of filament-like morphology is commonly observed on the surfaces of many transition metals corroded at a high pH [16–19]. The filament-like surface morphology is thus consistent with the expected growth of $Co(OH)_2$ at a reasonable rate at these potentials. XPS results show that oxide layer formed at -0.2 and $-0.4 V_{SCE}$ is $Co(OH)_2$. The filament-shaped oxide is also present on the surface of the Cr-rich phase but much more sparsely compared to the Co-rich phase, indicating that the rate of Co oxidation to Co^{II} leading Co^{II} oxide growth is slower on the Cr-rich phase than the Co-rich phase. This difference is amplified at $80\text{ }^\circ\text{C}$ compared to $25\text{ }^\circ\text{C}$. For longer polarization at a potential in Region III it is expected a layer of $Co(OH)_2$ would eventually be fully developed over the Cr-rich phase.

At $0.1 V_{SCE}$ (Region III), the Co-rich and Cr-rich areas show different surface morphologies; the oxide formed on the outer surface of the Cr-rich phase is platelet-like in shape while the oxide formed on the Co-rich phase has a filament-like network. These crystallite structures suggest that the oxide on the Cr-rich phase could be a spinel oxide (Co_3O_4) while the oxide on the Co-rich phase could be a Co^{III} hydroxide ($CoOOH$) [20]. Shim et al. showed that Co_3O_4 crystallinity became more pronounced as the temperature and potential were increased, and this observation explains why these crystallites were not visible on electrodes polarized at $25\text{ }^\circ\text{C}$ [20]. No polish lines are visible on an electrode polarized at $0.1 V_{SCE}$. This is consistent with the formation of a thicker underlying oxide layer, mainly Co^{II} oxides ($CoCr_2O_4/CoO/Co(OH)_2$). The platelet-like versus needle-like crystal structure suggests that the oxide on the Cr-rich phase is more likely Co_3O_4 , whereas the oxide on the

Co-rich phase is more likely CoOOH. The reason for the growth of two distinctly different oxides depending on Cr-content in the alloy phase is not clear. One possible explanation may be the difference in the passivity of the pre-formed Cr_2O_3 layers formed on the two phases. The air-formed Cr_2O_3 on the Cr-rich phase is likely denser than that on the Co-rich phase which may provide more passive surface. Due to a larger potential barrier the effective overpotential available for cobalt oxidation may be less on the Cr-rich phase, limiting the oxidation to Co_3O_4 . On the other hand, the cobalt oxidation on the Co-rich phase proceeds to the formation of CoOOH. At an effective overpotential where the formation of both Co_3O_4 and CoOOH can occur the oxidative conversion of $\text{Co}(\text{OH})_2$ to CoOOH is considered to be kinetically more favoured than the conversion to Co_3O_4 . Our XPS results show that oxide layer formed at $0.1 \text{ V}_{\text{SCE}}$ is Co_3O_4 and CoOOH.

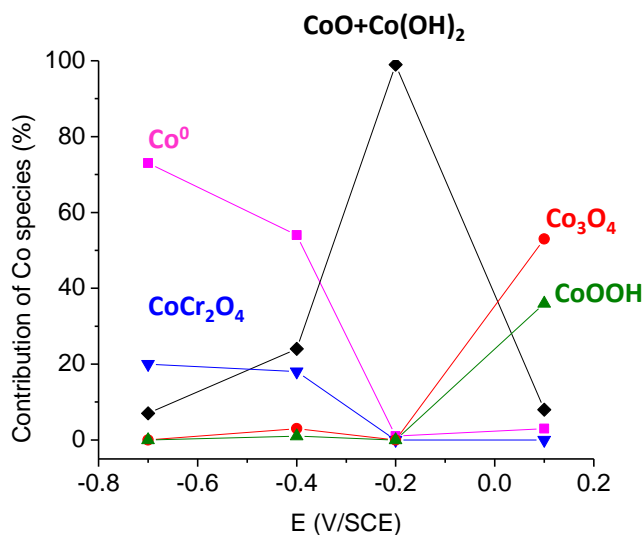


Figure 6.6: Speciation of the cobalt oxide on the surface of Stellite-6 as a function of applied potential determined by XPS analysis at 80 °C.

The change in the elemental composition with depth on the electrode surfaces were explored using AES with Ar^+ sputtering. The atomic percentage of each element as a function of sputter depth is shown in Figure 6.7. The outermost surface composition (at a nominal depth of 0 nm) is easily affected by carbon or by the adsorbed hydrated species. Thus, the data at 0 nm are not very meaningful. The AES data show that the atomic % of oxygen decreases with depth as expected. To observe more clearly the degree of oxidation of the two main alloying components and their relative abundance in the oxide, the AES data are presented as the ratios of $\text{O}/(\text{Co} + 1.5 \text{Cr})$ and $\text{Co}/(\text{Co} + \text{Cr})$, as a function of sputtered depth, in Figure 6.8.

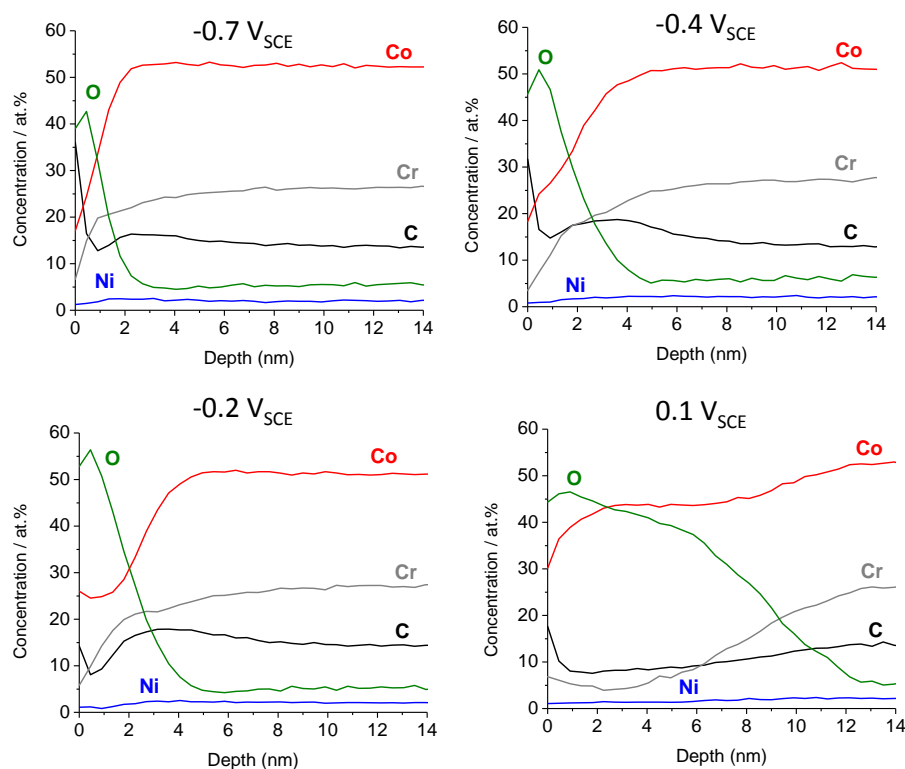


Figure 6.7: Depth profiles of all of the elements determined by AES of Stellite-6 surfaces corroded following 3 h polarization at $-0.7 \text{ V}_{\text{SCE}}$, $-0.4 \text{ V}_{\text{SCE}}$, $-0.2 \text{ V}_{\text{SCE}}$ and $0.1 \text{ V}_{\text{SCE}}$, at $\text{pH}_{25^\circ\text{C}} 10.6$, at 80°C .

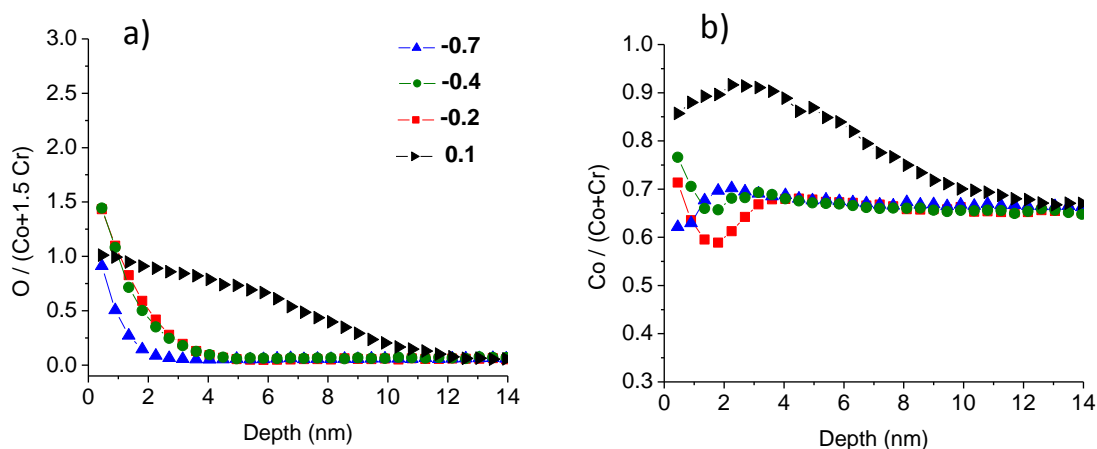


Figure 6.8: Depth profiles on the Stellite-6 surfaces following 3-h polarization at potentials in different regions at 80 °C showing the ratio of a) $O/(Co+1.5Cr)$ and b) $Co/(Co+Cr)$.

On the electrodes polarized at $-0.7 V_{SCE}$, the $O/(Co + 1.5Cr)$ ratio decreases exponentially from ~ 1.0 to 0 within 2 nm depth while the $Co/(Co+Cr)$ ratio increases from ~ 0.6 to a maximum value 0.7. This is followed by a small decrease in $Co/(Co + Cr)$ before reaching a constant value with depth equal to the value of the bulk of alloy of 0.67 at ~ 6 nm. The depth range where $Co/(Co + Cr)$ is higher than the bulk alloy ratio is due to depletion of Cr. This Cr depletion can be better seen from Figure 6.x. When the atomic fraction of O is nearly zero, the atomic fraction of Co is nearly constant with depth while that of Cr continually increase with depth, indicating depletion of Cr has occurred.

The $O/(Co + 1.5Cr)$ ratios observed on the electrodes polarized at $-0.4 V_{SCE}$ and $-0.2 V_{SCE}$ are same. They are initially higher at ~ 1.5 and decreases to 0 into a deeper depth of ~ 0.4 nm, compared to that observed at $-0.7 V_{SCE}$. Although the $O/(Co + 1.5Cr)$ ratios are the

same, the $\text{Co}/(\text{Co} + \text{Cr})$ ratios on the electrodes polarized at $-0.4 \text{ V}_{\text{SCE}}$ and $-0.2 \text{ V}_{\text{SCE}}$ are different. The depth profile obtained at the higher potential shows the minimum $\text{Co}/(\text{Co} + \text{Cr})$ ratio (at $\sim 2 \text{ nm}$) is lower than that obtained at the lower potential, suggesting more Co dissolution has occurred over the 3-h polarization. On these electrodes, the $\text{Co}/(\text{Co} + \text{Cr})$ ratio reaches a maximum before decreasing slightly to a constant value of 0.67, similar to that obtained at $-0.7 \text{ V}_{\text{SCE}}$.

The depth profile for an electrode polarized at $0.1 \text{ V}_{\text{SCE}}$ is quite different. The $\text{O}/(\text{Co} + 1.5\text{Cr})$ ratio starts at 1.0 and decreases slowly and steadily over $0 - 6 \text{ nm}$ range, and this is followed by a more rapid decrease until it reaches a value near 0 at a depth greater than 10 nm. Within 6 nm, the $\text{Co}/(\text{Co} + \text{Cr})$ ratio is high at 0.85-0.90, significantly higher than the bulk alloy phase of 0.67. In the deeper region the ratio decreases more rapidly. At this potential, the Co depletion region within the oxide layer was not observed. The examination of Figure 6.7 shows that in the range of $\sim 1 \text{ nm}$ and 6 nm, the atomic fraction of O is inversely related to that of Co. The higher atomic fraction of O than that of Co in the range of $0 - 3 \text{ nm}$ is consistent with the above claim that at $0.1 \text{ V}_{\text{SCE}}$ the cobalt oxidation has progressed to the formation of Co_3O_4 and CoOOH . In the deeper region between 3 nm and 6 nm, the atomic fraction of Co is nearly constant but the fraction of Cr increases, while the fraction of O decreases, with depth at slow rates. These results indicate that the oxide in the depth range is mainly CoO (dehydrated form of $\text{Co}(\text{OH})_2$). The shallow hump in the range of $0 - 6 \text{ nm}$ can then be attributed to the distribution of different Co oxides from the outer surface in the order of Co^{III} hydroxide, a mixed $\text{Co}^{\text{III}}/\text{Co}^{\text{II}}$ oxide and Co^{II} oxide. In the deeper region, where the ratios of $\text{O}/(\text{Co} + 1.5\text{Cr})$ and $\text{Co}/(\text{Co} + \text{Cr})$ decrease at similar rates, the

atomic ratios of both Co and Cr increases rapidly while that of O decreases rapidly. This is consistent with the claim that the oxide in this inner most depth range is more likely in the form of CoCr_2O_4 .

The SEM images and the AES depth profiles observed on the electrodes polarized at different potentials at 25 and 80 °C are consistent with the expectations arising from the reaction thermodynamic and kinetic considerations of the cobalt oxidation. The potential regions of thermodynamic stability for cobalt oxides at 80 °C are very similar to those at 25 °C, except for the wider range for Co_3O_4 at 80 °C. A similar change in thermodynamic stability due to increasing temperature above 70 °C is a well-known phenomenon for $\text{Fe}-\text{H}_2\text{O}$; the increase in oxidative conversion from Fe^{II} oxides/hydroxides to a spinel oxide, Fe_3O_4 is known as the Schikorr reaction [21].

Although the types of oxides that can be formed are still limited by the reaction thermodynamics at 80 °C, the current behavior observed during the potentiostatic polarization study suggest that the cobalt oxidation rate is faster at 80 °C than at 25 °C. The effect of the increase in the oxidation rate on oxide growth is difficult to determine at potentials below Region IV. However, the SEM images observed at 0.1 V_{SCE} show different morphologies over the Co-rich and Cr-rich phases. XPS analysis also showed the greater buildup of Co_3O_4 and CoOOH on Stellite polarized at a high potential. The corrosion study of the irradiated and un-irradiated coupons at 80 °C that is discussed in Chapter 7 shows the increase in metal oxidation also leads to metal dissolution as well as oxide growth at 80 °C.

6.3.4 Effect of Temperature on Corrosion Kinetics

Oxide growth and dissolution are two competing reactions involved in the oxidation of metals. The relative changes in the rates of oxidation and reduction elementary steps influence the competition between oxide growth and dissolution. Since the rates of the elementary steps have different temperature dependences, the current (the net corrosion rate) does not have a simple temperature dependence. An increase in temperature from 25 °C to 80 °C has a negligible effect on the stability regions of different cobalt oxides due to the fact that it has a negligible effect on the E_{eq} of Co oxidation reactions at $pH_{25^{\circ}C}$ 10.6 [14], and hence it does not alter the span of characteristic potential regions significantly. An increase in temperature can, however, affect metal cation transport across a solid semiconducting oxide layer as well as in solution [2]. The net effect is to increase the cobalt oxidation rate. This study indicates that the increase in the net cobalt oxidation leads to faster growth of oxide. When this is taken into account, the oxidative conversion from one oxide to another follows the modified Butler-Volmer equation but with an effective overpotential, as discussed in Chapter 5.

The time-dependent behaviour of $\log |i(t)|$ and $Q(t)$ indicate there is no significant temperature dependence in all regions, however, the value of Q is higher at 80 °C than at 25 °C in Regions II and III. Despite the fact that the oxidation is slightly promoted at 80 °C compared with 25 °C, in particular, at higher E_{APP} , we presume that the higher dissolution rate accounts for the significant increase in Q at 80 °C. These results are close to the

thermodynamic predictions of the behaviour of a Co-H₂O system at high temperature presented in Chapter 2.

6.4 CONCLUSION

The oxide formation on Stellite-6 is dependent on the magnitude of the applied potential and temperature. The type of oxide that can form in separate potential regions is determined by the thermodynamic stabilities of those oxides. In Region I, Co oxidation to Co^{II} occurs at a very slow rate and also in Region II, the metal oxidation is limited to the Co oxidation to form Co²⁺(aq) and CoCr₂O₄. The distinct difference between Region I and II can be observed from the time-dependent behaviour of $\log |i(t)|$ and $Q(t)$. In Region III there is a significant relationship between the current density and E_{APP} . A higher E_{APP} causes a higher rate of metal oxidation. In this region the continuous conversion of Cr₂O₃ to CoCr₂O₄ occurs as well as the growth of Co(OH)₂ as an outer layer. However, as time goes on, due to the increase in oxide thickness, the Co oxidation to Co^{II} slows down, and hence $Q(t)$ reaches a constant value. The potential regions determined from this polarization study at 80 °C are similar to those observed at 25 °C. However, the time-dependent behaviour of current and Q at different time stages appear to be different and these differences are more noticeable at $E_{APP} > 0.1 V_{SCE}$. A comparison of the magnitudes of Q at 25 °C and 80 °C shows that Q is larger at 80 °C, especially when the oxidation of metal becomes dominant over water reduction (Region II and III). This study, however, cannot provide any information on the effect of temperature on metal dissolution rate. The effect of temperature on both oxide growth and metal dissolution at different potentials were explored by performing corrosion

tests using coupons in leak-tight quartz cells in the absence and presence of radiation and by analyzing both corroded surfaces and the metal ions dissolved in the test solutions. This study is presented in Chapter 7.

6.5 REFERENCES

- [1] M. Behazin, M.C. Biesinger, J.J. Noël, J.C. Wren, Comparative study of film formation on high-purity Co and Stellite-6: Probing the roles of a chromium oxide layer and gamma-radiation, *Corros. Sci.*, 63 (2012) 40–50.
- [2] S.R.J. Saunders, M. Monteiro, F. Rizzo, The oxidation behaviour of metals and alloys at high temperatures in atmospheres containing water vapour: A review, *Prog. Mater. Sci.*, 53 (2008) 775–837.
- [3] T. Ohtsuka, N. Sato, Anodic oxide film on cobalt in weakly alkaline solution, *J. Electroanal. Chem.*, 147 (1983) 167–179.
- [4] C.F. Baes, *The Hydrolysis of Cations*, 2nd ed., Wiley, New York, 1986.
- [5] S.E. Ziemniak, M.A. Goyette, K.E.S. Combs, Cobalt (II) oxide solubility and phase stability in alkaline media at elevated temperatures, *J. Solution Chem.*, 28 (1999) 809–836.
- [6] M. Behazin, J.J. Noël, J.C. Wren, Combined effects of pH and γ -irradiation on the corrosion of Co-Cr alloy Stellite-6, *Electrochim. Acta*, 134 (2014) 399–410.
- [7] K. Daub, X. Zhang, J.J. Noël, J.C. Wren, Effects of γ -radiation versus H_2O_2 on carbon steel corrosion, *Electrochim. Acta*, 55 (2010) 2767–2776.
- [8] Q.W. Knapp, J.C. Wren, Film formation on type-316L stainless steel as a function of potential: Probing the role of gamma-radiation, *Electrochim. Acta*, 80 (2012) 90–99.
- [9] L. Wang, K. Daub, Q. Knapp, Z. Qin, J.J. Noel, J.C. Wren, Effect of ferrous ions on oxide film formation and conversion on stainless steel, *J. Electrochem. Soc.*, 159 (2012) C503–C512.
- [10] N. Perez, *Electrochemistry and Corrosion Science*, Kluwer Academic Publishers, Boston, 2004.
- [11] W.G. Burns, W.R. Marsh, W.S. Walters, The γ irradiation-enhanced corrosion of stainless and mild steels by water in the presence of air, argon and hydrogen, *Radiat. Phys. Chem.*, 21 (1983) 259–279.
- [12] R.J. Winsley, N.R. Smart, A.P. Rance, P.A.H. Fennell, B. Reddy, B. Kursten, Further studies on the effect of irradiation on the corrosion of carbon steel in alkaline media, *Corros. Eng. Sci. Technol.*, 46 (2011) 111–116.
- [13] M. Pourbaix, *Atlas of Electrochemical Equilibria in Aqueous Solution*, NACE, Houston, TX, 1996.

- [14] J. Chivot, L. Mendoza, C. Mansour, T. Pauporté, M. Cassir, New insight in the behaviour of Co–H₂O system at 25–150 °C, based on revised Pourbaix diagrams, *Corros. Sci.*, 50 (2008) 62–69.
- [15] A. Bandura, S.N. Lvov, The Ionization constant of water over wide ranges of temperature and density, *J. Phys. Chem. Ref. Data.*, 35 (2006) 16–30.
- [16] S.-L. Chou, J.-Z. Wang, H.-K. Liu, S.-X. Dou, Electrochemical deposition of porous Co(OH)₂ nanoflake films on stainless steel mesh for flexible supercapacitors, *J. Electrochem. Soc.*, 155 (2008) A926–A929.
- [17] J. Yang, H. Liu, W.N. Martens, R.L. Frost, Synthesis and characterization of cobalt hydroxide, cobalt oxyhydroxide, and cobalt oxide nanodiscs, *J. Phys. Chem. C*, 114 (2010) 111–119.
- [18] E. Zhang, Y. Tang, Y. Zhang, C. Guo, L. Yang, Hydrothermal synthesis of β-nickel hydroxide nanocrystalline thin film and growth of oriented carbon nanofibers, *Mater. Res. Bull.*, 44 (2009) 1765–1770.
- [19] L. Wang, K. Daub, Z. Qin, J.C. Wren, Effect of dissolved ferrous iron on oxide film formation on carbon steel, *Electrochim. Acta*, 76 (2012) 208–217.
- [20] H.-S. Shim, V.R. Shinde, H.J. Kim, Y.-E. Sung, W.B. Kim, Porous cobalt oxide thin films from low temperature solution phase synthesis for electrochromic electrode, *Thin Solid Films*, 516 (2008) 8573–8578.
- [21] G. Schikorr, The iron (II) hydroxide and a ferromagnetic iron (III) hydroxide, *Allg. Chem.*, 212 (1933) 33–39.

CHAPTER 7

Combined Effects of pH and γ -Radiation on Corrosion of Co-Cr Alloy Stellite-6 at 80 °C and 150 °C

7.1 INTRODUCTION

Aqueous corrosion is an electrochemical process consisting of interfacial redox and charge transfer reactions and mass and charge transport through the solution phase and, if present, the solid oxide phase. The aqueous environmental parameters pH and temperature, and the presence of water radiolysis products affect the individual elementary steps of the corrosion process differently. In Chapter 4, we examined the effect of γ -radiation on the corrosion of Stellite-6 at three different pH values at room temperature. The room temperature study found that γ -radiation increases the corrosion potential by producing strong oxidants from water radiolysis and hence increases the overall rate of cobalt oxidation at a given pH. However, the consequence of the increase in the rate of metal oxidation varies with pH; the increase in cobalt oxidation leads mainly to an increase in cobalt dissolution at pH 6.0, whereas it leads mainly to an increase in oxide growth at pH 10.6. This difference was attributed to a dependence of Co^{II} solubility on pH that affects the relative rates of the two competing reactions, the growth of cobalt oxides and the transport of $\text{Co}^{2+}(\text{aq})$ in the solution phase differently.

This chapter presents work on the combined effect of pH and γ -radiation on Stellite-6 corrosion at higher temperatures, 80 °C and 150 °C. For these studies, Stellite-6 coupons submerged in deaerated water were corroded in sealed quartz vials for 3 days in the absence and presence of radiation. At each temperature, the corrosion tests were performed at three different initial $\text{pH}_{25^\circ\text{C}}$ 6.0, 8.4 and 10.6. At the end of a 3-d corrosion period the changes in the coupon surfaces were examined by SEM, XPS and AES, and the concentrations of metal ions dissolved in the test solutions were analyzed by ICP-MS.

7.2 EXPERIMENTAL

The corrosion tests at 80 °C and 150 °C were performed with a test coupon, 3-mm thick and 9 mm in diameter, submerged in a deaerated electrolyte solution in a leak-tight quartz/borosilicate vial, similar to that used for the room temperature study described in Chapter 5. For the high temperature studies presented here the amount of solution added was limited to 7 ml so that the solution level at 80 °C and 150 °C (taking into account thermal expansion of the liquid) would remain below the quartz/borosilicate transition, and, hence, minimize the dissolution of silicate. (It was found that a significant amount of silicate is dissolved even from a quartz vial at the high temperatures. The silicate does not participate in the electrochemical corrosion process but it can precipitate on the coupon surface during drying.) The sealed vials were then placed inside a 250 mL type 316 stainless steel autoclave (Parr Instrument Company, model 4760) and the autoclave was partially filled with water to provide a pressure balance on the vials when heated. With this experimental design the seals

on all sample vials remained leak-tight throughout the tests. The experimental set-up and test vial arrangement in the pressure vessel is schematically shown in Figure 7.1.

The autoclave was heated to a desired temperature, 80 °C or 150 °C, which took approximately 15 or 40 min, respectively. Once the desired temperature was reached the autoclave was either left on the bench or placed inside a Cobalt-60 irradiator (MDS Nordion Gamma Cell 220 Excel) for 72 h (3 d). The gamma cell provided a dose rate of 5.5 kGy h⁻¹ during these tests, where 1 Gy is equal to 1 J·kg⁻¹. At the end of each test the heater was turned off and the autoclave was allowed to cool to a comfortable handling temperature (roughly 80 °C) for the 150 °C experiments (this took approximately 15 min). When the autoclave was sufficiently cooled, it was opened and the sample vials were removed. The vials were opened and the coupons were removed and dried with flowing argon gas. The oxide films on the coupons were then analyzed using various surface analysis techniques. The residual solution in the sample vials was analyzed for pH and dissolved metal content using ICP-MS.

The experiments at each temperature were performed at three different initial pH_{25°C} values, 6.0, 8.4, 10.6, where pH_{25°C} represents the pH measured at 25 °C. The electrolyte solutions were prepared such that the ionic strength was similar in all of the solutions. For the pH_{25°C} 6.0 solution, a 0.01 M boric acid solution was first prepared and its pH was adjusted by adding 0.01 M NaOH dropwise. For the pH_{25°C} 8.4 solution, a 0.01 M sodium borate solution was first prepared and its pH was adjusted by adding 0.5 M boric acid dropwise. For the pH_{25°C} 10.6 solution, the pH of the 0.01 M sodium borate solution was adjusted by

adding 1 M NaOH dropwise. The sodium borate and the boric acid solutions were prepared using reagent grade $\text{Na}_2\text{B}_4\text{O}_7 \cdot 10\text{H}_2\text{O}$ (99.5%, Caledon Laboratories Ltd.) and H_3BO_3 (99.5%, Caledon Laboratories Ltd.), respectively. The water was purified using a NANO pure Diamond UV ultra-pure water system from Barnstead International to remove organic and inorganic impurities; this water had a resistivity of 18.2 $\text{M}\Omega \text{ cm}$.

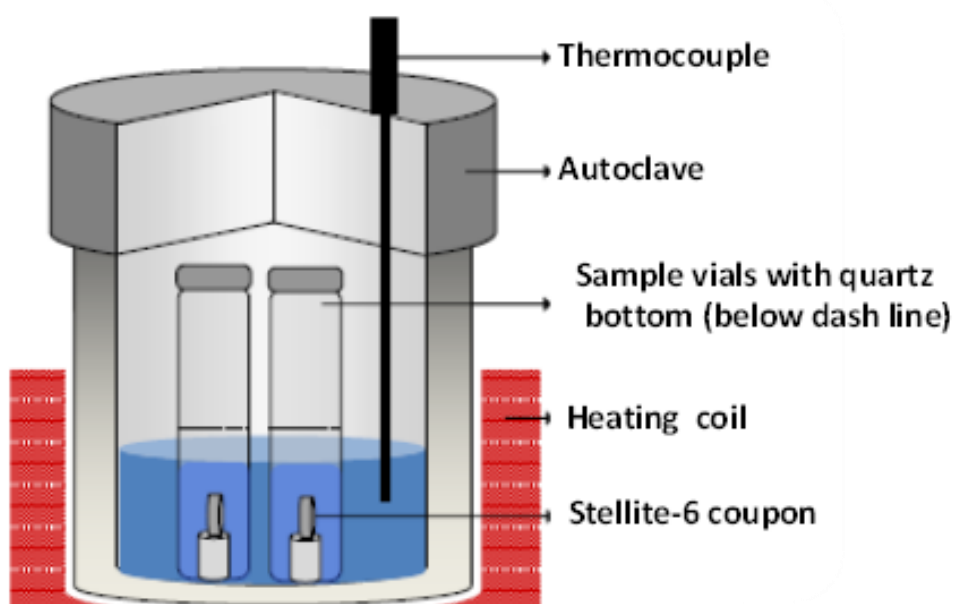


Figure 7.1: Schematic diagram of the experimental set-up, showing the test vial arrangement in the pressure vessel.

7.3 RESULTS

The effects of pH and γ -radiolysis on the 3-d corrosion of Stellite-6 were investigated by analyzing the corroded surfaces as well as the concentrations of Co and Cr dissolved in the test solutions. Each individual analysis method provides limited information on the

consequences of corrosion, but collectively they provide a more complete picture. The SEM and XPS analyses show the changes in morphology and oxidation state of metal in the surface oxide layer due to corrosion more clearly. The extent of corrosion can be seen more clearly from the depth profiles of the oxide layer as determined by AES, and the concentrations of Co and Cr dissolved in the post-test solutions provide information on the rate of metal dissolution. In discussing the results, the SEM and XPS analysis data are presented first, followed by the AES depth profiles and ICP-MS results.

7.3.1 Effects of pH and γ -radiolysis at 80 °C

7.3.1.1 SEM and XPS analysis results

The SEM images of the surfaces of the coupons corroded in the absence of γ -radiation show a small effect of pH on surface morphology (no-Rad in Figure 7.2). The coupons corroded at $\text{pH}_{25^\circ\text{C}}$ 6.0 and 8.4 show smooth surfaces, but the surface level of the Co-rich phase appears to be lower than that of the Cr-rich phase and the phase boundary also appears to be better defined than that observed for the freshly polished surface (also shown in Figure 7.2) and for coupons corroded at these pHs at 25 °C (Figure 5.1 in Chapter 5) [1]. These features are more pronounced on the coupon corroded at $\text{pH}_{25^\circ\text{C}}$ 8.4 than at $\text{pH}_{25^\circ\text{C}}$ 6.0. These results suggest that metal dissolution occurs more readily at the phase boundary and more readily from the surface of the Co-rich phase than from the Cr-rich phase, but corrosion appears to occur uniformly over each phase. The different surface levels of the two phases suggest that the oxide layer is not $\text{Co}(\text{OH})_2$, see further discussion below, but it is more likely Cr_2O_3 and/or Co^{II} incorporated into the chromium oxide. The coupon corroded at $\text{pH}_{25^\circ\text{C}}$ 10.6

shows a thin network of filaments over an inner oxide layer that has morphological features similar to those observed on coupons corroded at the lower pHs.

The analysis of the high resolution XPS spectra of the Co 2p bands taken for these surfaces (Figure 7.3a) indicates that the oxide layers present on the un-irradiated coupons corroded at $\text{pH}_{25^\circ\text{C}}$ 8.4 and 10.6 are thicker than the XPS analysis depth range (less than 9 nm), whereas the oxide layer present on the coupon corroded at $\text{pH}_{25^\circ\text{C}}$ 6.0 is very thin. The detailed XPS analysis presented in Table 7.1 shows that the oxides present on these surfaces are mostly in the form of Co(OH)_2 . In the presence of a thick oxide layer chromite (CoCr_2O_4) (seen on an un-irradiated coupon corroded at room temperature [1]) might be present as a very thin inner layer but its contribution to the XPS Co 2p band intensity would be small to be detected. The coupons corroded at $\text{pH}_{25^\circ\text{C}}$ 6.0 and 8.4 also show the presence of higher oxidation states of Co ($\text{Co}_3\text{O}_4/\text{CoOOH}$). Their presence are near background levels and may be due to air oxidation of surface adsorbed $\text{Co}^{2+}(\text{aq})$. (Air oxidation occurs more readily on a hotter surface and although we tried to minimize it may still have occurred during sample handling prior to the surface analyses.)

The coupons corroded in the presence of γ -radiation show more extensive morphological changes (images labeled Rad in Figure 7.2). The coupons corroded at the three different pHs all show a network of filaments with granular particulates distributed over this filament layer.

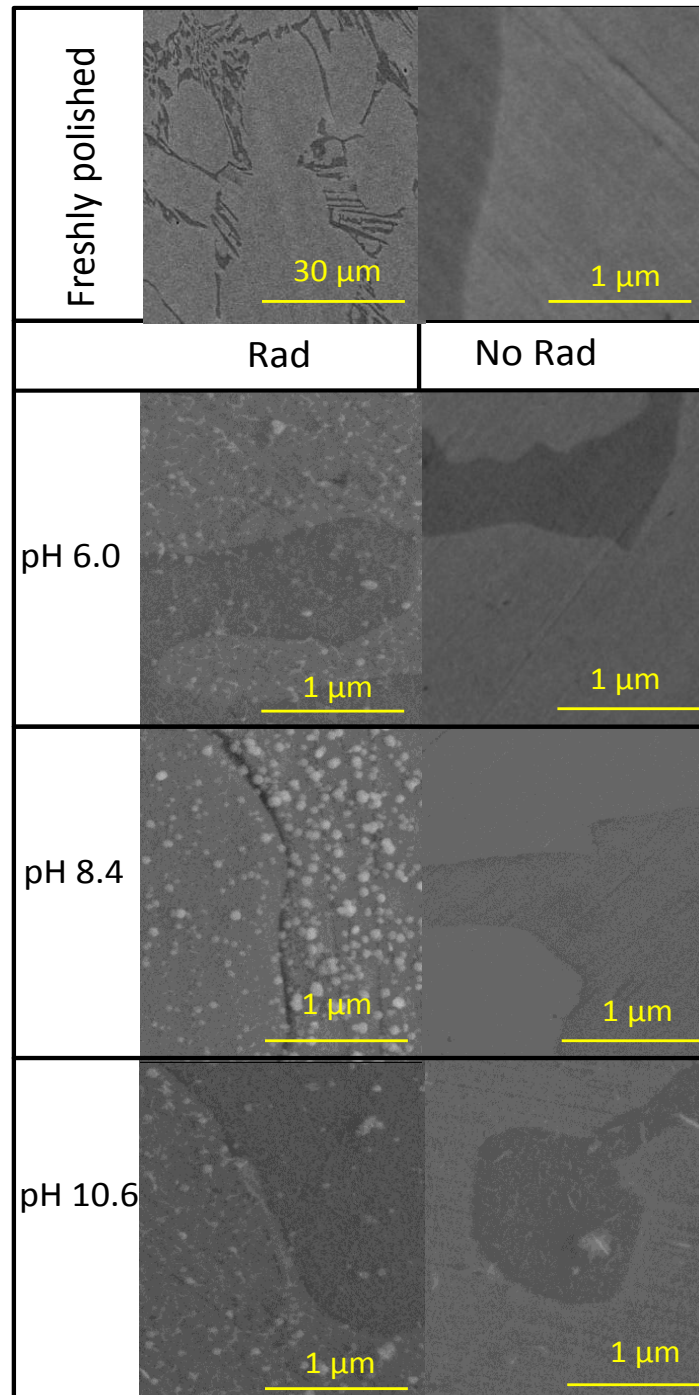


Figure 7.2: SEM images of the surfaces of Stellite-6 coupons corroded for 3 d at $\text{pH}_{25^\circ\text{C}}$ 6.0, 8.4 and 10.6 in the absence (no Rad) and in the presence of radiation (Rad) at 80°C . The darker coloured region corresponds to the Cr-rich phase.

The filament-like inner layer is denser and thicker at a higher pH. A filament-like morphology is a common feature associated with the more soluble form of many transition metal hydroxides (such as Co^{II} , Fe^{II} and Ni^{II} hydroxides) [2–7]. The XPS analysis of these surfaces shows that the layer is mostly composed of $\text{Co}(\text{OH})_2$ and that a thicker layer of $\text{Co}(\text{OH})_2$ is formed at a higher pH. The shape of the granular particulates suggests that they are less soluble oxides and the XPS results suggests that they are likely $\text{Co}^{\text{II}}/\text{Co}^{\text{III}}$ oxide (Co_3O_4) or Co^{III} oxide/hydroxide (CoOOH). The fractions of these oxides in the XPS Co 2p band are, however, near background levels and such assignments cannot be conclusive. The SEM images show that the particulates are distributed more densely on the Co-rich phase than on the Cr-rich phase, and the boundary between two phases are wider on the irradiated coupons than on the un-irradiated coupons. These changes are most clearly observed on the coupon irradiated at $\text{pH}_{25^\circ\text{C}} 8.4$; the particulates are the largest in size and appear most densely. These results suggest that metal dissolution has occurred preferentially along the phase boundaries and from the surface of the Co-rich phase compared to the Cr-rich phase. This preferential dissolution is magnified in the presence of radiation.

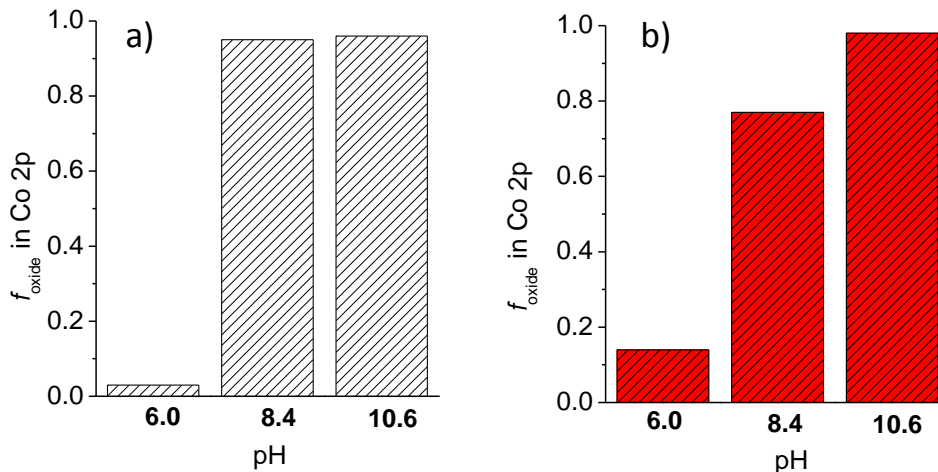


Figure 7.3: Ratio of the Co oxide component to the sum of the Co oxide and Co metal components in the high resolution XPS of the Co 2p bands (f_{oxide}) taken for a) the un-irradiated and b) the irradiated coupons at three $\text{pH}_{25^\circ\text{C}}$ values at 80°C .

Table 7.1: Cobalt speciation in the surface layer on the Stellite-6 coupons corroded at 80°C determined by the analysis of the high resolution XPS of the Co 2p bands.

Co Species	$\text{pH}_{25^\circ\text{C}} 10.6$		$\text{pH}_{25^\circ\text{C}} 8.4$		$\text{pH}_{25^\circ\text{C}} 6.0$	
	No Rad %	Rad %	No Rad %	Rad %	No Rad %	Rad %
Co^0	4	2	5	23	97	86
CoCr_2O_4	ND ¹	ND	ND	ND	ND	ND
$\text{Co}(\text{OH})_2$	96	98	93	75	1	13
Co_3O_4	ND	ND	1	1	1	0
CoOOH	ND	ND	1	1	1	1

1. Not detected

7.3.1.2 AES and ICP-MS analysis results

The depth profiles of the surface layers analyzed by AES with Ar^+ sputtering are shown in Figures 7.4 and 7.5. Figure 7.4 presents the atomic percentages of the elements analyzed as a function of sputtered depth. The results show that the outermost surface composition (at a nominal depth of 0 nm) is contaminated by carbon or adsorbed hydrated species and does not provide any meaningful information on the oxide formed during corrosion. The figure also illustrates that the atomic % of oxygen decreases gradually with depth, and accordingly the atomic % of all of the metallic elements increase with depth. The change in concentrations of the individual atom types can obscure changes in the oxides that are present. To observe more clearly the degree of oxidation of the two main alloying components and their relative abundances in the oxide, the AES data are presented as the ratios of $\text{O}/(\text{Co} + 1.5 \text{Cr})$ and $\text{Co}/(\text{Co} + \text{Cr})$ as a function of sputtered depth in Figure 7.5. The ratio of O to $(\text{Co} + 1.5 \text{Cr})$ equal to 1 corresponds to either a 1:1 mixture of CoO and Cr_2O_3 or a distinct phase of CoCr_2O_4 (chromite). If the oxide is $\text{Co}(\text{OH})_2$ the ratio will be 2.0. Note that the oxide layer formed on a corroding surface will not be in a pure phase with a constant ratio of metal to oxygen but the metal cation and oxygen anions will have concentration gradients across the oxide layer. Also in any sputtering technique the elemental composition at a given depth will be influenced by the bulk composition of the alloy.

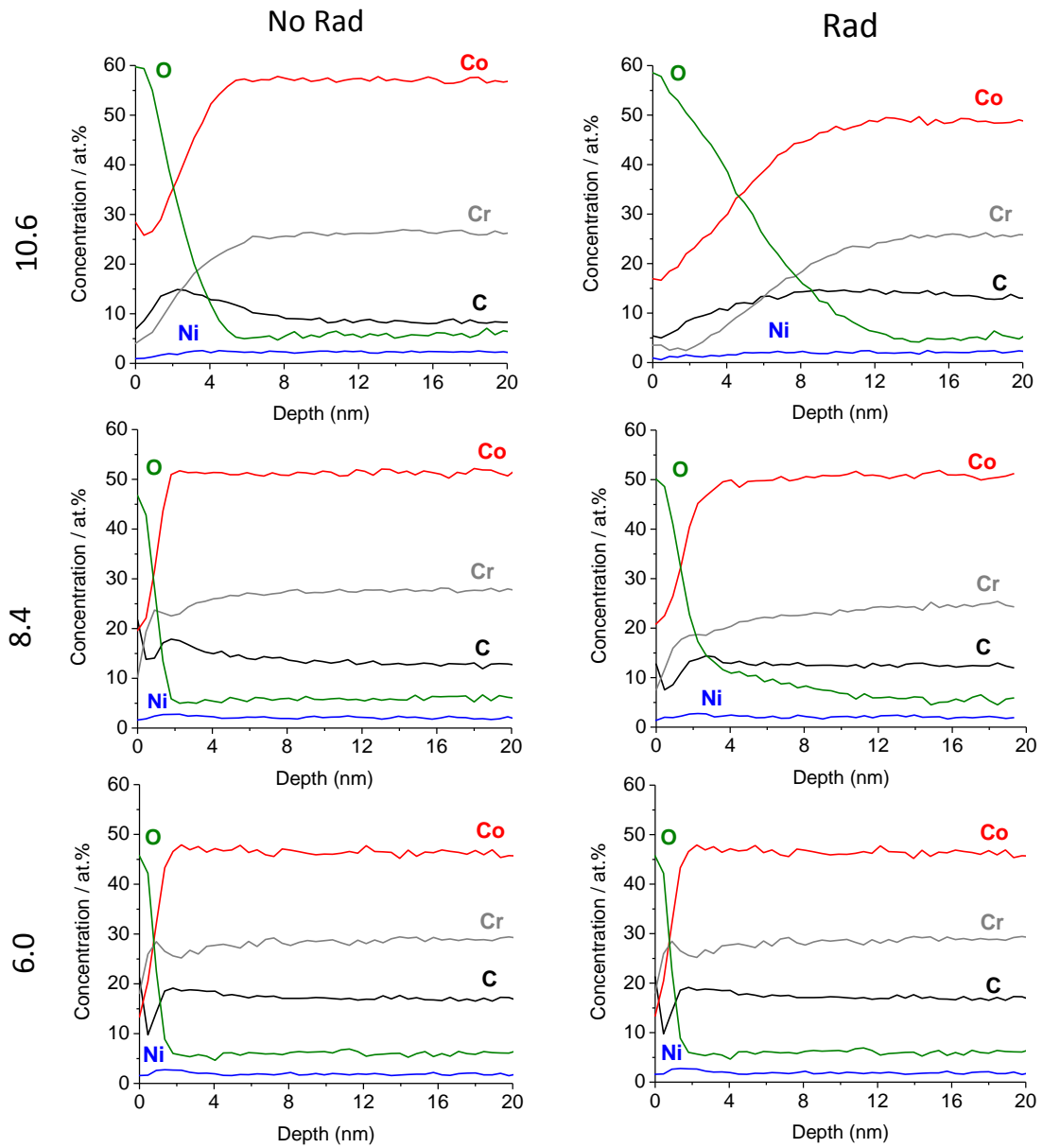


Figure 7.4: Depth profiles of the elements on Stellite-6 coupons corroded for 3 d in the absence of radiation (no Rad) and in the presence of radiation (Rad) at three pHs at 80 °C.

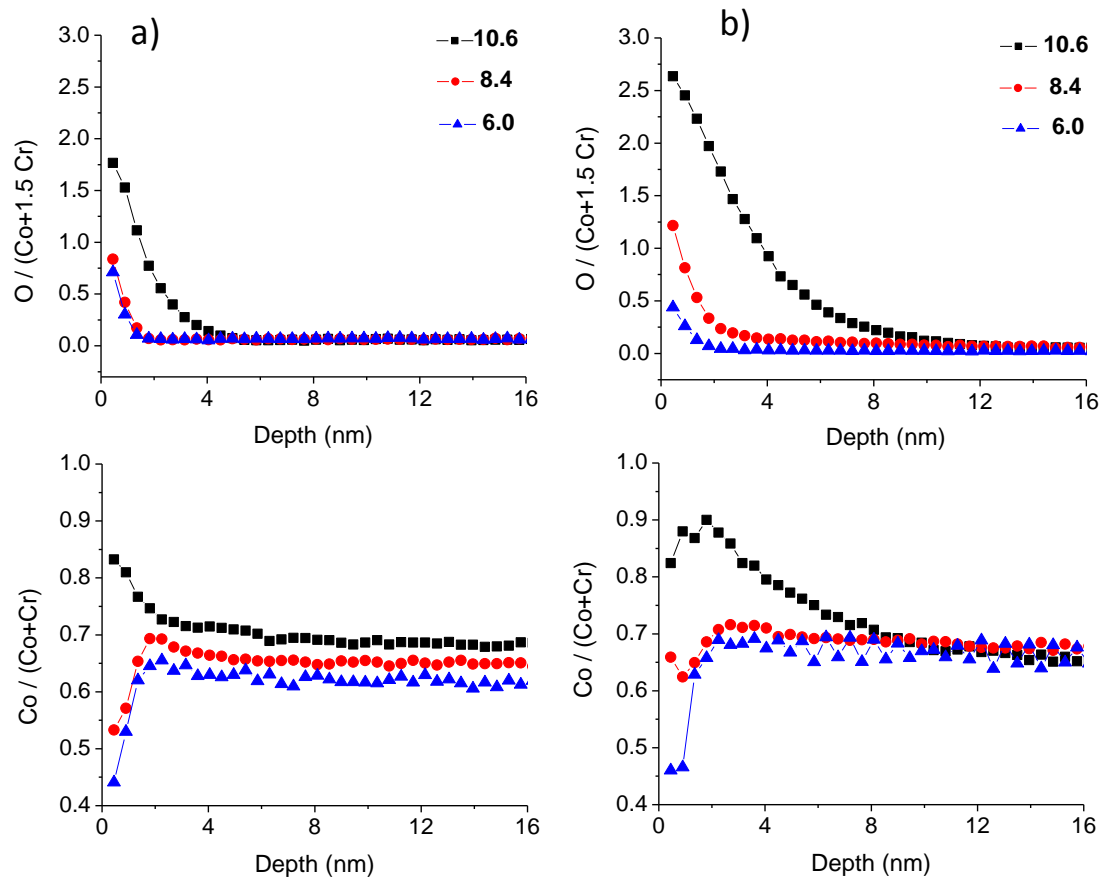


Figure 7.5: Depth profiles of $O/(Co + 1.5 Cr)$ and $Co/(Co + Cr)$ determined by AES on Stellite-6 coupons corroded at $pH_{25}^{\circ}C$: 10.6 (—■—), 8.4 (—●—), and 6.0 (—▲—). The left panel a) presents the results obtained in the absence of radiation and the right panel b) presents the results obtained in the presence of radiation at 80 °C.

The results of tests in the absence of radiation will be discussed first. On the coupon corroded at $pH_{25}^{\circ}C$ 6.0 without irradiation, the $O/(Co + 1.5 Cr)$ ratio decreases exponentially from ~ 0.7 to 0 with depth within the first 2 nm. Within this depth range the $Co/(Co + Cr)$ ratio increases steadily from about 0.4 to a maximum value of ~ 0.65 at ~ 2 nm, before it decreases slightly and reaches a constant value of ~ 0.63 at ~ 4 nm. The average ratio of

Co/(Co + Cr) in the bulk alloy phase is ~ 0.66 . Similar depth profiles were observed for the coupons corroded at $\text{pH}_{25^\circ\text{C}} 8.4$ without irradiation but with slightly higher values of O/(Co + 1.5 Cr) and Co/(Co + Cr). The depth profiles on the coupons corroded at $\text{pH}_{25^\circ\text{C}} 10.6$ without irradiation are very different from those observed at the two lower pHs. The O/(Co + 1.5 Cr) ratio near the surface is ~ 1.8 , higher than the values observed at $\text{pH}_{25^\circ\text{C}} 6.0$ and 8.4 , and this ratio decreases with depth, approaching zero at ~ 6 nm. The Co/(Co + Cr) ratio is also higher near the surface compared to the ratios observed at that location at the two lower pHs. More importantly, the Co/(Co + Cr) ratio decreases with depth from ~ 0.9 to ~ 0.66 at ~ 6 nm, showing the opposite depth dependence to that was seen at $\text{pH}_{25^\circ\text{C}} 8.4$ and 6.0 .

The ICP-MS results presented in Table 7.2 show that in the absence of radiation the largest Co dissolution occurred at $\text{pH}_{25^\circ\text{C}} 6.0$. Coupons in these tests have the thinnest oxide layer as well. The least dissolution occurred at $\text{pH}_{25^\circ\text{C}} 10.6$ and these coupons had the thickest oxide layer. The amounts of Cr dissolved in all un-irradiated tests are very small and approximated the same for all three pHs. The combined results of the ICP-MS and AES analyses indicate that the metal that was oxidized during aqueous corrosion with no radiation is mostly Co. The resultant Co^{II} is either incorporated into an oxide layer (as CoCr_2O_4 or CoO/Co(OH)_2) at a high pH or dissolved into the solution at a low pH. The pH dependent competition between oxide formation and dissolution determines how fast a protective oxide can grow.

Table 7.2: The concentrations of Co and Cr dissolved in the test solutions after 3-d corrosion at 80 °C determined by ICP-MS.

pH _{25°C}	No Rad		Rad	
	Co (µg/L)	Cr (µg/L)	Co (µg/L)	Cr (µg/L)
6.0	89	2	250	100
8.4	18	1	34	150
10.6	5	4	7	82

Besides the possibility of Co loss due to dissolution, a lower ratio of Co/(Co + Cr) near the surface than the normal ratio of the bulk alloy phase can also mean that the surface is enriched with Cr. Such enrichment is often attributed to Cr migration to the outer oxide surface during corrosion of Cr-containing alloys [8]. In our work, the combined ICP-MS and AES results suggest that this is not occurring and the thin (~ 2 nm) oxide layer present on the coupons corroded at pH_{25°C} 6.0 and 8.4 is only depleted in Co due to Co dissolution. The thin oxide layer that is formed at these pHs is likely defective chromium oxide that was created prior to the tests by air oxidation. At low pHs in the absence of radiation where Co^{II} dissolution occurs readily this layer is not altered. However, at pH_{25°C} 10.6 where the Co^{II} solubility is much lower, the Co^{II} that is formed can be incorporated into the chromium oxide layer converting it to thermodynamically more stable CoCr₂O₄ [9] (see also Chapters 4 and 5). This interpretation is also consistent with the surface morphologies observed by SEM (Figure 7.2) and the oxidation states of Co determined by XPS (Figure 7.3 and Table 7.1).

The effect of γ -radiation on the depth profiles of the ratios depends on pH. At $\text{pH}_{25}^{\circ}\text{C}$ 6.0, a coupon corroded in the presence of radiation shows depth profiles that are similar to those for corrosion in the absence of radiation. Within the first 2 nm, the $\text{O}/(\text{Co} + 1.5 \text{ Cr})$ ratio decreases with depth from ~ 0.5 to 0 while $\text{Co}/(\text{Co} + \text{Cr})$ increases from ~ 0.4 to ~ 0.66 , indicating this layer is mostly made of chromium oxide. However, the dissolved amounts of both Co and Cr (Table 7.2) are significantly higher in the irradiated tests. It appears that γ -radiation increases the rate of metal oxidation and at $\text{pH}_{25}^{\circ}\text{C}$ 6.0 this increase results in increased metal dissolution.

The depth profiles obtained for a coupon corroded at $\text{pH}_{25}^{\circ}\text{C}$ 8.4 in the presence of radiation show small differences from those observed in the absence of radiation. In the first 3 nm, $\text{O}/(\text{Co} + 1.5 \text{ Cr})$ decreases rapidly with depth (the same behaviour seen in the absence of radiation). However, the ratio is slightly higher near the surface (< 1 nm) at ~ 1.5 and decreases only to ~ 0.2 at ~ 3 nm. Within this depth range, the $\text{Co}/(\text{Co} + \text{Cr})$ ratio near the surface (< 1 nm) decreases from ~ 0.65 to ~ 0.6 and then increases with depth to a maximum value of 0.7 at ~ 3 nm. Further into the oxide $\text{O}/(\text{Co} + 1.5 \text{ Cr})$ continues to decrease but at a slower rate, reaching zero at ~ 10 nm, but $\text{Co}/(\text{Co} + \text{Cr})$ switches its depth dependence, decreasing slightly from the maximum value of 0.7 and reaching a constant value at ~ 0.66 at ~ 10 nm. The amounts of metal dissolved from the irradiated coupons (Table 7.2) are also higher than those from the un-irradiated coupon. At $\text{pH}_{25}^{\circ}\text{C}$ 8.4 γ -radiation leads to a significant increase in Cr dissolution but only a moderate increase in Co dissolution. The amount of dissolved Cr is higher while that of Co is lower at $\text{pH}_{25}^{\circ}\text{C}$ 8.4 compared to $\text{pH}_{25}^{\circ}\text{C}$ 6.0.

At $\text{pH}_{25^\circ\text{C}}$ 10.6 and 80°C , the depth profiles of $\text{O}/(\text{Co} + 1.5 \text{ Cr})$ and $\text{Co}/(\text{Co} + \text{Cr})$ of irradiated coupons are similar to those of un-irradiated coupons. Both ratios decrease with depth before they reach constant values at $\sim 10 \text{ nm}$. The $\text{Co}/(\text{Co} + \text{Cr})$ ratio near the surface (within the first 3 nm) is ~ 0.9 . In this region the $\text{O}/(\text{Co} + 1.5 \text{ Cr})$ ratio changes from ~ 2.5 to ~ 1.5 , indicating that this outer layer is mostly made of $\text{Co}(\text{OH})_2$, consistent with the XPS results (Table 7.1). Gamma-radiation at this pH increases Cr dissolution but not Co dissolution (Table 7.2).

The amounts of Co and Cr dissolved after 3-d corrosion at 80°C in the presence of γ -radiation are higher than those observed in absence of radiation (Table 7.2). The pH dependence of Co dissolution is similar in the presence or absence of radiation; the most Co dissolution occurs at $\text{pH}_{25^\circ\text{C}}$ 6.0 and the least at $\text{pH}_{25^\circ\text{C}}$ 10.6. Correspondingly, a coupon corroded at $\text{pH}_{25^\circ\text{C}}$ 6.0 has the thinnest oxide layer and the thickest oxide layer is made at $\text{pH}_{25^\circ\text{C}}$ 10.6. The behaviour at 80°C is the same as that seen at room temperature [1], γ -radiation increases the rate of oxidation of Co to Co^{II} and this leads mainly to Co dissolution at $\text{pH}_{25^\circ\text{C}}$ 6.0 and Co-oxide growth at $\text{pH}_{25^\circ\text{C}}$ 10.6.

The combined effect of γ -radiation and pH on Cr dissolution is very different from that on Co dissolution. At 80°C γ -radiation increases Cr dissolution significantly at all pHs (Table 7.2). The higher Cr dissolution shows no correlation with the depth profiles of the ratios of different elements (Figures 7.4 and 7.5). The reason for the increase is not clear. One possible explanation is that the Cr dissolution is a result of localized corrosion. The SEM images show that radiation increases corrosion and the Co oxidation is more significant

along the phase boundaries and on the Co-rich phase than on Cr-rich phase; the difference between the corrosion rates on different phases is most pronounced at $\text{pH}_{25^\circ\text{C}} 8.4$. The higher levels of Cr dissolution may be occurring because a more chromium enriched oxide layer is exposed to water.

Surface hydration of Cr^{III} oxides from Cr_2O_3 to CrOOH and to $\text{Cr}(\text{OH})_3$ occurs at a faster rate and the Cr^{III} solubility is higher at 80°C than at 25°C [10,11]. Both kinetics and thermodynamics favour increased Cr^{III} dissolution at a higher temperature. As more Co dissolves, more Cr^{III} is exposed to water and the more Cr dissolution occurs. Note that any freshly exposed Cr will be immediately oxidized to Cr_2O_3 due to its thermodynamic stability [12] and Cr dissolution occurs from Cr^{III} oxides/hydroxides. The potentiostatic polarization studies presented in Chapters 4 and 5 show that oxidation of Cr^{III} to soluble Cr^{VI} species requires highly oxidizing environments and this process cannot compete with Co oxidation even in the presence of radiation-enhanced redox potentials.

Surface hydration of transition metal oxides is known to increase with pH [13]. However, the Cr dissolution is highest at $\text{pH}_{25^\circ\text{C}} 8.4$ not at $\text{pH}_{25^\circ\text{C}} 10.6$. We suspect that the Cr dissolution at the higher pH is due to the faster growth of a protective Co oxide layer at $\text{pH}_{25^\circ\text{C}} 10.6$. Looking ahead, results will show that even thicker Co-oxides observed for corrosion at 150°C further suppress Cr dissolution (Section 7.4.1). The observed temperature and pH dependences of Cr dissolution cannot be explained by oxidative dissolution of Cr^{III} to Cr^{VI} (often referred to as transpassive dissolution) [14,15].

7.3.2 Effects of pH and γ -radiolysis at 150 °C

7.3.2.1 SEM and XPS analysis results

The SEM images of Stellite-6 coupons corroded for 3 d at three different pH values at 150 °C with and without irradiation are shown in Figure 7.7. Corrosion at 150 °C has brought more morphological changes than corrosion at 80 °C. In the absence of radiation, all coupons show a filament-like network but with varying degrees of size and length of the filaments. The XPS analyses of these surfaces show that the thickness of the oxide layer increases with increasing pH (Figure 7.7) and that these oxides mainly consist of CoCr_2O_4 and $\text{Co}(\text{OH})_2$ (Table 7.3). The fraction of Co in higher oxidation states (Co_3O_4 and CoOOH) is generally larger on the coupons corroded at 150 °C than at 80 °C and this is attributed to easier post-test air oxidation of the adsorbed $\text{Co}^{2+}(\text{aq})$ on a hotter surface as described earlier. The fraction of the sum of Co_3O_4 and CoOOH in the XPS Co 2p band is larger when the ratio of CoCr_2O_4 to $\text{Co}(\text{OH})_2$ is higher. The fraction is also larger at $\text{pH}_{25^\circ\text{C}}$ 6.0 and 10.6 than at $\text{pH}_{25^\circ\text{C}}$ 8.4. AES depth profile analysis (see later) shows that the oxide layer formed at $\text{pH}_{25^\circ\text{C}}$ 6.0 is very thin and is more depleted of Co near the surface, whereas the oxide layers formed at the other pHs are thicker and are more enriched in Co near the surface (Figure 7.9). The ICP-MS analysis (see later) shows that the amount of Co released decreases with increasing pH (Table 7.4). That the fraction of Co_3O_4 and CoOOH correlates better with the ratio of CoCr_2O_4 to $\text{Co}(\text{OH})_2$ than the oxide thickness and the Co concentration in the oxide layer indicates that an outer layer of Co_3O_4 and CoOOH is more easily formed from CoCr_2O_4 than

from Co(OH)_2 . These results further support our belief that the observed higher oxidation state Co-oxides are likely to have been formed by air oxidation of adsorbed $\text{Co}^{2+}(\text{aq})$.

The greatest impact of γ -radiation on oxide surface morphology at 150 °C was observed on the coupons corroded at $\text{pH}_{25^\circ\text{C}}$ 6.0 (Figure 7.6). Instead of a filament-like structure, granular particulates similar to those observed on coupons corroded at 80 °C, albeit in much smaller sizes, can be seen distributed on the irradiated coupon. As well the Cr-rich phase also appears to be protruded compared to the Co-rich phase. The XPS analysis of the coupons also shows a thinner oxide on the irradiated coupon than the un-irradiated coupon at this pH (Figure 7.7). Gamma-radiation induces a negligible morphological change for the coupons corroded at $\text{pH}_{25^\circ\text{C}}$ 8.4 except for the density of the filament-like network (Figure 7.6). The XPS analysis shows a thicker oxide on the irradiated coupon than on the un-irradiated coupon but no change in the oxide composition; the oxides on both surfaces are mostly made of Co(OH)_2 (Table 7.3). The effect of γ -radiation at $\text{pH}_{25^\circ\text{C}}$ 10.6 is similar to that at $\text{pH}_{25^\circ\text{C}}$ 8.4. Radiation only increases the density of the filament-like network. The XPS analysis shows that the oxides on both irradiated and un-irradiated coupons at this pH are thicker than the instrument analysis depth (< 9 nm). The relative fraction of Co(OH)_2 to CoCr_2O_4 is higher on the irradiated coupon than on the un-irradiated coupon indicating that irradiation favours faster growth of Co(OH)_2 (Table 7.3).

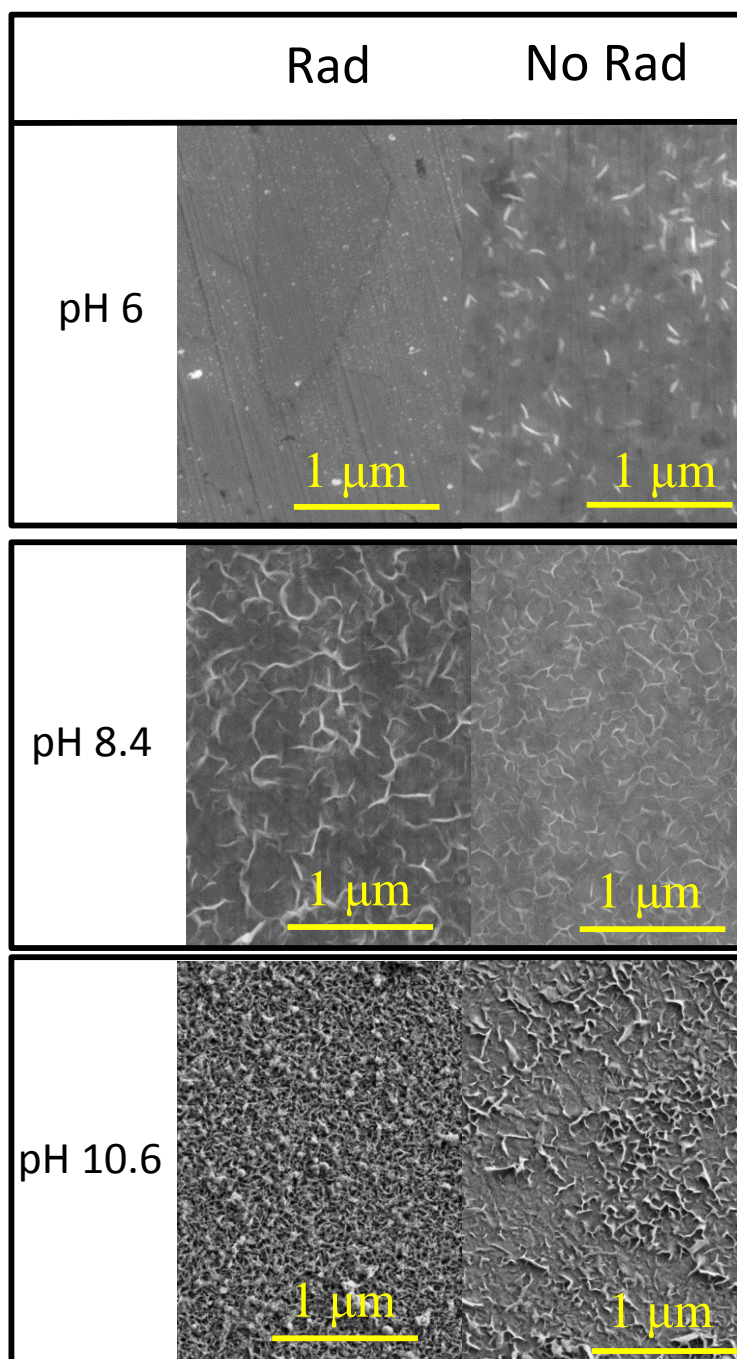


Figure 7.6: SEM images of the surfaces of the Stellite-6 coupons corroded for 3 d at three different $\text{pH}_{25}^{\circ}\text{C}$ values, in the absence and presence of radiation, at 150°C .

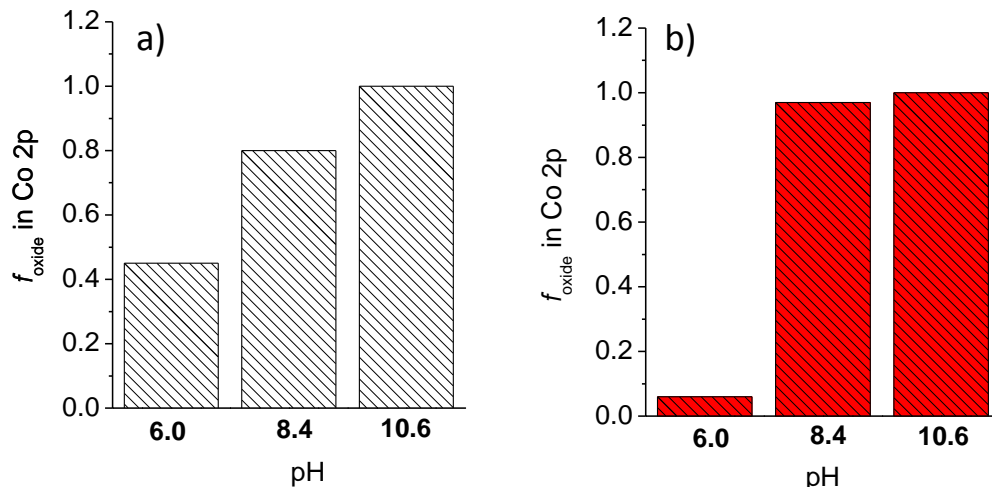


Figure 7.7: Ratio of oxide to sum of oxide and Co metal (f_{oxide}) as determined by XPS analysis of a) un-irradiated, and b) irradiated coupons at three pH values at 150 °C.

Table 7.3: Cobalt speciation in the surface layer on the Stellite-6 coupons corroded at 150 °C determined by the analysis of high resolution XPS of the Co 2p bands.

Co Species	pH _{25°C} 10.6		pH _{25°C} 8.4		pH _{25°C} 6.0	
	No Rad %	Rad %	No Rad %	Rad %	No Rad %	Rad %
Co ⁰	ND ¹	ND	20	1	60	94
CoCr ₂ O ₄	41	8	1	4	19	ND
Co(OH) ₂	52	91	78	91	8	5
Co ₃ O ₄	7	1	1	2	8	0
CoOOH	0	0	0	0	5	1

1. Not detected

7.3.2.2 AES and ICP-MS analysis results

Figure 7.8 shows the atomic percentages of the elements present on the surface as a function of sputtered depth for the coupons corroded at 150 °C. For the reasons described earlier these data are replotted as the ratios of $O/(Co + 1.5 Cr)$ and $Co/(Co + Cr)$ as a function of depth in Figure 7.9.

On the coupon corroded at $pH_{25^{\circ}C}$ 6.0 without irradiation the $O/(Co + 1.5 Cr)$ ratio decreases exponentially from ~ 1.0 to 0 within the first 2 nm. Within this depth range, $Co/(Co + Cr)$ is initially constant at ~ 0.4 and then increases rapidly to ~ 0.6 . The $Co/(Co + Cr)$ ratio continues to increase for another 1 nm before it approaches a constant value of 0.65. These depth profiles of $O/(Co + 1.5 Cr)$ and $Co/(Co + Cr)$ are very similar to those observed at $pH_{25^{\circ}C}$ 6.0 and 8.4 at 80 °C. The ICP-MS results presented in Table 7.4 show that the concentration of dissolved Co in the test solution is $22 \mu\text{g}\cdot\text{L}^{-1}$. This is lower than that observed at $pH_{25^{\circ}C}$ 6.0 for the un-irradiated coupon at 80 °C (Table 7.2). The XPS analysis of the surface also shows the presence of more Co-oxide in the Co 2p band compared to that seen at the same pH at 80 °C (Figure 7.3 vs. Figure 7.7). These results indicate that oxide growth is not negligible, even at $pH_{25^{\circ}C}$ 6.0, at 150 °C, and over a long period (3 d) a oxide has developed that is sufficiently thick to slow down Co dissolution. The XPS analysis (Table 7.3) shows that this protective oxide layer is $\text{CoCr}_2\text{O}_4/\text{Co}(\text{OH})_2$ (before the outer layer was air-oxidized to $\text{Co}_3\text{O}_4/\text{CoOOH}$).

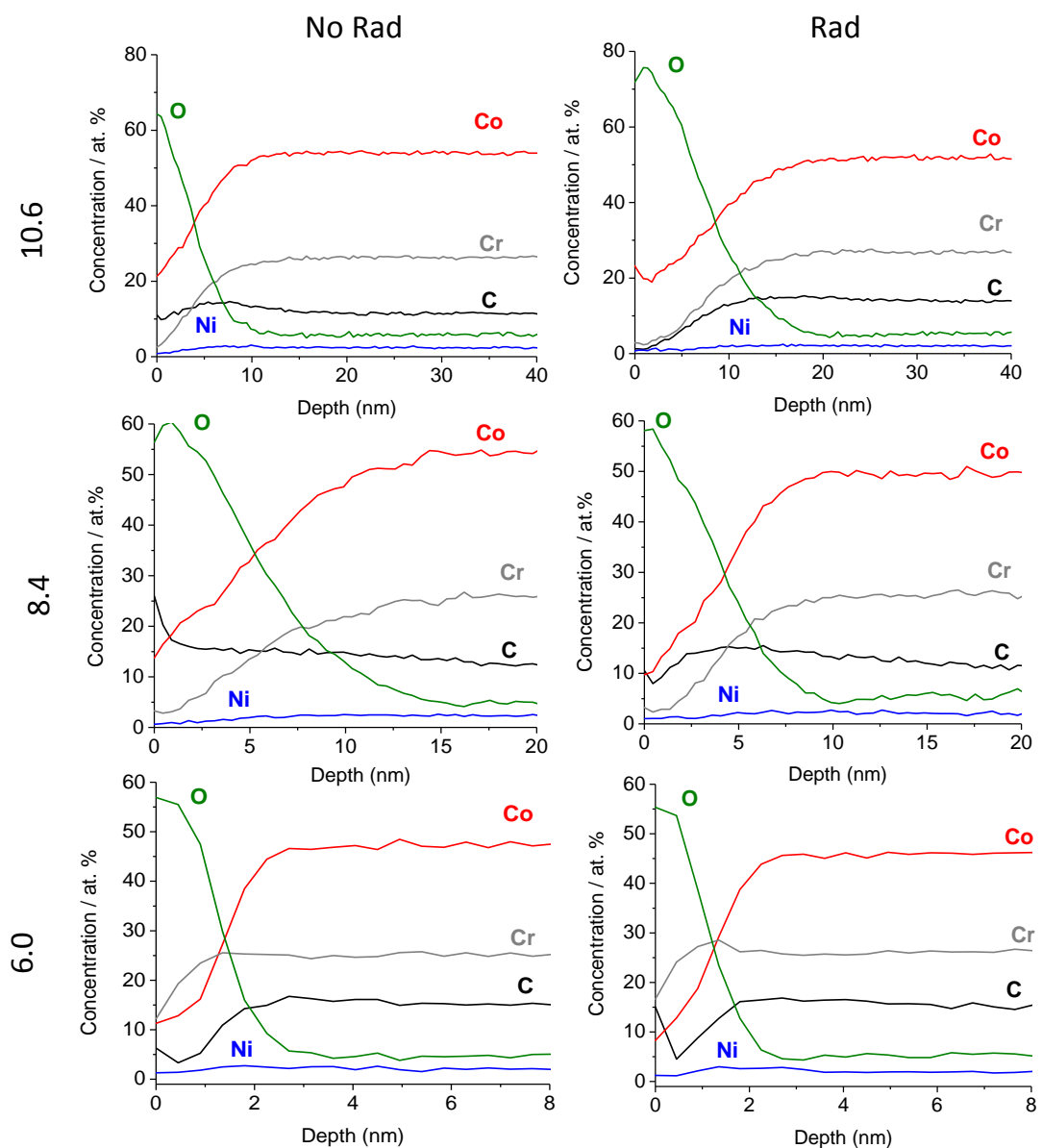


Figure 7.8: Depth profiles of the elements determined by AES of Stellite-6 coupons corroded for 3 d in the absence of radiation (left hand side) and in the presence of radiation (right hand side) at pH_{25°C} 10.6, 8.4, 6.0, at 150 °C.

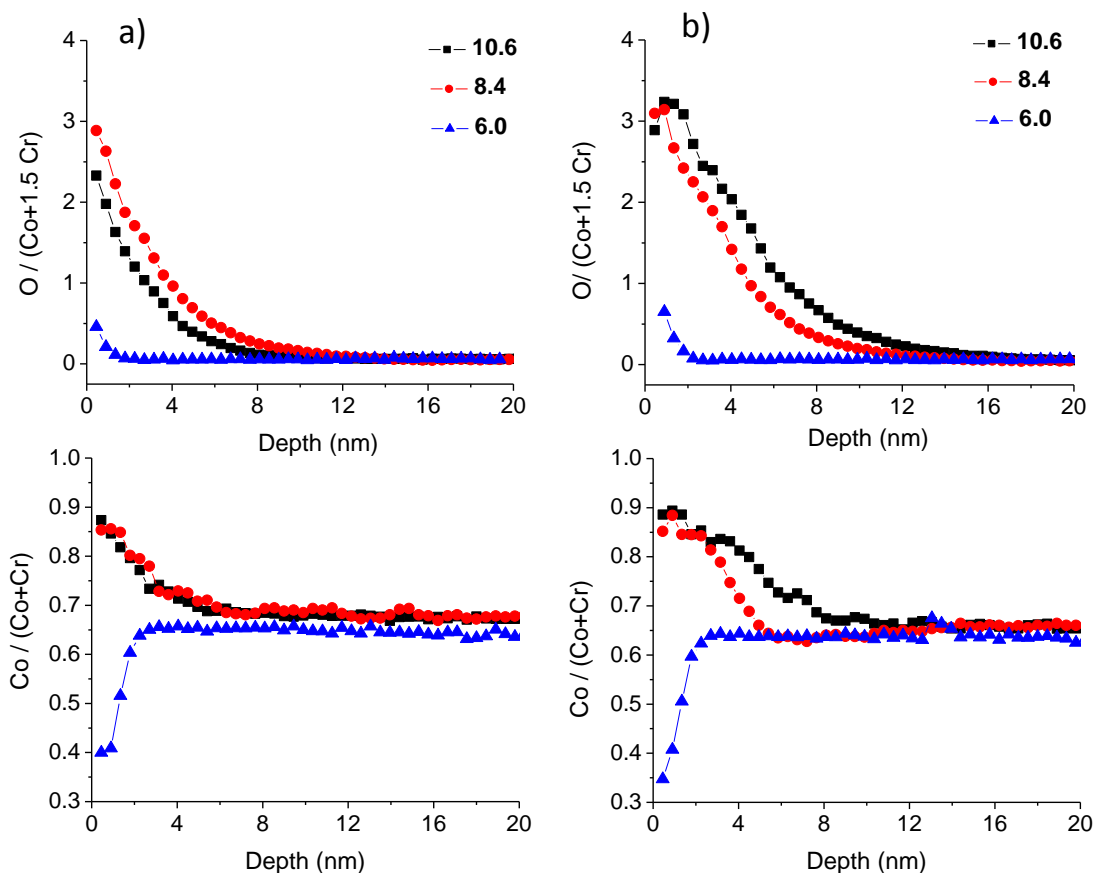


Figure 7.9: Depth profiles of $O/(Co + 1.5 Cr)$ and $Co/(Co + Cr)$ determined by AES on Stellite-6 coupons corroded at $pH_{25}^{\circ}C$: 10.6 (—■—), 8.4 (—●—), and 6.0 (—▲—). The left panel a) presents the results obtained in the absence of radiation and the right panel b) presents the results obtained in the presence of radiation, at 150 °C.

Table 7.4: Dissolved concentrations of Co and Cr after 3-d corrosion at 150 °C determined by ICP-MS.

$pH_{25}^{\circ}C$	No Rad		Rad	
	Co ($\mu g/L$)	Cr ($\mu g/L$)	Co ($\mu g/L$)	Cr ($\mu g/L$)
6.0	22	1	6098	29
8.4	18	3	17	ND
10.6	9	5	10	8

At $\text{pH}_{25^\circ\text{C}} 8.4$ in the absence of radiation, the depth profiles $\text{O}/(\text{Co} + 1.5 \text{ Cr})$ and $\text{Co}/(\text{Co} + \text{Cr})$ for the coupons corroded at 150°C are very different from those observed at 80°C . They resemble more closely those observed at $\text{pH}_{25^\circ\text{C}} 10.6$ at 80°C . In the depth range of 0 - 2 nm, the $\text{O}/(\text{Co} + 1.5 \text{ Cr})$ ratio decreases with depth from ~ 3.0 to 2.0 while the $\text{Co}/(\text{Co} + \text{Cr})$ ratio is nearly constant with depth at ~ 0.85 . In the range between 2 nm and 10 nm, both $\text{O}/(\text{Co} + 1.5 \text{ Cr})$ and $\text{Co}/(\text{Co} + \text{Cr})$ decrease with depth before reaching constant values of zero and ~ 0.7 , respectively. The ICP-MS results show that the amount of Co dissolved at $\text{pH}_{25^\circ\text{C}} 8.4$ in the absence of radiation is nearly the same at both 80°C and 150°C (Table 7.2 vs Table 7.4). This could be because the Co dissolution at $\text{pH}_{25^\circ\text{C}} 8.4$ at 150°C occurs during early stages of corrosion and, as the Co^{II} oxide/hydroxide layer grows, the Co dissolution slows down. We expect the oxide growth to occur faster at 150°C than at 80°C , see further discussion in Section 7.4.1.

At $\text{pH}_{25^\circ\text{C}} 10.6$ in the absence of radiation at 150°C , the oxide layer formed is slightly thinner than the layer formed at $\text{pH}_{25^\circ\text{C}} 8.4$. Comparison of the XPS analysis of the two surfaces (Table 7.3) shows a higher contribution of CoCr_2O_4 compared to $\text{Co}(\text{OH})_2$ at $\text{pH}_{25^\circ\text{C}} 10.6$ than at $\text{pH}_{25^\circ\text{C}} 8.4$. This difference can be attributed to a faster conversion of Cr_2O_3 to CoCr_2O_4 at the higher pH which then slows down the subsequent oxidation of Co. At $\text{pH}_{25^\circ\text{C}} 10.6$ the depth profiles of $\text{O}/(\text{Co} + 1.5 \text{ Cr})$ and $\text{Co}/(\text{Co} + \text{Cr})$ for coupons corroded at 150°C are similar to those observed at 80°C , except for a higher $\text{O}/(\text{Co} + 1.5 \text{ Cr})$ ratio near the surface and a thicker oxide layer. The ICP-MS results show that the amount of Co dissolved at $\text{pH}_{25^\circ\text{C}} 10.6$ in the absence of radiation is slightly higher at 150°C than at 80°C (Table 7.2

vs Table 7.4). These results arise because increasing temperature increases the net Co oxidation. At $\text{pH}_{25^\circ\text{C}} 10.6$ this leads to mainly an increase in oxide growth at 150°C , as was seen for corrosion at 80°C .

The pH dependence of γ -radiation on Stellite-6 corrosion at 150°C is similar to that observed at 80°C . At $\text{pH}_{25^\circ\text{C}} 6.0$, the coupons corroded in the presence of radiation have similar depth profiles to those corroded in the absence of radiation, except for a slightly thicker oxide layer and a lower $\text{Co}/(\text{Co} + \text{Cr})$ ratio near the surface. Note that although the AES depth profiles in Figure 7.9 show a thicker layer of Co and Cr oxides/hydroxides, the XPS analysis presented in Figure 7.7 shows a thinner oxide layer on the irradiated coupon than on the un-irradiated coupon. This difference may be due to the different penetration depths of electron beams used in the different techniques. The XPS results are more consistent with the AES analysis results which include all of the elements presented in Figure 7.8. These results may also be due to the changes in the surface adsorbed layer during air drying of the coupon samples prior to the surface analyses. Determination of the oxygen fraction does not necessarily provide an accurate picture of metal oxidation that has occurred during corrosion.

Gamma-irradiation increases the dissolved amounts of Co and Cr at $\text{pH}_{25^\circ\text{C}} 6.0$ at higher temperatures (Table 7.4). More interestingly, the Co dissolution is higher while the Cr dissolution is lower at 150°C than at 80°C . These results, combined with the surface analysis results, are consistent with the conclusion drawn from the corrosion tests at room temperature [1] and at 80°C . At 150°C radiation increases the rate of metal oxidation (the

metal oxidized is mainly Co) and at $\text{pH}_{25^\circ\text{C}} 6.0$ this increase mostly results in Co dissolution which also promotes Cr dissolution until a protective layer is formed. At 150°C the protective Co-oxide layer forms fast enough within 3 d to suppress later Cr dissolution.

At $\text{pH}_{25^\circ\text{C}} 8.4$ the depth profiles for a coupon corroded in the presence of radiation show only small differences from those observed in the absence of radiation. In the depth range of 0 – 4 nm, $\text{O}/(\text{Co} + 1.5 \text{Cr})$ decreases from ~ 3.0 to 1.0 while $\text{Co}/(\text{Co} + \text{Cr})$ decreases from ~ 0.85 to ~ 0.7 . However, in the range from 4 to 12 nm $\text{O}/(\text{Co} + 1.5 \text{Cr})$ decreases at a similar rate while $\text{Co}/(\text{Co} + \text{Cr})$ decreases at a faster rate on the irradiated coupon compared to an un-irradiated coupon. In this range the depth profile of $\text{Co}/(\text{Co} + \text{Cr})$ shows a dip, before the ratio reaches a constant value at 12 nm. The XPS results of the coupons corroded $\text{pH}_{25^\circ\text{C}} 8.4$ show that there are higher fractions of both CoCr_2O_4 and $\text{Co}(\text{OH})_2$ on the irradiated coupon. The amounts of dissolved Co for the irradiated and un-irradiated tests are nearly the same (Table 7.2). As well, the results show that γ -radiation does not lead to an increase in Cr dissolution.

At $\text{pH}_{25^\circ\text{C}} 10.6$ the depth profiles of $\text{O}/(\text{Co} + 1.5 \text{Cr})$ and $\text{Co}/(\text{Co} + \text{Cr})$ on an irradiated coupon show a significant increase in the oxide thickness. In the range of 0 - 5 nm where $\text{O}/(\text{Co} + 1.5 \text{Cr})$ decreases from ~ 3.0 to 1.0, $\text{Co}/(\text{Co} + \text{Cr})$ decreases slowly with depth. Further into the oxide $\text{Co}/(\text{Co} + \text{Cr})$ decreases faster with depth. These results, in combination of the XPS (Figure 7.9) and ICP-MS (Table 7.2) results show that the increased cobalt oxidation at 150°C and $\text{pH}_{25^\circ\text{C}} 10.6$ mainly increases oxide growth, the same behaviour observed at room temperature [1] and 80°C .

The effect of γ -radiation on Cr dissolution at 150 °C is small at all pHs, unlike the situation seen for corrosion at 80 °C (Table 7.4 vs. Table 7.2). At 150 °C the greatest increase in Cr dissolution due to γ -radiolysis occurs at $\text{pH}_{25^\circ\text{C}}$ 6.0 where Co dissolution is also the highest. As observed at 80 °C, the dissolved Cr concentration shows no correlation with the depth profiles of the ratios of different elements (Figures 7.8 and 7.9). As seen at 80 °C, radiation at 150 °C a higher level of Co dissolution accompanies a higher level of Cr dissolution since the former exposed more chromium oxide to water. This is as expected. The rate of surface hydration of Cr^{III} oxides from Cr_2O_3 to CrOOH and to $\text{Cr}(\text{OH})_3$ should occur faster at a higher temperature and the oxides should dissolve more readily at 150 °C than at 80 °C. As discussed earlier, the only plausible explanation for less Cr dissolution at the higher temperature is a faster growth of a protective Co oxide layer which suppresses dissolution of Co and Cr.

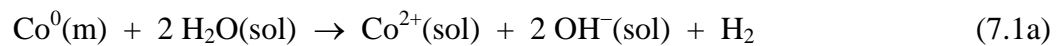
7.4 DISCUSSION

The results from tests at 150 °C and other work at lower temperatures clearly demonstrate that corrosion has a complex dependence on aqueous redox environmental parameters and specifically pH, temperature and the concentration of aqueous redox active species generated by γ -radiolysis. The work shows why corrosion behaviour observed under a narrow range of aqueous conditions cannot be simply extrapolated to a wider range of conditions simply. One must consider the corrosion reaction kinetics the influence of the different aqueous environmental parameters on the rate of metal oxidation and the competition between dissolution and oxide formation. The elementary reaction steps

involved in Stellite-6 corrosion and the parameters that dictate the rates of the individual elementary processes are briefly discussed here first. This is followed by a discussion of the observed results based on the mechanistic understanding of Stellite-6 corrosion.

7.4.1 Corrosion mechanism

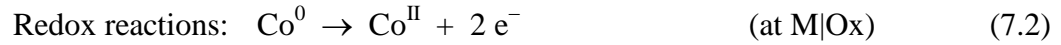
Aqueous corrosion consists of chemical reactions and transport processes involving at least three different phases (metal, metal oxide and solution) and two interfaces. For Stellite-6, the overall corrosion reaction can be expressed as:



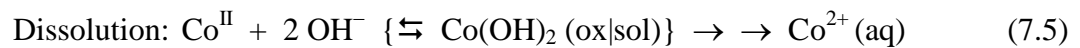
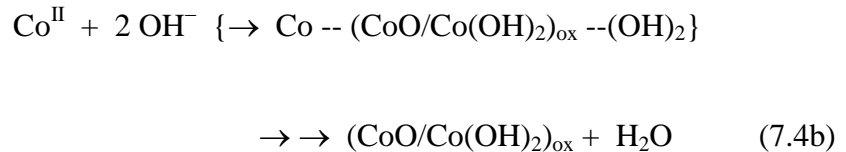
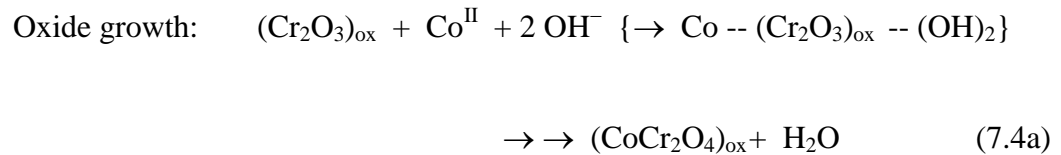
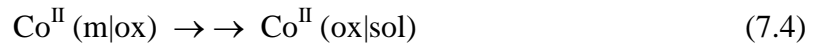
where $\text{Co}^{2+}(\text{sol})$ represents the Co^{II} species dissolved in solution and $\text{Co-O}(\text{ox})$ represents the Co^{II} species incorporated into an oxide lattice. For simplicity possible cobalt oxidation to a higher oxidation state (Co^{III}) is not shown in the above reaction. To determine the net corrosion rate the overall reaction can be considered to consist of a series of elementary reactions and transport processes whose rates can be expressed as a well-defined function of aqueous environmental parameters.

We have previously proposed a corrosion reaction mechanism for Stellite-6 in Chapter 4. This mechanism described the cobalt oxidation kinetics as during corrosion under potentiostatic polarization at different pHs at room temperature [1] and 80 °C (chapter 6). This corrosion reaction scheme is summarized below and schematically reproduced in Figure 7.10 [1]. For simplicity, only Co oxidation to Co^{II} is considered. Similarly, only water is

considered for the aqueous species that is reduced. Any additional oxidation or reduction processes can be incorporated as additional separate elementary reactions.



Net solid-state transport of Co^{II} across an oxide layer:



The oxides or hydroxides of transition metals that are initially present or growing during corrosion typically exhibit semiconducting properties [16–21]. For a chemically inert semiconductor, charge transport through the semiconductor is normally accomplished by electrons (for an n-type semiconductor) and holes (for a p-type semiconductor). On a corroding surface, transport of more massive charged species, metal cations (and/or oxygen/hydroxide anions), also occurs [22]. The transport of metal cations and oxygen

anions through a solid oxide phase is not easy. To account for the charge flux through a solid oxide lattice, many mechanisms, such as transport of metal cations (or oxygen anions) via interstitials or cation and anion vacancies, and electron hopping (or ion exchanges), have been proposed [18,23–26]. Irrespective of the ion transport mechanism, the result of a net charge flux on a corroding system is the net transport of metal from the alloy phase to the solution phase (i.e. from the M|Ox interface to the Ox|Sol interface). This does not necessarily mean the physical movement ions across the entire oxide depth but rather the relative movement of the interfaces.

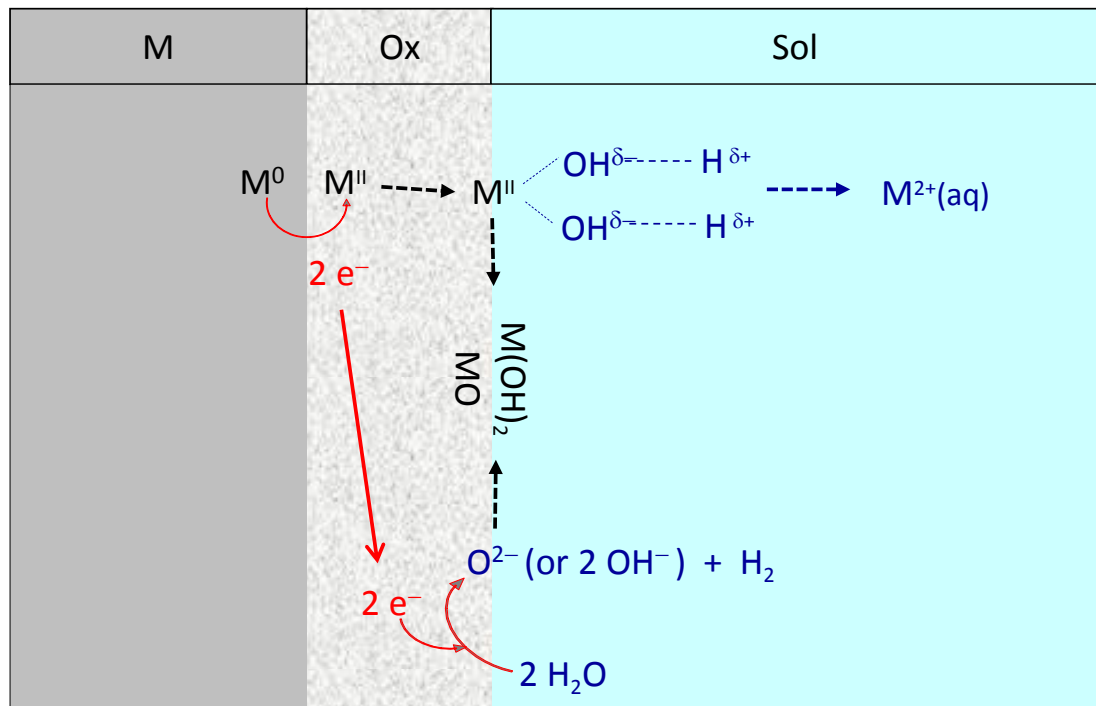


Figure 7.10: Schematic illustration of corrosion reactions in the presence of an oxide layer.

In our previous studies [1,9], we have argued that irrespective of the charge transport mechanism the corrosion kinetics must follow a classical (macroscopic) rate law based on mass and charge balance. Thus, the rates of the individual elementary processes in the corrosion mechanism shown in Figure 7.10 cannot vary independently. The mass and charge balance requirements dictate that at any given time, the net rate of corrosion and the rates of elementary steps must satisfy

Net rate (7.1a + 7.1b)

$$= \text{rate (7.2a)} = \text{rate (7.2b)} = \text{rate (7.3)} = \text{rate (7.4)} + \text{rate (7.5)} \quad (7.6)$$

The condition of equal rates for metal oxidation and water reduction dictates the potential on a naturally corroding surface (E_{corr}) and the net current at E_{corr} is thus zero. Under polarization in an electrochemical cell, the rate of oxidation (or reduction) occurring on the working electrode made of an alloy of interest must be the same as the rate of reduction (or oxidation) occurring on the chemically inert counter electrode (typically Pt), and this rate depends on the polarization potential (E_{APP}) [1,9], see Chapters 4 and 5.

The mass and charge balance requirements dictate that the rates of reactions that occur in series must be the same and that the overall rate of reactions in parallel is the sum of the individual rates. Hence, the slowest in a series of reactions dictates the oxidation rate. Metal dissolution and oxide formation compete for metal cations at the Ox|Sol interface. If the rate of metal ion dissolution is significantly higher than the rate of solid oxide formation, there will be no significant changes in the oxide layer and the corrosion rate with time as corrosion progresses. However, if the rate of oxide formation and growth is comparable to or

greater than the rate of metal dissolution, there will be changes in the oxide layer [20] and this will tend to slow the corrosion rate as the oxide becomes thicker.

7.4.2 Corrosion rate parameters

The rate of the electrochemical redox reaction (7.2a and 7.2b) can be described by a modified Butler-Volmer equation with an effective overpotential for the redox reaction at time t , $\eta_{\text{ox}}^{\text{eff}}(t)$:

$$k_{\text{ox}}(t) \approx k_{0,\text{ox}} \cdot \left(\exp \left(\frac{\alpha \cdot n \cdot F}{RT} \cdot \eta_{\text{ox}}^{\text{eff}}(t) \right) \right) \quad (7.7a)$$

$$k_{\text{red}}(t) \approx k_{0,\text{red}} \cdot \left(\exp \left(\frac{\beta \cdot n \cdot F}{RT} \cdot \eta_{\text{red}}^{\text{eff}}(t) \right) \right) \quad (7.7b)$$

$$k_{\text{ox}}(t) = k_{\text{red}}(t) \quad (7.7c)$$

where $k_{\text{ox}}(t)$ and $k_{\text{red}}(t)$ are the rates of metal oxidation (7.2a) and reduction of aqueous species (7.2b) at time t , $k_{0,\text{ox}}$ and $k_{0,\text{red}}$ are the rates at equilibrium, α and β are the transfer coefficients (typically 0.5), z is the number of electrons transferred in the reaction, F is the Faraday constant, and R is the gas constant. The equality in equation (7.7c) arises from the requirement that the flux of the positive charges (metal cations) and the flux of the negative charges (electrons and oxygen anions) must be same.

The electrochemical redox reaction is an interfacial charge transfer reaction and its driving force (the overpotential) is the difference between the total chemical potential of the reaction system at time t and that of the system at chemical and phase equilibrium (E_{eq}). The

total chemical potential for the overall corroding system is measured as E_{corr} on an open circuit (it is E_{APP} during polarization). With just two (metal and solution) phases and one (m|sol) interface, the effective overpotential is determined by:

$$\eta_{\text{ox}}^{\text{eff}}(t) = E_{\text{corr}}^t - E_{\text{ox}}^{\text{eq}} \quad (7.8a)$$

$$\eta_{\text{red}}^{\text{eff}}(t) = E_{\text{red}}^{\text{eq}} - E_{\text{corr}}^t \quad (7.8b)$$

On a naturally corroding surface the corrosion potential is the potential at which the rate of oxidation is the same as the rate of reduction. A difference between the equilibrium potentials for the metal oxidation and aqueous reduction results in an overpotential that drives the rate of the metal oxidation.

$$\eta_{\text{ox}}^{\text{eff}}(t) + \eta_{\text{red}}^{\text{eff}}(t) = \Delta E_{\text{rdx}}^{\text{eq}} = E_{\text{red}}^{\text{eq}} - E_{\text{ox}}^{\text{eq}} \quad (7.9)$$

It should be noted that the two half redox reactions cannot occur independently, their separation is used for convenience in evaluating reaction thermodynamics. By convention the reference point for electrochemical potential is the standard hydrogen electrode (SHE) potential (i.e., potential of SHE = 0). However, it is important to remember that whether a chemical reaction (any observable phenomenon) can occur depends only on a difference in potential and not the absolute potential anywhere in the system.

With an oxide layer present the effective overpotential is the significantly less due to an electrochemical potential barrier across the semiconducting oxide layer ($\Delta E_f(t)$). This arises

from a chemical potential barrier for the oxidation reaction accompanied by an electric field potential barrier for charge carriers (the main charge carrier is electrons):

$$\eta_{\text{ox}}^{\text{eff}}(t) = E_{\text{corr}}^t - E_{\text{ox}}^{\text{eq}} - \Delta E_f(t) \quad (7.10a)$$

$$\eta_{\text{red}}^{\text{eff}}(t) = E_{\text{red}}^{\text{eq}} - E_{\text{corr}}^t - \Delta E_f(t) \quad (7.10b)$$

There may be other electric field potential barriers across Schottky and double layer barriers. During corrosion these barriers should be smaller than the potential barrier across the oxide layer.

On a chemically inert semiconductor electrode the potential barrier across the semiconducting layer does not change with time (constant $\Delta E_f(t)$ with time) as an electrolytic reaction (reactions of solution species) progresses on the electrode [27]. However, on a corroding surface the potential barrier increases as the oxide layer thickens because incorporation of metal cations and oxygen anions into the oxide lattice is increasingly difficult (there is a higher chemical potential barrier) as the oxide layer thickens [20,26]. Hence, $\Delta E_f(t)$ is not constant but increases time with oxide growth. Hence, even under the constant redox conditions (i.e., $\Delta E_{\text{rdx}}^{\text{eq}}$ is constant), the net metal oxidation rate decreases with time as the oxide layer thickens. We observe this as a continuous decrease in current with time during corrosion under potentiostatic polarization when the oxide growth is favoured over metal dissolution (see Chapters 4 and 5).

Equations (7.7) to (7.10) show that in the presence of an oxide layer the rate of metal oxidation (or the rate of aqueous reduction) depends on both $\Delta E_{\text{rdx}}^{\text{eq}}$ and $\Delta E_f(t)$. The values of

$E_{\text{red}}^{\text{eq}}$ and $E_{\text{ox}}^{\text{eq}}$ will depend on the actual aqueous reduction and metal oxidation steps that are involved in the overall corrosion reaction. For example, reduction of other redox active species, such as H_2O_2 in solution, can couple more effectively with the oxidation of cobalt. Likewise, there may be more than one oxidation reaction of cobalt (e.g., forming dissolved $\text{Co}^{2+}(\text{aq})$, CoCr_2O_4 , CoO or $\text{Co}(\text{OH})_2$, etc.).

Equation (7.10) shows that the net metal oxidation also depends on $\Delta E_f(t)$. The potential drop across the oxide layer depends on the type and thickness of the oxide that is growing. The studies on cobalt oxidation kinetics as a function of electrode potential under potentiostatic polarization at 25 °C and 80 °C (Chapters 4 and 5) have shown that the type of oxide that can grow depends on the electrode potential (E_{APP} or E_{CORR}). However, the rate of the oxide growth and the final thickness of the oxide film depend strongly on pH and temperature.

Since metal oxidation leads to both metal cation dissolution and oxide formation, the competing kinetics of these two pathways can affect the rate of oxide growth [1], and hence, how fast the oxidizing surface can be passivated, if at all. The morphology and phase structure, and the chemical and electrochemical properties of an oxide film that is being formed can influence the subsequent corrosion reaction pathways [28]. Aqueous conditions (notably pH, temperature, concentrations of redox active species, ionic strength, and ionic product) all have different effects on metal oxidation and the competing kinetics of dissolution and oxide formation. The corrosion behaviour observed as a function of pH,

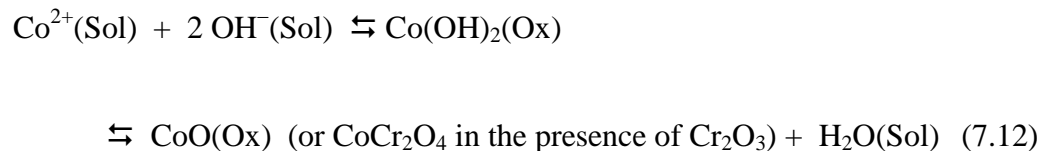
temperature and γ -radiolysis can then be explained by examining how these aqueous parameters affect the rate parameters that dictate the individual elementary processes.

7.4.3 Effects of pH, temperature and γ -radiolysis on rate parameters

The effect of pH on $\Delta E_{\text{rdx}}^{\text{eq}}$ for a given redox couple is very small since both $E_{\text{red}}^{\text{eq}}$ and $E_{\text{ox}}^{\text{eq}}$ are affected in the same direction (-59 mV per one pH unit increase) for a redox reaction involving an H^+/e^- ratio of one. However, pH strongly affects the hydrolysis equilibria of metal ions and hence their solubility:



These hydrolysis reactions are acid-base equilibrium reactions and the equilibrium in the solution phase is reached very quickly compared to the rates of other reactions involved in the corrosion process. The hydrated Co^{II} species ($\text{Co}^{2+}(\text{sol})$) are also in phase equilibrium with solid Co^{II} hydroxide and Co^{II} oxides:



where K is the equilibrium constant at 25°C .

Due to the hydrolysis and the phase equilibria the solubility of a transition metal cation is very sensitive function of pH at a given temperature. The effect of pH on the Co^{II} solubility at room temperature is shown in Figure 7.11 [12,29].

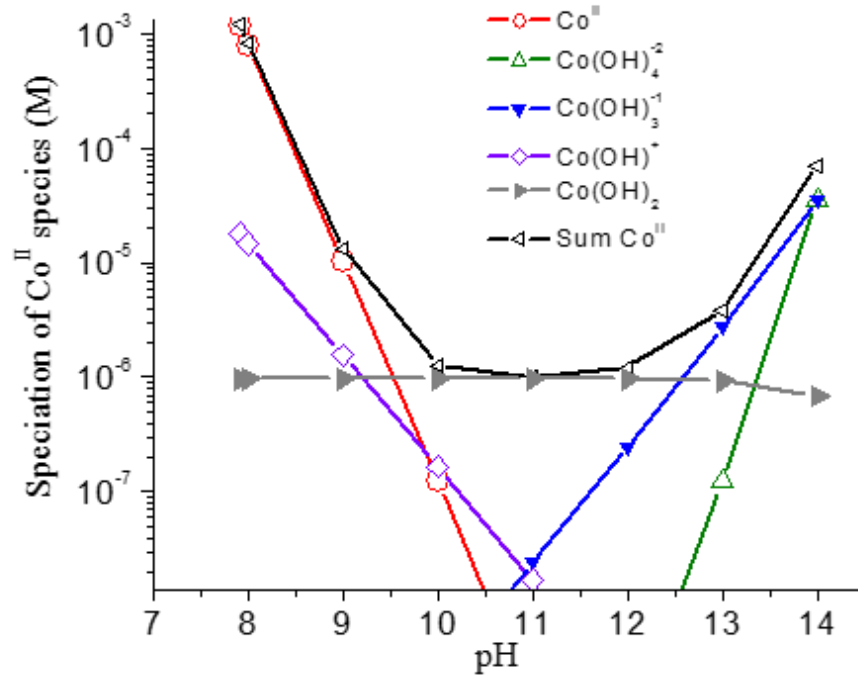


Figure 7.11: Solubility of hydrolyzed Co^{2+} species as a function of pH at 25 °C.

The hydrolysis and the phase equilibria also depend on temperature. The temperature dependences of the thermodynamic functions for the cobalt species are available over a limited pH range [5,12,30]. Figure 7.12 shows the solubility of Co^{II} oxides as a function of temperature calculated at a few $\text{pH}_{25^\circ\text{C}}$ values based on the thermodynamic functions provided in reference [30]. At a given pH the solubility of Co(OH)_2 increases range from a

factor of ~ 3 at $\text{pH}_{25^\circ\text{C}} 11.31$ to less than a factor of 2 at $\text{pH}_{25^\circ\text{C}} 9.11$ when the temperature increases from 25°C to 150°C [30]. The effect of temperature on the hydrolysis and the phase equilibria is smaller than the effect of pH (over the range normally considered). However, temperature can have a more important effect on the hydrolysis kinetics and aqueous diffusion rates of the Co^{II} species, see discussion below.

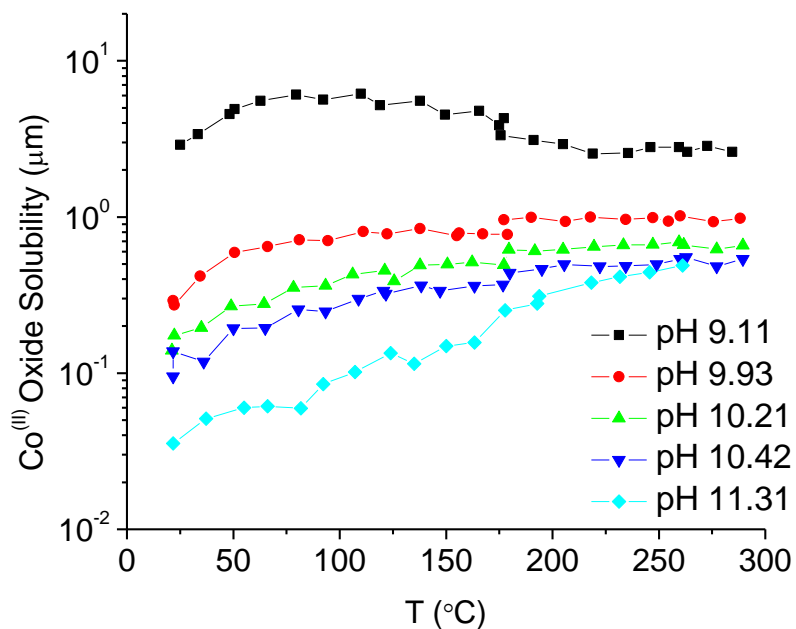


Figure 7.12: The solubility of Co(II) oxides as a function of temperature at different pHs [30].

Temperature not only affects the reaction thermodynamics by shifting the hydrolysis and phase equilibria but it also affects the rates of thermal processes which include chemical reactions (oxide growth and surface hydration) and transport processes (aqueous and solid state diffusion). The rate of many chemical reactions can be expressed using an Arrhenius

equation which can be a very sensitive function of temperature. The conductivity (or charge transport rate) of a semiconductor increases with increasing temperature although its change with temperature is smaller normally. The relative changes in the rates of these elementary steps influence the competition between oxide growth and dissolution. Since the rates of the elementary steps can all have different temperature dependences, the current (the net corrosion rate) will not have simple temperature dependence. Nevertheless, we can attempt to determine this temperature dependence. The rate constants of the individual chemical reactions and transport steps as a function of temperature are often well established and independently validated. Alternatively there are good methods for their approximation (and approximation of their temperature dependence). The net effect of a temperature change can then be obtained by solving the chemical reaction and transport kinetics for the coupled elementary reactions involved in the corrosion.

Gamma-radiation does not directly induce any chemical changes in solid metal or metal oxide phases; the absorbed radiation energy is dissipated mostly as heat. However, continuous γ -radiation can induce important chemical changes in water [31,32] as it explained in chapter 2, section 2.4. Water decomposes to a range of redox active species almost immediately upon interaction with a γ -photon:



The hydrated electron ($\bullet\text{e}_{\text{aq}}^-$) and hydroxyl radical ($\bullet\text{OH}$) are strong reductants and oxidants respectively [32,33]. They are very effective in changing redox solution chemistry [34,35]. For surface reactions the key radiolytic oxidant is H_2O_2 since it can accumulate to a

relatively high concentration when continuous radiation is applied to a solution and can diffuse to the surface [31,36]. The equilibrium potential of the H_2O_2 reduction to 2OH^- (reaction 7.14) is significantly higher than that of water reduction to H_2 :



Thus, $\Delta E_{\text{rdx}}^{\text{eq}}$ is larger in the irradiated water and this is observed as an increase in E_{corr} [1,37] as discussed in Chapter 4. The room temperature results are reproduced in Figure 7.13. Changes in the corrosion potentials caused by the presence of radiation at higher temperatures were not obtained because a reference electrode that is stable under the combination of high temperature and irradiation could be found.

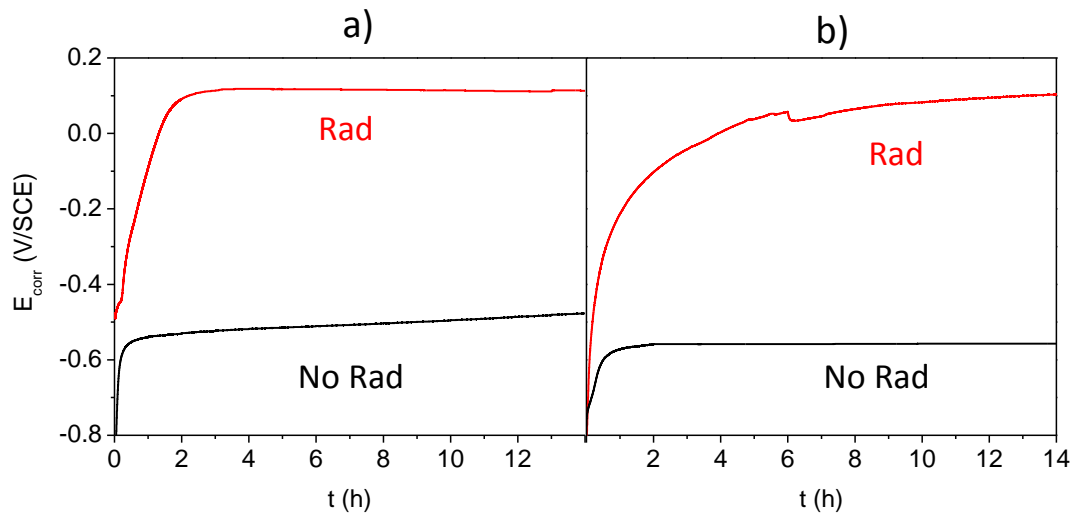


Figure 7.13: E_{corr} as a function of time recorded on the Stellite-6 electrodes at and 25°C in the absence (—), and the presence of radiation (—) at (a) $\text{pH}_{25^\circ\text{C}} 10.6$ and (b) $\text{pH}_{25^\circ\text{C}} 8.4$.

Heating is not very effective in changing the chemical potential of a bulk phase and even less effective in changing the $\Delta E_{\text{rdx}}^{\text{eq}}$, the difference in chemical potential of metal and aqueous phases. Hence, changing temperature is expected to have only a small effect on the driving force for the electrochemical reaction ($\Delta E_{\text{rdx}}^{\text{eq}}$). Figure 7.14 shows that the final E_{corr} in the absence of radiation for two pHs and three temperatures are about $-0.45 \text{ V}_{\text{SCE}}$ and $-0.41 \text{ V}_{\text{SCE}}$ at $80 \text{ }^\circ\text{C}$ and $-0.13 \text{ V}_{\text{SCE}}$ and $-0.24 \text{ V}_{\text{SCE}}$ at $150 \text{ }^\circ\text{C}$, higher than those observed in the absence of radiation at $25 \text{ }^\circ\text{C}$. The increase in E_{corr} with temperature observed in the absence of radiation is mostly due to growth of a thicker oxide at a higher temperature, thus increasing $\Delta E_{\text{f}}(t)$. The final E_{corr} observed in the absence of radiation at $150 \text{ }^\circ\text{C}$ is still lower than the final E_{corr} observed in the presence of radiation at $25 \text{ }^\circ\text{C}$.

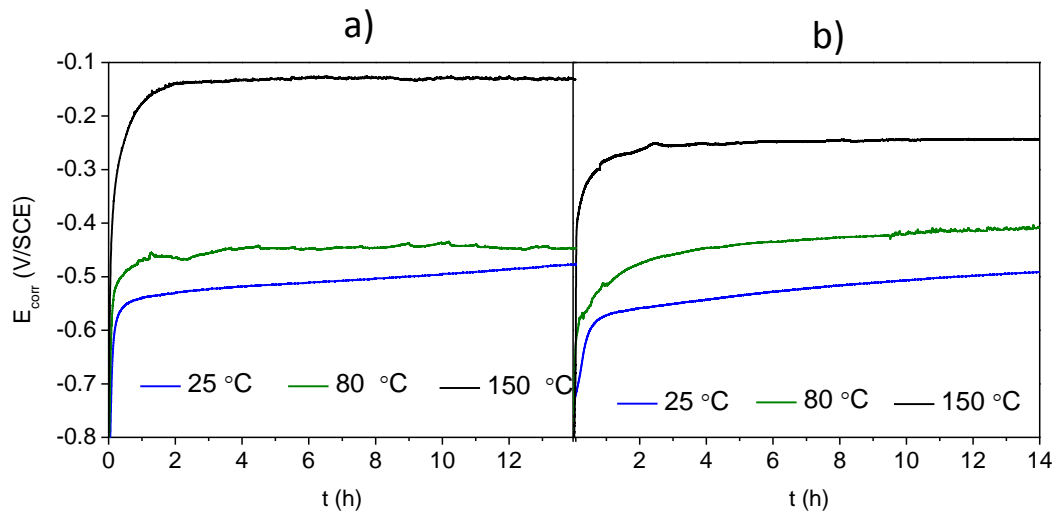


Figure 7.14: E_{corr} as a function of time recorded on the Stellite-6 electrodes at $25 \text{ }^\circ\text{C}$ (—), $80 \text{ }^\circ\text{C}$ (—), and $150 \text{ }^\circ\text{C}$ (—) in absence of radiation at $\text{pH}_{25^\circ\text{C}}$, (a) 10.6, (b) 8.4.

7.5 CONCLUSIONS

We observed that the net rate of corrosion does not have a simple temperature dependence and this dependency varies with both pH and the presence of water radiolysis products. At pH 6.0 where the solubility of Co species is high an increase in temperature from 25 to 150 °C in the absence of radiation does not linearly increase the oxide formation. An increase in temperature from 25 to 80 °C mostly promotes the dissolution over oxide formation. However, an increase in temperature from 80 to 150 °C moderately increases the rate of oxide formation (Figure 7.14b), and consequently lowers the dissolution rate (Table 7.2 and Table 7.4). An opposite trend observed in the presence of radiation. When temperature increases in the presence of radiation, the surface of the coupons appears to be clean with no distinct change. The fraction of oxide decreases and the highest amount of dissolved Co is detected in the solution at a temperature of 150 °C. We can conclude that at $\text{pH}_{25^\circ\text{C}}$ 6.0, increasing temperature in the presence of radiation promotes the dissolution over the rate of oxide formation.

At $\text{pH}_{25^\circ\text{C}}$ 10.6 the solubility of Co species is at a minimum and oxide formation is preferred over dissolution, and therefore an increase in temperature thickens the oxide film. Figure 7.16 clearly shows this effect. As the temperature increases from 25 °C to 150 °C both SEM and XPS results also show the formation of thicker oxide films. The presence of radiation further promotes this thickening process, and in fact, increasing the temperature in the presence of radiation strongly promotes oxide formation over dissolution. At $\text{pH}_{25^\circ\text{C}}$ 8.4, the main pathway in the absence of radiation at 80 °C is dissolution, but oxide formation is

promoted in the presence of radiation. At 150 °C regardless of radiation presence oxide formation is dominant.

7.6 REFERENCES

- [1] M. Behazin, J.J. Noël, J.C. Wren, Combined effects of pH and γ -irradiation on the corrosion of Co-Cr alloy Stellite-6, *Electrochim. Acta*, 134 (2014) 399–410..
- [2] S.-L. Chou, J.-Z. Wang, H.-K. Liu, S.-X. Dou, Electrochemical deposition of porous $\text{Co}(\text{OH})_2$ nanoflake films on stainless steel mesh for flexible supercapacitors, *J. Electrochem. Soc.*, 155 (2008) A926–A929
- [3] J. Yang, H. Liu, W.N. Martens, R.L. Frost, Synthesis and characterization of cobalt hydroxide, cobalt oxyhydroxide, and cobalt oxide nanodiscs, *J. Phys. Chem. C.*, 114 (2010) 111–119.
- [4] L. Wang, K. Daub, Z. Qin, J.C. Wren, Effect of dissolved ferrous iron on oxide film formation on carbon steel, *Electrochim. Acta*, 76 (2012) 208–217.
- [5] J.R.S. Brownson, C. Lévy-Clément, Nanostructured α - and β -cobalt hydroxide thin films, *Electrochim. Acta*, 54 (2009) 6637–6644.
- [6] E. Zhang, Y. Tang, Y. Zhang, C. Guo, L. Yang, Hydrothermal synthesis of β -nickel hydroxide nanocrystalline thin film and growth of oriented carbon nanofibers, *Mater. Res. Bull.*, 44 (2009) 1765–1770.
- [7] D.P. Dubal, V.J. Fulari, C.D. Lokhande, Effect of morphology on supercapacitive properties of chemically grown β -Ni(OH)₂ thin films, *Microporous Mesoporous Mater.*, 151 (2012) 511–516.
- [8] A. Kocijan, I. Milosev, B. Pihlar, Cobalt-based alloys for orthopaedic applications studied by electrochemical and XPS analysis., *J. Mater. Sci. Mater. Med.*, 15 (2004) 643–50.
- [9] M. Behazin, M.C. Biesinger, J.J. Noël, J.C. Wren, Comparative study of film formation on high-purity Co and Stellite-6: Probing the roles of a chromium oxide layer and gamma-radiation, *Corros. Sci.*, 63 (2012) 40–50.
- [10] Y.O.U. Hai-xia, Potential pH diagrams of Cr-H₂O system at elevated temperatures, *Trans. Nonferrous Met. Soc. China*, 20 (2010) s26–s31.
- [11] S.E. Ziemniak, M.E. Jones, K.E.S. Combs, Solubility and phase behavior of Cr (III) oxides in alkaline media at elevated temperatures, *J. Solution Chem.*, 27 (1998) 33–65.
- [12] M. Pourbaix, *Atlas of Electrochemical Equilibria in Aqueous Solution*, NACE, Houston, TX, 1996.
- [13] T.J. Oblonsky, T.M. Devine, A surface enhanced Raman spectroscopic study of the passive films formed in borate buffer on iron, nickel, chromium and stainless, *Corros. Sci.*, 37 (1995) 17–41.

- [14] I. Betova, M. Bojinov, T. Laitinen, M. Kari, The transpassive dissolution mechanism of highly alloyed stainless steels II. Effect of pH and solution anion on the kinetics, *Corros. Sci.*, 44 (2002) 2699–2723.
- [15] D. Marijan, M. Gojic, Electrochemical study of the chromium electrode behaviour in borate buffer solution, *J. Appl. Electrochem.*, 32 (2002) 1341–1346.
- [16] J. Kim, E. Cho, H. Kwon, Photo-electrochemical analysis of passive film formed on Cr in pH 8.5 buffer solution, *Electrochim. Acta*, 47 (2001) 415–421.
- [17] J. Pal, P. Chauhan, Study of physical properties of cobalt oxide (Co_3O_4) nanocrystals, *Mater. Charact.*, 61 (2010) 575–579.
- [18] L.F. Lin, C.Y. Chao, D.D. Macdonald, A point defect model for anodic passive films II. Chemical breakdowns and pit initiation, *J. Electrochem. Soc.*, 128 (1981) 1187–1194.
- [19] S.R.J. Saunders, M. Monteiro, F. Rizzo, The oxidation behaviour of metals and alloys at high temperatures in atmospheres containing water vapour: A review, *Prog. Mater. Sci.*, 53 (2008) 775–837.
- [20] F.R. Billman, Effects of scale porosity, second-phase oxides, and doping in the high-temperature oxidation of cobalt and dilute cobalt-chromium alloys, *J. Electrochem. Soc.*, 119 (1972) 1198–1204.
- [21] L. Wang, K. Daub, Q. Knapp, Z. Qin, J.J. Noel, J.C. Wren, Effect of ferrous ions on oxide film formation and conversion on stainless steel, *J. Electrochem. Soc.*, 159 (2012) C503–C512.
- [22] N. Perez, *Electrochemistry and Corrosion Science*, Kluwer Academic Publishers, Boston, 2004.
- [23] B. Krishnamurthy, R.E. White, H.J. Ploehn, Non-equilibrium point defect model for time-dependent passivation of metal surfaces, *Corros. Sci.*, 46 (2001) 3387–3396.
- [24] A. Seyeux, V. Maurice, P. Marcus, Oxide film growth kinetics on metals and alloys: I. Physical model, *J. Electrochem. Soc.*, 160 (2013) C189–C196.
- [25] K. Leistner, C. Toulemonde, B. Diawara, A. Seyeux, P. Marcus, Oxide film growth kinetics on metals and alloys: II. Numerical simulation of transient behavior, *J. Electrochem. Soc.*, 160 (2013) C197–C205.
- [26] M. Kamrunnihar, J. Bao, D.D. Macdonald, Challenges in the theory of electron transfer at passive interfaces, *Corros. Sci.*, 47 (2005) 3111–3139.
- [27] N. Cabrera, N.F. Mott, Theory of the oxidation of metals, *Rep. Prog. Phys.*, 12 (1949) 163–184.
- [28] K. Daub, X. Zhang, L. Wang, Z. Qin, J.J. Noël, J.C. Wren, Oxide growth and conversion on carbon steel as a function of temperature over 25 and 80 °C under ambient pressure, *Electrochim. Acta*, 56 (2011) 6661–6672.
- [29] C.F. Baes, R.E. Mesmer, *The Hydrolysis of Cations*, 2nd Ed., Wiley, New York, 1986.
- [30] S.E. Ziemniak, M.A. Goyette, K.E.S. Combs, Cobalt (II) oxide solubility and phase stability in alkaline media at elevated temperatures, *J. Solution Chem.*, 28 (1999) 809–836.
- [31] R.J. Wood, J.W.T. Spinks, *An Introduction to Radiation Chemistry*, 3rd Ed., Wiley-Interscience, New York, 1990.

- [32] P.A. Yakabuskie, J.M. Joseph, J.C. Wren, The effect of interfacial mass transfer on steady-state water radiolysis, *Radiat. Phys. Chem.*, 79 (2010) 777–785.
- [33] J.M. Joseph, B.S. Choi, P.A. Yakabuskie, J.C. Wren, A combined experimental and model analysis on the effect of pH and $O_2(aq)$ on γ -radiolytically produced H_2 and H_2O_2 , *Radiat. Phys. Chem.*, 77 (2008) 1009–1020.
- [34] L.M. Alrehaily, J.M. Joseph, M.C. Biesinger, D.A. Guzonas, J.C. Wren, Gamma-radiolysis-assisted cobalt oxide nanoparticle formation, *Phys. Chem. Chem. Phys.*, 15 (2013) 1014–24.
- [35] L.M. Alrehaily, J.M. Joseph, A.Y. Musa, D.A. Guzonas, J.C. Wren, Gamma-radiation induced formation of chromium oxide nanoparticles from dissolved dichromate., *Phys. Chem. Chem. Phys.*, 15 (2013) 98–107.
- [36] K. Daub, X. Zhang, J.J. Noël, J.C. Wren, Effects of γ -radiation versus H_2O_2 on carbon steel corrosion, *Electrochim. Acta*, 55 (2010) 2767–2776.
- [37] Q.W. Knapp, J.C. Wren, Film formation on type-316L stainless steel as a function of potential: Probing the role of gamma-radiation, *Electrochim. Acta*, 80 (2012) 90–99.

CHAPTER 8

Effects of Borate on Corrosion of Stellite-6

8.1 INTRODUCTION

The general objective of the work presented in this chapter was to investigate the effect of the ionic strength of a solution on the corrosion behaviour of Stellite-6. The electrolyte solutions used in all of the studies presented in the previous chapters were conducted in a 0.01 M sodium borate solution with the pH adjusted by adding strong acid or strong base dropwise to maintain the total ionic strength of the different test solutions relatively the same. The addition of an electrolyte salt into the test solution is necessary for any electrochemical study of corrosion to minimize the contribution of solution resistance to the overall circuit behaviour. However, the water used in nuclear reactor systems is very clean, the ion conductivity in the water is controlled to be as low as possible, and borate is not normally present.

Borate is stable under γ -irradiation and is not a redox active species. Thus, it will not be directly involved in interfacial redox reactions. However, the addition of sodium borate increases the concentration of ions in the solution (ionic strength) which can affect the adsorbed OH^- concentration on the oxide surface and/or influence ion mobility in the presence of an electric field, and subsequently affect the charge and concentration distribution of the redox active species near the electrode surface [1]. This work was

undertaken with two specific objectives in mind: (a) to determine the impact of a borate solution on oxide film formation at 80 °C and 150 °C at $\text{pH}_{25^\circ\text{C}}$ 10.6, and (b) to determine the impact of borate on the dissolution of oxide film constituents. For these studies, corrosion tests using Stellite-6 coupons in leak-tight quartz vials for 3 days. This work is only a limited study on the effect of ionic solution to determine whether there is, or is not, an important effect,

These tests were performed at an initial $\text{pH}_{25^\circ\text{C}}$ 10.6 because this allows the thickest oxide film growth due to the low solubility of Co species at this pH [2,3]. The corrosion tests were performed either in an NaOH-only solution or in a mildly basic solution containing 0.01 M sodium borate, referred to as NaOH-only and borate solutions hereafter. The effect of borate was explored at two temperatures, 80 °C and 150 °C, and in the absence and the presence of radiation. At the end of 3-d corrosion tests the changes on the coupon surfaces were examined by SEM, XPS and AES, and the concentrations of metal ions dissolved in the test solutions were analyzed by ICP-MS.

8.2 EXPERIMENTAL

The corrosion cells and the coupon samples used for this study were prepared in the same way as described in Chapters 5 and 7. The solutions were prepared using reagent grade $\text{Na}_2\text{B}_4\text{O}_7 \cdot 10\text{H}_2\text{O}$ (Caledon Laboratories Ltd.) and water purified using a NANOpure Diamond UV ultra-pure water system (Barnstead International), with a resistivity of 18.2 $\text{M}\Omega\cdot\text{cm}$. Reagent grade 1 M NaOH (Caledon Laboratories Ltd.) was added dropwise to a

borate solution to adjust the $\text{pH}_{25^\circ\text{C}}$ to 10.6. A borate free solution was prepared with 0.01 M NaOH and pure water with at the same pH. The procedures and equipment used in these tests were the same as those described in previous chapters.

8.3 RESULTS AND DISCUSSION

8.3.1 Results at 80 °C

The results obtained at 80 °C are shown in Figures 8.1- 8.3, and Table 8.1. Figure 8.1 shows that the coupons corroded in the absence of radiation in the NaOH-only solution have a similar surface morphology to those corroded in the borate solution. However, the coupon surface corroded in the NaOH-only solution seems to have fewer oxide features than are seen on a coupon corroded in a borate solution.

The difference in morphology is more amplified on the coupons corroded in the presence of radiation. Compared to the coupons irradiated in the borate solution, the coupons irradiated in the NaOH-only solution show a denser and thicker layer of the filament-like oxide network evenly covering the surface; no polishing lines are visible. In addition, grainy crystallites are present on coupons corroded in both solutions.

The underlying grainy crystallites are more clearly observed in the backscattered electron (BSE) images of the coupons corroded in a NaOH-only solutions shown in Figure 8.2. The BSE images visibly reveal the topography and shape contrast of the grainy crystallites which are distributed over the surface, more densely over the Co-rich phase than

over the Cr-rich phase. The distribution of the crystallites on the coupon irradiated in the NaOH-only solution is similar to that observed for the corrosion in the borate solution.

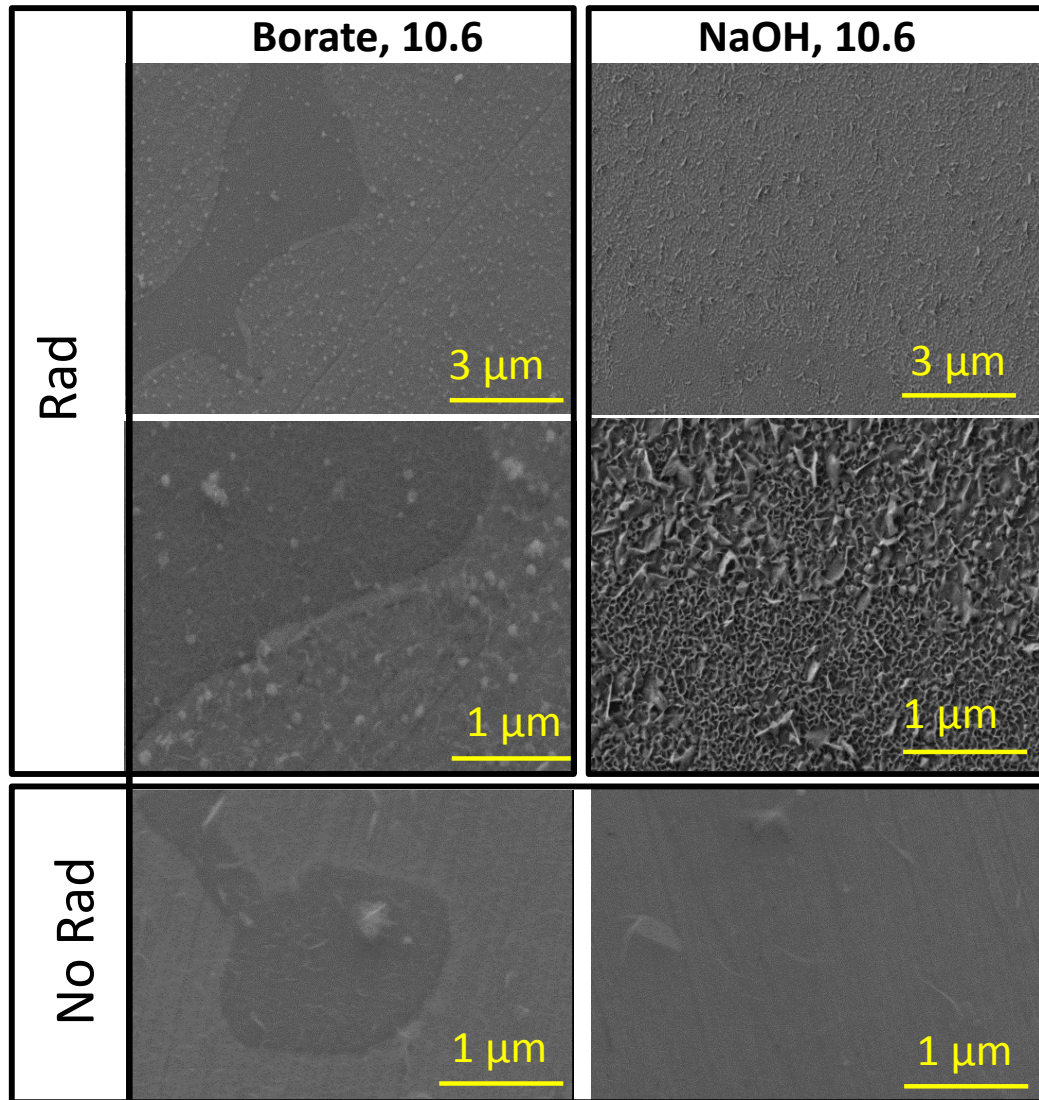


Figure 8.1: SEM images of samples corroded in NaOH-only and borate solutions at pH 10.6 in the presence and absence of radiation at 80 °C.

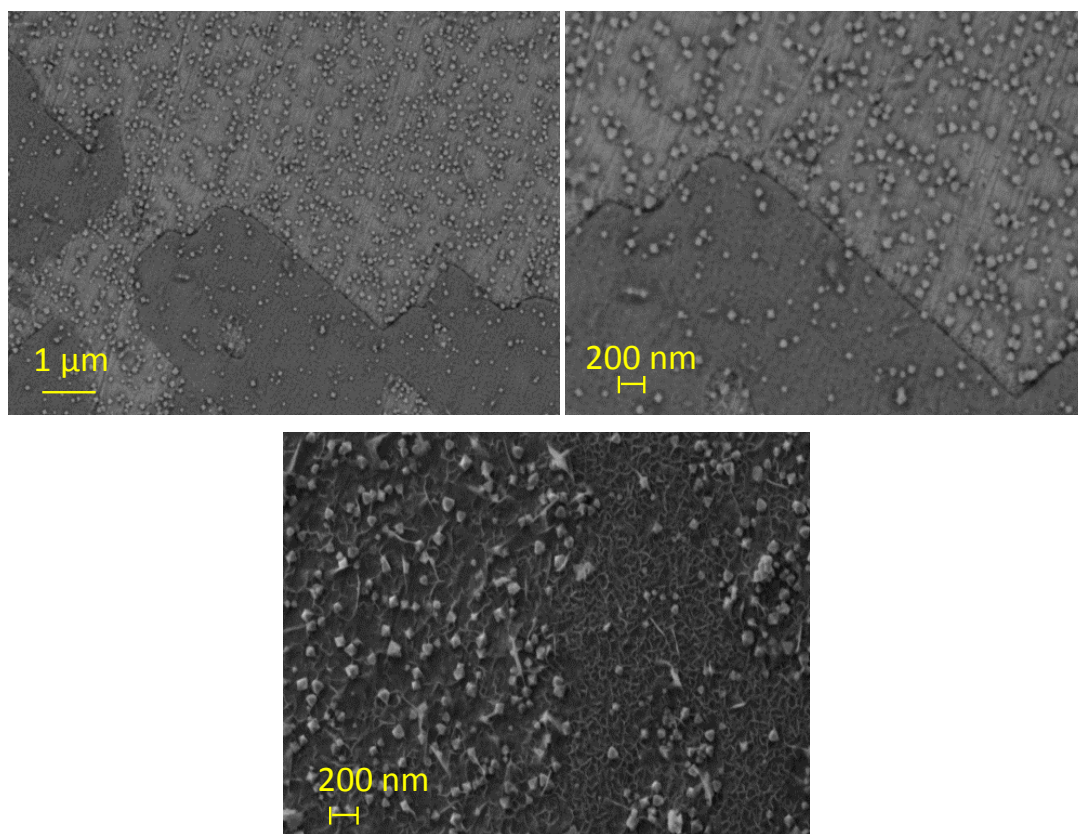


Figure 8.2: Backscattered electron images of surfaces corroded in an NaOH-only solution in the presence of radiation at 80 °C.

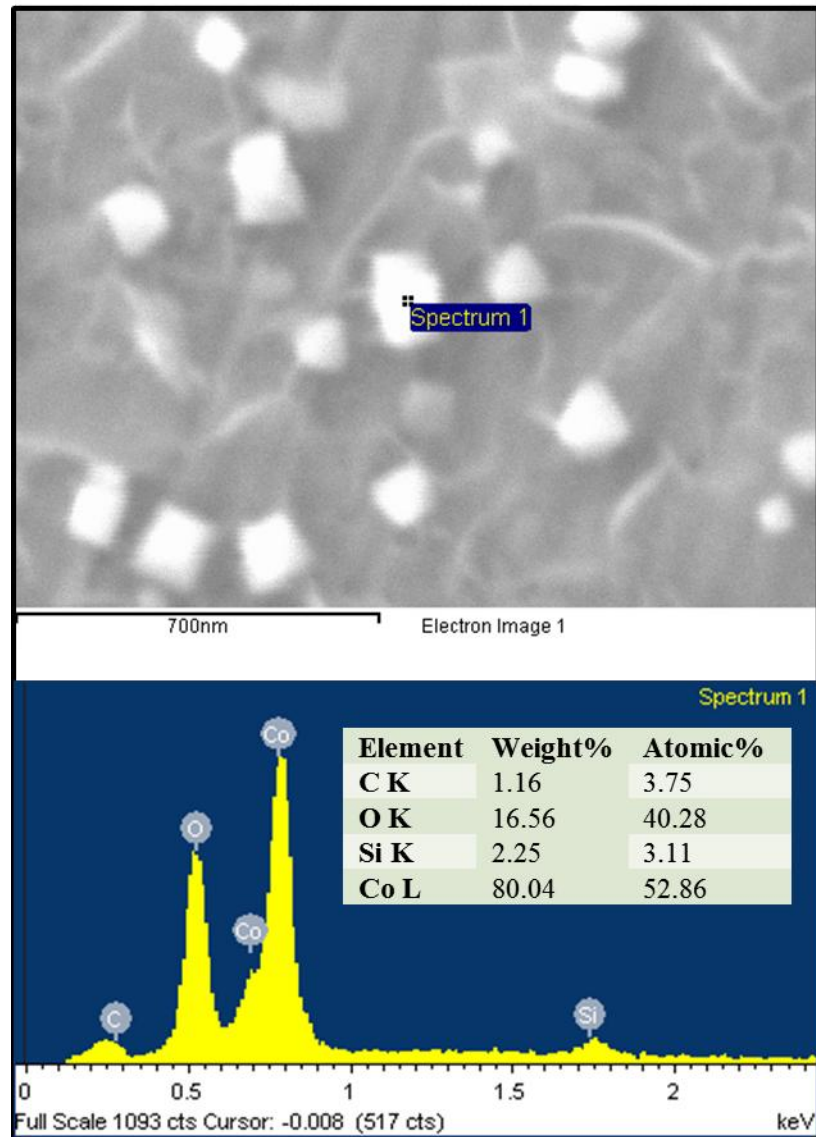


Figure 8.3: EDX analysis of a selected crystallite on the surface corroded in an NaOH-only solution in the presence of radiation at 80 °C.

To determine any change in the thicknesses of oxides formed on coupons corroded in borate and NaOH-only solutions, AES analysis was performed. The variations of the elemental composition of the surface oxide layer with depth are shown in Figure 8.4. To

identify more clearly the degree of oxidation of the different elements and their relative abundance in the oxide layer, the AES data are presented as the ratios of $O/(Co + 1.5 Cr)$ and $Co/(Co+Cr)$ as a function of sputtered depth in Figure 8.5.

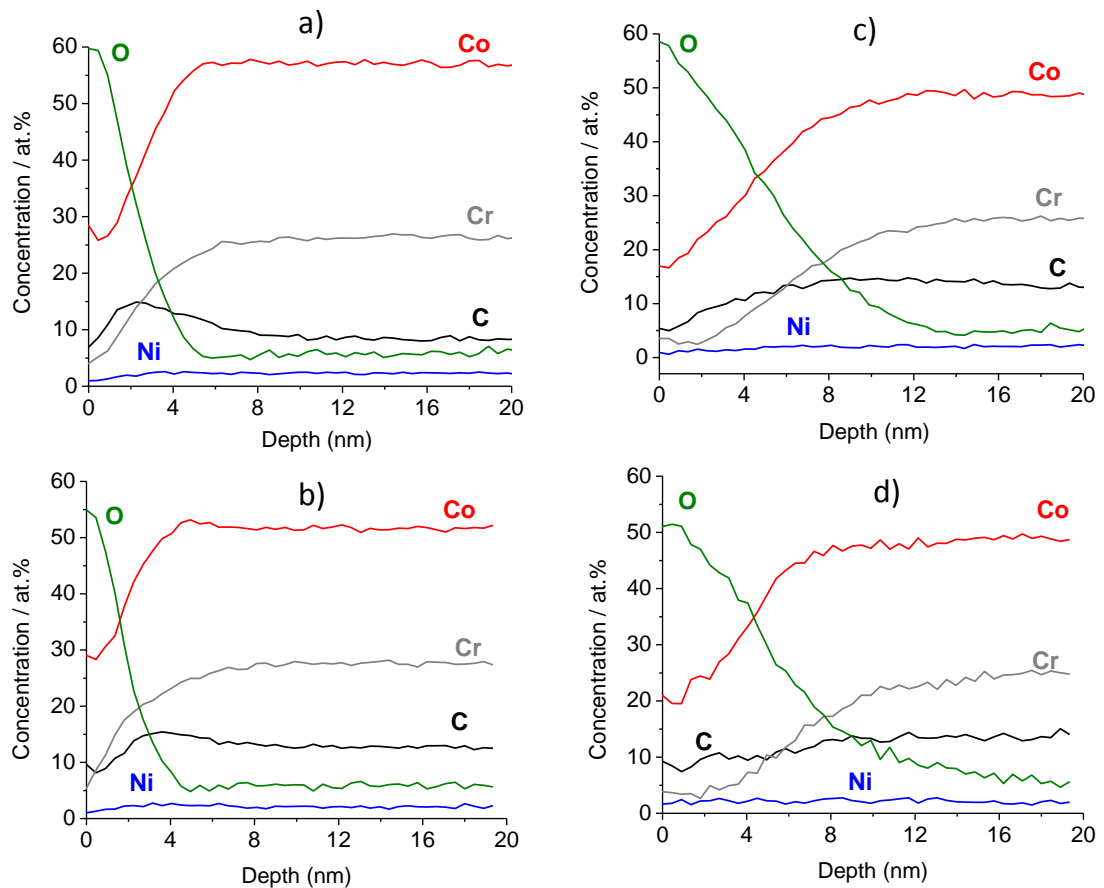


Figure 8.4: Depth profiles of the elements determined by AES of Stellite-6 coupons corroded for 3 d in the absence of radiation (left hand side) and in the presence of radiation (right hand side) in (a,c) borate, and (b,d) NaOH-only solutions at 80 °C.

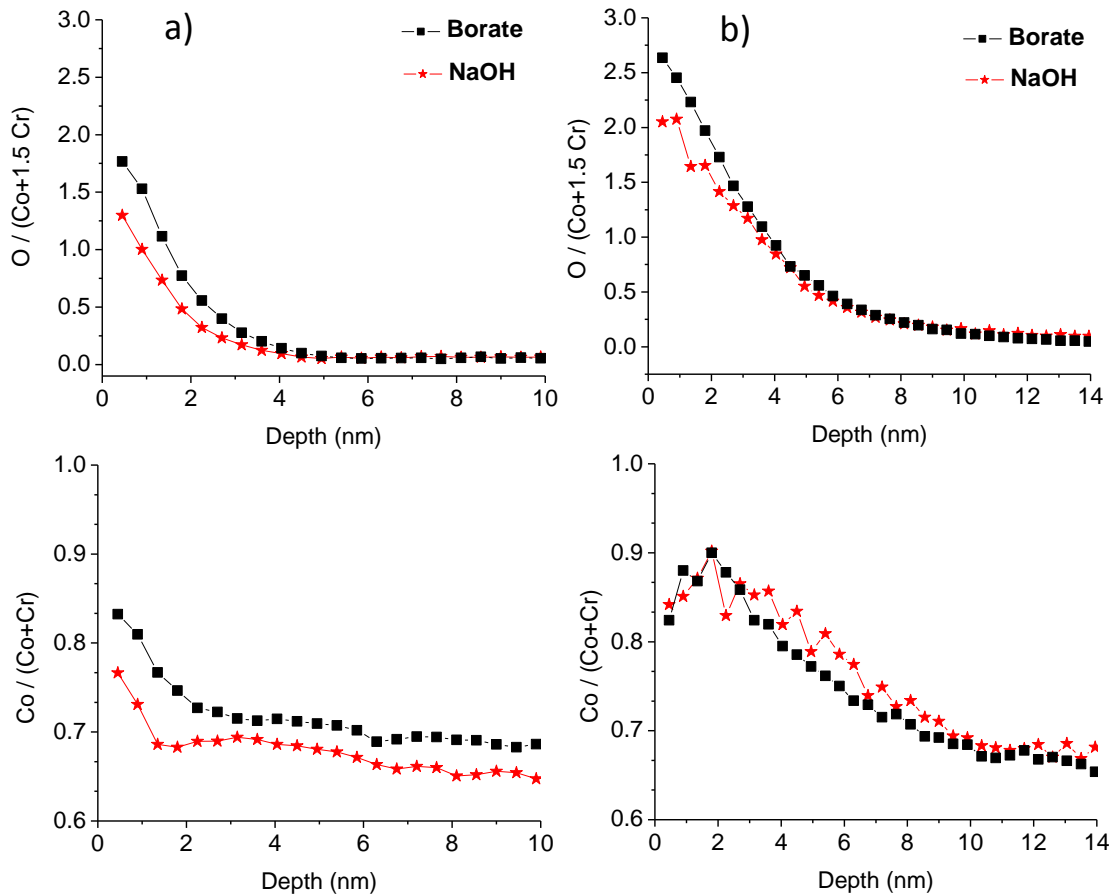


Figure 8.5: Depth profiles of $O/(Co+1.5 Cr)$ and $Co/(Co+Cr)$ determined by AES on coupons corroded in NaOH-only and borate solutions at pH 10.6, a) in the absence, and b) in the presence of radiation at 80 °C.

On the coupon corroded in a borate solution in the absence of radiation the $O/(Co + 1.5 Cr)$ ratio decreases exponentially from ~ 1.7 to 0 with depth within the first 4 nm. Within this depth range the $Co/(Co+Cr)$ ratio also decreases from 0.82 and reaches a constant value of 0.69. On the coupon corroded in an NaOH-only solution in the absence of radiation, the $O/(Co + 1.5 Cr)$ and $Co/(Co+Cr)$ ratios both decrease within the first 4 nm. The initial values

for both $O/(Co + 1.5 Cr)$ and $Co/(Co+Cr)$ ratios are slightly lower than those seen for oxides formed in the borate solution, and the $Co/(Co+Cr)$ ratios for the NaOH-only corroded coupon levels out at 0.65. We do not know the reason for the apparent differences of the deep $Co/(Co+Cr)$ ratios seen for different electrolytes with no radiation. The differences could be due to differences in instrument calibration. As this was a preliminary study, no effort was made to investigate the differences.

Results of coupons corroded in borate and NaOH-only solutions in the absence of radiation show subtle but interesting differences in the depth profiles. The $O/(Co + 1.5 Cr)$ ratio observed in borate solution shows a slower decrease up to ~ 1 nm followed by a faster and near exponential decay. The ratio observed in NaOH-only solution is lower and does not show the initial slow decrease observed in borate solution but decreases exponentially with depth from 0 nm (Figure 8.5). In both solutions the $Co/(Co + Cr)$ ratio decreases with depth until the $O/(Co + 1.5 Cr)$ ratio decreases to ~ 0.5 . In an NaOH-only solution, the decrease in $Co/(Co + Cr)$ is followed by small increase before it starts decreasing with depth again until it reaches a constant value. The depth profiles of $O/(Co + 1.5 Cr)$ and $Co/(Co + Cr)$ suggest that the oxides formed in both solutions consist of primarily $CoCr_2O_4/Co(OH)_2$ and the outer $Co(OH)_2$ layer is slightly thicker on the coupon corroded in a borate solution than in an NaOH-only solution.

The $Co/(Co + Cr)$ ratio observed in an NaOH-only solution is lower over a wider depth range (> 10 nm). The lower $Co/(Co + Cr)$ suggests that more dissolution of Co has occurred in an NaOH-only solution than in borate solution. As discussed in Chapter 7, the

rate of metal dissolution is affected not only by the solubility of the metal but also by the rate of surface hydration. The surface hydration of metal oxide is known to increase with temperature [4] due to the decreasing bulk dielectric constant and increasing acidity of the solvent as well as with the increase in concentration of adsorbed OH^- [5]. In borate solution borate anions can compete with OH^- for the adsorption sites on the metal surface and suppress the surface hydration of Co^{II} and Cr^{III} . This can explain the lower $\text{Co}/(\text{Co} + \text{Cr})$ (Figure 8.4) as well as the higher amount of dissolved Co (Table 8.1) observed in an NaOH-only solution than in borate solution.

The AES results show that radiation increased the thickness of the oxide formed in both solutions as expected. Similar to the no radiation cases, the differences in the $\text{O}/(\text{Co} + 1.5 \text{ Cr})$ and $\text{Co}/(\text{Co} + \text{Cr})$ ratios observed between the coupons corroded in borate and NaOH-only solutions are subtle (Figure 8.3). On the coupon corroded in NaOH solution, $\text{O}/(\text{Co} + 1.5 \text{ Cr})$ is lower initially but also decreases more slowly compared to that observed in borate solution until the ratio reaches a value of ~ 0.5 at ~ 5 nm. The $\text{Co}/(\text{Co} + \text{Cr})$ ratio observed in an NaOH-only solution also shows a small difference from that observed in borate solution, showing a flatter profile within 5 nm but higher values except for the first 3 nm of depth. The depth profiles of $\text{O}/(\text{Co} + 1.5 \text{ Cr})$ and $\text{Co}/(\text{Co} + \text{Cr})$ suggest that the thicknesses of the oxide layers formed in the two solutions are very similar and that the oxides consist of mainly a $\text{CoCr}_2\text{O}_4/\text{Co}(\text{OH})_2$ layer with the outer-most layer possibly converted to Co_3O_4 and CoOOH . The higher $\text{Co}/(\text{Co} + \text{Cr})$ ratio in the depth range of 4 – 10 nm observed for the NaOH-only solution while the $\text{O}/(\text{Co} + 1.5 \text{ Cr})$ ratio is the same in both

solutions further suggests that more Cr dissolution has occurred prior to the deposition of the cobalt oxide layer.

The amounts of Co and Cr dissolved in the irradiated solution were also very different in borate and NaOH-only solutions (Table 8.1). Gamma-radiation increased the dissolved amounts of both metals. However, the effect was more pronounced in an NaOH-only solution. In both solutions, the amount of dissolved Cr is about 15 times higher than the amount of dissolved Co. Gamma-radiation affected Cr dissolution more than Co dissolution. The above results show that electrolyte concentration does not influence significantly the type and thickness of oxide that can be eventually formed on Stellite-6 either in the presence or absence of radiation. However, electrolyte concentration can have a significant effect on metal dissolution, particularly that of Cr.

Table 8.1: Dissolved Co and Cr concentrations after 3-d corrosion at 80 °C determined by ICP-MS.

pH_{25°C} 10.6	No Rad		Rad	
	Co (µg/L)	Cr (µg/L)	Co (µg/L)	Cr (µg/L)
NaOH	19	3	23	363
Borate	5	4	7	82

8.3.2 Results at 150 °C

Figure 8.6 shows SEM images of coupons corroded in an NaOH-only solution at pH 10.6 in the presence and absence of radiation at 150 °C. The coupon surface corroded in the absence of radiation in an NaOH-only solution shows a less dense and thinner oxide than that seen on a coupon corroded in a borate solution. Also the Cr-rich phase is depressed compared to the Co-rich phase in an NaOH-only solution. On the irradiated coupon in NaOH solution the phase difference was not clearly observed due to a thicker oxide formation. The surface corroded in the presence of radiation appears to be more uniform for both NaOH-only and borate solutions, but it still seems thinner for the NaOH-only solution than for the borate solution case. The morphology of the oxides formed on surfaces in both sets of conditions are flaky in shape and very similar.

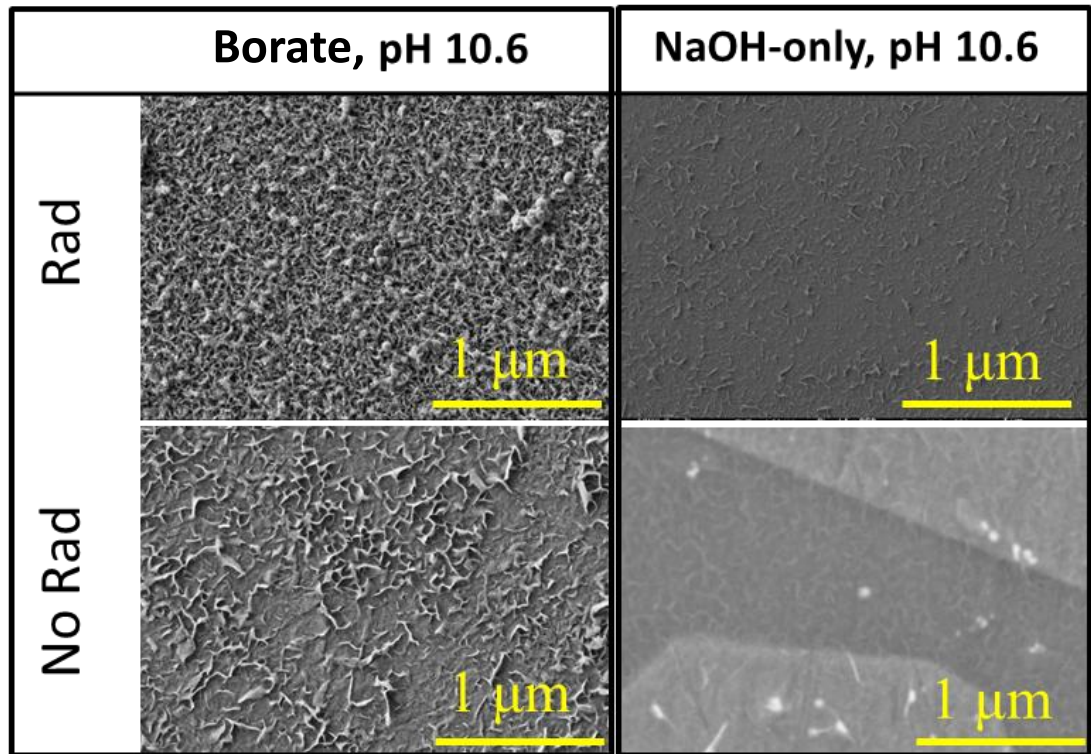


Figure 8.6: SEM images of coupons corroded in NaOH-only at pH 10.6 in the presence and absence of radiation at 150 °C.

The variations of the elemental composition of the surface oxide layer with depth are shown in Figure 8.7. As before, the AES data are also presented as the ratios of $O/(Co + 1.5 Cr)$ and $Co/(Co+Cr)$, as a function of sputtered depth, in Figure 8.8.

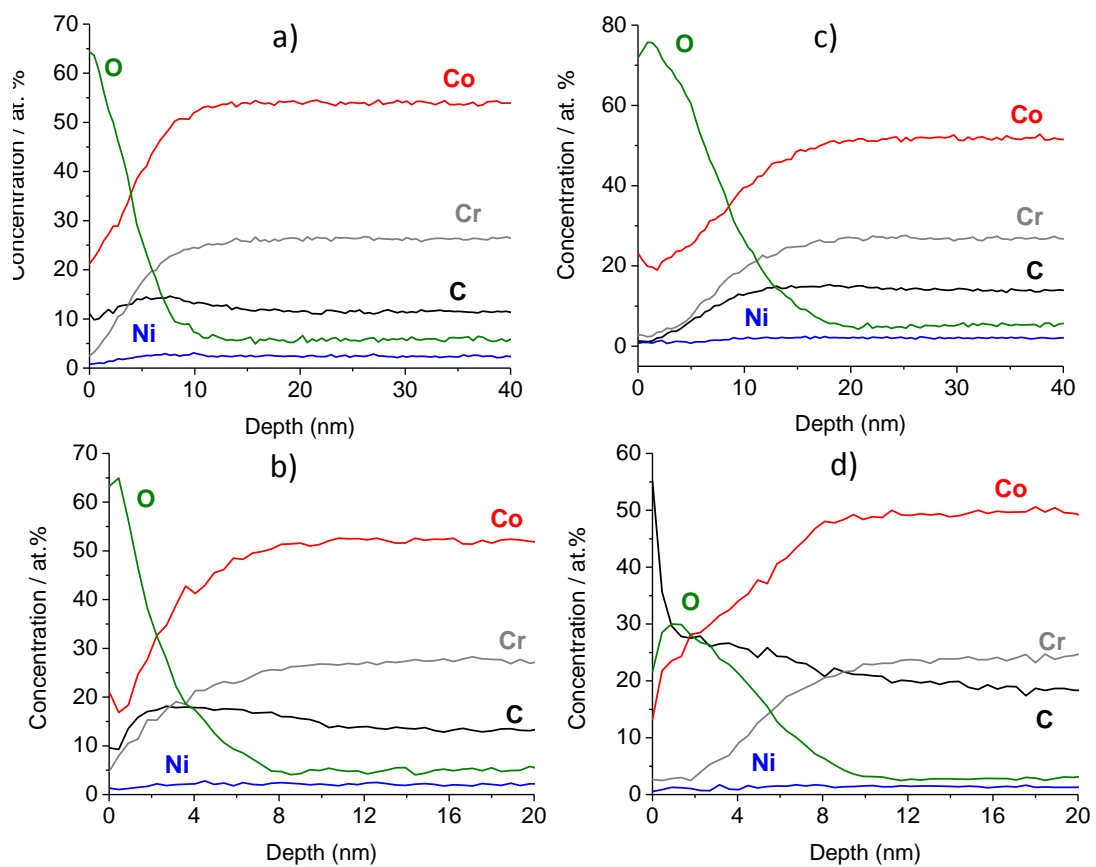


Figure 8.7: Depth profiles of the elements determined by AES of Stellite-6 coupons corroded for 3 d in the absence of radiation (left hand side) and in the presence of radiation (right hand side), in (a,c) borate and (b,d) NaOH-only solutions at 150 °C.

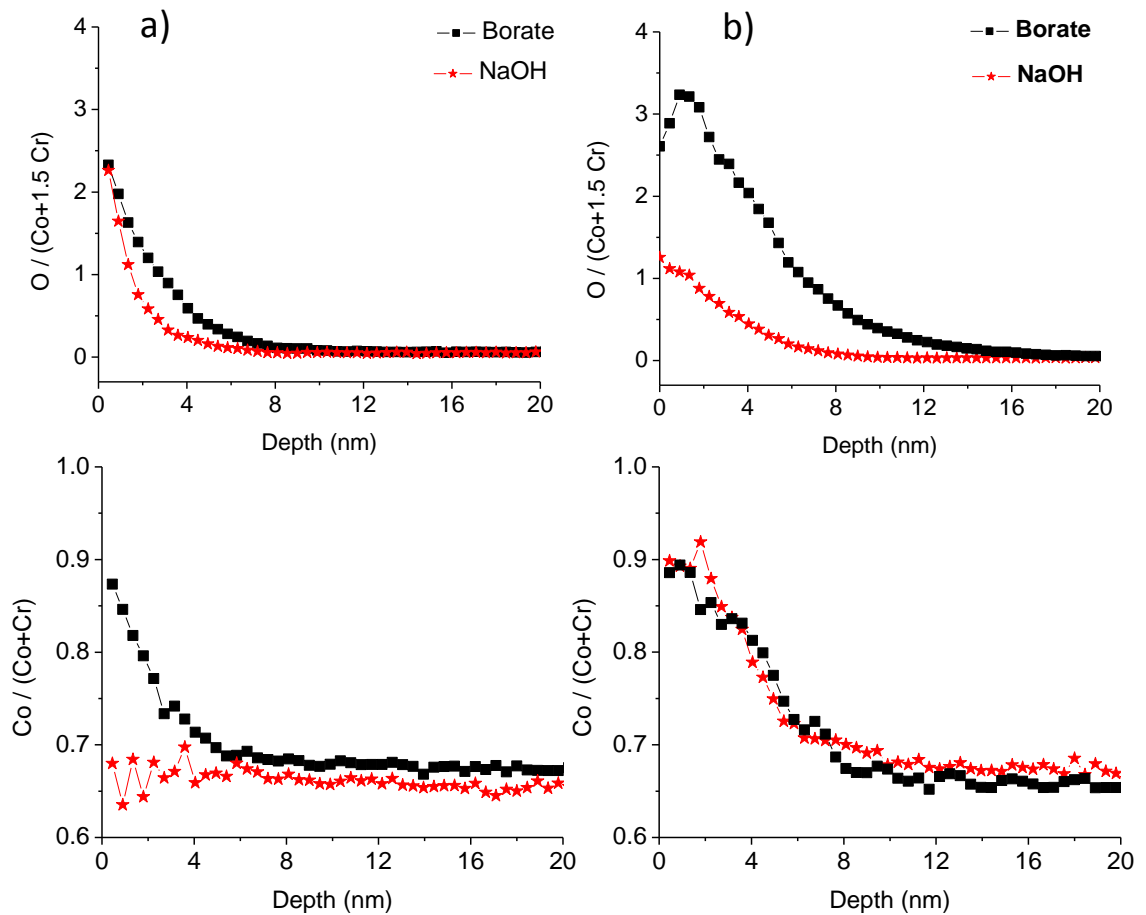


Figure 8.8: Depth profiles of $O/(Co+1.5 Cr)$ and $Co/(Co+Cr)$ determined by AES on coupons corroded in NaOH-only and borate solutions at $pH_{25^{\circ}C}$ 10.6, a) in the absence and b) in the presence of radiation at 150 °C.

On the coupon corroded in a borate solution in the absence of radiation, the $O/(Co+1.5 Cr)$ ratio decreases exponentially from ~ 2.5 to 0 with depth within the first 8 nm. Within this depth range the $Co/(Co+Cr)$ ratio also decreases from ~ 0.9 and reaches a value of 0.69. On the coupon corroded in NaOH-only solution in the absence of radiation, the $O/(Co+1.5 Cr)$ also decreases from ~ 2.5 to 0 but slight faster and it reaches a minimum

within the first 4 nm. Within this depth range the $\text{Co}/(\text{Co}+\text{Cr})$ ratio for a coupon corroded in a borate solution does not start at the high value seen in the NaOH-only case. Instead, it fluctuates over a range from 0.70 to 0.63 before it stabilizes at 0.67 (the bulk alloy ratio) at about 6 nm in depth. Again, as seen at 80 °C, we see a difference in the values of $\text{Co}/(\text{Co}+\text{Cr})$ in the bulk alloy for corrosion in borate and NaOH-only solutions that we cannot explain.

On a coupon corroded in a borate solution in the presence of radiation, the $\text{O}/(\text{Co} + 1.5 \text{ Cr})$ increases steadily from ~ 2.8 to a maximum value of 3.2 at ~ 2 nm. The ratio then decreases steadily until it reaches a final value of 0 at a depth of ~ 16 nm. In sharp contrast, on a coupon corroded in an NaOH-only solution in the presence of radiation, the $\text{O}/(\text{Co} + 1.5 \text{ Cr})$ starts at a much lower value (1.1) at the surface, and this ratio decreases steady to a value of 0 after only ~ 8 nm.

The behaviour of the $\text{Co}/(\text{Co}+\text{Cr})$ ratio is quite different. Unlike the case where there is no radiation present, with radiation the depth profiles of the $\text{Co}/(\text{Co}+\text{Cr})$ ratios are essentially identical for both the borate and NaOH solutions. The ratio starts at a value of ~ 0.9 and decreases steadily to a value of 0 within the first 12 nm. The AES results clearly show that a thicker oxide is formed during corrosion in the presence of radiation in the borate solution. The results also show that there is no depletion of Co in the oxide that is dependent on the nature of the electrolyte solution.

The ICP-MS results at 150 °C are shown in Table 8.2. The solution analysis shows the amounts of Co and Cr in both NaOH-only and borate solutions are similar in the absence of radiation, albeit slightly higher in borate solution. In the presence of radiation, the amount

Co in both solutions is the same. However, the amount Cr in solution is very much higher (386 $\mu\text{g/L}$) after corrosion in an NaOH-only solution compared to corrosion in a borate solution ($< 10 \mu\text{g/L}$). We can also note that the concentrations of Co and Cr in the different solutions are not strongly dependent on the corrosion temperature. The concentration of Cr is 386 $\mu\text{g/L}$ at 150 °C and 363 $\mu\text{g/L}$ at 80 °C.

Table 8.2: Dissolved Co and Cr concentrations after 3-d corrosion at 150 °C determined by ICP-MS.

pH_{25°C} 10.6	No Rad		Rad	
	Co ($\mu\text{g/L}$)	Cr ($\mu\text{g/L}$)	Co ($\mu\text{g/L}$)	Cr ($\mu\text{g/L}$)
NaOH	5.55	2.94	9.29	386
Borate	8.95	4.97	9.63	<10

Comparing the ICP-MS results at 80 °C and 150 °C shows some similarities and differences. At both temperatures the amount of Cr dissolved is high only for the corrosion in NaOH-only and a radiation field. The amount of Cr seen in solution for corrosion at 150 °C in a borate solution with a radiation field is significantly reduced compared to that seen at 80 °C. The depth profile of two sets of O/(Co+1.5 Cr) ratios for coupons corroded in a borate solution at 80 °C and 150 °C also support the ICP-MS results, as the oxide thickness at 80 °C is almost of half of that formed at 150 °C (as we explained in chapter 7).

A substantial difference in the corrosion of Stellite-6 in two electrolyte solution used here is only seen in the results of corrosion at 150 °C with radiation present. We see a thinner

oxide being formed for coupons corroded in the NaOH-only solution and more Cr dissolution. These two differences are well correlated as the formation of a protective thicker oxide should prevent the oxidative dissolution of underlying Cr.

The Na^+ cation and the borate (BO_3^{3-}) anion are not expected to participate directly in the corrosion process on Stellite-6 (e.g., by incorporation of either ion into the growing oxide lattice). Instead, they are expected to have their most significant impact on corrosion through their contributions to the ionic strength of the corroding solution. Changes in ionic strength alter the charge carrier's net electrostatic effect in solution and thereby change the thickness of the double layer at an interface [6]. This change in the double layer thickness affects the potential distribution across the Ox/Sol region and the charge transport behaviour in the double layer region. The higher the ionic strength, the thinner the double layer becomes. A thinner double layer can lead to a steeper diffusion layer (concentration gradient) at the M/Sol interface and increase the rate of mass transport of a metal cation away from the charged surface [7]. The net effect of changing the ionic strength of the electrolyte however, will depend on the relative contributions of the potential dependent metal oxidation rate and the metal cation mass transport rate to the net corrosion rate. That being said, we might expect a higher ionic strength in the solution to promote the rate of metal dissolution (by increasing the rate of metal ion transport away from the corroding surface). However, the AES data indicates that oxide growth is actually favoured in the higher ionic strength borate solution at 150 °C. The effect is slightly weaker at 80 °C.

To explain our results, we speculate that borate anions in solution have two impacts on the oxide formation in this system. As mentioned earlier, the borate anion can compete for the adsorption sites on the M/Sol interface with OH^- . The accumulation of BO_3^{3-} ions on the interface can prevent access of OH^- to the inner Helmholtz layer. This can slow down the surface hydration of Co. The dissolution of Co from the oxide surface occurs as a hydration of the outer oxide surface even at pH 10.6 where the Co solubility is low, and hence promotes the formation of a thicker oxide. As the Co oxide grows thicker, less $\text{Cr}_2\text{O}_3/\text{CoCr}_2\text{O}_4$ are exposed to the solution and dissolution of Cr_2O_3 (or in a hydrated form CrOOH and $\text{Cr}(\text{OH})_3$ into the aqueous phase will be reduced. In the presence of radiation the potential is high enough to oxidize Cr^{3+} (form $\text{Cr}(\text{OH})_3$ or CrOOH) to highly soluble Cr^{6+} [8,9]. This is why we see such high dissolved Cr concentrations with radiation at 150 °C. The rate of conversion of Cr_2O_3 to $\text{Cr}(\text{OH})_3$ is known to be higher at a higher potential (created by radiolysis) [10].

The OH^- concentration must be the same in both an NaOH-only solution and a borate solution with the same pH. However we expect easier access of OH^- to the M/Sol interface in the NaOH-only solution so that the hydrolysis of Co is easier in the solution. This effect becomes even more important at 150 °C where the reaction rates are faster. As a consequence, for the coupons corroded in NaOH-only solution in 150 °C with radiation present the oxide layer is thin, as seen in Figure 8.8b. The higher metal dissolution rate in an NaOH-only solution than in a borate solution can also explain the more pronounced difference seen in surface morphologies of the Cr-rich versus Co-rich phases and the widening of the gap along the phase boundary (Figures 8.1 and 8.2).

8.4 CONCLUSION

It appears clear that changes in the ionic strength and in particular, the nature of the electrolyte can affect the degree of Stellite-6 oxidation, especially at elevated temperatures in the presence of a radiation field. Although the number of tests that we performed to explore this dependence was limited, we observed that presence of borate (BO_3^{3-} ions) can lead to the thicker oxide film and significantly suppress the dissolution of Cr. Our results do indicate that it would not be appropriate to extrapolate corrosion rate measurements under high temperature conditions without taking into account the nature and concentration of ionic species in solution. Further work would be required to do so within the framework of a mechanistic understanding of how the ionic species affect surface oxide stability, ion transport and oxide growth.

8.5 REFERENCES

- [1] P.H. Tewari, A.B. Campbell, Temperature dependence of point of zero charge of cobalt and nickel oxides and hydroxides, *J. Colloid Interface Sci.*, 55 (1976) 531–539.
- [2] C.F. Baes, R.E. Mesmer, *The Hydrolysis of Cations*, 2nd Ed., Wiley, New York, 1986.
- [3] S.E. Ziemniak, M.A. Goyette, K.E.S. Combs, Cobalt (II) oxide solubility and phase stability in alkaline media at elevated temperatures, *J. Solution Chem.*, 28 (1999) 809–836.
- [4] D.J. Wesolowski, M.L. Machesky, M.K. Ridley, D.A. Palmer, Z. Zhang, P. Fenter, M. Předota, P.T. Cumming, Ion adsorption on metal oxide surfaces in hydrothermal conditions, *ECS Trans.*, 11 (2008) 167–180.
- [5] S. Goldberg, H.S. Foster, E.L. Heick, Boron adsorption mechanisms on oxides, clay minerals, and soils inferred from ionic strength effects, *Soil Sci. Soc. Am. J.*, 75 (1993) 704–708.
- [6] C.M.A. Brett, A.M.O. Brett, *Electrochemistry: Principles, Methods, and Applications*, Oxford, New York, 1994.
- [7] J. Wiebe, E. Spohr, Double layer effects in a model of proton discharge on charged electrodes, *Beilstein J. Nanotechnol.*, 5 (2014) 973–982.

- [8] I. Betova, M. Bojinov, T. Laitinen, M. Kari, The transpassive dissolution mechanism of highly alloyed stainless steels II . Effect of pH and solution anion on the kinetics, *Corros. Sci.*, 44 (2002) 2699–2723.
- [9] S.E. Ziemniak, M.E. Jones, K.E.S. Combs, Solubility and phase behavior of Cr (III) oxides in alkaline media at elevated temperatures, *J. Solution Chem.*, 27 (1998) 33–65.
- [10] L.J. Oblonsky, T.M. Devine, A surface enhanced raman spectroscopic study of the passive films formed in borate buffer on iron, nickel, chromium and stainless, *Corros. Sci.*, 37 (1995) 17–41.

CHAPTER 9

Summary and Future Work

9.1 SUMMARY

This thesis examined the mechanism of Stellite-6 corrosion and the effects of gamma radiation on the corrosion process. We have found that the corrosion mechanism is sensitive to pH, temperature and the chemical potential of the solution phase. The change in the chemical potential induced by either addition of redox active species or by γ -radiolysis changes the corrosion potential. Change on the metal surface can also affect the corrosion potential. Thus, even in the absence of radiation with constant pH and temperature we observed the corrosion potential on Stellite-6 in deaerated water at pH 6.0 remains nearly constant with time over a long period, whereas the corrosion potential at pH 10.6 increases slowly with time as corrosion progresses.

Electrochemical studies of both pure Co and the Co-Cr alloy Stellite-6 showed that corrosion occurs with characteristic growth of different oxides. The corrosion potential on the metal limits the type of oxides that can grow. Different oxides are stable and preferentially formed in different potential regions. Furthermore, as corrosion progresses and an oxide layer covers and/or grows, the corrosion potential must be sufficiently high enough to overcome the Coulombic as well as the chemical potential barrier imposed by the oxide layer that is growing.

Gamma-irradiation causes the corrosion potential of the system to rise substantially due to radiolytic production of oxidizing species such as H_2O_2 . For Co and Stellite-6 the presence of ionizing radiation shifts the corrosion potential from a potential in Regions I/II to a potential in Region III for both metals. For Stellite-6 at pH 10.6 and 25 °C, the corrosion potential increases as corrosion progresses and the oxide layer thickens. Nevertheless, the corrosion potential in the absence of radiation increases very slowly within Region I/II until it reaches the transition potential between Region I/II and Region III. In the presence of radiation the corrosion potential moves through Region I/II very quickly and continues to increase through Region III until it reaches the transition potential between Regions III and IV. The transition from Region I/II to III occurs near $-0.4 V_{SCE}$, the equilibrium potential for Co to CoO/Co(OH)₂ oxidation, while the transition from Region III to Region IV occurs at $\sim 0.1 V_{SCE}$, the equilibrium potential for CoO/Co(OH)₂ conversion to mixed Co^{II/III} or Co^{III} oxides/hydroxides. Hence the presence of irradiation must be considered in predicting the nature and rate of oxide growth on these materials.

During cyclic voltammetry we see the oxidation of Co to Co^{II} starts at a lower potential on Stellite-6 than on Co. The anodic activity at the lower potential is due to the fact that in the presence of Cr₂O₃ the Co oxidation product, CoCr₂O₄ is thermodynamically more stable than CoO or Co(OH)₂. The presence of an air-formed Cr^{III} oxide layer on a metal is generally attributed to for increasing passivity of the metal. Our study shows that although the presence of Cr₂O₃ slows down the metal oxidation and hence, lower current in the mid potential range, its corrosion product CoCr₂O₄ provides the additional passivity of the Co-Cr alloy.

We have performed corrosion kinetic studies under potentiostatic conditions that are more relevant to corrosion conditions where the solution chemical environment does not change significantly. At a given corrosion potential the cobalt oxidation on Stellite-6 may not continue at a constant rate. Depending on solution environment, the corroding surface may change as corrosion progresses and the oxide layer converts and/or thickens. The effect of slow growing oxide on corrosion rate is difficult to capture from the CV study.

In the presence of an oxide film, the rate of metal oxidation (or the rate of aqueous reduction) depends on both $\Delta E_{\text{rdx}}^{\text{eq}}$ and $\Delta E_f(t)$. The values of $E_{\text{red}}^{\text{eq}}$ and $E_{\text{ox}}^{\text{eq}}$ will depend on the actual aqueous reduction and metal oxidation steps that are involved in the overall corrosion reaction. Incorporation of metal cations and oxygen anions into the oxide lattice also becomes difficult since the potential barrier has increased ($\Delta E_f(t)$ is no longer constant). Hence, even under the constant redox conditions (i.e., $\Delta E_{\text{rdx}}^{\text{eq}}$ is constant), the net metal oxidation rate decreases with time as the oxide layer thickens. We observed that this as a continuous decrease in current with time during corrosion under potentiostatic polarization when the oxide growth is favoured over metal dissolution.

The rate of change in the oxide layer on Stellite-6 depends strongly on overpotential, pH and temperature. These dependences arise since there is a competition between dissolution of oxidized metal and incorporation of the oxidized metal into a growing oxide layer. An increase in effective overpotential increases metal oxidation rate, where the effective overpotential is the corrosion potential minus the potential barrier imposed by the oxide layer. The increase in the metal oxidation rate increases both the competing reactions

for the oxidized metal. Solution pH and temperature have a strong influence on the net oxidation or corrosion rate. The solution pH affects the rate primarily through its effect on metal solubility since the solubility is the main driving force for metal dissolution. The solubilities of Co^{II} species are highly dependent on pH because of the hydrolysis equilibrium of Co^{II} and the solid-liquid phase equilibrium of $\text{Co}(\text{OH})_2$. The solubilities of Co^{II} species vary by several orders of magnitude over the pH range from 6 to 10. At near neutral pH (6.0), Co^{II} species are highly soluble and the dissolution dominates over oxide formation. The solubility of Co^{II} is near minimum at pH 10.6 and at this pH oxide formation is preferred over dissolution. Gamma-irradiation increases the corrosion potential and increases the cobalt oxidation rate. This increases both cobalt dissolution and cobalt oxide growth. At pH 6.0, the increase in metal oxidation primarily appears as an increase in dissolution. At pH 10.6 it primarily increases metal oxide growth, which subsequently impedes cobalt oxidation. At pH 8.4, intermediate behaviour is seen; the main corrosion process is metal dissolution in the absence of radiation, but oxide formation becomes more important comparable in rate with cobalt dissolution in the presence of radiation.

Increasing temperature also affects the hydrolysis and the phase equilibria that determine the solubility of Co^{II} species, but its effect is smaller than the effect of pH. However, temperature can have a significant effect on the hydrolysis kinetics and aqueous diffusion rate of the Co^{II} species. Thus, increasing temperature will increase metal dissolution rate but its effect will be limited at pH 6.0 for Co^{II} dissolution. The combination of high temperature and high pH, however, increases Cr^{III} dissolution. Thus, a large amount of Cr^{III} can be dissolved before a uniform protective layer of cobalt oxides can be formed.

Temperature not only affects the reaction thermodynamics and shifts the hydrolysis and phase equilibria but also affects the rates of thermal processes which include chemical reactions (oxide growth and surface hydration) and transport processes (aqueous and solid state diffusion). Since the rates of the elementary steps have different temperature dependences the net corrosion rate does not have simple temperature dependence.

These findings are important because the growth of a thicker oxide slows further oxidation and this, in turn, reduces the rate of metal dissolution that must still occur when oxide formation eventually slows.

An important goal of this work was to gain a sound understanding of the corrosion process on Stellite and the influence of environmental conditions and radiation on the corrosion process. We have achieved this goal and shown how the rates of the corrosion processes are affected by the corrosion conditions. Importantly, we have also identified the conditions under which the rate of dissolution of Co can be minimized because this dissolution presents a challenge to the nuclear industry.

9.2 FUTURE WORK

We have demonstrated how a combination of data from electrochemical and corrosion tests can be effectively used to understand in detail the nature of oxide films that grow on Stellite-6, and how the growth of those films can influence the dissolution of metal from the alloy, and particularly Co. However, performing additional corrosion tests as a function of time (starting from shorter duration, e.g. 5 h) using coupons in the quartz cell

would be desirable to fully understand the corrosion kinetics of Stellite-6 in the presence of radiation at different temperatures.

Our work spanned a relatively narrow range of pHs (6 to 10) and temperatures up to 150 °C. While corrosion at pHs outside of our studied range are of limited interest to the nuclear industry, there may be applications of Co-Cr alloys where work at acidic or more alkaline pHs would be useful. More importantly, there is an opportunity to extend our work to even higher temperatures. Water systems in nuclear reactors operate at temperatures up to 325 °C and there may be circumstances in which an understanding of corrosion at even higher temperatures (perhaps associated with upset conditions) could be useful. The challenge in performing well-characterised electrochemistry experiments at such high temperatures is not trivial. Design of such tests and the test objectives should be carefully performed to justify the effort and the value of the results.

There are still some uncertainties about the effect of borate on corrosion of Stellite-6 and how adsorption of borate anions on the interface can significantly suppress the Cr dissolution compared with a free-borate solution. It would be useful to examine the effects of different concentrations of borate on corrosion of Stellite-6 at high temperature, in particular, in the presence of radiation as well.

A more interesting and potentially fruitful avenue for future work would be a multi-disciplinary study that combined mechanical wear with corrosion. The Stellite applications of greatest interest, including applications in the nuclear industry where radiation is present, invoke the wear resistance of the alloy. Wear involves the mechanical contact of surfaces

and the abrasive removal of oxide material. Clearly this process depends intimately on the characteristics of the oxide surface (morphology, chemical nature, oxide thickness and density, oxide toughness, etc.). Our work has shown how the nature of the oxide changes depending on the environmental conditions. Addition of mechanical wear as a further environmental factor opens the door to a new suite of studies. Wear will remove oxide and this will allow more competition from dissolution than would normally be expected (as based on this study a thicker oxide impedes dissolution). Analysis of combined corrosion and wear would also substantially extend the sophistication demands for a time-dependent corrosion model.

Appendix A.

Copyrights

6/30/2014

Rightslink Printable License

ELSEVIER LICENSE TERMS AND CONDITIONS

Jun 30, 2014

This is a License Agreement between Mehran Behazin ("You") and Elsevier ("Elsevier") provided by Copyright Clearance Center ("CCC"). The license consists of your order details, the terms and conditions provided by Elsevier, and the payment terms and conditions.

All payments must be made in full to CCC. For payment instructions, please see information listed at the bottom of this form.

Supplier	Elsevier Limited The Boulevard, Langford Lane Kidlington, Oxford, OX5 1GB, UK
Registered Company Number	1982084
Customer name	Mehran Behazin
Customer address	171, 1560 Adelaide st north london, ON N5X2C1
License number	3419000285969
License date	Jun 30, 2014
Licensed content publisher	Elsevier
Licensed content publication	Corrosion Science
Licensed content title	Comparative study of film formation on high-purity Co and Stellite-6: Probing the roles of a chromium oxide layer and gamma-radiation
Licensed content author	M. Behazin, M.C. Biesinger, J.J. Noël, J.C. Wren
Licensed content date	October 2012
Licensed content volume number	63
Licensed content issue number	None
Number of pages	11
Start Page	40
End Page	50
Type of Use	reuse in a thesis/dissertation
Portion	full article
Format	both print and electronic
Are you the author of this Elsevier article?	Yes
Will you be translating?	No

<https://s100.copyright.com/AppDispatchServlet>

1/7

6/30/2014

Rightslink Printable License

Title of your thesis/dissertation	Radiation Induced Corrosion of Stellite-6
Expected completion date	Sep 2014
Estimated size (number of pages)	200
Elsevier VAT number	GB 494 6272 12
Permissions price	0.00 USD
VAT/Local Sales Tax	0.00 USD / 0.00 GBP
Total	0.00 USD
Terms and Conditions	

INTRODUCTION

1. The publisher for this copyrighted material is Elsevier. By clicking "accept" in connection with completing this licensing transaction, you agree that the following terms and conditions apply to this transaction (along with the Billing and Payment terms and conditions established by Copyright Clearance Center, Inc. ("CCC"), at the time that you opened your Rightslink account and that are available at any time at <http://myaccount.copyright.com>).

GENERAL TERMS

2. Elsevier hereby grants you permission to reproduce the aforementioned material subject to the terms and conditions indicated.

3. Acknowledgement: If any part of the material to be used (for example, figures) has appeared in our publication with credit or acknowledgement to another source, permission must also be sought from that source. If such permission is not obtained then that material may not be included in your publication/copies. Suitable acknowledgement to the source must be made, either as a footnote or in a reference list at the end of your publication, as follows:

"Reprinted from Publication title, Vol /edition number, Author(s), Title of article / title of chapter, Pages No., Copyright (Year), with permission from Elsevier [OR APPLICABLE SOCIETY COPYRIGHT OWNER]." Also Lancet special credit - "Reprinted from The Lancet, Vol. number, Author(s), Title of article, Pages No., Copyright (Year), with permission from Elsevier."

4. Reproduction of this material is confined to the purpose and/or media for which permission is hereby given.

5. Altering/Modifying Material: Not Permitted. However figures and illustrations may be altered/adapted minimally to serve your work. Any other abbreviations, additions, deletions and/or any other alterations shall be made only with prior written authorization of Elsevier Ltd. (Please contact Elsevier at permissions@elsevier.com)

6. If the permission fee for the requested use of our material is waived in this instance, please be advised that your future requests for Elsevier materials may attract a fee.

7. Reservation of Rights: Publisher reserves all rights not specifically granted in the combination of (i) the license details provided by you and accepted in the course of this licensing transaction, (ii)

<https://s100.copyright.com/AppDispatchServlet>

2/7

these terms and conditions and (iii) CCC's Billing and Payment terms and conditions.

8. License Contingent Upon Payment: While you may exercise the rights licensed immediately upon issuance of the license at the end of the licensing process for the transaction, provided that you have disclosed complete and accurate details of your proposed use, no license is finally effective unless and until full payment is received from you (either by publisher or by CCC) as provided in CCC's Billing and Payment terms and conditions. If full payment is not received on a timely basis, then any license preliminarily granted shall be deemed automatically revoked and shall be void as if never granted. Further, in the event that you breach any of these terms and conditions or any of CCC's Billing and Payment terms and conditions, the license is automatically revoked and shall be void as if never granted. Use of materials as described in a revoked license, as well as any use of the materials beyond the scope of an unrevoked license, may constitute copyright infringement and publisher reserves the right to take any and all action to protect its copyright in the materials.

9. Warranties: Publisher makes no representations or warranties with respect to the licensed material.

10. Indemnity: You hereby indemnify and agree to hold harmless publisher and CCC, and their respective officers, directors, employees and agents, from and against any and all claims arising out of your use of the licensed material other than as specifically authorized pursuant to this license.

11. No Transfer of License: This license is personal to you and may not be sublicensed, assigned, or transferred by you to any other person without publisher's written permission.

12. No Amendment Except in Writing: This license may not be amended except in a writing signed by both parties (or, in the case of publisher, by CCC on publisher's behalf).

13. Objection to Contrary Terms: Publisher hereby objects to any terms contained in any purchase order, acknowledgment, check endorsement or other writing prepared by you, which terms are inconsistent with these terms and conditions or CCC's Billing and Payment terms and conditions. These terms and conditions, together with CCC's Billing and Payment terms and conditions (which are incorporated herein), comprise the entire agreement between you and publisher (and CCC) concerning this licensing transaction. In the event of any conflict between your obligations established by these terms and conditions and those established by CCC's Billing and Payment terms and conditions, these terms and conditions shall control.

14. Revocation: Elsevier or Copyright Clearance Center may deny the permissions described in this License at their sole discretion, for any reason or no reason, with a full refund payable to you. Notice of such denial will be made using the contact information provided by you. Failure to receive such notice will not alter or invalidate the denial. In no event will Elsevier or Copyright Clearance Center be responsible or liable for any costs, expenses or damage incurred by you as a result of a denial of your permission request, other than a refund of the amount(s) paid by you to Elsevier and/or Copyright Clearance Center for denied permissions.

LIMITED LICENSE

The following terms and conditions apply only to specific license types:

15. Translation: This permission is granted for non-exclusive world **English** rights only unless your license was granted for translation rights. If you licensed translation rights you may only translate this content into the languages you requested. A professional translator must perform all translations and reproduce the content word for word preserving the integrity of the article. If this license is to re-use 1 or 2 figures then permission is granted for non-exclusive world rights in all languages.

16. Posting licensed content on any Website: The following terms and conditions apply as follows: Licensing material from an Elsevier journal: All content posted to the web site must maintain the copyright information line on the bottom of each image; A hyper-text must be included to the Homepage of the journal from which you are licensing at <http://www.sciencedirect.com/science/journal/xxxxx> or the Elsevier homepage for books at <http://www.elsevier.com>; Central Storage: This license does not include permission for a scanned version of the material to be stored in a central repository such as that provided by Heron/XanEdu.

Licensing material from an Elsevier book: A hyper-text link must be included to the Elsevier homepage at <http://www.elsevier.com>. All content posted to the web site must maintain the copyright information line on the bottom of each image.

Posting licensed content on Electronic reserve: In addition to the above the following clauses are applicable: The web site must be password-protected and made available only to bona fide students registered on a relevant course. This permission is granted for 1 year only. You may obtain a new license for future website posting.

For journal authors: the following clauses are applicable in addition to the above: Permission granted is limited to the author accepted manuscript version* of your paper.

***Accepted Author Manuscript (AAM) Definition:** An accepted author manuscript (AAM) is the author's version of the manuscript of an article that has been accepted for publication and which may include any author-incorporated changes suggested through the processes of submission processing, peer review, and editor-author communications. AAMs do not include other publisher value-added contributions such as copy-editing, formatting, technical enhancements and (if relevant) pagination.

You are not allowed to download and post the published journal article (whether PDF or HTML, proof or final version), nor may you scan the printed edition to create an electronic version. A hyper-text must be included to the Homepage of the journal from which you are licensing at <http://www.sciencedirect.com/science/journal/xxxxx>. As part of our normal production process, you will receive an e-mail notice when your article appears on Elsevier's online service ScienceDirect (www.sciencedirect.com). That e-mail will include the article's Digital Object Identifier (DOI). This number provides the electronic link to the published article and should be included in the posting of your personal version. We ask that you wait until you receive this e-mail and have the DOI to do any posting.

Posting to a repository: Authors may post their AAM immediately to their employer's institutional repository for internal use only and may make their manuscript publically available after the journal-specific embargo period has ended.

Please also refer to [Elsevier's Article Posting Policy](#) for further information.

18. For book authors the following clauses are applicable in addition to the above: Authors are permitted to place a brief summary of their work online only.. You are not allowed to download and post the published electronic version of your chapter, nor may you scan the printed edition to create an electronic version. **Posting to a repository:** Authors are permitted to post a summary of their chapter only in their institution's repository.

20. Thesis/Dissertation: If your license is for use in a thesis/dissertation your thesis may be submitted to your institution in either print or electronic form. Should your thesis be published commercially, please reapply for permission. These requirements include permission for the Library and Archives of Canada to supply single copies, on demand, of the complete thesis and include permission for UMI to supply single copies, on demand, of the complete thesis. Should your thesis be published commercially, please reapply for permission.

Elsevier Open Access Terms and Conditions

Elsevier publishes Open Access articles in both its Open Access journals and via its Open Access articles option in subscription journals.

Authors publishing in an Open Access journal or who choose to make their article Open Access in an Elsevier subscription journal select one of the following Creative Commons user licenses, which define how a reader may reuse their work: Creative Commons Attribution License (CC BY), Creative Commons Attribution – Non Commercial - ShareAlike (CC BY NC SA) and Creative Commons Attribution – Non Commercial – No Derivatives (CC BY NC ND)

Terms & Conditions applicable to all Elsevier Open Access articles:

Any reuse of the article must not represent the author as endorsing the adaptation of the article nor should the article be modified in such a way as to damage the author's honour or reputation.

The author(s) must be appropriately credited.

If any part of the material to be used (for example, figures) has appeared in our publication with credit or acknowledgement to another source it is the responsibility of the user to ensure their reuse complies with the terms and conditions determined by the rights holder.

Additional Terms & Conditions applicable to each Creative Commons user license:

CC BY: You may distribute and copy the article, create extracts, abstracts, and other revised versions, adaptations or derivative works of or from an article (such as a translation), to include in a collective work (such as an anthology), to text or data mine the article, including for commercial purposes without permission from Elsevier

CC BYNC SA: For non-commercial purposes you may distribute and copy the article, create extracts, abstracts and other revised versions, adaptations or derivative works of or from an article

6/30/2014

Rightslink Printable License

(such as a translation), to include in a collective work (such as an anthology), to text and data mine the article and license new adaptations or creations under identical terms without permission from Elsevier

CC BY NC ND: For non-commercial purposes you may distribute and copy the article and include it in a collective work (such as an anthology), provided you do not alter or modify the article, without permission from Elsevier

Any commercial reuse of Open Access articles published with a CC BY NC SA or CC BY NC ND license requires permission from Elsevier and will be subject to a fee.

Commercial reuse includes:

- Promotional purposes (advertising or marketing)
- Commercial exploitation (e.g. a product for sale or loan)
- Systematic distribution (for a fee or free of charge)

Please refer to [Elsevier's Open Access Policy](#) for further information.

21. Other Conditions:

v1.7

If you would like to pay for this license now, please remit this license along with your payment made payable to "COPYRIGHT CLEARANCE CENTER" otherwise you will be invoiced within 48 hours of the license date. Payment should be in the form of a check or money order referencing your account number and this invoice number 501340495. Once you receive your invoice for this order, you may pay your invoice by credit card. Please follow instructions provided at that time.

Make Payment To:
Copyright Clearance Center
Dept 001
P.O. Box 843006
Boston, MA 02284-3006

For suggestions or comments regarding this order, contact RightsLink Customer Support: customercare@copyright.com or +1-877-622-5543 (toll free in the US) or +1-978-646-2777.

Gratis licenses (referencing \$0 in the Total field) are free. Please retain this printable license for your reference. No payment is required.

<https://s100.copyright.com/AppDispatchServlet>

6/7

6/30/2014

Rightslink Printable License

ELSEVIER LICENSE TERMS AND CONDITIONS

Jun 30, 2014

This is a License Agreement between Mehran Behazin ("You") and Elsevier ("Elsevier") provided by Copyright Clearance Center ("CCC"). The license consists of your order details, the terms and conditions provided by Elsevier, and the payment terms and conditions.

All payments must be made in full to CCC. For payment instructions, please see information listed at the bottom of this form.

Supplier	Elsevier Limited The Boulevard, Langford Lane Kidlington, Oxford, OX5 1GB, UK
Registered Company Number	1982084
Customer name	Mehran Behazin
Customer address	171, 1560 Adelaide st north london, ON N5X2C1
License number	3419000449320
License date	Jun 30, 2014
Licensed content publisher	Elsevier
Licensed content publication	Electrochimica Acta
Licensed content title	Combined Effects of pH and γ -Irradiation on the Corrosion of Co-Cr Alloy Stellite-6
Licensed content author	M. Behazin, J.J. Noël, J.C. Wren
Licensed content date	10 July 2014
Licensed content volume number	134
Licensed content issue number	None
Number of pages	12
Start Page	399
End Page	410
Type of Use	reuse in a thesis/dissertation
Intended publisher of new work	other
Portion	full article
Format	both print and electronic
Are you the author of this Elsevier article?	Yes

<https://s100.copyright.com/AppDispatchServlet>

1/7

6/30/2014

Rightslink Printable License

Will you be translating?	No
Title of your thesis/dissertation	Radiation Induced Corrosion of Stellite-6
Expected completion date	Sep 2014
Estimated size (number of pages)	200
Elsevier VAT number	GB 494 6272 12
Permissions price	0.00 USD
VAT/Local Sales Tax	0.00 USD / 0.00 GBP
Total	0.00 USD
Terms and Conditions	

INTRODUCTION

1. The publisher for this copyrighted material is Elsevier. By clicking "accept" in connection with completing this licensing transaction, you agree that the following terms and conditions apply to this transaction (along with the Billing and Payment terms and conditions established by Copyright Clearance Center, Inc. ("CCC"), at the time that you opened your Rightslink account and that are available at any time at <http://myaccount.copyright.com>).

GENERAL TERMS

2. Elsevier hereby grants you permission to reproduce the aforementioned material subject to the terms and conditions indicated.

3. Acknowledgement: If any part of the material to be used (for example, figures) has appeared in our publication with credit or acknowledgement to another source, permission must also be sought from that source. If such permission is not obtained then that material may not be included in your publication/copies. Suitable acknowledgement to the source must be made, either as a footnote or in a reference list at the end of your publication, as follows:

"Reprinted from Publication title, Vol /edition number, Author(s), Title of article / title of chapter, Pages No., Copyright (Year), with permission from Elsevier [OR APPLICABLE SOCIETY COPYRIGHT OWNER]." Also Lancet special credit - "Reprinted from The Lancet, Vol. number, Author(s), Title of article, Pages No., Copyright (Year), with permission from Elsevier."

4. Reproduction of this material is confined to the purpose and/or media for which permission is hereby given.

5. Altering/Modifying Material: Not Permitted. However figures and illustrations may be altered/adapted minimally to serve your work. Any other abbreviations, additions, deletions and/or any other alterations shall be made only with prior written authorization of Elsevier Ltd. (Please contact Elsevier at permissions@elsevier.com)

6. If the permission fee for the requested use of our material is waived in this instance, please be advised that your future requests for Elsevier materials may attract a fee.

<https://s100.copyright.com/AppDispatchServlet>

2/7

6/30/2014

Rightslink Printable License

7. Reservation of Rights: Publisher reserves all rights not specifically granted in the combination of (i) the license details provided by you and accepted in the course of this licensing transaction, (ii) these terms and conditions and (iii) CCC's Billing and Payment terms and conditions.

8. License Contingent Upon Payment: While you may exercise the rights licensed immediately upon issuance of the license at the end of the licensing process for the transaction, provided that you have disclosed complete and accurate details of your proposed use, no license is finally effective unless and until full payment is received from you (either by publisher or by CCC) as provided in CCC's Billing and Payment terms and conditions. If full payment is not received on a timely basis, then any license preliminarily granted shall be deemed automatically revoked and shall be void as if never granted. Further, in the event that you breach any of these terms and conditions or any of CCC's Billing and Payment terms and conditions, the license is automatically revoked and shall be void as if never granted. Use of materials as described in a revoked license, as well as any use of the materials beyond the scope of an unrevoked license, may constitute copyright infringement and publisher reserves the right to take any and all action to protect its copyright in the materials.

9. Warranties: Publisher makes no representations or warranties with respect to the licensed material.

10. Indemnity: You hereby indemnify and agree to hold harmless publisher and CCC, and their respective officers, directors, employees and agents, from and against any and all claims arising out of your use of the licensed material other than as specifically authorized pursuant to this license.

11. No Transfer of License: This license is personal to you and may not be sublicensed, assigned, or transferred by you to any other person without publisher's written permission.

12. No Amendment Except in Writing: This license may not be amended except in a writing signed by both parties (or, in the case of publisher, by CCC on publisher's behalf).

13. Objection to Contrary Terms: Publisher hereby objects to any terms contained in any purchase order, acknowledgment, check endorsement or other writing prepared by you, which terms are inconsistent with these terms and conditions or CCC's Billing and Payment terms and conditions. These terms and conditions, together with CCC's Billing and Payment terms and conditions (which are incorporated herein), comprise the entire agreement between you and publisher (and CCC) concerning this licensing transaction. In the event of any conflict between your obligations established by these terms and conditions and those established by CCC's Billing and Payment terms and conditions, these terms and conditions shall control.

14. Revocation: Elsevier or Copyright Clearance Center may deny the permissions described in this License at their sole discretion, for any reason or no reason, with a full refund payable to you. Notice of such denial will be made using the contact information provided by you. Failure to receive such notice will not alter or invalidate the denial. In no event will Elsevier or Copyright Clearance Center be responsible or liable for any costs, expenses or damage incurred by you as a result of a denial of your permission request, other than a refund of the amount(s) paid by you to Elsevier and/or Copyright Clearance Center for denied permissions.

LIMITED LICENSE

<https://s100.copyright.com/AppDispatchServlet>

3/7

The following terms and conditions apply only to specific license types:

15. Translation: This permission is granted for non-exclusive world **English** rights only unless your license was granted for translation rights. If you licensed translation rights you may only translate this content into the languages you requested. A professional translator must perform all translations and reproduce the content word for word preserving the integrity of the article. If this license is to re-use 1 or 2 figures then permission is granted for non-exclusive world rights in all languages.

16. Posting licensed content on any Website: The following terms and conditions apply as follows: Licensing material from an Elsevier journal: All content posted to the web site must maintain the copyright information line on the bottom of each image; A hyper-text must be included to the Homepage of the journal from which you are licensing at <http://www.sciencedirect.com/science/journal/xxxx> or the Elsevier homepage for books at <http://www.elsevier.com>; Central Storage: This license does not include permission for a scanned version of the material to be stored in a central repository such as that provided by Heron/XanEdu.

Licensing material from an Elsevier book: A hyper-text link must be included to the Elsevier homepage at <http://www.elsevier.com>. All content posted to the web site must maintain the copyright information line on the bottom of each image.

Posting licensed content on Electronic reserve: In addition to the above the following clauses are applicable: The web site must be password-protected and made available only to bona fide students registered on a relevant course. This permission is granted for 1 year only. You may obtain a new license for future website posting.

For journal authors: the following clauses are applicable in addition to the above: Permission granted is limited to the author accepted manuscript* of your paper.

***Accepted Author Manuscript (AAM) Definition:** An accepted author manuscript (AAM) is the author's version of the manuscript of an article that has been accepted for publication and which may include any author-incorporated changes suggested through the processes of submission processing, peer review, and editor-author communications. AAMs do not include other publisher value-added contributions such as copy-editing, formatting, technical enhancements and (if relevant) pagination.

You are not allowed to download and post the published journal article (whether PDF or HTML, proof or final version), nor may you scan the printed edition to create an electronic version. A hyper-text must be included to the Homepage of the journal from which you are licensing at <http://www.sciencedirect.com/science/journal/xxxx>. As part of our normal production process, you will receive an e-mail notice when your article appears on Elsevier's online service ScienceDirect (www.sciencedirect.com). That e-mail will include the article's Digital Object Identifier (DOI). This number provides the electronic link to the published article and should be included in the posting of your personal version. We ask that you wait until you receive this e-mail and have the DOI to do any posting.

Posting to a repository: Authors may post their AAM immediately to their employer's

institutional repository for internal use only and may make their manuscript publically available after the journal-specific embargo period has ended.

Please also refer to [Elsevier's Article Posting Policy](#) for further information.

18. For book authors the following clauses are applicable in addition to the above: Authors are permitted to place a brief summary of their work online only.. You are not allowed to download and post the published electronic version of your chapter, nor may you scan the printed edition to create an electronic version. **Posting to a repository:** Authors are permitted to post a summary of their chapter only in their institution's repository.

20. Thesis/Dissertation: If your license is for use in a thesis/dissertation your thesis may be submitted to your institution in either print or electronic form. Should your thesis be published commercially, please reapply for permission. These requirements include permission for the Library and Archives of Canada to supply single copies, on demand, of the complete thesis and include permission for UMI to supply single copies, on demand, of the complete thesis. Should your thesis be published commercially, please reapply for permission.

Elsevier Open Access Terms and Conditions

Elsevier publishes Open Access articles in both its Open Access journals and via its Open Access articles option in subscription journals.

Authors publishing in an Open Access journal or who choose to make their article Open Access in an Elsevier subscription journal select one of the following Creative Commons user licenses, which define how a reader may reuse their work: Creative Commons Attribution License (CC BY), Creative Commons Attribution – Non Commercial - ShareAlike (CC BY NC SA) and Creative Commons Attribution – Non Commercial – No Derivatives (CC BY NC ND)

Terms & Conditions applicable to all Elsevier Open Access articles:

Any reuse of the article must not represent the author as endorsing the adaptation of the article nor should the article be modified in such a way as to damage the author's honour or reputation.

The author(s) must be appropriately credited.

If any part of the material to be used (for example, figures) has appeared in our publication with credit or acknowledgement to another source it is the responsibility of the user to ensure their reuse complies with the terms and conditions determined by the rights holder.

Additional Terms & Conditions applicable to each Creative Commons user license:

CC BY: You may distribute and copy the article, create extracts, abstracts, and other revised versions, adaptations or derivative works of or from an article (such as a translation), to include in a collective work (such as an anthology), to text or data mine the article, including for commercial purposes without permission from Elsevier

6/30/2014

Rightslink Printable License

CC BY NC SA: For non-commercial purposes you may distribute and copy the article, create extracts, abstracts and other revised versions, adaptations or derivative works of or from an article (such as a translation), to include in a collective work (such as an anthology), to text and data mine the article and license new adaptations or creations under identical terms without permission from Elsevier

CC BY NC ND: For non-commercial purposes you may distribute and copy the article and include it in a collective work (such as an anthology), provided you do not alter or modify the article, without permission from Elsevier

Any commercial reuse of Open Access articles published with a CC BY NC SA or CC BY NC ND license requires permission from Elsevier and will be subject to a fee.

Commercial reuse includes:

- Promotional purposes (advertising or marketing)
- Commercial exploitation (e.g. a product for sale or loan)
- Systematic distribution (for a fee or free of charge)

Please refer to [Elsevier's Open Access Policy](#) for further information.

21. Other Conditions:

v1.7

If you would like to pay for this license now, please remit this license along with your payment made payable to "COPYRIGHT CLEARANCE CENTER" otherwise you will be invoiced within 48 hours of the license date. Payment should be in the form of a check or money order referencing your account number and this invoice number 501340500. Once you receive your invoice for this order, you may pay your invoice by credit card. Please follow instructions provided at that time.

Make Payment To:
Copyright Clearance Center
Dept 001
P.O. Box 843006
Boston, MA 02284-3006

For suggestions or comments regarding this order, contact RightsLink Customer Support: customer@copyright.com or +1-877-622-5543 (toll free in the US) or +1-978-646-2777.

Gratis licenses (referencing \$0 in the Total field) are free. Please retain this printable license for your reference. No payment is required.

<https://s100.copyright.com/AppDispatchServlet>

6/7

Mehran Behazin's Curriculum Vitae

EDUCATION

Ph.D. candidate in Physical Chemistry, University of Western Ontario
(Sept. 2009-Sept. 2014)

Master of Science in Physical Chemistry, K.N.T University of Technology
(Sept. 2005- Dec. 2007)

Bachelor of Science in Applied chemistry, Sharif University of Technology
(Sept. 2000-Dec. 2004)

WORK EXPERIENCE

- Occupational Health and Safety Officer, Western University (June 2011-Sept. 2014)
- Project leader of undergraduate students, Dr. Wren lab, Western University (May 2010, June 2012, June 2013)
- Chief Steward, Western University (Dec. 2000-July 2011)
- Teaching Assistant, First year chemistry, Western University (Sept. 2009-May 2014)
- Research Assistant, Western University (Sept. 2009-Sept. 2014)
- Lab Assistant, Electrochemistry Lab, K.N.Toosi of Technology (Oct. 2006-Dec. 2007)

PUBLICATIONS

Peer-Reviewed Articles

M. Behazin, J.J. Noël, J.C. Wren, Combined Effects of pH and gamma-Irradiation on Stellite-6 Corrosion, *Electrochimica Acta*, 134 (2014) 399-410.

A.Y Musa, **M Behazin**, Q Knapp, D. Mizzi, J.C Wren. Effect of Water Radiolysis on Corrosion: Steel, Cobalt and Nickel Alloys, in the proceedings of 34th Annual Conference of the Canadian Nuclear Society, June 9-12, 2013, 13 pages.

M. Behazin, M. C. Beisinger, J.J. Noël, J. C. Wren, Radiation-Induced Corrosion of Stellite-6 at Elevated Temperature, in the proceedings of Nuclear Plant Chemistry Conference, Paris, September 24–28 (2012), page 1-8.

M. Behazin, X. Zhang, J.J. Noël, J.C. Wren, Comparative Study of Oxide Film Formation as a Function of Potential on Pure Co and Stellite-6, *Corrosion Science*, 63 (2012) 40–50.

Non-Refereed Articles

- M. Behazin**, J.J. Noël, J. C. Wren, Temperature Dependence of Radiation-Induced Corrosion of Stellite-6 at pH 10.6, in the proceedings of 33^d Annual Canadian Nuclear Society Conference, Saskatoon, June 10-13, 2012. (2012)
- M. Behazin**, X. Zhang, J.J. Noël, J.C. Wren, The Influence of Radiation Exposure and Hydrogen Peroxide on the Corrosion Behaviour of Cobalt and Stellite-6, in the proceedings of 32nd Annual Canadian Nuclear Society Conference, Niagara, June 5-8 (2011).

SELECTED POSTERS AND PRESENTATIONS

Oral presentations

- M. Behazin**, J.J. Noël, J.C. Wren, Gamma-radiation Induced Stellite-6 Corrosion: pH and Temperature Dependences. UNENE Workshop, Toronto, Dec 11-13, 2013.
- M. Behazin**, J.J. Noël, J. C. Wren, Effect of Gamma-Irradiation on Stellite-6 Corrosion: Dependence on pH and Temperature, MS&T conference, Montreal, Oct 27-31, 2013.
- M. Behazin**, J.J. Noël, J. C. Wren, Effect of Gamma-Irradiation on Stellite-6 Corrosion, IRC meeting, Western University, London, June 24th, 2013
- M. Behazin**, J.J. Noël, J. C. Wren, Effect of Gamma-Irradiation on Stellite-6 Corrosion: Dependence on pH and Temperature, NACE symposium, Western University, London, June 24th, 2013.
- M. Behazin**, J.J. Noël, J. C. Wren, Effect of Gamma-Irradiation on Stellite-6 Corrosion: Dependence on pH and Temperature ECS conference, Toronto, May 12-16, 2013.
- M. Behazin**, X. Zhang, J.J. Noël, J.C. Wren, Film Formation and Conversion of Stellite-6 and Pure Co as a Function of Potential. Joint Student Corrosion Symposium, McMaster University, Hamilton, ON, May 18, 2011.

Poster presentations

- M. Behazin**, J.J. Noël, J.C. Wren, Decreasing Radiation Exposure to Nuclear Workers By Corrosion Control, Sustainability and Green Chemistry Showcase, London, March 6, 2014.
- M. Behazin**, J.J. Noël, J.C. Wren, Effect of Gamma-Irradiation on Stellite-6 Corrosion: Dependence on pH and Temperature, Surface Science Canada conference, London, May 6-8, 2013.
- M. Behazin**, J.J. Noël, J.C. Wren, Radiation Induced Film Formation on Stellite-6. UNENE, R&D Workshop. Toronto, ON, Dec 12, 2012.
Gordon Research Conference, New London, United State, July 7-13, 2012.
- M. Behazin**, J.J. Noël, J.C. Wren, Temperature Dependence of Radiation-Induced Corrosion of Stellite-6 at pH 10.6. 33^d Annual Canadian Nuclear Society Conference, Saskatoon, June 10-13, 2012.